High-Energy Cosmic Ray Anisotropies

by

Glenn Barry

G.B. Hyland, B.Sc. (Hons), University of Tasmania

submitted in fulfilment

of the requirements for the degree of

Doctor of Philosophy

University of Tasmania

Hobart

December, 1990

To Melissa

This thesis contains no material which has been accepted for the award of any other degree or diploma in any university.

To the best of my knowledge and belief, the thesis contains no material previously published or written by another person, except where due reference is made in the text.

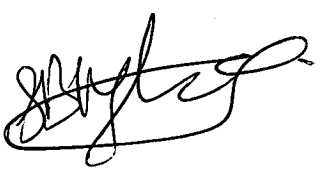

G.B. Hyland

Contents

Acknowledgements

I wish to thank my supervisor, Dr J.E. Humble, for his guidance and encouragement during the course of this work. It is also a pleasure to thank Dr K.B. Fenton for the many helpful discussions, and for providing supervision during the absence of Dr. Humble. I also acknowledge the efforts of Dr A.G. Fenton towards the construction and installation of the telescopes.

I am extremely grateful to Mr P. Button and Mr K. Bolton for their technical advice regarding the data recording system used in the project.

Finally, my thanks go to those staff members and students at the Physics Department who have shown interest in the project, and to those people who gave advice and support throughout my candidature.

Summary

The cosmic-ray group at the University of Tasmania has operated a number of muon telescopes at the Poatina underground cosmic ray station (latitude 41.8°S, 357 hg cm^{-2} below the top of the atmosphere) since 1972. The most recently constructed telescopes comprise four trays of 2 metre long proportional counters arranged to give a total effective collecting area of approximately 4 m^2. The muon threshold energy for vertical incidence at the depth of the station is 100 GeV corresponding to a median primary energy of 1.2 TeV.

In 1983 the recording system of one telescope was upgraded to register the arrival direction of incident particles. This system utilizes the telescope configuration which provides an angular resolution for vertically incident particles of approximately $5° \times 5°$. For the current project, the same recording system was further upgraded with the construction of a high-precision temperature controlled clock which provides the arrival time of incident particles to the nearest millisecond.

Data collected over the period August 1987 to January 1989 have been used to search for possible narrow-angle anisotropies in the declination band 20°N to 90°S. No significant deviation from an isotropic distribution of arrival directions has been found. In particular, the observations fail to confirm the existence of a previously reported narrow-angle excess of particles observed at the same station; providing further evidence of the apparent limited duration of such anisotropies. An upper limit on the particle flux from possible point sources has been calculated as 6.1×10^{-9} $cm^{-2}\,s^{-1}$ at the 95% confidence level.

In addition, the particle arrival time data has been used to search for a time modulated underground muon flux from the direction of the Vela pulsar. The observations reveal no evidence for the existence of any steady periodic emission

from the pulsar, but two marginally significant bursts of pulsed emission of duration several hours have been observed. Perhaps more significantly, these episodes of periodic enhancement were observed just before a glitch in the pulsar period; the first burst occurred 20 days before the glitch and the second just 2 hours before the initial frequency jump. If the enhancements are genuine signals, the measured underground muon flux is substantially higher than would be expected based on extrapolations from ground-based gamma-ray observations to the underground observing site using standard high-energy particle interaction models.

Chapter 1

Introduction

The cosmic-ray group at the University of Tasmania operates a number of muon telescopes at various surface and underground sites in the southern hemisphere. The data provided by these telescopes are primarily used to study cosmic-ray sidereal variations. This work is concerned with the utilization of one of the underground muon telescopes for the measurement of narrow-angle features in the high-energy cosmic-ray flux.

This chapter provides some background for the scientific aspects of the project. Section 1 describes the various muon production processes and Section 2 briefly outlines the important properties of the underground muon flux. Section 3 presents a brief review of observations of some high-energy gamma-ray sources, with particular regard to certain anomalous muon measurements. The final section of the chapter presents a precis of the other chapters of the thesis.

1.1 Muon Production

On entering the Earth's atmosphere, a primary cosmic ray will collide with the nucleus of an atmospheric atom or molecule. The absorption length for protons in air is ~ 120 g cm^{-2}, and considerably less for the heavier nuclei. The depth of the atmosphere is ~ 1030 g cm^{-2} so the initial interaction will usually take place in the first tenth of the atmosphere.

The nuclear collision results in the ejection of one or several nucleons from the

target nucleus. The initiating particle will lose on average more than half its energy during the interaction (i.e. inelasticity > 0.5). The target nucleus does not gain much energy from the collision. The detached nucleons, if sufficiently energetic, are capable of undergoing further nuclear collisions producing what is described as a *nucleonic cascade*.

Nuclear interactions are inelastic, the energy lost in collisions being channeled into the creation of other particles. The majority of secondary particles are pions, although kaons and other heavier hadrons may also be produced. At low primary energies, the relative proportion of kaons to pions is small, but increases to ~ 15% for primaries of energy > 100 GeV (Thompson 1973).

Pions exist in three states of charge, singly positive or negative, and neutral. For sufficiently energetic primaries, they are believed to be produced in equal numbers for each charge. Neutral pions have a mass of 135 MeV/c^2, a half-life of 8.7×10^{-17} s, and effectively decay immediately into two high energy gamma-rays. The gamma-rays are sufficiently energetic to undergo pair-production in the field of an atmospheric nucleus, creating an electron-positron pair. The electrons and positrons accelerated in the field of a nucleus undergo bremsstrahlung producing further gamma-rays. This repetitive process gives rise to what is known as the *electron-photon* (or *electromagnetic*) *cascade*.

Charged pions have a mass of 140 MeV/c^2 and a half-life of 2.6×10^{-8} s. Kaons also occur in three states of charge. Charged kaons have a mass of 494 MeV/c^2 and a half-life of ~ 1.2×10^{-8} s. Positive kaons are more likely to be produced in cosmic ray interactions than negative ones. The neutral kaon has a mass of 497 MeV/c^2 and together with its anti-particle occurs in two quantum mechanically mixed states, K°_S and K°_L. The kaons and charged pions may themselves interact with atmospheric nuclei, or decay. The most common decay processes (which give rise to muons) for the particles are

$$\pi^{\pm} \rightarrow \mu^{\pm} + \nu_{\mu}\,(\nabla_{\mu}) \qquad (100.0\%)$$

$$K^{\pm} \rightarrow \mu^{\pm} + \nu_{\mu}\,(\nabla_{\mu}) \qquad (63.5\%)$$

$$\rightarrow \mu^{\pm} + \nu_{\mu}\,(\nabla_{\mu}) + \pi^{\circ} \qquad (3.2\%)$$

$$K^{\circ}_{L} \rightarrow \mu^{\pm} + \nu_{\mu}\,(\nabla_{\mu}) + \pi^{\mp} \qquad (27.1\%)$$

The figures in brackets are the decay branching ratios (Particle Data Group, 1986). Other kaon decay modes give rise to pions, which either interact or decay, and electrons.

The muon-neutrinos produced in the decay of pions, kaons and muons (see below) also give rise to a small flux of muons which is significant for deep underground detectors. These neutrino induced muons are produced via the *charged-current* process

$$\nu_{\mu} + N \rightarrow \mu^{\pm} + X$$

The small cross-section of this interaction is such that the Earth's diameter represents only 10^{-4} of an interaction length. Neutrino induced muons are usually observed in deep underground detectors where the flux of conventional muons (i.e. from pion and kaon decays) is comparable to the flux of muons from neutrino interactions in the rock or water surrounding the detector. The flux of neutrino induced muons increases with zenith angle, being a maximum for horizontal viewing directions. Thus, they are observed as large zenith angle events ($\theta > 60°$) in detectors such as the Kolar Gold Fields (KGF) detector (Krishnaswamy *et al.* 1986), where the background due to conventional muons is negligible due to their steep zenith angle distribution (see Section 1.2.2). In proton decay detectors, such as IMB (Svoboda *et al.* 1987) and Kamioka (Hirata *et al.* 1988), neutrino induced muons are observed as upwardly moving events originating from neutrinos entering from the opposite side of the earth

and interacting in the rock below the detector.

A further source of muons is through the semi-leptonic decay of charmed particles, mainly D-mesons and Λ_c-hyperons. These are short-lived particles with lifetimes of a few $\times 10^{-13}$ s which give rise to so-called *prompt* muons via the following decay processes

$$D \rightarrow K + \mu + \nu \qquad (\sim 7.0\%)$$

$$\Lambda_c \rightarrow \Lambda_o + \mu + \nu \qquad (\sim 4.5\%)$$

These directly produced muons have an energy spectrum which falls off more slowly, by about a factor of E, than the spectrum of conventional muons (see below). Thus, at some high energy the prompt muon flux will be equal to the conventional muon flux and will dominate at higher energies. Calculations by Bugaev *et al.* (1987) predict that this cross-over point should be somewhere in the region 50 - 200 TeV. Due to the short lifetimes of the parent particles, prompt muons display an almost isotropic angular distribution as opposed to the "sec θ" dependence of muons from pion and kaon decay (see Section 1.2.2). Studies of prompt muon production are made by direct or indirect measurements of the muon sea-level energy spectrum (see Section 1.2.1), or by measuring deviations of the angular distribution of muons from the "sec θ" law (e.g. Bilokon *et al.* 1985).

Muons are charged particles with a mass of 106 MeV/c^2. A relatively long half-life of 2.2×10^{-6} s results in muons with Lorentz factors > 20 being able to reach sea-level. Less energetic muons decay in flight according to the process

$$\mu^{\pm} \rightarrow e^{\pm} + \nu_e\,(\bar{\nu}_e) + \bar{\nu}_\mu\,(\nu_\mu)$$

Muons are *weakly-interacting* particles, losing energy via ionization at a rate of

~ 2 MeV $(g\ cm^{-2})^{-1}$. High energy muons ($E > 2$ GeV) will therefore survive to sea-level. At higher muon energies (> 500 GeV) the energy loss is dominated by the processes of bremsstrahlung and pair production which introduce large fluctuations in the muon survival probability. The maximum rate of muon production is found to occur at an atmospheric depth of $\sim 100\ g\ cm^{-2}$, close to the absorption length of protons in air; the distribution of particle intensity with atmospheric depth is shown in Figure 1.1.

The total flux of muons ($p > 0.35$ GeV/c) at sea-level is $(1.44 \pm 0.09) \times 10^{-2}$ $cm^{-2}\ s^{-1}$ with an median energy of ~ 1 GeV. The differential muon spectrum at sea-level can be described by a power law with a spectral index that decreases with momentum, being -3.0 at about 100 GeV/c (Stephens and Golden, 1987).

1.2 Underground Measurements

The muon component is more penetrating than either the nucleon or electromagnetic component, so measurements of the muon flux are made by covering surface detectors with thick absorbers or by locating detectors underground and using the natural overburden as the absorber. At moderate underground depths ($> \sim 10$ m) the muon component is unaccompanied by other particles, except for a small flux of electrons produced via the *knock-on* process.

1.2.1 Depth-Intensity Variation

The variation of muon intensity with depth underground has been measured by many workers at depths ranging from sea-level to $> 10^7\ g\ cm^{-2}$ (e.g. Crouch *et al.* 1978). Due to the complexity of muon production processes and energy loss mechanisms it is difficult to derive a simple analytical expression for the muon depth-

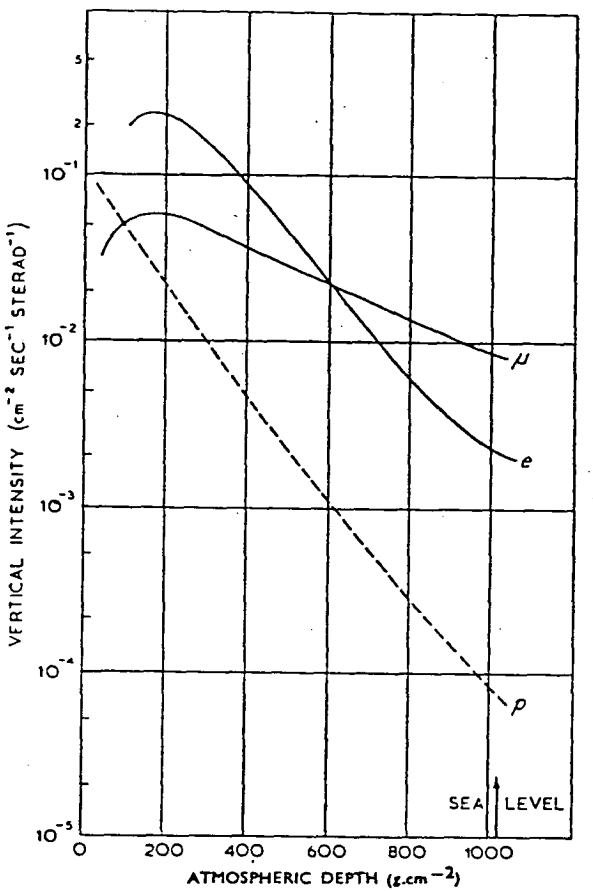

Figure 1.1 The variation of particle intensity with atmospheric depth (from Rossi 1952)

intensity variation. The variation is usually represented by empirical expressions, such as the semi-empirical expression proposed by Miyake (1973) which is based on approximations to muon production and energy loss mechanisms, or purely empirical expressions which give the best fit to the observational data (e.g. Cassidy *et al.* 1973). Barret *et al.* (1952) have collated the depth-intensity measurements of many workers; the results are shown in Figure 1.2. Similarly, Crouch (1987) has produced a "World Survey" curve of cosmic ray intensity as a function of large depths underground; the curve is shown in Figure 1.3.

At muon energies less than several TeV, the sea-level muon spectrum is usually determined by magnetic spectrograph measurements, the muon momentum being determined directly from the deflection of the muon in a magnetic field (e.g. Allkofer *et al.* 1971). At higher muon energies, information on the sea-level spectrum comes from indirect methods such as measurements of bursts produced by muons in lead or iron plates and underground muon intensity measurements (e.g. Bergamasco *et al.* 1983).

The vertical intensity $I_v(h)$ at depth h is related to the muon energy differential spectrum $J(E)$ by the relation

$$I_v(h) = \int_{E_{th}}^{\infty} P(E,h)\, J(E)\, dE \qquad (1.1)$$

where

$P(E,h)$ is the probability that a muon of energy E reaches the depth h,

and

E_{th} is the smallest value of E for which $P(E,h) > 0$.

Thus, a precise determination of the muon energy spectrum from the muon depth-intensity variation requires detailed knowledge of the chemical composition and topography of the detector overburden as well as muon interaction cross-sections. There are inherent uncertainties in depth determination for most underground

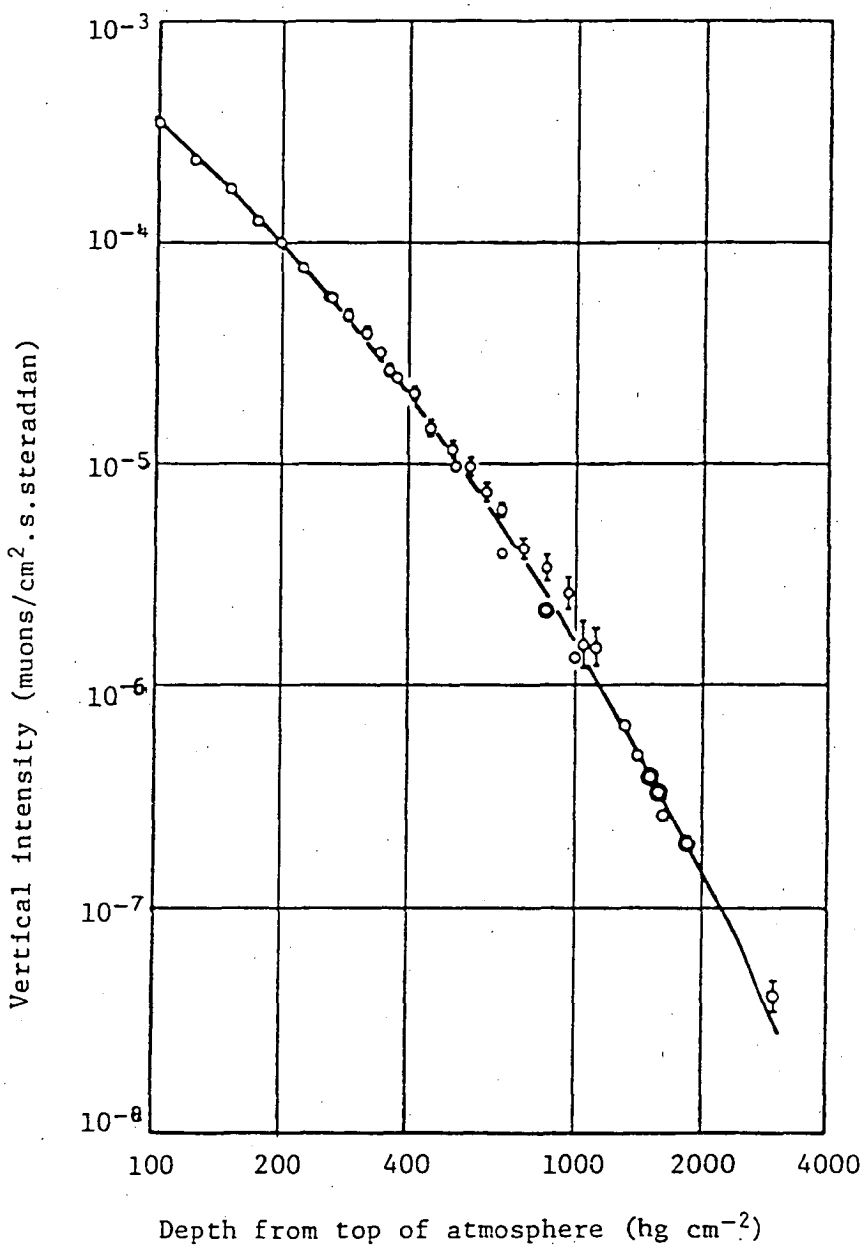

Figure 1.2 The variation of muon intensity for relatively shallow underground depths (from Barret *et al.* 1952)

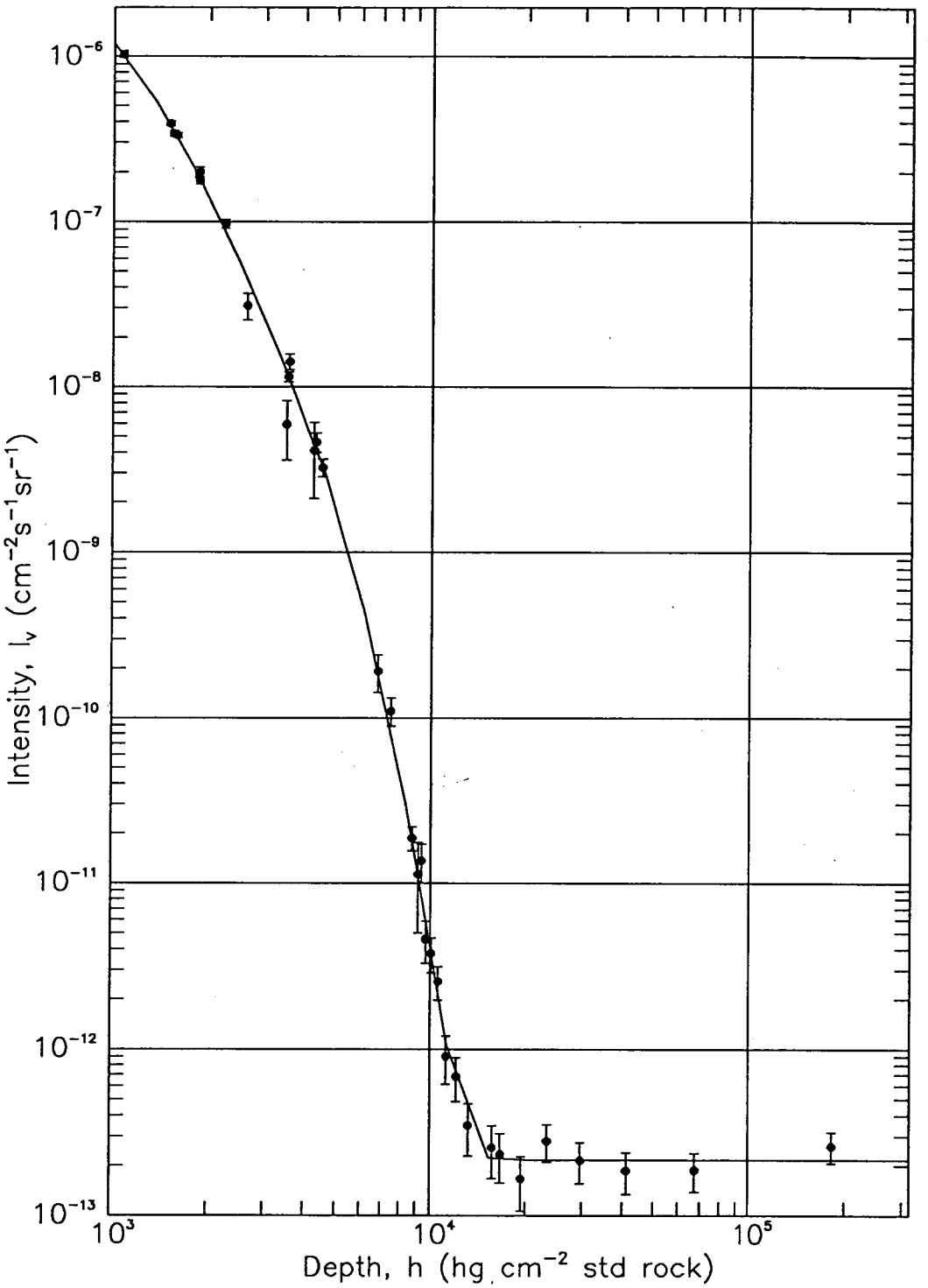

Figure 1.3 The variation of muon intensity for large depths underground (from Crouch 1987).

installations due to the extreme depths of the detectors, large variations in surface terrain and unknown rock composition. This of course is not the case for underwater detectors where the composition of the overburden is well-known.

1.2.2 Zenith Angle Distribution

The muon intensity measured by a detector located at a vertical depth h at zenith angle θ is usually expressed as

$$I(h,\theta) = I_v(h) \cos^n \theta \tag{1.2}$$

where n is approximately 2. This expression is appropriate for shallow depths and flat surface topographies. At larger depths, a good approximation to the zenith angle distribution of intensities is

$$I(h,\theta) = I_v(h \sec \theta) \sec \theta \tag{1.3}$$

The $\sec \theta$ enhancement factor arises from the increased decay probability for pions travelling at large zenith angles. Such pions spend more time in the tenuous parts of the atmosphere and are therefore more likely to decay before interacting with atmospheric nuclei.

1.2.3 Atmospheric Modulation

It has long been known that the count rates of ground-based and underground cosmic-ray detectors are strongly influenced by changes in meteorological conditions. The importance of precisely determining these atmospheric effects is to allow corrections to be made, thereby revealing the underlying primary variations. The

subject of meteorological corrections has been studied by many workers over the last 40 years so the mechanisms of and theory behind atmospheric modulations are well understood (e.g. Dorman 1987).

The atmospheric contributions to the intensity variations recorded by underground muon detectors can be obtained using the four-fold regression equation

$$\frac{\Delta I}{\langle I \rangle} = b_P \Delta P + b_H \Delta H + b_T \Delta T \qquad (1.4)$$

where $\Delta I / \langle I \rangle$ represents the fractional change in muon intensity from some long-term average. The three coefficients b_P, b_H, b_T are the *partial* pressure, height and temperature coefficients respectively corresponding to fractional changes in air pressure, ΔP, mean muon production height, ΔH, and temperature at the pion production level, ΔT.

Whereas at large underground depths the mass absorption (b_P) and muon decay (b_H) effects are negligible, the effect of temperature on muon production (b_T) is appreciable, producing a relatively large influence on the muon intensity. Sagisaka *et al.* (1979) have detailed the total barometer coefficients measured at various underground stations; the results are shown in Figure 1.4.

1.2.4 Multiple Muons

Multiple coincident muons (or muon bundles) observed in underground detectors are the remnants of air showers produced in the atmosphere by high energy cosmic ray protons and heavy nuclei. The production rate of muon bundles is sensitive to the energy spectrum and composition of primary cosmic rays, due to the different muon yields from nuclei of different mass and the same total energy. Bundles with increasing multiplicity correspond, on average, to higher energy primaries. Thus, the

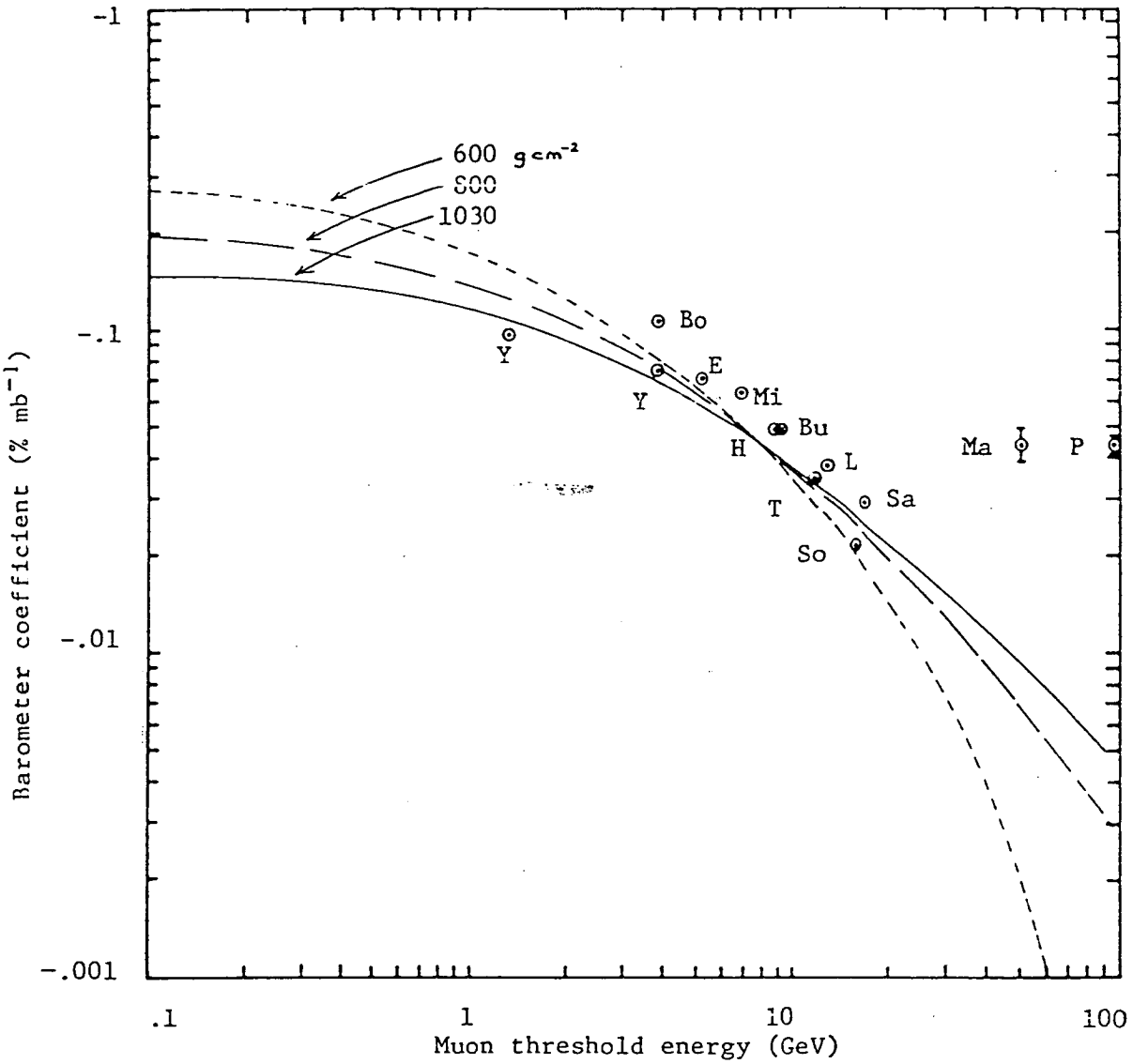

	Station	Atm. depth (g cm^{-2})
Bo	Bolivia	520
Bu	Budapest	980
E	Embudo	750
H	Hobart (Cambridge)	1000
L	London	sea level
Mi	Misato	940
Sa	Sakashita	980
So	Soccoro	850
Ta	Takeyama	sea level
Y	Yakutsk	1020
Ma	Matsushiro	—
P	Poatina	1000

Figure 1.4 Underground barometer coefficients (from Sagisaka *et al.* 1979). The inflated Poatina coefficient has since been shown to be almost entirely due to a correlation between surface air pressure and upper air temperature, together with temperature measurement errors (Lyons *et al.* 1981).

composition near the *knee* of the primary spectrum, where it is least well defined, can be investigated by a study of high multiplicity muon bundles in deep underground detectors (e.g. Bologna *et al.* 1985).

Multiple muon events also allow determination of the average characteristics of high energy nuclear interactions, since the muons are weakly-interacting particles and thus carry direct information about charged secondaries produced in the earliest stages of the cascade development.

Observations of muon bundles are usually presented in terms of the muon multiplicity distribution and the lateral distribution of muons within the bundle. These are compared to predictions which, due to the complex interplay between the energy spectrum of different primary nuclei and muon production and energy loss mechanisms, are usually derived from Monte Carlo simulations of the cascade development in the atmosphere and muon propagation in the detector overburden (e.g. Gaisser and Stanev, 1985).

1.2.5 Angular Resolution

There are three major contributions to the angular uncertainty associated with primary particle directions as measured by underground detectors, apart from the intrinsic angular resolution of the detector itself. These are transverse momentum imparted to muons produced in high energy collisions, deflection of muons in the Earth's magnetic field, and multiple Coulomb scattering in the detector overburden.

The mean transverse momentum of secondary particles produced in high energy collisions can be parametrized (in agreement with collider data) as

$$\langle P_t \rangle = 0.0151 \ln(E / \mathrm{GeV}) + 0.24 \ \mathrm{GeV/c} \qquad (1.5)$$

for particles of energy E in the laboratory system (Acharya and Capdevielle, 1985). To a first approximation the angular deviation from the parent direction is then given by

$$\langle\theta\rangle = \frac{\langle P_t\rangle c}{E} \tag{1.6}$$

For example, $E = 100$ GeV gives $\langle P_t\rangle = 0.31$ GeV/c and $\langle\theta\rangle = 0.18°$.

Geomagnetic deflection is mostly important for low energy muons ($E_\mu < 500$ GeV) as observed by detectors at relatively shallow underground depths. The angular deviation of a muon in the plane normal to the field B is given by

$$\Delta\theta = 3 \times 10^{-5} \frac{h B}{E_\mu} \sin\alpha \tag{1.7}$$

where

E_μ is the muon energy in GeV,

B is the magnetic field strength in Gauss,

h is the distance along the shower axis from the detector to the point of muon production in metres, and

α is the angle between the magnetic field and the muon trajectory.

For example, the maximum angular deflection of a muon of energy $E_\mu = 100$ GeV with $h = 15$ km in a field of 0.3 G is $\Delta\theta = 0.08°$.

Multiple Coulomb scattering is the main contributor to the angular uncertainty for extremely deep detectors. The distribution of angular deflections in the direction of a muon passing through X hg cm^{-2} of matter can be approximated by a Gaussian distribution with zero mean and standard deviation given by

$$\sigma = \langle\theta^2\rangle^{1/2} = 0.04 \frac{X^{1/2}}{E_\mu} \tag{1.8}$$

where E_μ is the energy of the muon in GeV (Scott 1963). The approximation is valid

for small deflection angles, i.e. $\theta < 2\sigma$. For example, for $X = 347$ hg cm^{-2} and $E_\mu = 100$ GeV, $\sigma = 0.43°$.

1.3 Gamma-ray Sources

Observations of high-energy gamma-ray sources have been traditionally the domain of ground-based Cerenkov gamma-ray telescopes (at VHE energies, 10^{11} - 10^{14} eV) and air shower arrays (at energies > 10^{14} eV). However, in recent years, many underground installations have directed their attention to the observation of particular celestial objects, following the surprising detection by two separate nucleon decay experiments of an underground muon flux from the direction of the high-energy gamma-ray source Cygnus X-3. In each case, the muon flux appeared to be modulated with the 4.8 hour periodicity of the source.

The Soudan-1 detector recorded an excess of events between the phases 0.65 and 0.9 (Marshak *et al.* 1985) and the NUSEX detector found an excess of events between phases 0.7 and 0.8 (Battistoni *et al.* 1985). Both phase distributions are shown in Figure 1.5. Marshak *et al.* report that the signal strength was maximized by accepting events from within a 3° cone whose centre is slightly offset from the direction of the source, whereas Battistoni *et al.* found the apparent signal was a maximum in a $10° \times 10°$ bin centered on the source.

The size of the angular search window used in each case is significantly greater than the angular resolution of the detector (i.e. ~ 1°). The main source of angular uncertainty of muon arrival directions at the depths of observation (i.e. 1800 hg cm^{-2} for Soudan-1 and 5000 hg cm^{-2} for NUSEX), results from multiple Coulomb scattering of muons in the overburden (see Section 1.2.5). Nakatsuka *et al.* (1987) have carried out detailed calculations of the expected scattering angle distributions, and estimate the mean scattering angle of muons to be $< 0.6°$ at the

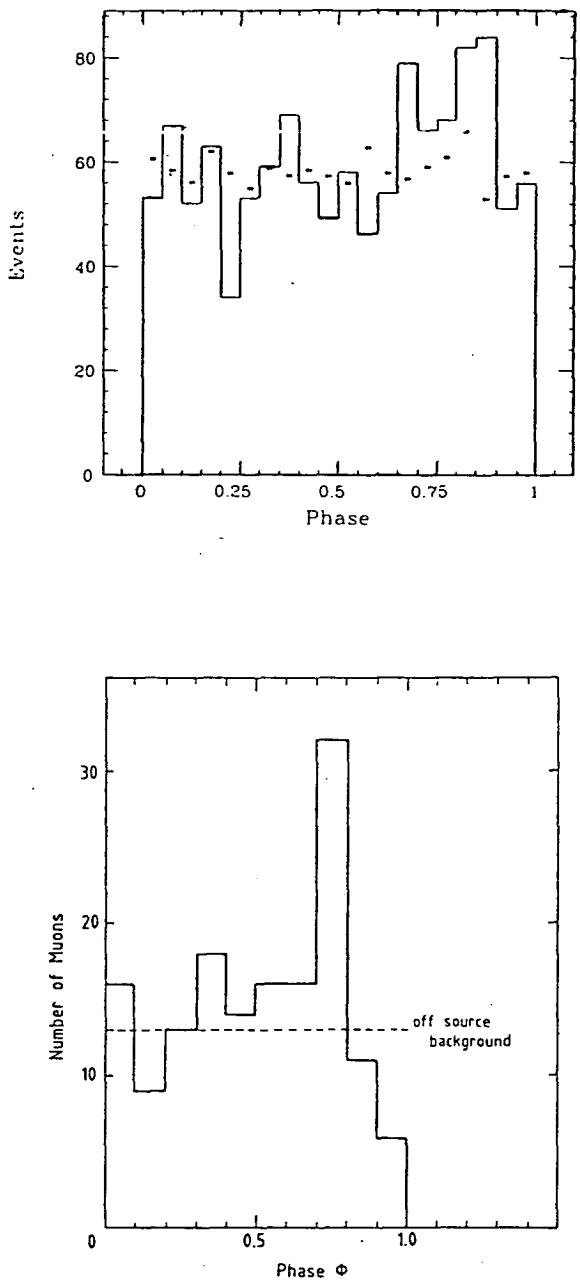

Figure 1.5 (Top) Phase plot for events within 3° of the observed position of Cygnus X-3. The points represent the expected number of events for a constant, isotropic source (from Marshak *et al.* 1985).

(Bottom) Phase distribution for muons coming from an observation window of 10° × 10° centred on Cygnus X-3 (from Battistoni *et al.* 1985).

depths of the two detectors.

The reported muon flux observed by both underground detectors was comparable to the VHE gamma-ray flux as observed by ground-based Cerenkov telescopes and air shower arrays. The observed muon flux was therefore inconsistent with the particles from Cyg X-3 being gamma-rays, since the flux of atmospheric muons at ground level was expected to be only $\sim 10^{-3}$ of the gamma-ray flux from the source (see below). The observed zenith angle distribution of the excess muons was, in each case, compatible with the expected distribution for atmospheric muons, which ruled out neutrinos as the muon progenitors. Neutrons could also be discounted since a prohibitively large flux of the highest energy neutrons ($E_N > 10^{18}$ eV for time dilation to prevent decay en-route) would be required to produce the observed underground effects.

Partially contemporaneous and subsequent searches for a modulated muon flux by underground detectors of similar or larger collecting area have found no evidence for any periodic enhancement in events from the direction of Cyg X-3 (Oyama *et al.* 1986; Berger *et al.* 1986; Bionta *et al.* 1987).

It had been thought for many years that the muon content of gamma-ray initiated air showers would be much less than that of cosmic ray initiated air showers (e.g. Wdowczyk 1965), due to the fact that the photoproduction cross-section is ~ 100 times smaller than that for production by protons. More recent calculation by Edwards *et al.* (1985) and Stanev *et al.* (1985) confirmed this view that the muon content of gamma-ray initiated showers should be $\sim 1/10$ of that of proton initiated showers. However, some experimental results seem to contradict this expectation.

Observations of Cyg X-3 by the Kiel group revealed an excess of events from a $\sim 4° \times 3°$ bin centred on the source, which appeared to be modulated with the 4.8 hour periodicity of the source (Samorski and Stamm, 1983a). More importantly, the

muon content of the gamma-ray showers was essentially the same as the expected muon content of cosmic ray initiated showers (Samorski and Stamm, 1983b). Similarly, in an excess of air showers observed by the Lodz group from the direction of the Crab Nebula, the ratio of muons in gamma-ray showers to that of cosmic-ray showers was ~ 0.6 (Dzikowski *et al.* 1983). Short duration bursts of showers from the direction of Hercules X-1, as observed by the *Cygnus* experiment, also showed no significant difference in muon content than would have been expected from cosmic ray initiated showers (Dingus *et al.* 1988).

The underground muon observations of Cyg X-3 and the high muon content of air showers observed by some groups cannot be explained in terms of currently known physical mechanisms. If both effects are real, it would signal the existence of either a new light neutral particle from Cyg X-3, which interacts hadronically in the atmosphere (e.g. Baym *et al.* 1985; Stenger 1985), or an enhanced photon-nucleus interaction at energies above ~ 1 TeV (e.g. Halzen *et al.* 1987).

1.4 Thesis Outline

The project described in this thesis is a continuation of an observing program begun (Wilson 1985a) in 1983 to search for galactic narrow angle anisotropies in the high-energy ($E > 100$ GeV) cosmic ray flux. The program, which utilizes an underground muon telescope, has been extended for the current project to include measurements of the arrival time of incident particles. Such data have been used to search for an underground muon signal from the Vela pulsar, one of a number of high-energy gamma-ray sources in the southern celestial sky.

Chapter 2 comprehensively describes the muon telescope, data recording system and the on-line event reconstruction procedures. The pre-existing data recording instrumentation was upgraded for the current project with the construction

of a high precision temperature controlled clock which provides the arrival time of incident particles to the nearest millisecond. The new recording system has been used to collect data over the 18 month period from August 1987 to January 1989.

A detailed calculation of the telescope gathering power is presented at the beginning of Chapter 3. The results are used to determine local sources of variation in the measured flux of particles, and to ensure the complete set of observed arrival directions displays the expected characteristics for underground muons.

Chapter 4 begins with a brief review of previously reported detections of galactic narrow-angle anisotropies. The data collected during the current investigation are then searched for evidence of such anisotropies in the declination band 20°N to 90°S. No significant deviation from an isotropic distribution of arrival directions is found, and upper limits to the underground muon flux from possible point sources are obtained.

The Vela pulsar has been the subject of astronomical observations over various wavelength regimes since its discovery in 1969. These observations are reviewed at the beginning of Chapter 5. Selected events from the general direction of the pulsar are then examined for evidence of pulsed emission. No evidence for steady pulsed emission is found, but two marginally significant bursts of pulsed emission of duration several hours were observed just before the 1988 glitch of the pulsar. The concluding chapter summarizes and discusses the results and suggests lines of future research.

Chapter 2

Instrumentation

2.1 Introduction

The Poatina cosmic-ray observing station is located in an underground hydro-electric power station approximately 130 km north of Hobart, at longitude 146.9°E and latitude 41.8°S (see location map, Figure 2.1). The station is at a vertical depth of 160 metres below ground level or 357 hg cm^{-2} below the top of the atmosphere (Fujii and Jacklyn, 1979). Ground level vertically above the station is 363 metres above sea level.

Observations began at the station in late 1971 following the installation of three semi-cubic particle telescopes utilizing Geiger tubes and totalling 3 m^2 sensitive area. The telescopes are configured to register the solar hourly rate of events for use in conventional anisotropy work (e.g. Humble *et al.* 1985). The event rates are recorded on printed paper tape which are collected on a monthly basis. The telescopes are currently being replaced by a set of larger semi-cubic telescopes of 4 m^2 sensitive area, utilizing proportional counters. The first, installed in 1983, incorporated an additional recording system to log the arrival direction of incident particles. Although the telescopes were not specifically designed to measure particle arrival directions, the configuration of the proportional counters (see Section 2.2) make them well suited for the task. The second of these larger telescopes was installed in 1986 and has been used for the current project to continue the observing program begun in 1983 to search for narrow-angle anisotropies.

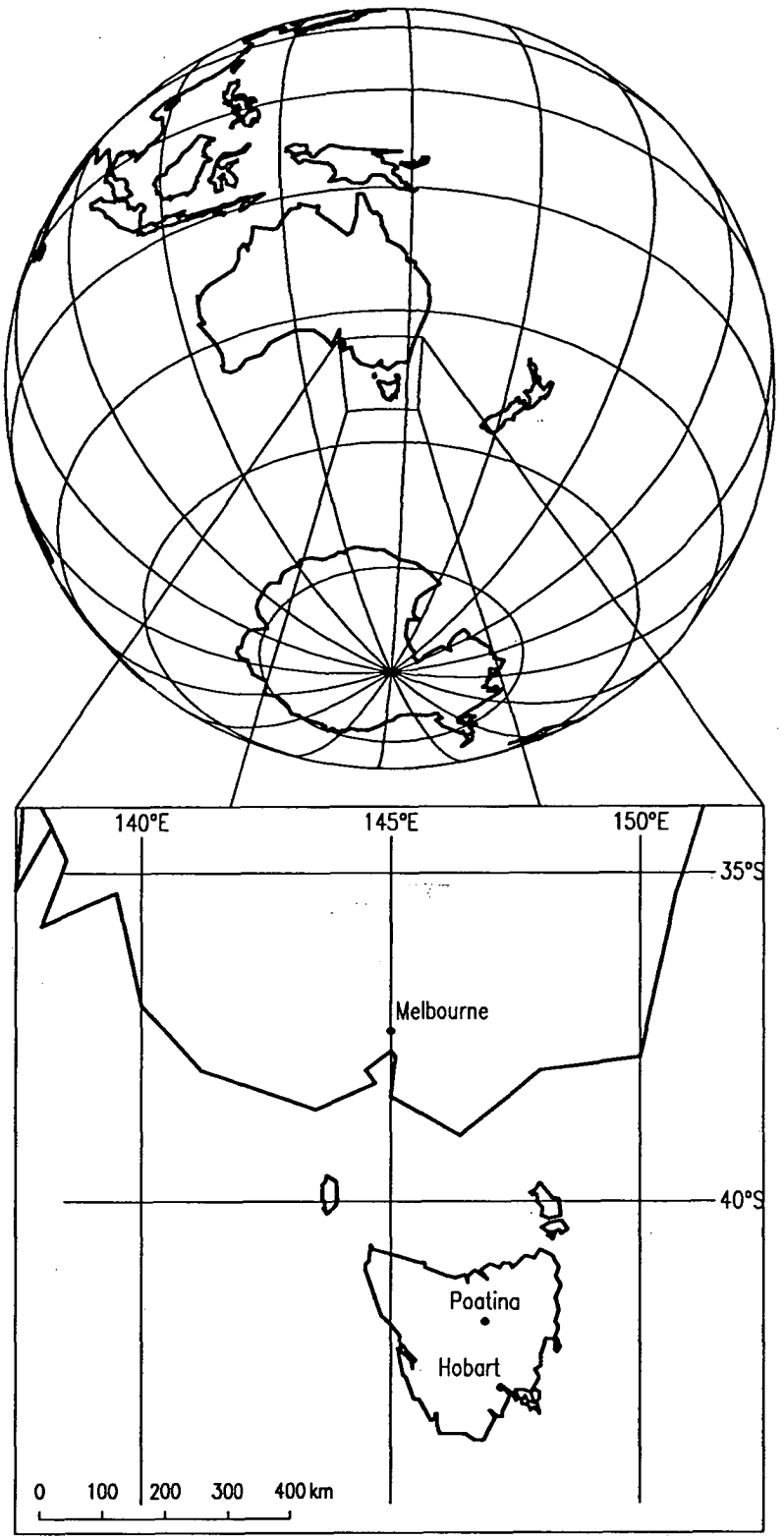

Figure 2.1 South-eastern Australia location map.

2.2 The Telescope

The semi-cubic particle telescope utilizes cylindrical proportional counters set up in a hodoscope arrangement. The counters, whose physical dimensions are given in Table 2.1, are constructed of copper tubing filled with a gas mixture comprising 90% Argon and 10% Methane at atmospheric pressure.

Table 2.1

Physical Properties of the Proportional Counters

sensitive length	193.00 cm
internal diameter	10.16 cm
wall thickness	0.10 cm
operating voltage	2300 volts

As shown in Figure 2.2 the counters are laid out in four trays with each tray comprising 19 counters. These trays are grouped in pairs and arranged so the counter axes in adjacent trays are orthogonal. The two groups of paired trays are mounted on a rigid steel frame and separated by a vertical distance of 1 metre. Also attached to the telescope framework are the detector electronics and the high and low voltage power supplies. The telscope configuration provides a maximum viewing angle of 70° and an angular resolution for vertical viewing directions of 5.7°.

The efficiency of each proportional counter was monitored throughout the experimental period by monthly measurement of the individual rates of each counter. At no time did any counter show a variation in count rate, other than that expected from statistical fluctuations, which would have altered the gathering power (defined in Section 3.2) of the telescope to a significant degree.

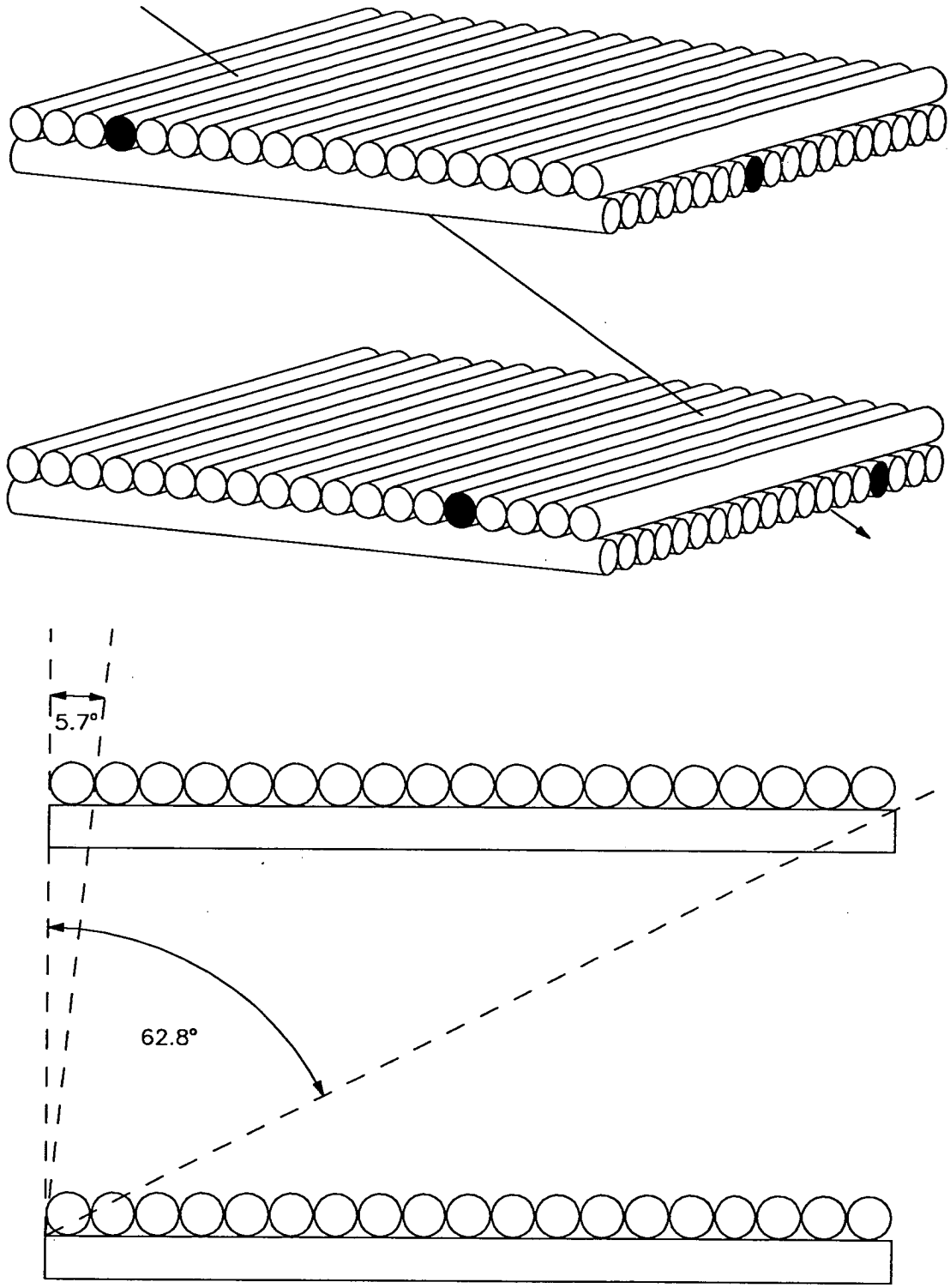

Figure 2.2 Poatina semi-cubic particle telescope.

The telescope is located on the second lowest level in the power station. The layout of the station and the position and orientation of the telescope within the station complex are shown in Figures 2.3 and 2.4. One important feature of the station complex that influences the particle intensity as seen by the telescope is the vertical access shaft which houses transmission cables and a personnel lift from the station to the surface. The proximity of the telescope to the shaft has the effect of producing a localized increase in intensity for viewing angles close to the zenith (refer to Section 3.3 for details).

The muon threshold energy at the depth of the station is 100 GeV so the telescope is sensitive to muons originating from particles having a median primary energy of 1.2 TeV (Lyons 1981). Approximate differential response functions of muons as a function of primary particle rigidity for various viewing angles are shown in Figure 2.5.

The average event rate for the telescope is approximately 0.6 Hz. The principal source of background events is the natural radioactivity of the environment, which produces a 64 Hz event rate in each proportional counter. The 4-fold coincidence requirement for the detection of an event results in a negligible background coincidence rate of 0.04% of the total event rate. There is an additional background rate resulting from the detection of a background event in coincidence with a cosmic ray event. This background interference rate is approximately 0.8% of the total event rate.

2.3 Data Logger

The Data Logger is a microprocessor controlled recording system specifically designed to record the arrival direction of particles detected by the telescope. It was constructed as part of an earlier research project by Wilson (1985a). When the logger

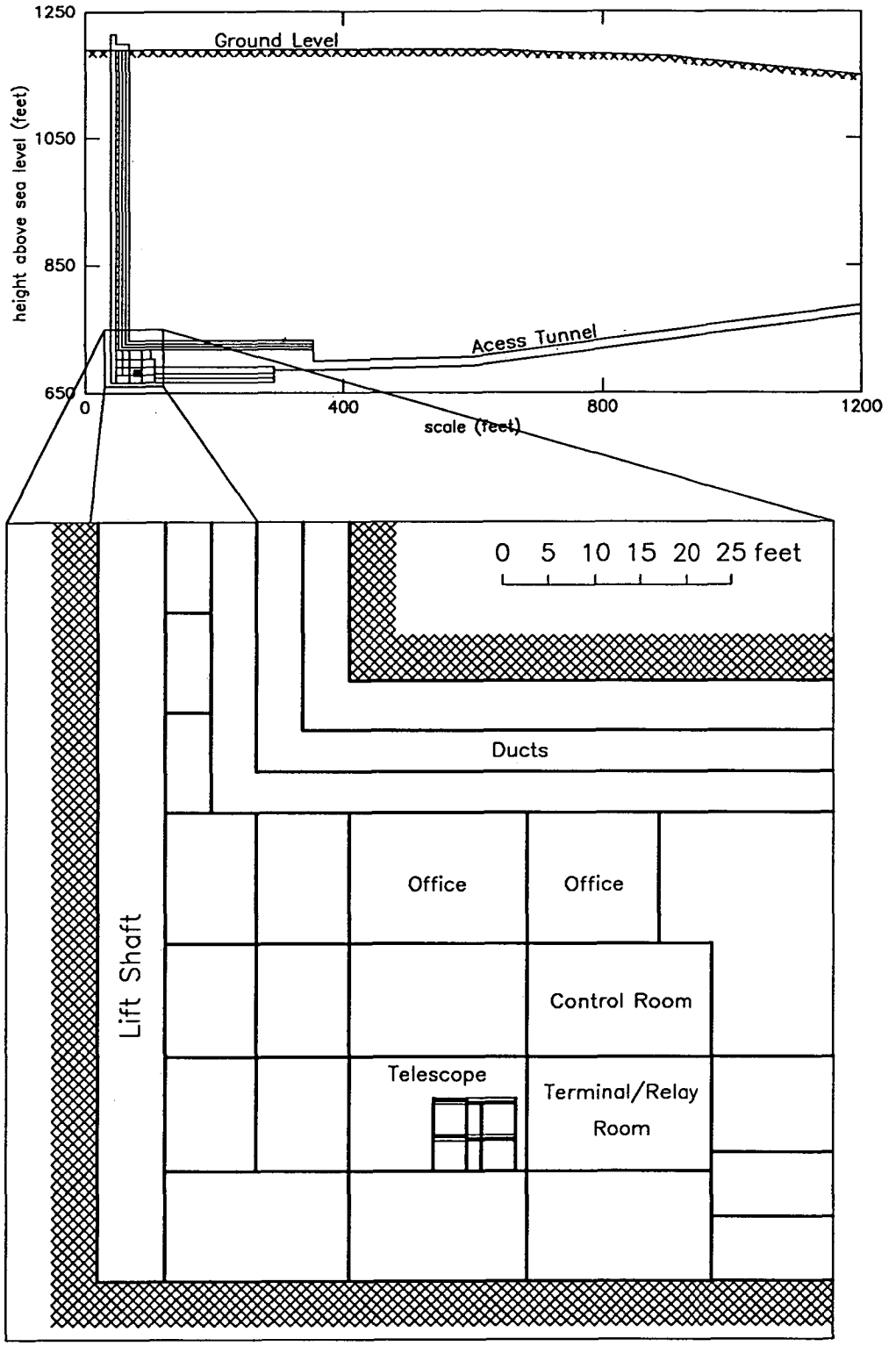

Figure 2.3 General schematic of power station showing the location of the telescope within the station complex. The shading indicates the start of solid rock.

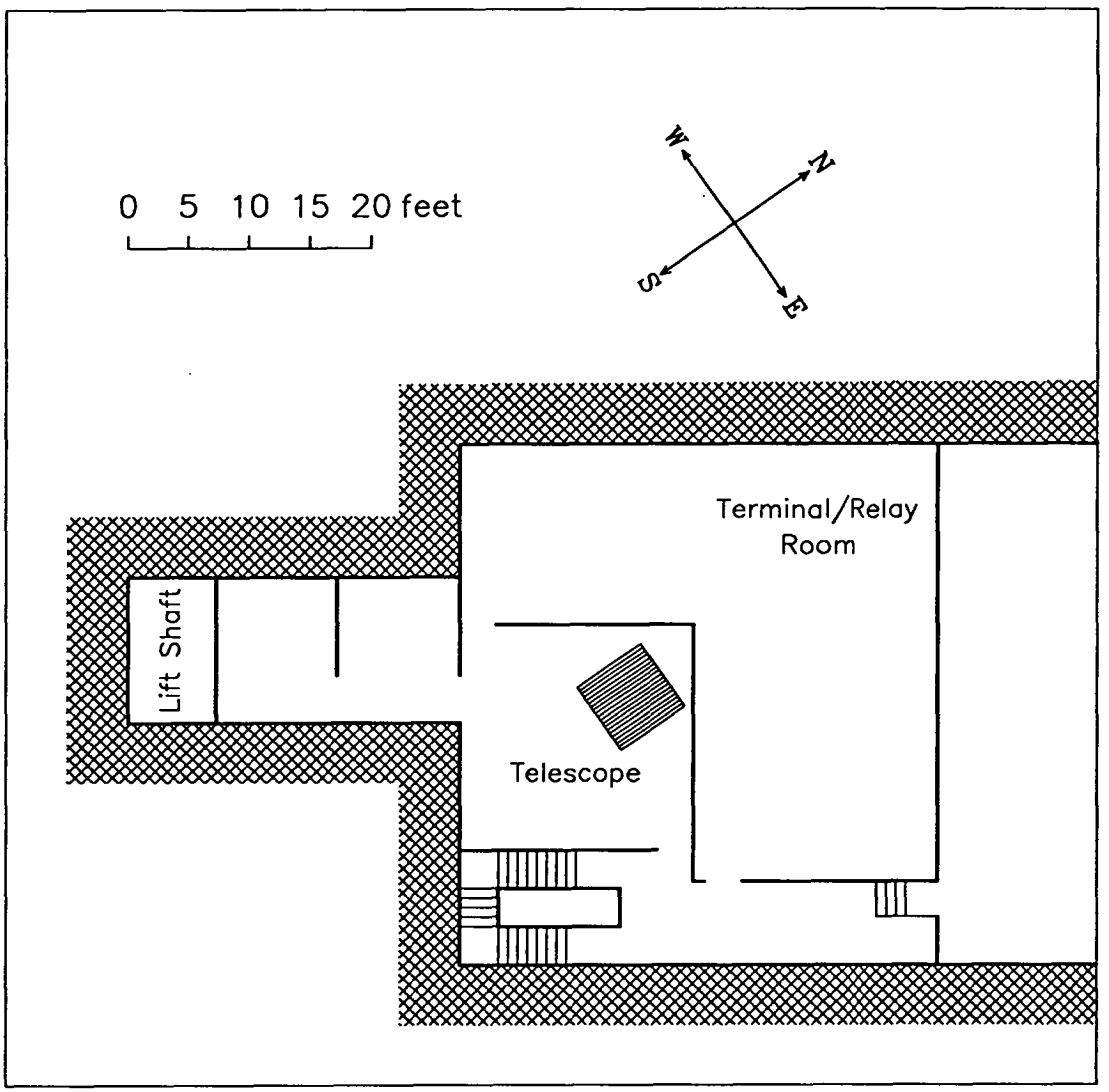

Figure 2.4 Plan of the station showing the orientation of the telescope and relative position of the vertical access shaft. The shading indicates the start of solid rock.

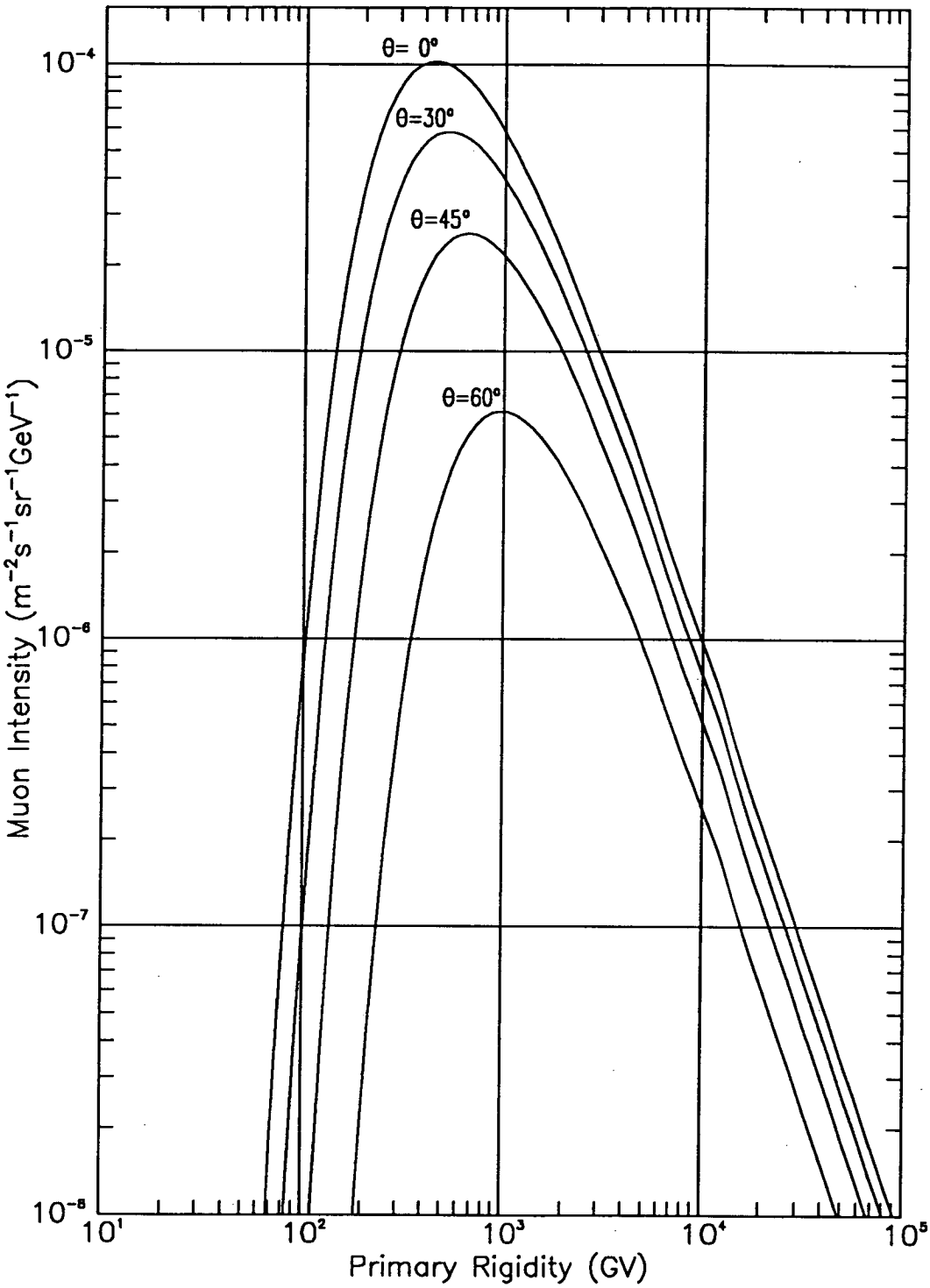

Figure 2.5 Differential muon response curves for various viewing directions at a vertical depth of 347 hg cm^{-2}. The curves were calculated from the approximate formula derived by Fujimoto *et al.* (1977).

was first installed in 1983 it was configured to record the status of each counter of the telescope for every event to allow for maximum flexibility in subsequent data analysis. With this arrangement the total amount of data generated by the logger was 2 Mbytes per week which was stored on standard audio cassette tape.

Several modifications were made to the data logger for the current project. Firstly, the existing data storage device was replaced by an IBM XT-compatible microcomputer which incorporated a 20 Mbyte hard disk. Secondly, a high-precision temperature controlled clock was constructed to provide the arrival time of incident particles to an accuracy of one millisecond. Finally, the event reconstruction analysis was moved on-line in order to reduce the quantity of recorded data to a manageable level. The additional recording of the event arrival times increased the weekly data output by 1 Mbyte. The on-line analysis replaced the counter status information with the number of counters involved in each event and a pair of coordinates indicating the incident direction of the event relative to the telescope. This resulted in a 40% decrease in the amount of data recorded by the logger to a total of 1.8 Mbytes per week.

With regard to the experimental setup, only a limited number of options were available due to severe financial constraints. Given the current interest in point source observations by the cosmic-ray community, it was decided to direct available funds towards the construction of the high-precision clock and the purchase of adequate data storage facilities. This allowed the arrival times of events to be recorded to a high degree of accuracy, thus enabling the data to be used subsequently to search for evidence of periodic emission from known point sources, the Vela pulsar in particular.

2.3.1 Basic Operation

The data logger can be divided into three main modules: the Telescope

Interface, the Interface Control Computer and the Event Decoding Computer. The inter-relationships between the three modules and the other major components of the recording system are shown Figure 2.6.

2.3.1.1 Telescope Interface.

The passage of a charged particle through the telescope (an event) is detected by the 4-fold coincidence of at least one discharged counter in each of the four trays. The pulsed signal (a 2 microsecond square logic pulse) from the coincidence circuit results in the Telescope Interface latching the 76 ($= 4 \times 19$) signals from the telescope counters and the 24 event time signals from the clock into the event buffer. The temporary storage buffer enables the signals to be retained long enough for them to be read into memory by the Interface Control Computer (ICC). Once data has been latched into the buffer further event detection is disabled until the data has been read from the buffer.

The time required to read and transfer data from the event buffer is known as the *dead time* of the system since an event occurring during this period will not be recorded. The dead time is approximately 150 microseconds. To reduce this time to a negligible level a second event buffer is built into the Telescope Interface. The transfer of data to the event buffers is controlled by the Buffer Control Logic (BCL). The BCL monitors the state of each buffer and redirects incoming data to the next free buffer. If no buffer is available, the event data is lost.

Given that an event has just been detected, the Poisson probability that another event will occur in the next 150 microseconds, using the average rate of 0.6 Hz, is 9×10^{-5}. Therefore, if the data logger used only one buffer for the latching of events, approximately 1 event would have been lost every 5 hours. The probability that two events will occur within 150 microseconds of the detection of an event is 4×10^{-9}, or

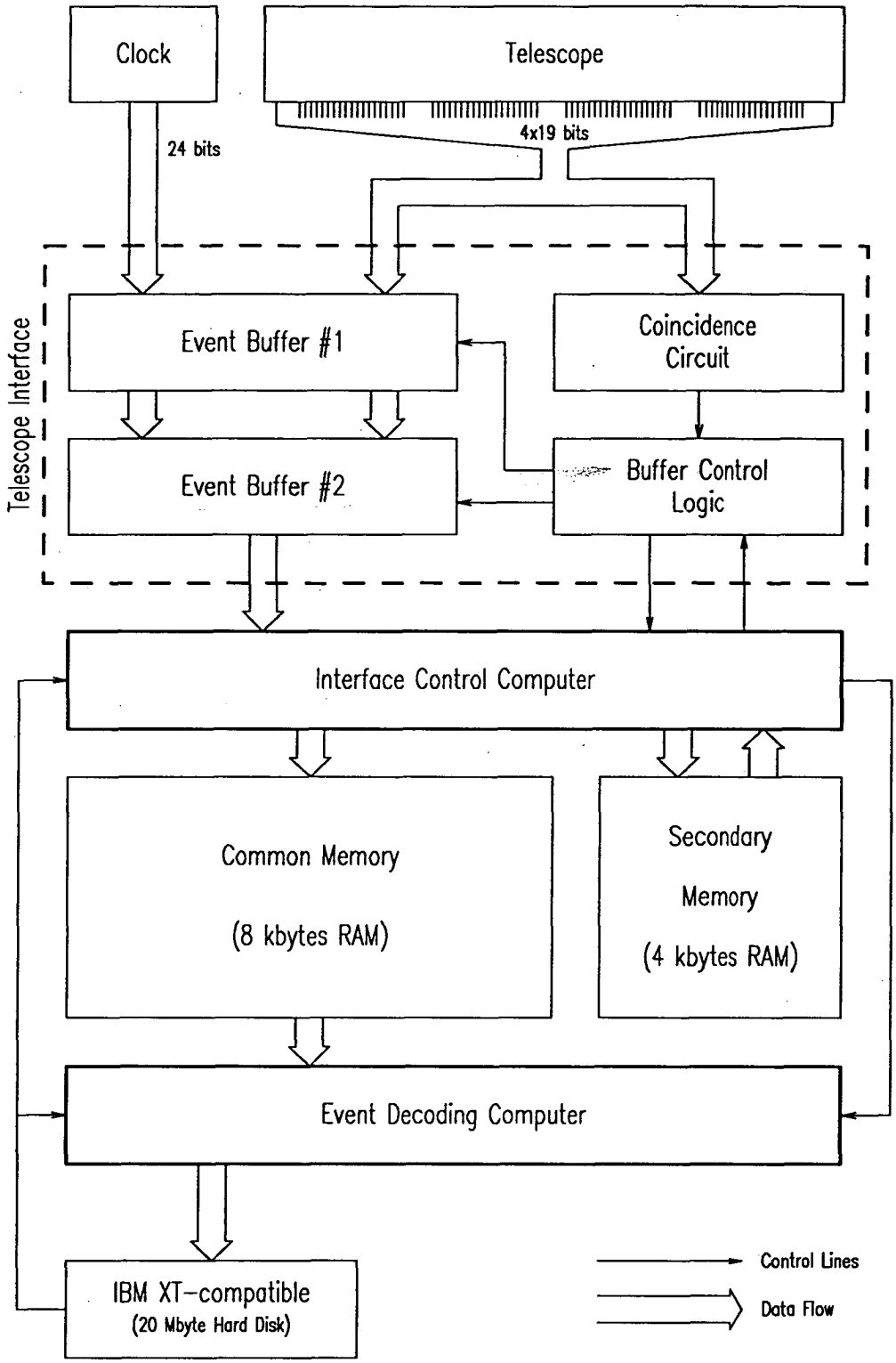

Figure 2.6 General schematic of data recoding system.

one such occurrence every 13 years. Thus the double buffering arrangement essentially reduces the dead time of the system to the duration of the coincidence signal, i.e. 2 microseconds.

2.3.1.2 Interface Control Computer

The sole function of the Interface Control computer is to transfer data from the event buffers to an 8 kbyte common memory area, thereby making it accessible to the Event Decoding computer (EDC). The ICC determines which buffer to read by examining status flags set by the BCL. Before reading the data, the ICC ensures there is sufficient common memory available to store the data. If memory is available, the ICC transfers the data and clears the appropriate BCL status flag, thereby making the buffer available for latching further event data.

Once common memory has been completely filled with event data the EDC is started via a signal from the ICC. Whilst the EDC is analyzing the data common memory is not available to the ICC so data from the event buffers is stored in a secondary memory area. Once the EDC has completed its task the data in secondary memory is transferred by the ICC to common memory and all subsequent data from the event buffers is transferred to this area.

2.3.1.3 Event Decoding Computer

The primary function of the Event Decoding computer is to analyse the recorded pattern of activated counters, assigning a direction to events where possible (refer to Section 2.3.2). The resulting directional data is sent via an RS232 serial link to the IBM XT-compatible microcomputer where it is stored on a 20 Mbyte hard disk. Once a month the data are transferred from the hard disk to the physics

department VAX 11/750 computer from which they are transferred to 2400 ft. magnetic tapes and stored for further analysis.

The storage requirement for the event data direct from the telescope is 15 bytes per event (i.e. 4 × 3 counter status bytes plus 3 bytes for the arrival time). The common memory area is therefore capable of storing data from 520 events with some space reserved for data analysis. The event reconstruction analysis (see Section 2.3.2) reduces the quantity of data to 5 bytes per event (i.e. 1 byte for each direction coordinate plus the 3 timing bytes) for the majority of events. At the average event rate of about 2100 per hour the directional data are therefore transferred to the microcomputer approximately every 15 minutes.

Although the main function of the microcomputer is to store the data generated by the data logger, its secondary role is to act as system controller. This involves reading and setting the clock and carrying out performance tests on all modules (hardware and software) of the recording system. In addition, the function of each of the data logger's two computer systems can be altered by downloading programs from the microcomputer. For example, during each monthly 48 hour observation down time (refer to section 2.4) the EDC was reprogrammed to perform an efficiency check of each of the proportional counters. The analysis involved keeping a tally of the number of times each counter was involved in an event.

The requirement for two computer systems within the data logger to record and analyse the data from the telescope is necessitated by the random nature of the cosmic-ray flux being measured. The Telescope Interface coupled with the ICC reduce the random occurrence of events to a uniform flow of data to the EDC. Hence the EDC is able to analyse and transfer the event data at a leisurely pace without the possibility of data loss. With only one computer system a large dead time would have occurred during the event reconstruction analysis and data transfer procedures, resulting in a periodic loss of data.

2.3.2 Event Reconstruction

Event reconstruction is the process of attempting to determine the trajectories of particles giving rise to an event from the recorded pattern of discharged counters. The precision with which trajectories can be reconstructed is governed by the angular and spatial resolution provided by the telescope. The ability to trace particles through a telescope with good spatial resolution, and to detect additional particles produced within the telescope, usually requires a large number of detector elements. The telescope used in this investigation is at a disadvantage in this respect, in that it has only two layers of detectors with which to determine the spatial location of particles traversing the telescope. It was therefore necessary to make several general assumptions concerning the nature of recorded events to facilitate the event reconstruction analysis. These are

(1) events are produced by single or multiple high-energy muons unaccompanied by secondary particles from interactions in the nearby rock.

(2) the trajectories of all particles defining an event are straight paths through the telescope.

(3) the trajectories of all muons associated with multiple particle events are parallel within the intrinsic angular resolution of the telescope.

These assumptions are correct for the majority of events recorded by the telescope (see Table 2.2).

The local direction of an event relative to the telescope is determined by projecting the path(s) of the particle(s) defining the event onto two perpendicular planes *U* and *V*. Each plane is formed by an upper and lower tray in which the counter

axes are normal to the plane. All counters in a tray are numbered relative to one side of the tray. The relative telescope coordinate (u or v) in each plane is then taken to be the difference in discharged counter number between the upper and lower tray in that plane. Since there are 19 counters per tray each relative telescope coordinate lies in the range −18 to +18.

Having determined the direction of the event relative to the telescope it is then only necessary to know the position and orientation of the telescope to enable transformation of the event to any other coordinate system. For the present vertical pointing telescope, the counters of which are aligned north-south and east-west, conversion of the relative telescope coordinates (u,v) to the zenith and azimuth angle coordinates (θ,ϕ) is easily achieved via the relations

$$\tan \phi = {}^{v}/_{u}$$

$$\tan \theta = {}^{d}/_{h}\,(u^2 + v^2)^{1/2} \qquad (2.1)$$

where

d is the horizontal separation of adjacent counters in a tray (i.e. the external diameter of the counters), and

h is the vertical separation of similarly orientated upper and lower trays.

The event direction data were stored as relative telescope coordinates (u,v) because, being integer numbers, they require less storage space than the corresponding zenith and azimuth angle coordinates (θ,ϕ).

2.3.2.1 Event Classification

The success of the event reconstruction procedure depends on the decodability

of the recorded pattern of discharged counters. Each recorded pattern is assigned to one of four classes which reflects the amount of information that can be extracted about the event by the reconstruction analysis. The classification is based on the previously stated assumptions concerning the nature of the recorded events. The four classes and the relative number of events in each class are listed in Table 2.2.

Table 2.2

Event Classification

Classification	Class Number	Events/hr	% of Total
Single	1	1732.8	83.3
Multiple	2	58.1	2.8
Complex	3	286.2	13.8
Lost	4	2.3	0.1

The event reconstruction procedure views the event in each of the two planes and determines a classification and a coordinate for each view. The final description of the event is formed by combining the results from each of these views. That is, the direction is given by the relative coordinate (u,v) and the classification by the maximum class number from each of the two views.

If there is some ambiguity in the form of the event, it is decoded, wherever possible, as a single particle event. The ambiguity arises for events where there are two adjacent discharged counters in a single tray, and although the configuration of discharged counters could have been caused by multiple particles, there is a greater probability of it being due to a single inclined particle traversing both counters. The reconstructed trajectory of the particle(s) defining such an event will be identical irrespective of any ambiguity in the event classification.

2.3.2.2 Event Direction

The decoding of single particle events is straightforward and involves identifying which counter discharged in each tray. Viewed in one plane, a single particle traversing the telescope, with a direction coordinate in the range –2 to +2, can only discharge one counter per tray. Outside of this coordinate range however, a single particle may discharge more than one counter in a single tray. Such an event is initially classified as *multiple*. If the multiple particle event reconstruction procedure determines that the event has a multiplicity of one then the event is reclassified as *single*. Approximately 70% of single particle events discharge only one counter per tray. As an example, the single particle event depicted in Figure 2.2 is shown decoded in Figure 2.7.

Events classified as *multiple* must be consistent with a group of particles having parallel trajectories fully contained within the telescope aperture. An algorithm developed by Wilson (1985a) for reconstructing multiple particle events is outlined in Appendix A. The algorithm basically compares the pattern of traversed counters in the upper and lower trays. Allowance is made for the fact that the two patterns may not necessarily be identical due to the traversal of adjacent counters by a single particle if the event is sufficiently inclined from the vertical. The algorithm determines the incident direction coordinate and estimates the multiplicity and lateral spread (i.e. separation of the outer-most particles) of the event. An example of a typical 3 particle event is shown in Figure 2.8.

If the multiple particle algorithm cannot decode a particular pattern of discharged counters, the event is classified as *complex*. These nondecodable patterns are produced by events to which it is not possible to assign an unambiguous direction. Such events are easily explained by the occurrence of either of the following two processes. Firstly, a single high energy particle is accompanied by low energy knock-on electrons produced either in the concrete floor situated approximately one metre

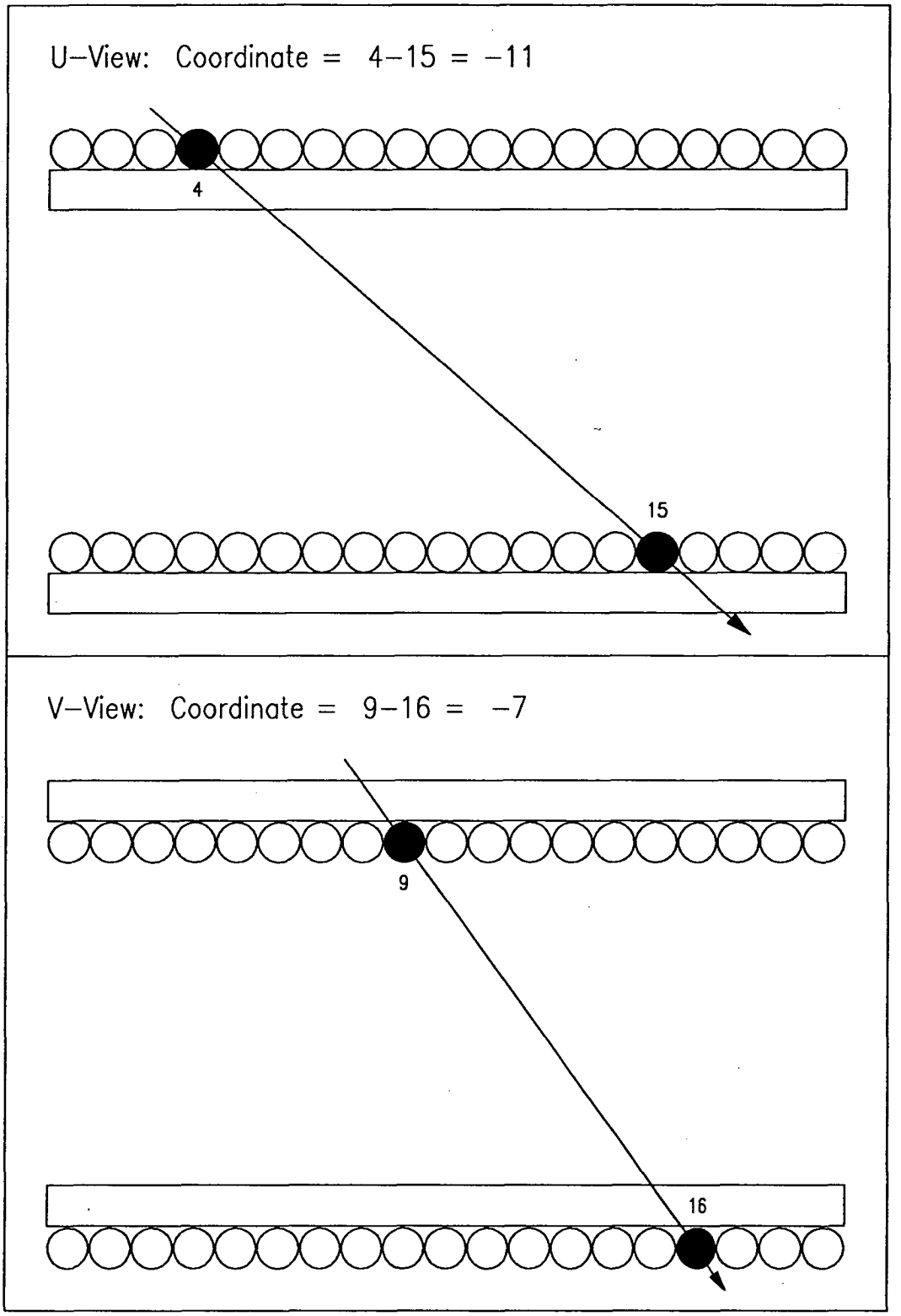

Figure 2.7 Example of the event reconstruction procedure. The event depicted is a single particle event (classification 1) to which is assigned the relative telescope coordinates (–11,–7).

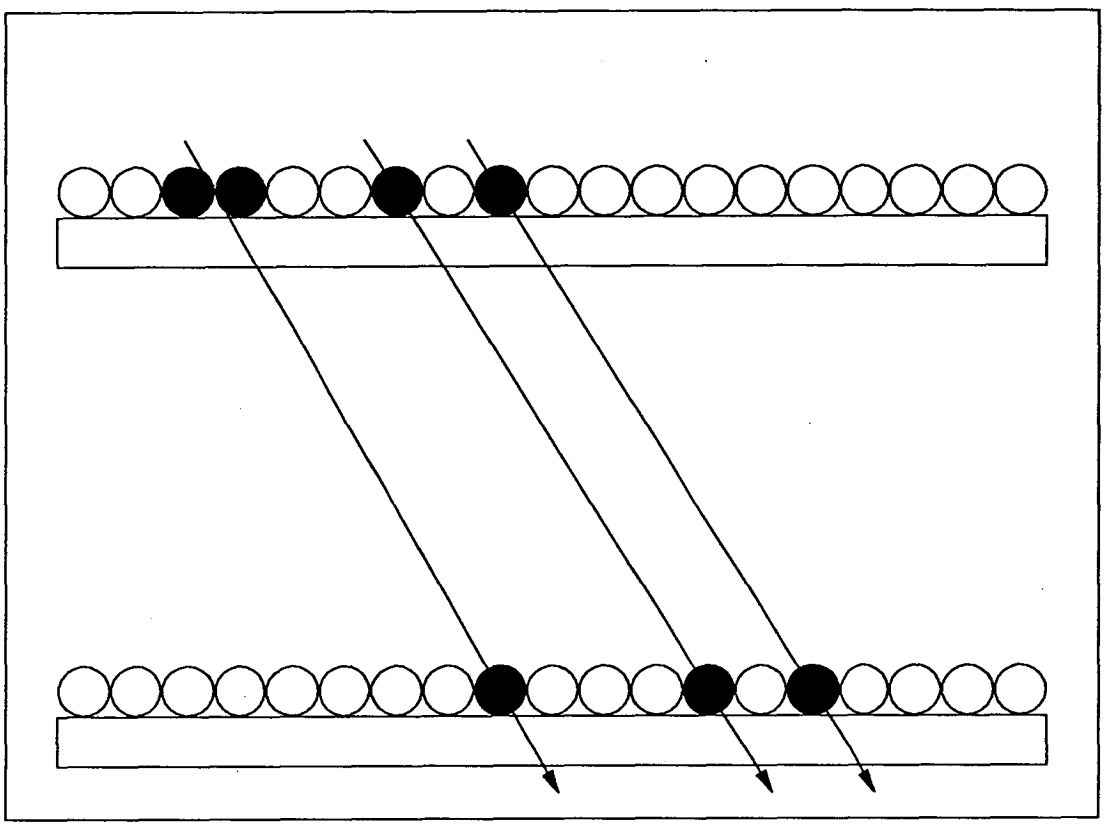

Figure 2.8 A typical 3 particle event. The lateral spread of the event is 6 (i.e. 6 counter diameters).

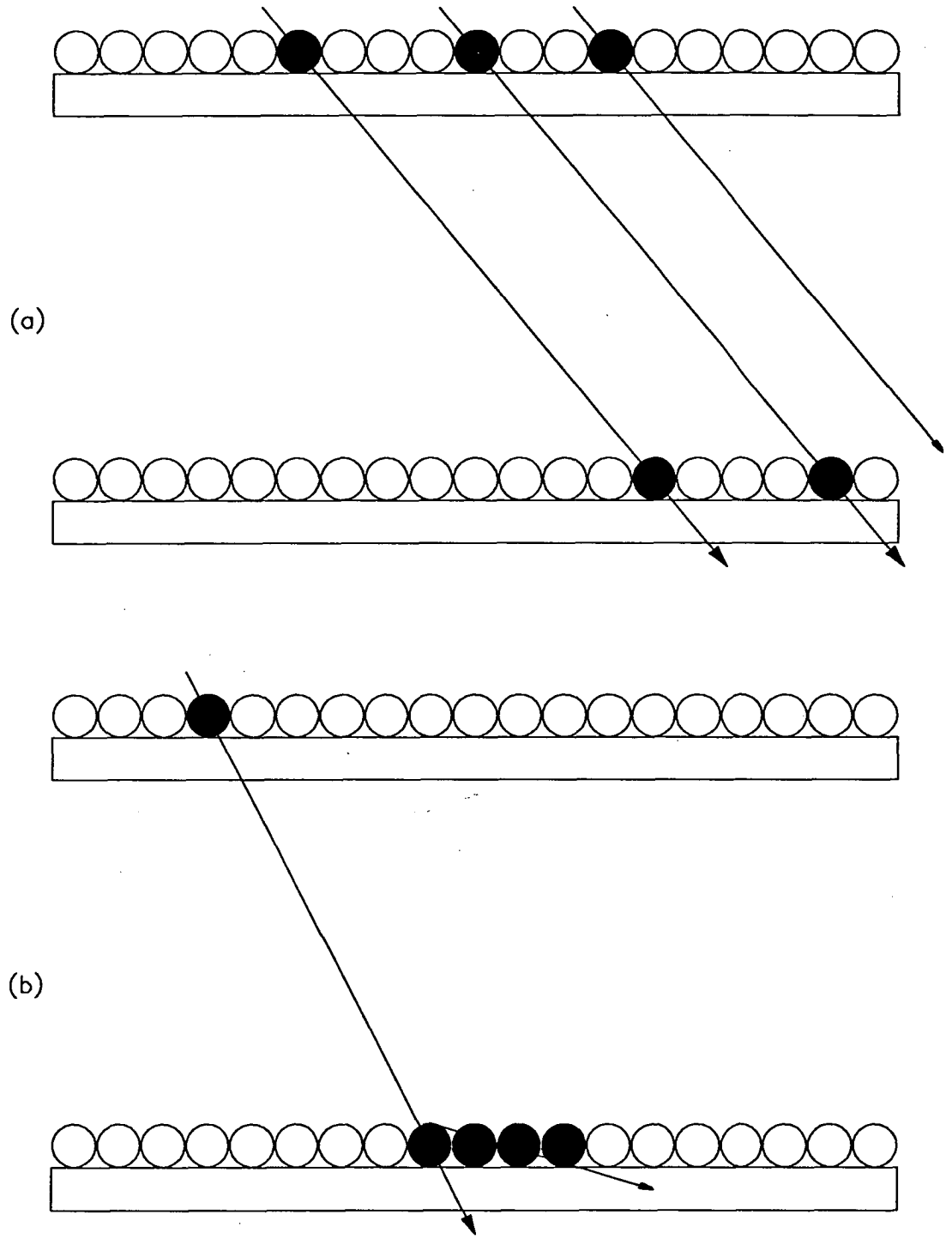

Figure 2.9 Examples of complex events;
(a) the multiple particle event is not fully contained in the telescope aperture,
(b) an additional particle is produced within the telescope.

above the telescope or in the counter walls. Secondly, a complex event may arise if a multiple particle event is not fully contained within the telescope aperture. An example of each type of complex event is shown in Figure 2.9. Background events occurring in coincidence with a single particle event will in most cases transform it into a complex event. However, the background interference rate of 0.8% of the total event rate is too low to produce a significant number of complex events.

Events classified as *lost* result when a coincidence is detected but the recorded pattern from one plane shows a tray with no discharged counter. It is difficult to explain how these events arise. One suggestion is that they could be produced by the chance coincidence of background events, the loss of data occurring during the delay between the production of the coincidence signal and the latching of the event data. However, the background coincidence rate for the telescope is only 0.04% of the total event rate. Thus, the lost event rate is far too high to have been entirely caused by unrelated random background particles.

There is another puzzling feature of the lost events. For most of the events the pattern from one plane is decodable into a single particle event with the resulting distribution of arrival directions following the expected distribution for single particle cosmic ray events. If the lost events were produced by background particles the distribution of arrival directions should be uniform due to the random nature of the background particles. This would indicate that a cosmic ray particle has actually passed through the telescope with subsequent loss of data via some unknown mechanism.

2.3.2.3 Event Count Matrix

Those events for which the reconstruction analysis can assign a direction are binned according to their direction. Since each relative telescope coordinate ranges

from -18 to $+18$ the rates of single particle events are accumulated in a 37×37 event count matrix. Unique relative telescope coordinates (u,v) are associated with each bin of the matrix.

2.4 Arrival Times

One of the proposed aims of the current project was to search for periodic emission from southern hemisphere high-energy gamma-ray sources. The usual method of detecting periodic emission from such sources is to fold the arrival times of detected particles with the known or suspected period of the source in an attempt to raise the periodic signal above the assumed isotropic background radiation level. Flux levels observed from gamma-ray sources are extremely low, so it is obviously advantageous to be able to perform such an analysis over long periods of observation since the signal, if present, should appear from the background with the additional accumulation of data. However, if the analysis is to remain coherent, the event arrival times need to be measured to a high degree of accuracy (at least 1 millisecond) over the total observing period. Moreover, the measured arrival times must be referenced to some absolute time standard. To meet these requirements a clock was built employing a temperature controlled quartz crystal oscillator with a quoted minimum frequency stability of one part in 10^9 under ideal conditions.

The clock was sufficiently stable to give the required timing accuracy over approximately one month of observation. To extend this accuracy over the entire period of observation (initially proposed to be 1 year) required the clock output to be compared with a more stable time reference. This was initially chosen to be the radio broadcasts of the Australian standard frequency and time signal station VNG, which were available with reasonable strength and clarity at the observing site. However, the closure of VNG at short notice prior to the commencement of the observations necessitated a quick search for another time reference.

Reception of WWV transmissions at the power station were weak and intermittent, and external land lines were not available as the station's communications use an internal system. The next available (low cost) reference was the rubidium crystal controlled clock operated by the radio astronomy group at the university. The clock was compared with the rubidium standard each month. This required transporting the clock from Poatina to the radio-astronomy observatory near Hobart, causing an observing down time of approximately 48 hours per month.

The drift of the clock relative to the rubidium standard over a 6 month period is given in Figure 2.10, showing the clock drift to be smooth and well defined. Fitting a quadratic polynomial (see below) to the comparison points allowed all event arrival times to be corrected to the standard with an uncertainty of not more than a few milliseconds. Once the uncertainties in the fitted corrections became comparable to the required timing accuracy, the crystal oscillator was retuned and the clock reset to the rubidium time standard. This occurred, on average, after every 5 months of operation.

The coefficients of the fitting polynomial can be directly related to the intrinsic characteristics of the crystal oscillator as follows. The output frequency of the oscillator as a function of time can be described by

$$f(t) = f_{osc} + \alpha_{osc}\, t \qquad (2.2)$$

where

f_{osc} is the fundamental frequency of the oscillator (i.e. 1 MHz),

α_{osc} is the inherent instability (or aging rate) of the crystal oscillator,

and

t is the elapsed time in seconds.

For simplicity sake, α_{osc} is assumed to be time independent, although its value will vary (albeit slightly) with changes in ambient temperature and supply voltage. The

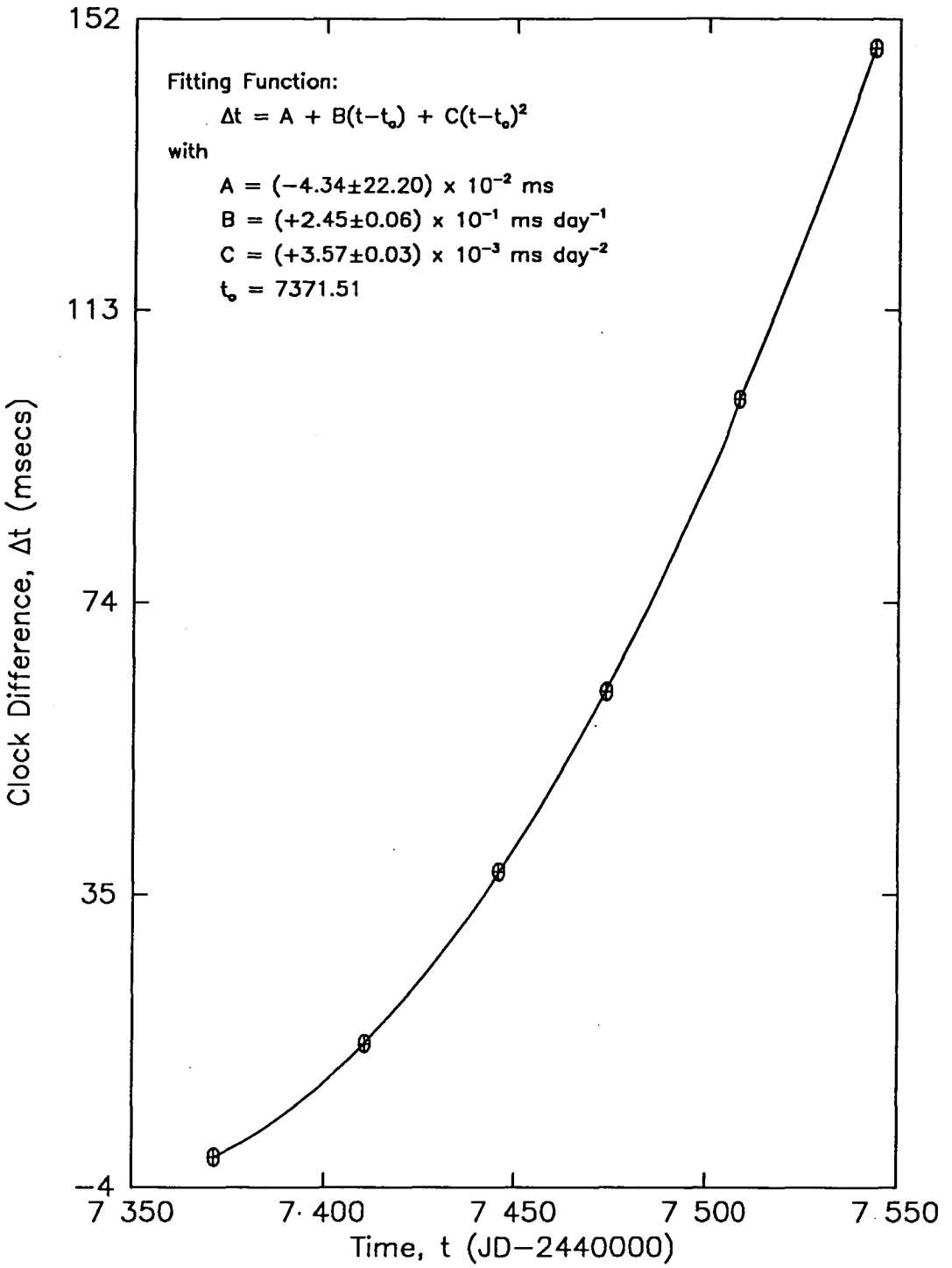

Figure 2.10 Clock drift relative to rubidium time standard. The line is the best fit quadratic polynomial to the clock reference points.

number of fundamental clock units (i.e. MHz^{-1} = microseconds) after time T is then given by

$$N(T) = \int_0^T f(t)\,dt = f_{osc}\,T + \tfrac{1}{2}\,\alpha_{osc}\,T^2 \qquad (2.3)$$

Comparison with the rubidium time standard produces a time difference in fundamental clock units of

$$\Delta N = (f_{osc} - f_{rub})\,T + \tfrac{1}{2}\,\alpha_{osc}\,T^2 \qquad (2.4)$$

where α_{rub} is assumed to be negligible relative to α_{osc}. From Figure 2.10, $C = 0.0036$ ms day^{-2}, therefore

$$\alpha_{osc} = \frac{2\,C\,1000}{(24 \times 60 \times 60)^2} \sim 1.0 \times 10^{-9}\ s^{-2} \qquad (2.5)$$

Chapter 3

Telescope Behaviour

3.1 Introduction

In this chapter a detailed calculation of the telescope response will be presented, together with a precise determination of various properties of the underground muon flux. Calculation of these quantities not only enables a check to be made of the entire data-set to ensure it displays the expected characteristics, but also allows verification of the correct operation of the telescope and data analysis programs.

A total of 18×10^6 events were recorded between August 1987 and January 1989. The live-time over this 18 month period was 369.5 days which corresponds to an observing efficiency of 71%. The major source of off-time was brief interruptions to the power supply at the station. Although the data recording system was designed to be self-starting in the event of a power failure, there were several instances where this procedure failed to operate correctly. These usually required a trip to the station to reset and restart the system. The staff at the power station checked the recording system as often as possible, nevertheless there were occasions where equipment failure went unnoticed for several weeks. A further source of off-time was the time required to bring the clock from the power station to Hobart to be referenced against the rubidium time standard.

3.2 Telescope Response

The telescope can be thought of as comprising a large number ($19^4 = 130321$)

of elementary telescopes each formed by two crossed counters in the top two trays, and two crossed counters in the bottom two trays (see Figure 2.2). Many of these elementary telescopes have identical viewing directions and can be grouped accordingly to form direction bins. The central viewing direction of a bin is simply the relative telescope coordinates (u,v) assigned to events recorded by the bin. The viewing direction can be expressed in conventional zenith and azimuth angles by the application of Equation (2.1). The number of elementary telescopes comprising a direction bin is given by

$$N(u,v) = (19 - |u|)\,(19 - |v|) \tag{3.1}$$

For example, the vertical direction bin (0,0) consists of $19 \times 19 = 361$ elementary telescopes whereas the extreme diagonal direction bin (–18,–18) comprises $1 \times 1 = 1$ elementary telescope.

3.2.1 Angular Resolution

The intrinsic angular resolution of the elementary telescopes is primarily determined by the geometry of the telescope construction, i.e. the diameter of the proportional counters and the vertical separation of the trays. The resolution with which arrival directions can be determined is also dependent on the event reconstruction procedure, since this establishes the limits within which particle directions can be resolved without ambiguity. The ambiguity arises because for certain viewing directions the fields of view of adjacent elementary telescopes overlap, the degree of overlap increasing with increasing viewing angle. Thus, a single particle sufficiently inclined from the vertical can register within more than one elementary telescope, i.e. by traversing two counters in a single tray. Such an event can be handled in two ways; the event can be shared between the two elementary telescopes, as was done by Sheldon (1973), or randomly assigned to one of the elementary

telescopes as done in this experiment. The random choice is achieved by calculating the incident direction using the rightmost discharged counter in any tray containing more than one discharged counter (see Appendix A), and relying on the variation in the lateral position of similar events to distribute them over all possible elementary telescopes. An example of the resulting angular resolution of an inclined elementary telescope is illustrated in Figure 3.1.

Elementary telescopes with near vertical viewing directions are mutually exclusive with respect to event detection and therefore remain unaffected by the event reconstruction procedure. The angular resolution of these elementary telescopes is solely determined from geometrical considerations (see Figure 3.1 for example). The angular resolution and detector sensitivity (i.e. the *effective* detector area normal to the viewing direction) of all direction bins along half of one directional axis of the Poatina telescope are shown in Figures 3.2 and 3.3 respectively. These are compared with the same quantities for an ideal telescope, i.e. one with identical physical dimensions but utilizing counters with zero thickness and having 100% detection efficiency. This comparison will be discussed further in the following section. It is sufficient to note at this point that the angular resolution and sensitivity of the elementary telescopes do not differ dramatically from those for an ideal telescope.

3.2.2 Geometrical Factor

The counting rate, C, of a fixed particle telescope utilizing ideal detectors can be expressed as

$$C = \Gamma I_o \tag{3.2}$$

where

I_o is the absolute vertical intensity of the incident particle flux, and

Γ is the *gathering power* (or *acceptance*) of the telescope. That is

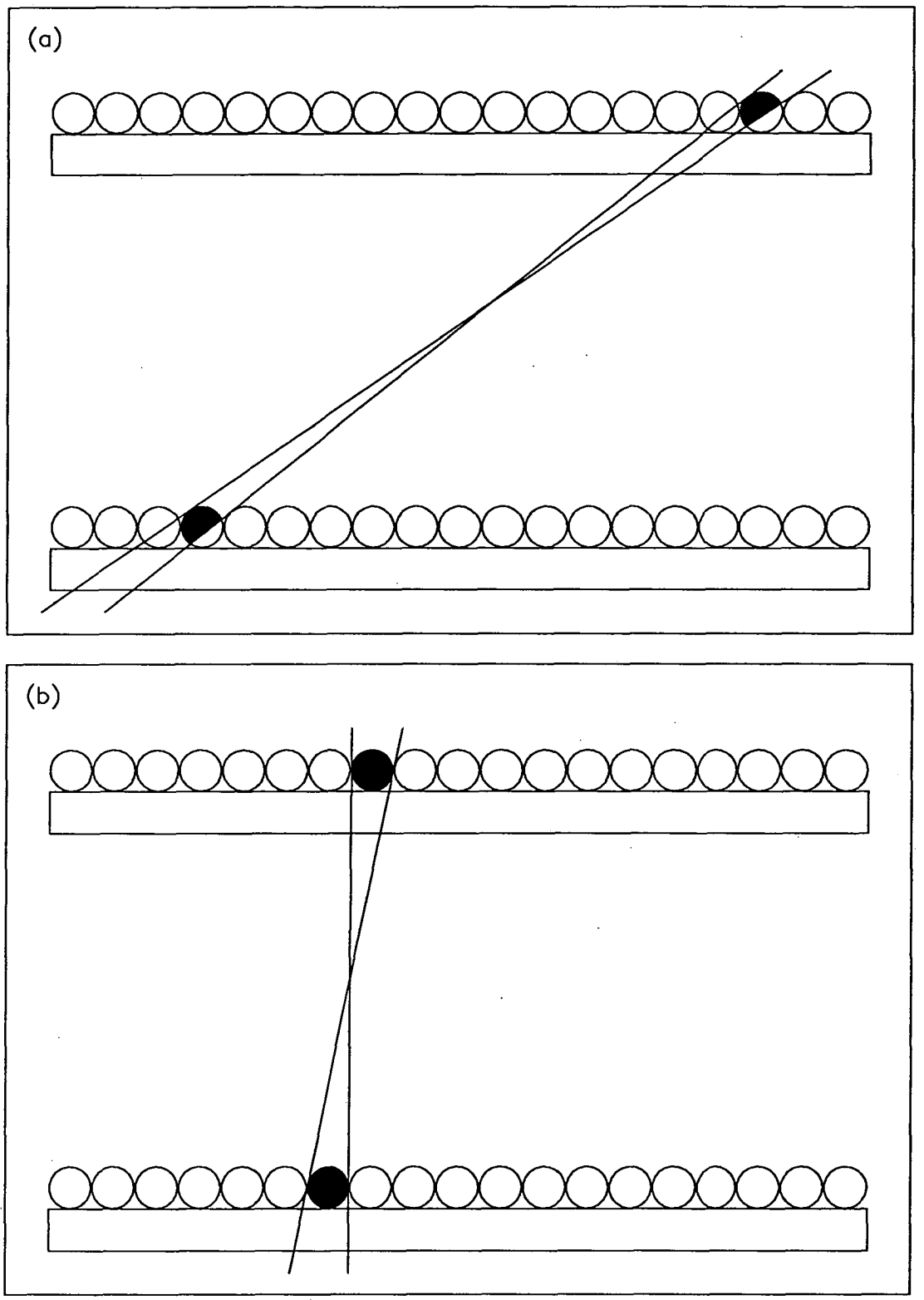

Figure 3.1 Illustration of angular resolution of (a) an inclined elementary telescope, and (b) a near vertical elementary telescope. The shaded regions indicate the *effective* cross-sectional area of the counters.

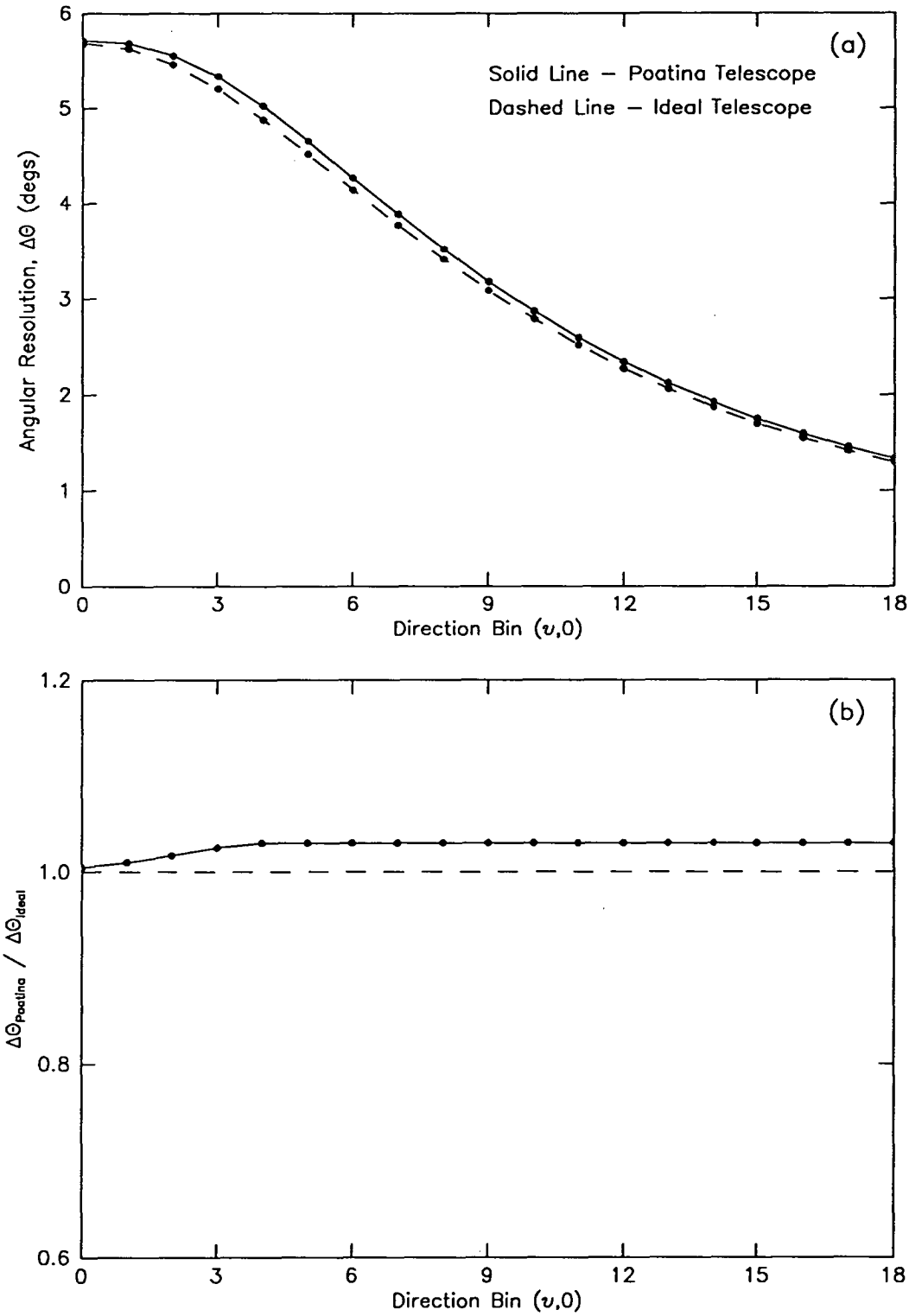

Figure 3.2 (a) Angular resolution of direction bins along half of one directional axis of the Poatina telescope and an ideal telescope. (b) Comparison of the two curves in (a).

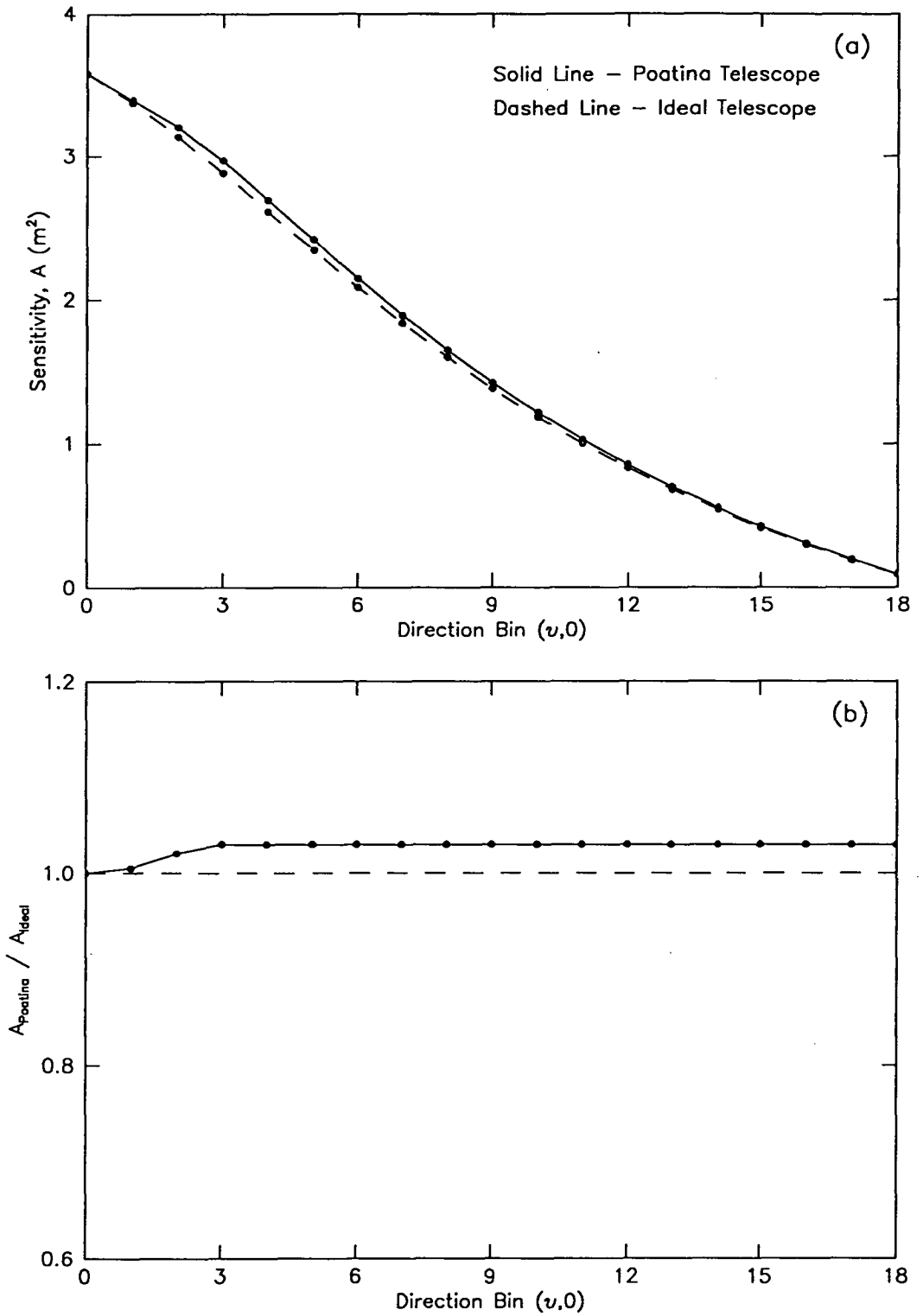

Figure 3.3 (a) Detector sensitivity of direction bins along half of one directional axis of the Poatina telescope and an ideal telescope. (b) Comparison of the two curves in (a).

$$\Gamma = \int_{\Omega} A(\omega)\, F(\omega)\, d\omega \tag{3.3}$$

where

$d\omega$ is the element of solid angle,

Ω is the domain of ω (i.e. the telescope aperture),

$F(\omega)$ is the angular dependence of the radiation intensity, and

$A(\omega)$ is the *directional response* (or *sensitivity*) function of the telescope.

The directional response function is a purely geometrical quantity defined as

$$A(\omega) = \int_{S} d\underline{\sigma} \cdot \hat{\underline{r}} \tag{3.4}$$

where

$d\underline{\sigma}$ is the element of surface area of the last detector element of the telescope to be penetrated,

$\hat{\underline{r}}$ is a unit vector in direction ω, and

S is the total area of the last detector element.

Thus, given an observed event rate C, the usual method of determining $F(\omega)$ involves assuming an initial form for $F(\omega)$ and employing an iterative scheme to find the true form of the intensity variation.

However, the subdivision of the telescope into elementary telescopes allows the intensity variation to be determined in a more straightforward manner. If the elementary telescopes effectively sample the incident particle intensity at discrete viewing directions, the intensity variation can be easily reconstructed from these sample points. The effectiveness of the reconstruction is governed by the angular resolution of the elementary telescopes. Assuming the fields of view of the elementary telescopes are such that the intensity over the field of view is essentially constant, then the following approximation can be made. Assume the gathering power of an elementary telescope, with central viewing direction α, can be expressed as

$$\Gamma = \int_{\Omega} A(\omega)\, F(\omega)\, d\omega = F(\alpha) \int_{\Omega} A(\omega)\, d\omega = F(\alpha)\, G(\alpha) \qquad (3.5)$$

where $G(\alpha)$ is the *geometrical factor* of the elementary telescope, i.e. the gathering power for isotropic flux. The counting rate for the elementary telescope is then given by

$$C(\alpha) = \Gamma(\alpha)\, I_o = F(\alpha)\, G(\alpha)\, I_o, \qquad (3.6)$$

and the total event rate for the corresponding direction bin is $N\,C(\alpha)$ where N is given by Equation (3.1). Equation (3.6) lends itself to a direct determination of the angular dependence of the radiation intensity since G depends solely on the geometry of the telescope.

For telescopes having particular geometries, explicit formulae for the geometrical factor do exist. One such formula, appropriate for the rectangular geometry of the Poatina telescope, is given in Appendix B (Equation B.5). To determine an explicit expression for the gathering power is more difficult, since the calculation depends not only on the geometry of the telescope but also on the functional form of the intensity variation. The task is made easier if the intensity variation over the field of view of the telescope can be described by

$$I(\theta) = I_o \cos^n \theta \qquad (3.7)$$

when n is an integral value. The calculation has been carried out by Wilson (1985a) for $n = 2$; the resulting formula is also given in Appendix B (Equation B.3). The form of the intensity variation given by Equation (3.7) with $n = 2$ is expected to be a good approximation to the variation as seen by underground telescopes at the depth of the Poatina station. Therefore, the formulae given in Appendix B can be used to test the validity of the approximation made in Equation (3.6) for the Poatina telescope. If the approximation is a reasonable one, the values of the function

$$E(\theta) = \frac{\Gamma(\theta) - G(\theta)\cos^2\theta}{\Gamma(\theta)} \tag{3.8}$$

should be approximately zero. The function is plotted in Figure 3.4 for each direction bin of the telescope. It is apparent from these differences that Equation (3.6) is applicable to the Poatina telescope, at least for the ideal case.

As stated previously, the formulae for the geometrical factor and gathering power given in Appendix B are applicable to an ideal telescope. To determine the necessary corrections to the geometrical factor for a telescope utilizing non-ideal detector elements, a Monte Carlo simulation of the telescope and the event reconstruction procedure was performed.

The method is described in detail by Sullivan (1971), but briefly the simulation involves choosing a random point (x,y) on the opening aperture of the telescope and a random trajectory (θ,ϕ) through this point. The effect of an isotropic flux of particles is achieved by choosing $\cos^2\theta$ and ϕ at random from a set of uniformly distributed numbers. In the present case, θ was limited to angles less than the maximum viewing angle of the telescope, θ_{max}, so as not to waste time on events that could not possibly be detected by the telescope. Furthermore, each trajectory was followed through the telescope and the number of counters penetrated in each of the four counter trays was determined. Efficiency corrections were applied by calculating the path length of the trajectory in each struck counter, and requiring that this be greater than the minimum path length necessary to discharge the counter. Those surviving events that produced at least a four-fold coincidence were reconstructed (as described in Chapter 2) and accumulated in an event count matrix, C. For comparison the simulation was also performed for an ideal telescope utilizing flat detectors.

900 million events were generated during the simulation, of which approximately 345 million survived. The count matrix of surviving events was used to calculate the geometrical factor for each telescope direction bin as follows:

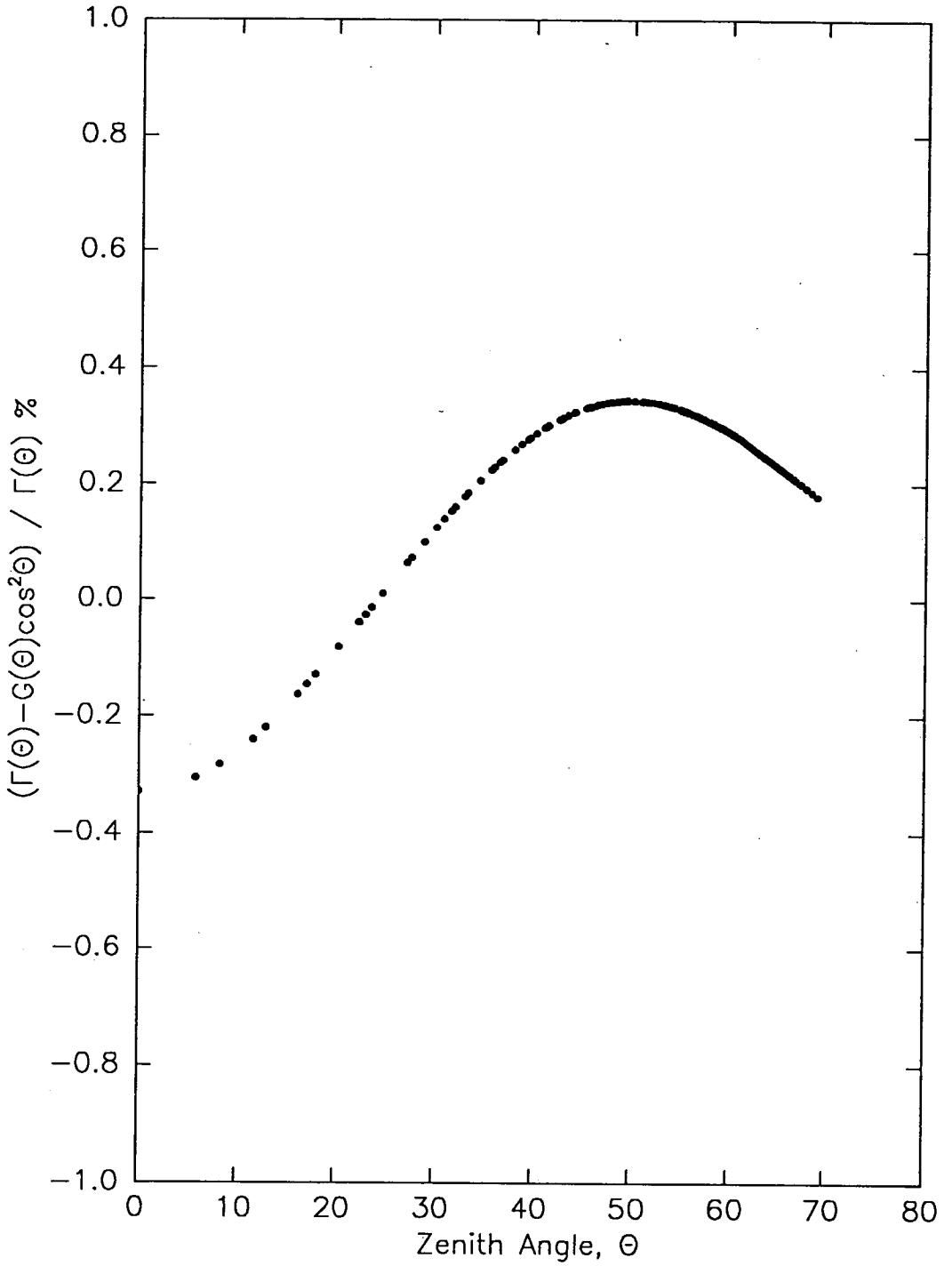

Figure 3.4 Approximation errors as a function of zenith angle with one point for each direction bin of the telescope. See text for details.

The geometrical factor for a direction bin (u,v) is given by

$$G(u,v) = G_o \frac{C(u,v)}{N_s} \tag{3.9}$$

where

N_s is the total number of events generated during the simulation,

$C(u,v)$ is the number of events recorded by the (u,v) direction bin, and

G_o is the geometrical factor of the telescope opening aperture, i.e. for a single planar detector of area S,

$$G_o = \int_\Omega A(\omega)\, d\omega = S \iint \cos\theta \sin\theta \, d\theta \, d\phi \tag{3.10}$$

The integrals are evaluated for the viewing angle limits used in the simulation:

$$\int_0^{2\pi} d\phi \int_0^{\Theta_{max}} \cos\theta \sin\theta \, d\theta = \pi \sin^2 \theta_{max} \tag{3.11}$$

so that

$$G(u,v) = \pi S \frac{C(u,v)}{N_s} \sin^2 \theta_{max} \tag{3.12}$$

Shown in Figure 3.5 are comparisons of the geometrical factor calculated in this manner for both the Poatina and ideal telescope and via the analytical method in Appendix B. Values of the geometrical factor for selected telescope direction bins are also listed in Table 3.1.

When no corrections were applied the values of the geometrical factor determined from the simulation were found to be in excellent agreement with the values calculated analytically. The corrections resulted in an overall 6% increase in the total geometrical factor. Note the similarity at near vertical viewing directions between the geometrical factor variation shown in Figure 3.5 and that for the angular resolution and sensitivity variation shown respectively in Figures 3.2 and 3.3, when compared with the same quantities for an ideal telescope. The variation in each case is

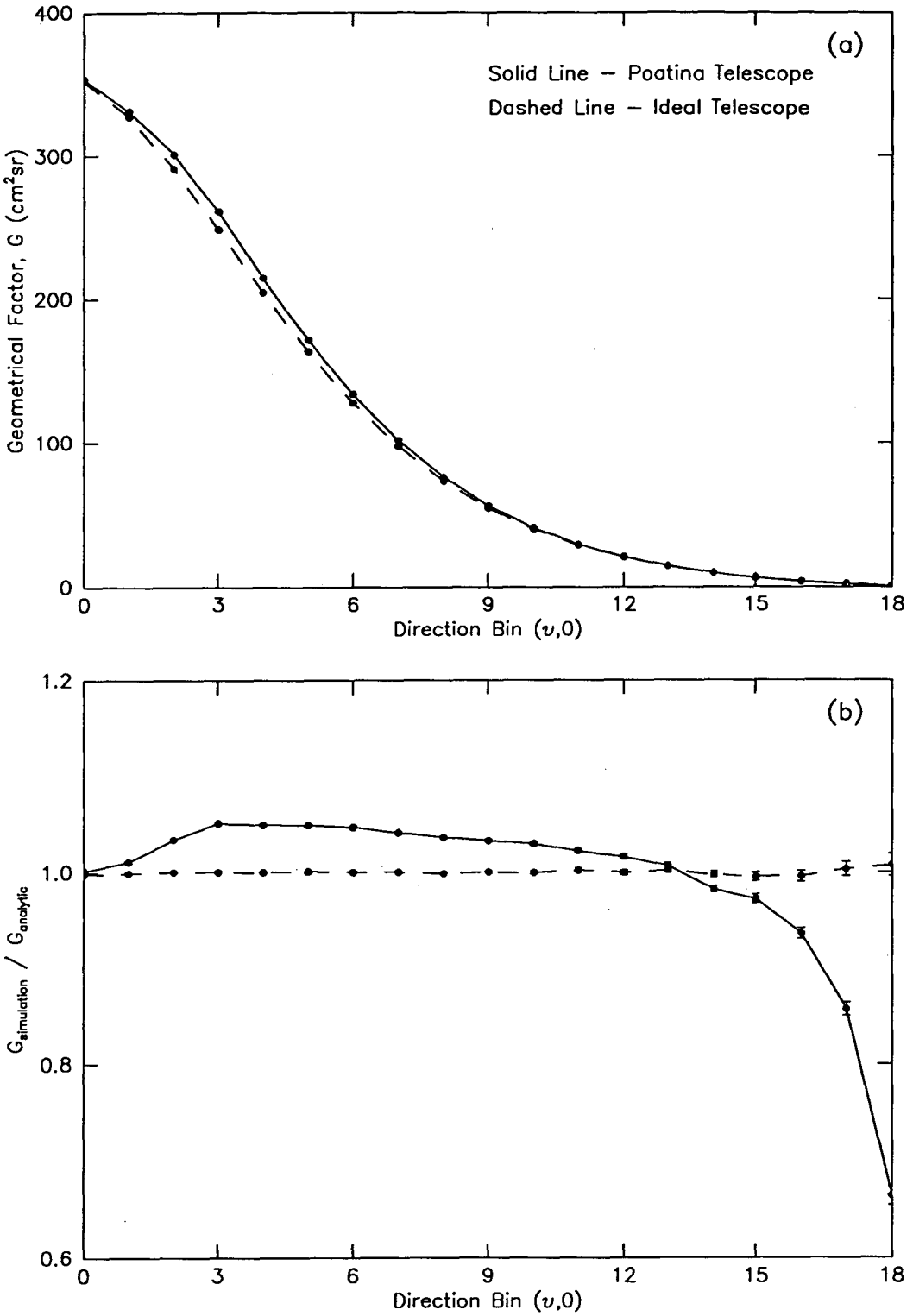

Figure 3.5 (a) Geometrical factor of direction bins from Monte Carlo simulation of the Poatina telescope and an ideal telescope. (b) The two curves in (a) compared with geometrical factor values calculated analytically.

due to the fact that cylindrical detectors always present a full cross-sectional diameter, d, normal to all lines of viewing, whereas for flat detectors the diameter normal to the line of viewing varies as $d \cos \theta$. The comparative increase is, however, restricted at larger viewing angles by the overlapping fields of view of adjacent elementary telescopes and the resulting decrease in the *effective* cross-sectional diameter of the counters, as illustrated in Figure 3.1.

The reduced geometrical factor for those direction bins with increasing viewing angle results from the loss of sensitivity for those elementary telescopes which include a counter located on the border of the telescope. The effect is illustrated in Figure 3.6. Even though the loss of sensitivity increases slightly with zenith angle, the reduction in geometrical factor becomes more evident at larger viewing angles because the direction bins also have an increasing proportion of elementary telescopes which include a counter located on the border of the telescope, i.e. N in Equation (3.1) decreases with increasing zenith angle. Note that this edge effect was not taken into account when calculating the angular resolution and sensitivity of the telescope direction bins as shown in Figures 3.2 and 3.3 respectively.

Table 3.1

Geometrical factor (in units of cm^2 sr) for selected direction bins of the Poatina telescope.

Direction Bin Coordinates	Analytic (Ideal Telescope)	Simulation (Ideal Telescope)	Simulation (Poatina Telescope)
(0,0)	352.93	352.31	353.69
(9,9)	54.55	54.57	56.41
(9,18)	0.96	0.97	0.64
Total (all bins)	43121	43127	45752

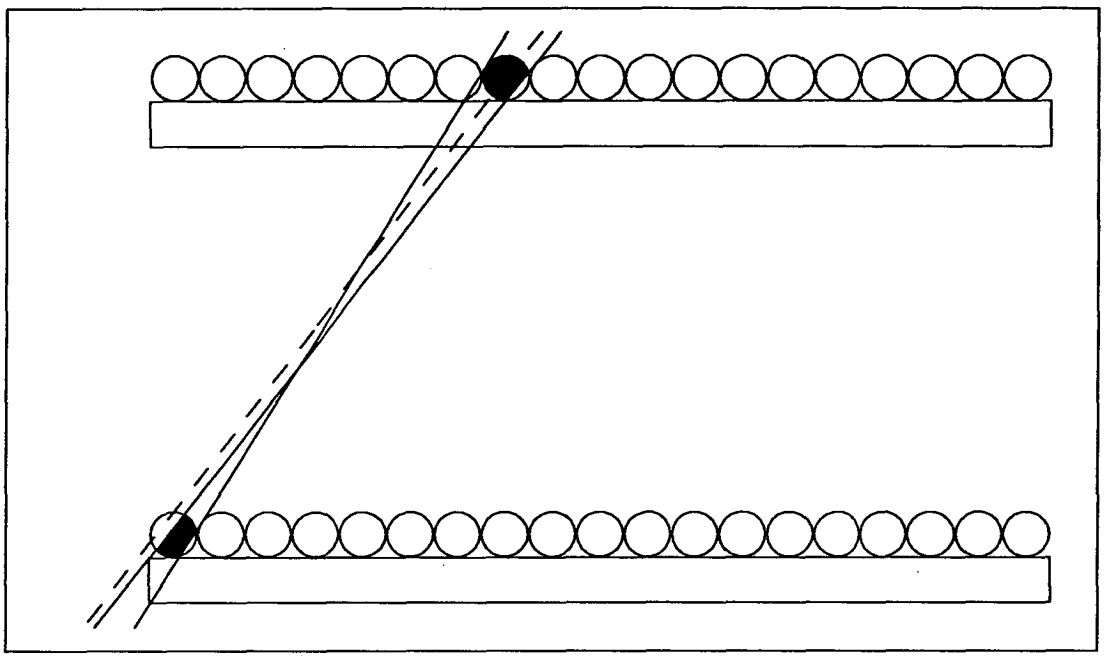

Figure 3.6 Illustration of reduced detector sensitivity and angular resolution for those elementary telescopes containing a counter located on the border of the telescope. The reduction occurs because the particles are constrained to pass through all 4 detector planes, i.e. a particle with a trajectory given by the dashed line would not produce a 4-fold coincidence since it does not pass through the lowest detector plane.

Although it is not apparent from Figure 3.5, the applied efficiency corrections had little or no effect on the geometrical factor. To show this more clearly, the sensitivity of each direction bin along half of one directional axis of the telescope is shown in Figure 3.7 for various values of the minimum path length. It is apparent that at large zenith angles the efficiency corrections have a negligible effect on the sensitivity and hence on the geometrical factor of the bins. For near vertical viewing directions there is again very little effect, except for large (and unrealistic) values of minimum path length. It is impossible to ascertain the true extent of this effect from the measured event rate, since the vertical access shaft produces a large localized increase in intensity for most of the near vertical viewing directions.

3.2.3 Intensity Calculations

The intensity associated with each direction bin was calculated directly from Equation (3.6) using the measured single particle event rates and the geometrical factors obtained from the Monte Carlo simulation. The total observing time (or live-time) of the telescope was obtained directly from the arrival times recorded with each event and adjusted to take account of those events (*complex*, *multiple* and *lost*) which were not included in the analysis. The adjustment consisted of a reduction in the observing time in proportion to the number of excluded events to the total number of observed events.

The error in the intensity calculation is primarily the Poisson statistical error from the total counts registered by a direction bin. The approximation error ($\sim 0.3\%$) resulting from the use of Equation (3.6) is comparable to the Poisson error for near vertical bins but negligible otherwise. A larger error of several percent may occur if the angular distribution of those events excluded from the analysis is not the same as the distribution of the single particle events. Given that most of the excluded events are *complex* events, mainly arising from secondary particles produced within the

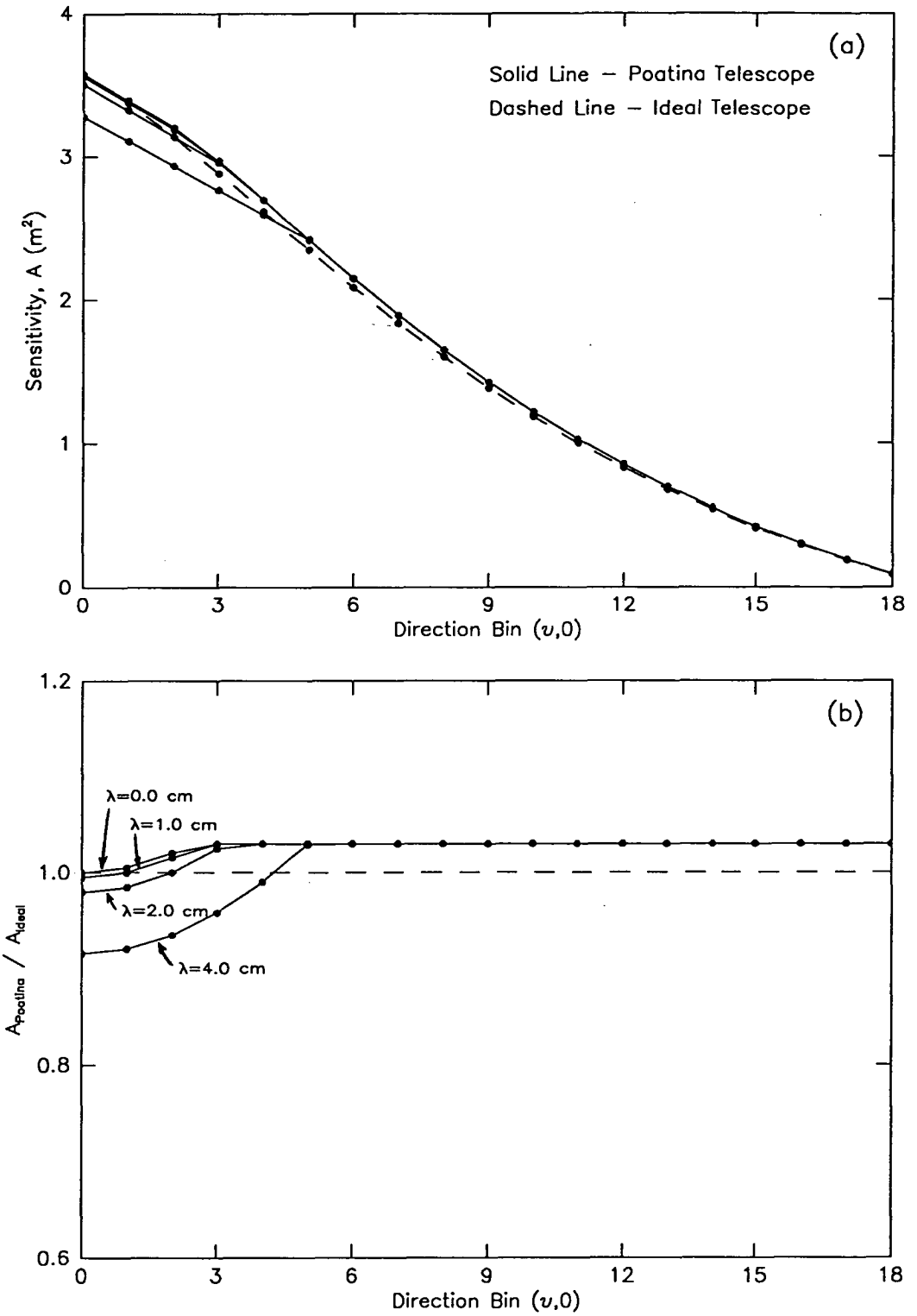

Figure 3.7 (a) Sensitivity of direction bins along half of one directional axis of the Poatina telescope for selected values of the minimum path length. (b) Sensitivity values in (a) compared with those for an ideal telescope.

telescope or nearby rock, then there is no obvious reason why the two distributions should be significantly different.

3.3 Zenith Angle Distribution

The form of the intensity variation given by Equation (3.7) is the expected variation for underground measurements at the depth of the Poatina cosmic ray station. Although there is some doubt about the exact value of n, it is generally assumed to be in the range 2.0 - 2.2 (e.g. Crookes and Rastin, 1971).

Derivation of useful results from Equation (3.7) requires a flat surface topography above the telescope. This does not exist at Poatina where the station is located at the foot of the Great Western Tiers mountain range. Cross-sections of the overburden showing the variation in ground level for both directional axes of the telescope are shown in Figure 3.8, and a 3-D relief map of the entire surface terrain over the field of view of the telescope is shown in Figure 3.9. It is apparent that there is no significant variation in ground level for north-south viewing directions, but a large variation for east-west viewing directions. Therefore, the expression can only be regarded as approximate for the present case.

Equation (3.7) was fitted to the data using a *least squares* method (Bevington 1969). Those direction bins at the extreme edges of the telescope, and those bins whose intensities were influenced by the vertical access shaft, were not included in the analysis. The measured and fitted zenith angle distributions are shown in Figure 3.10, and the coefficients resulting from the fit are listed in Table 3.2. Comparisons of the measured and expected intensities along both directional axes are shown in Figure 3.11. As expected, there is a good fit to the data along one directional axis, i.e. the north-south view, but only a reasonable fit along the other. The effect of the vertical access shaft is clearly seen as an excess intensity for near vertical directions

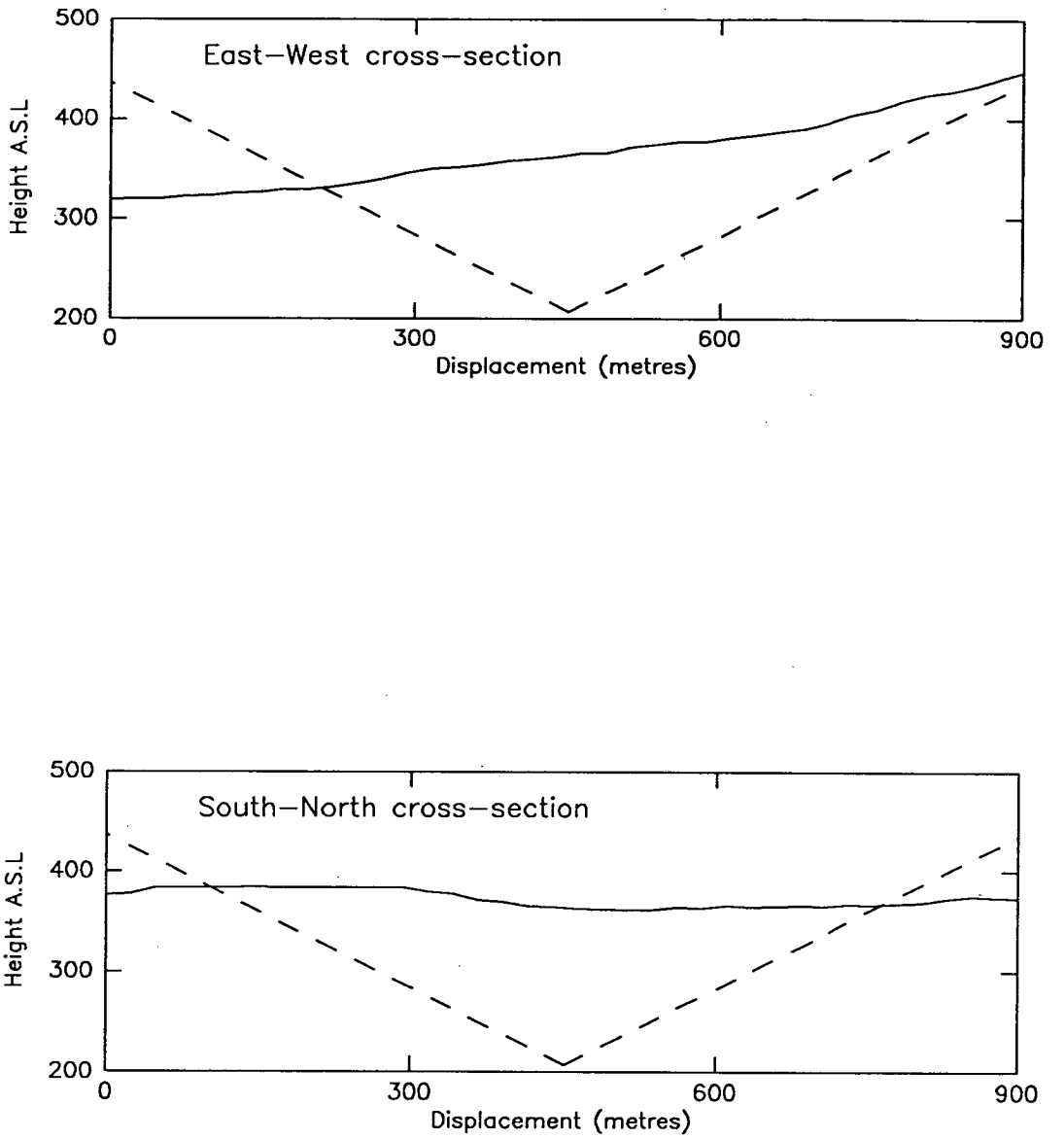

Figure 3.8 Cross-sections of the overburden showing ground-level variations along both directional axes of the Poatina telescope. The dashed lines indicate the field of view of the telescope.

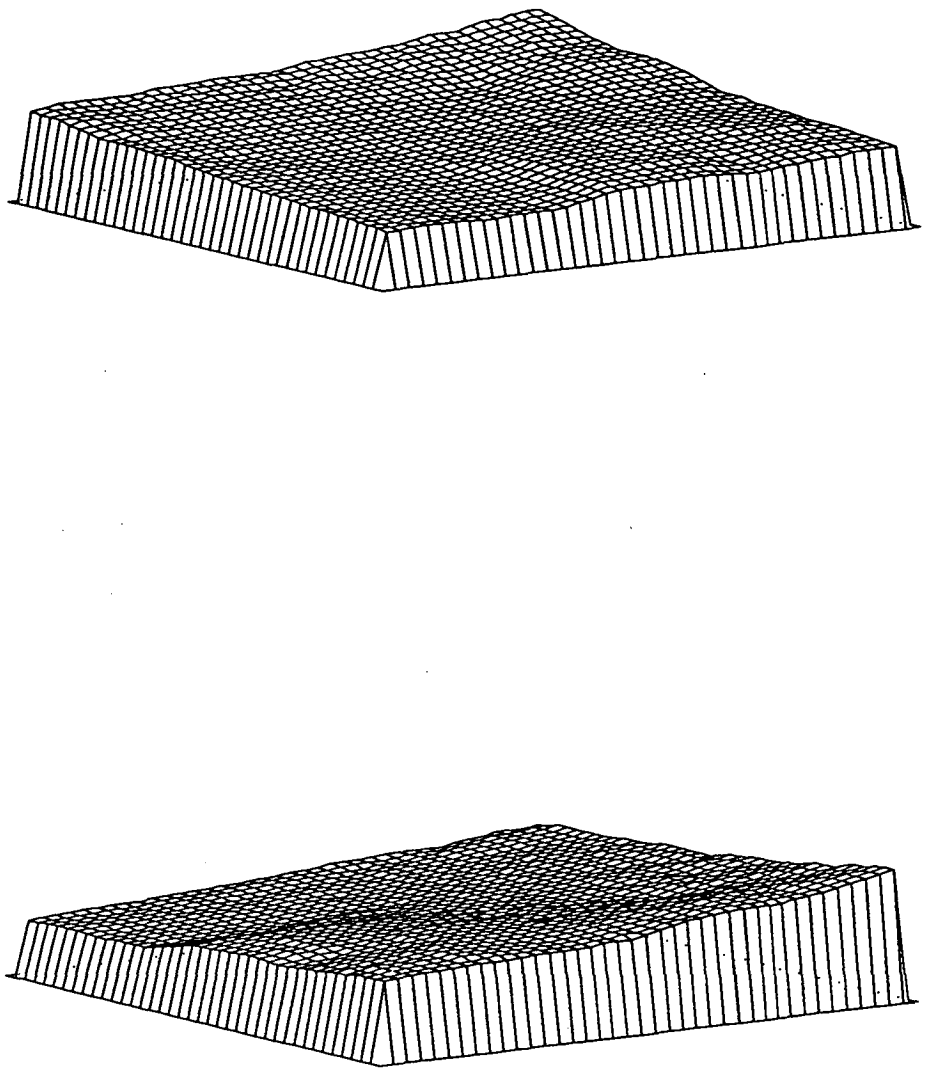

Figure 3.9 3-D relief map of the surface above the Poatina station (drawn to scale).
(Top) Viewed from due East (i.e. West into the page). South is to the left of the page and North to the right.
(Bottom) Viewed from due North. East is to the left of the page and West to the right.

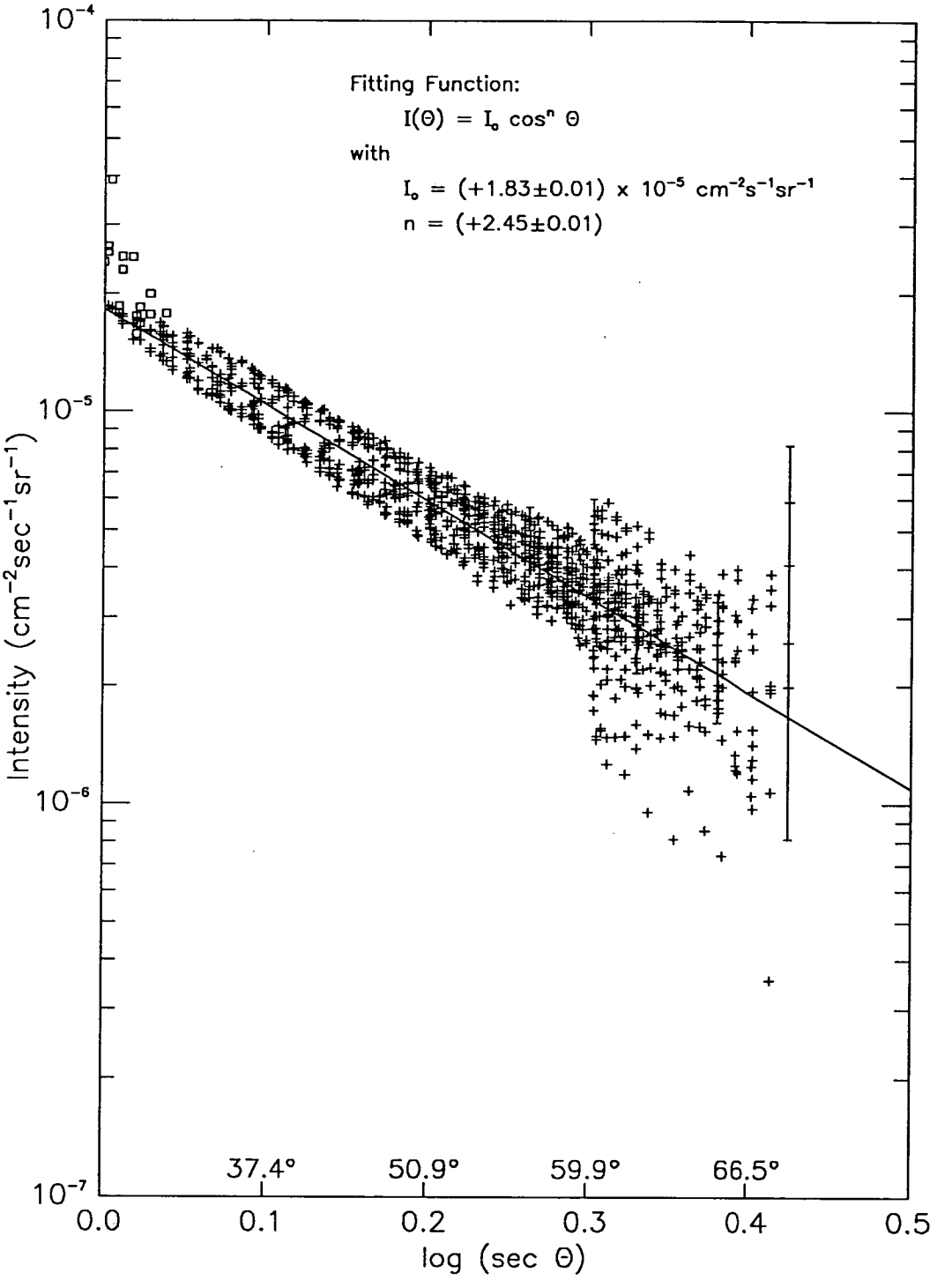

Figure 3.10 Distribution of measured intensities with one point for each direction bin of the telescope. The points marked by squares indicate those bins whose intensities were influenced by the vertical access shaft. Typical error bars are shown for a few selected bins. Note that the errors associated with near vertical bins are smaller than the points drawn. The line is the "best fit" function as indicated on the graph.

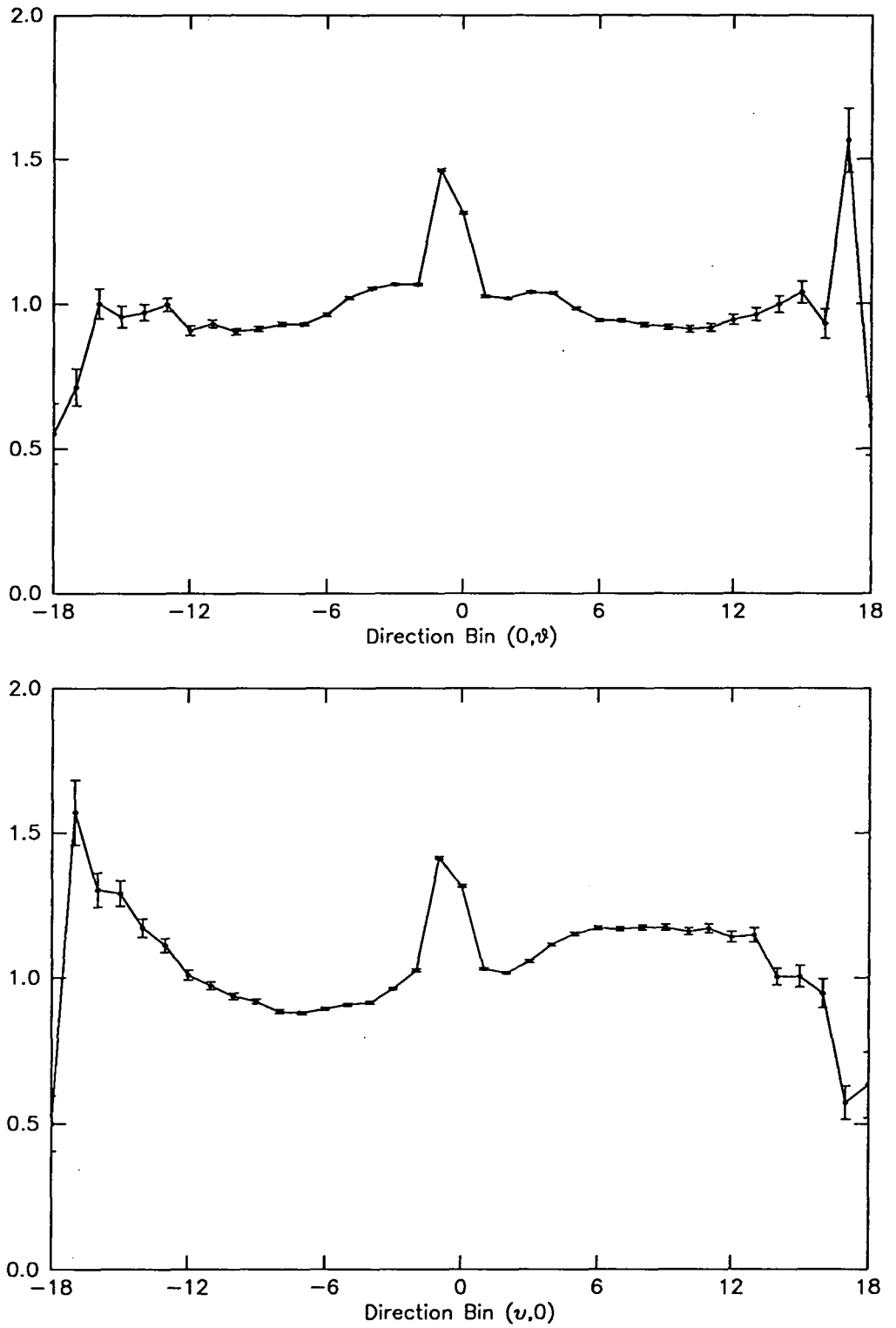

Figure 3.11 Measured intensity divided by the expected intensity for direction bins along both directional axes of the Poatina telescope. The excess intensity due to the vertical access shaft is clearly visible at near vertical viewing directions.

along both directional axes.

In circumstances where the surface topography is not flat, a more applicable form of the zenith angle distribution is

$$I(h) = I_o (h/h_o)^{-n} \tag{3.13}$$

where

h is the distance along a particular trajectory from the surface to the telescope (i.e. the slant depth), and

h_o is the vertical depth of the telescope.

The relation is valid over a limited range of depth Δh, and is identical to Equation (3.7) when the surface topography is flat.

To determine the slant depth associated with each telescope direction bin the overburden was assumed to be homogeneous and the slant depths were simply obtained using a detailed contour map of the surface above the telescope. A more exact calculation would use detailed knowledge of the composition of the material between the telescope and the surface. In the present case, however, the approximate method is more than adequate to determine the origin of local intensity variations with sufficient accuracy. A 20 metre square grid was superimposed on the contour map and the surface height was calculated at each intersection on the grid. A slant depth for each direction bin was obtained by averaging the surface height values from all grid intersections which lay within the field of view of a direction bin. To take account of the sensitivity variation over the field of view of each direction bin, each value was weighted with the relative distance of the grid intersection from the point corresponding to the central viewing direction of a bin.

The fit to Equation (3.13) is shown in Figure 3.12 and the coefficients resulting from the fit are also listed in Table 3.2.

Table 3.2

Zenith Angle Distribution Fitting Coefficients.

Fitting Function	I_o ($\times 10^{-5}$ cm^{-2} s^{-1} sr^{-1})	n	χ^2 (per deg. of freedom)	R
(A) $I_o \cos^n \theta$	1.83 ± 0.01	2.45 ± 0.01	20.1	0.96
(B) $I_o (h_o / h)^n$	1.81 ± 0.01	2.34 ± 0.01	9.0	0.98

Note: R is the *linear-correlation coefficient*, representing the degree of correlation between the data and fitting function. The value of R ranges from 0, when there is no correlation, to ± 1, when there is complete correlation (Bevington 1969).

The high values of the correlation coefficient for each fit indicate that both functions provide a reasonable description of the intensity variation. However, there is obviously better agreement between the data and function *B*, particularly for near vertical viewing angles, whereas the deviations of the data from fitting function *A* appear to be systematically larger than the uncertainties in the data. The two fits can be compared quantitatively by application of the F-test, which tests for the equality of two variances possessing χ^2 distributions (Hoel 1971). For the present case, the χ^2 values in Table 3.2 give $F = {}^{20.1}/_{9.0} = 2.2$. The 1% critical value, above which the variances being compared are considered statistically unequal, is $F \sim 1.1$ for more than 1000 data points. Thus, the fit to function *B* is a significant improvement over that to function *A*.

The large scatter in the tail of both distributions is mainly due to statistical fluctuations, although there is a hint in the distribution shown in Figure 3.12 that the

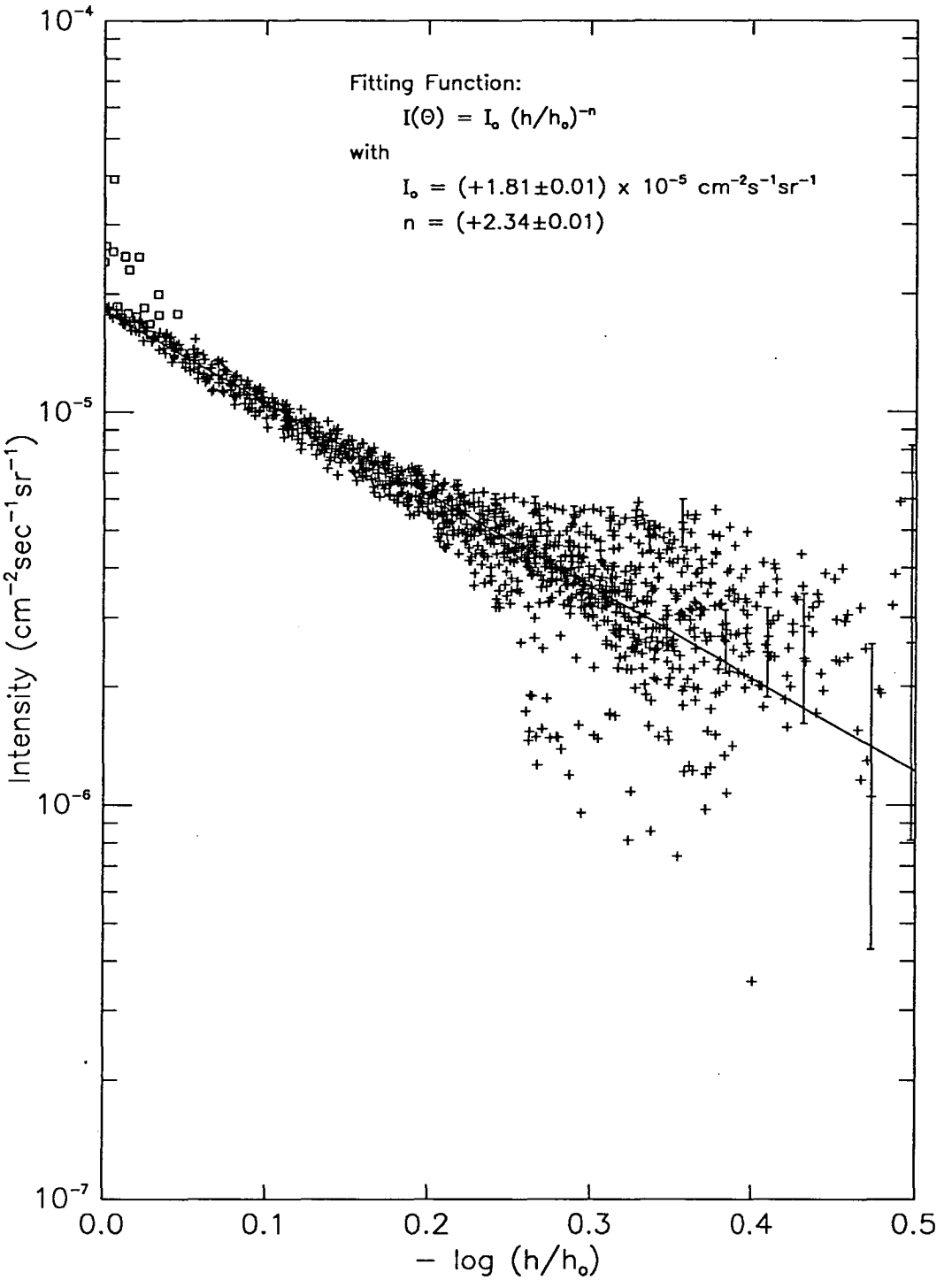

Figure 3.12 Measured intensity as a function of slant depth with one point for each direction bin of the telescope. The points marked by squares indicate those bins whose intensities were influenced by the vertical access shaft. Typical error bars are shown for a few selected direction bins. Note that the errors associated with near vertical bins are smaller than the points drawn. The line is the "best fit" function as indicated on the graph.

slant depths at large viewing angles may have been somewhat over-estimated. However, in view of the relatively low statistical significance of these data, it is doubtful whether a more precise determination of the slant depths would improve the fit to a significant degree, at least for the current data-set.

The value of the absolute vertical intensity from each fit can be compared with that predicted by the depth versus intensity relation of Miyake (1963) with adjusted coefficients as used by Fujii and Jacklyn (1979):

$$I(h) = \frac{8\, h^{-1.13} \exp(-8.25 \times 10^{-4}\, h)}{h + 35} \qquad (3.14)$$

where

h is the vertical depth below the top of the atmosphere in hg cm^{-2}.

For $h = 357$ hg cm^{-2}, $I = 1.98 \times 10^{-5}$ cm^{-2} s^{-1} sr^{-1}. This is slightly higher than those values given in Table 3.2, but considering the uncertainties produced by the presence of the vertical access shaft, the disagreement is not significant. Furthermore, both values of n are higher than expected. The fact that n decreases when ground level variations above the telescope are taken into account, indicates that this discrepancy might be entirely removed by a more rigorous treatment of the overburden. However, given the degree of scatter shown by the data, both of these discrepancies, in the author's opinion, are not worrying features.

3.4 Azimuth Angle Distribution

The azimuth angle distribution of single particle events was calculated by use of a procedure which attempts to convert the measured discrete distribution to the actual continuous distribution. This was necessary, since a straightforward binning of events with respect to azimuth angle would not reveal, with sufficient detail, the important features of the distribution, due to the relatively low angular resolution

provided by the telescope. Because the telescope direction bins represent the minimum directional unit of the telescope, it was necessary to employ an approximate representation of the angular distribution of events recorded by each bin. Given that the direction bins closely resemble those for an ideal telescope, the event distributions were approximated using the gathering power formulae listed in Appendix B.

The procedure is as follows; each direction bin is subdivided into small segments and the gathering power of each segment is calculated analytically. Each value is weighted so that the total gathering power for a direction bin is normalized to the measured average event rate of the bin, and then distributed with respect to the central azimuth angle of each segment's viewing cone. The smoothness of the final distribution depends on the degree of segmentation and was chosen, in the present case, to reveal the main features of the distribution without requiring excessive computational time.

The expected distribution was determined using the same procedure, with the exception of the normalization step, and is therefore based on the assumption of a flat surface topography. Thus, differences between the two distributions should directly reflect the variations in ground depth over the field of view of the telescope. The two distributions are shown in Figure 3.13.

The fourth harmonic modulation evident in the expected distribution is entirely due to the rectangular acceptance of the telescope. The maximum of the measured distribution corresponds to a large predominance of particles from the south-west (i.e. $\phi = -140°$), the position of the vertical access shaft relative to the telescope. As previously mentioned, ground level drops away towards the east (see Figure 3.8), which produces the observed increase in event rate for easterly viewing directions. Conversely, ground level rises towards the west resulting in the decreased intensity for westerly viewing directions which is, however, almost completely overshadowed by the large increase in intensity due to the vertical access shaft.

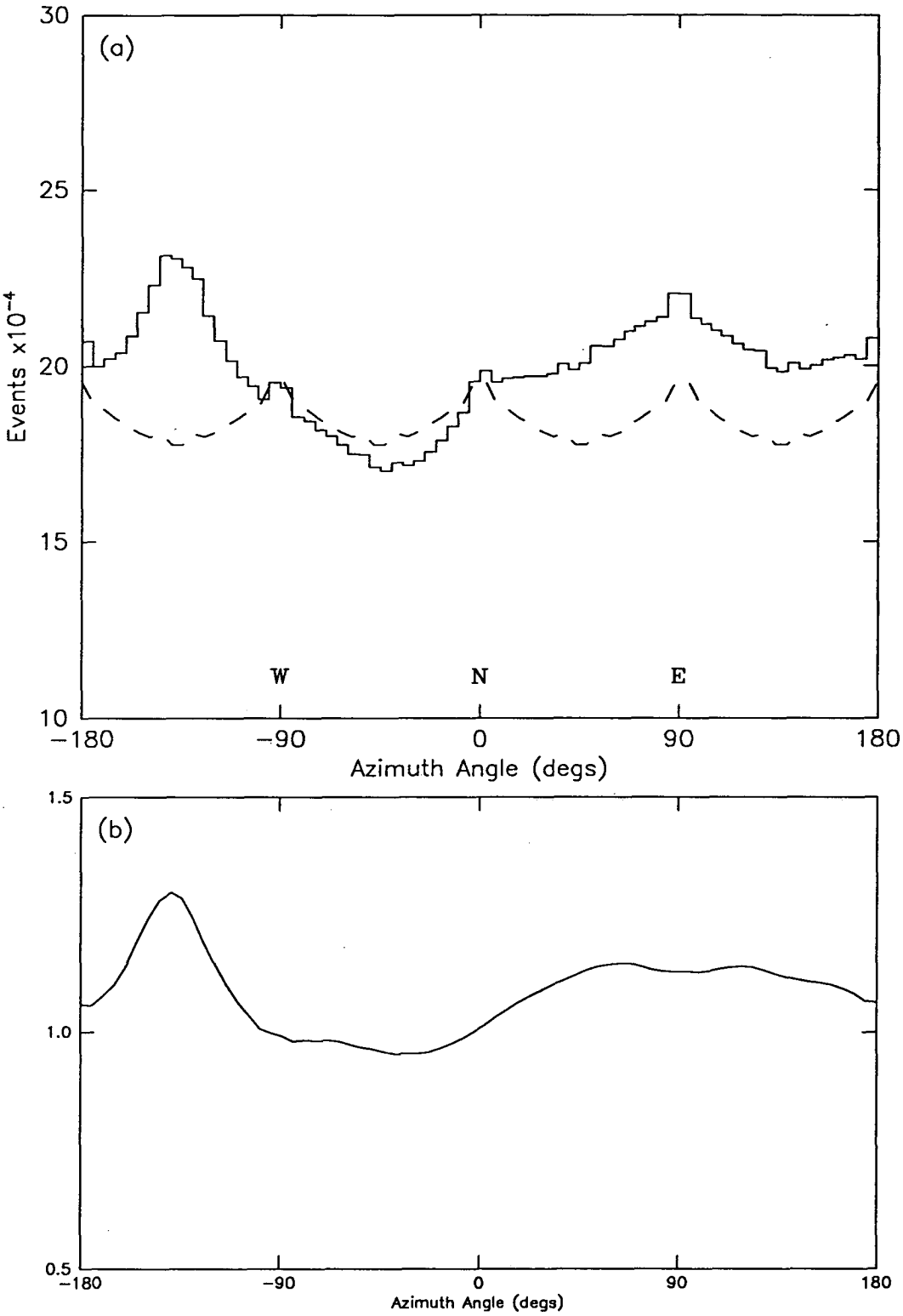

Figure 3.13 (a) Single particle event distribution in azimuthal angle. The histogram is the measured distribution and the dashed line is the expected distribution assuming a flat surface topography. The two curves have been normalized at $\phi = 0$. (b) Measured divided by the expected distribution. The effect of the vertical access shaft is clearly visible.

3.5 Multiple Particle Analysis

The multiple particle event analysis (see Appendix A) was hampered by a programming error in the multiple particle reconstruction algorithm, which was not detected until a large majority of the data had already been collected. This has resulted in an inflated number of muon pair events. Bearing this in mind, the relative detection rate of multiple particle events as a function of multiplicity and lateral separation are shown in Figures 3.14 and 3.15 respectively.

Multiple particle events are caused by several high energy atmospheric muons produced from a single primary particle. Almost all observed muons at the relatively shallow depth of the Poatina telescope are generated by primary protons. Therefore, an efficient study of the cosmic ray primary composition, using the Poatina telescope, would require the detection of muon bundles of the highest detectable multiplicity and hence the highest average primary energy. However, the statistical significance of such events would be severely limited by the reduction in effective telescope size for the detection of events with increasing multiplicity, because of the increased spatial separation of the particles defining the event. Moreover, the average lateral spread of muons at a depth underground of 347 hg cm^{-2} is ~ 17 m (Gaisser and Stanev 1985), which is considerably larger than the physical dimensions of the telescope. In fact, Gaisser and Stanev estimate the optimal size of a muon detector for composition studies at this depth to be approximately 12000 m^2, based on extrapolations from larger depths. In view of these facts, a complete analysis of the multiple particle events was not attempted.

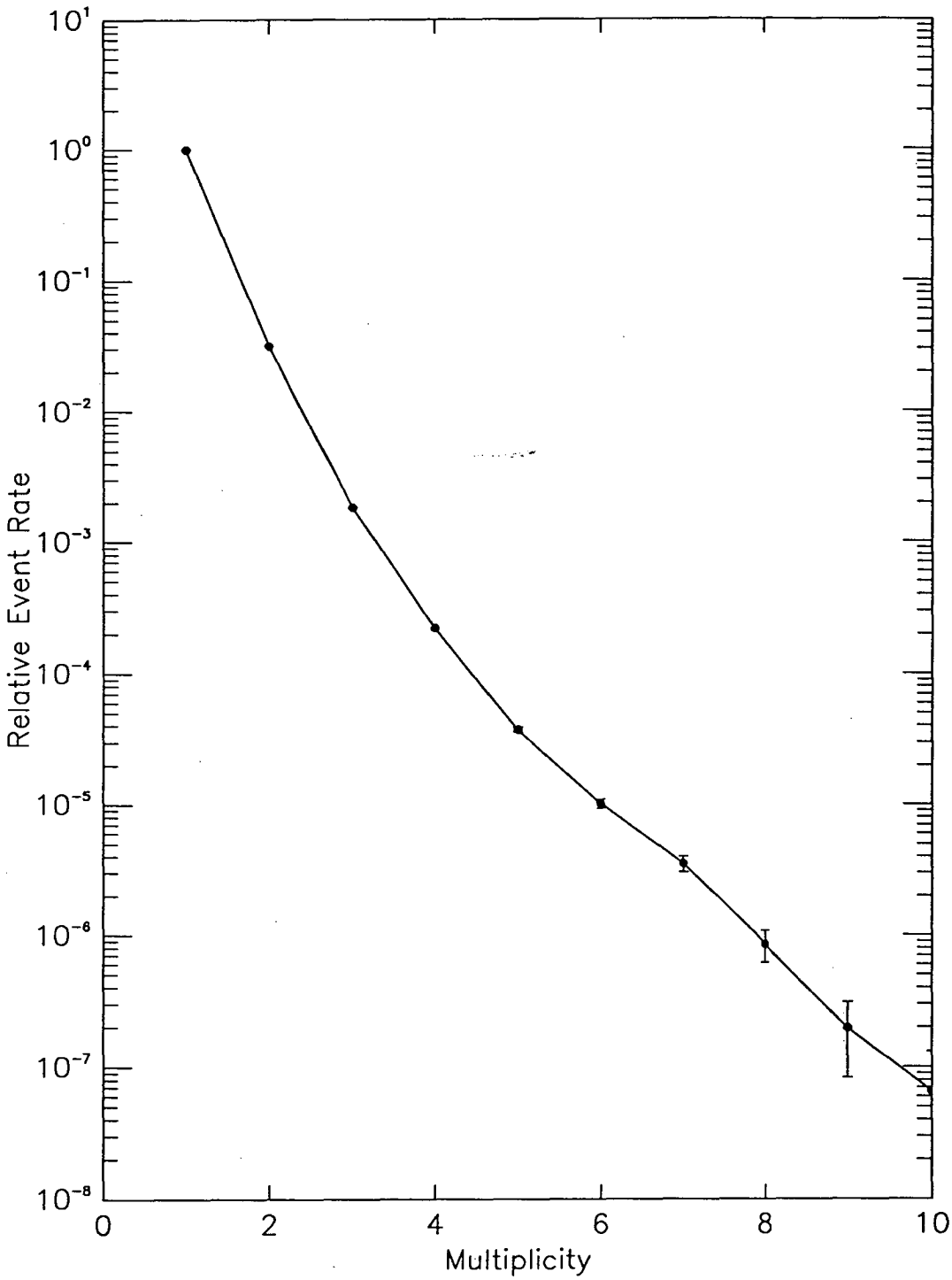

Figure 3.14 Relative detection rate of multiple particle events as a function of event multiplicity.

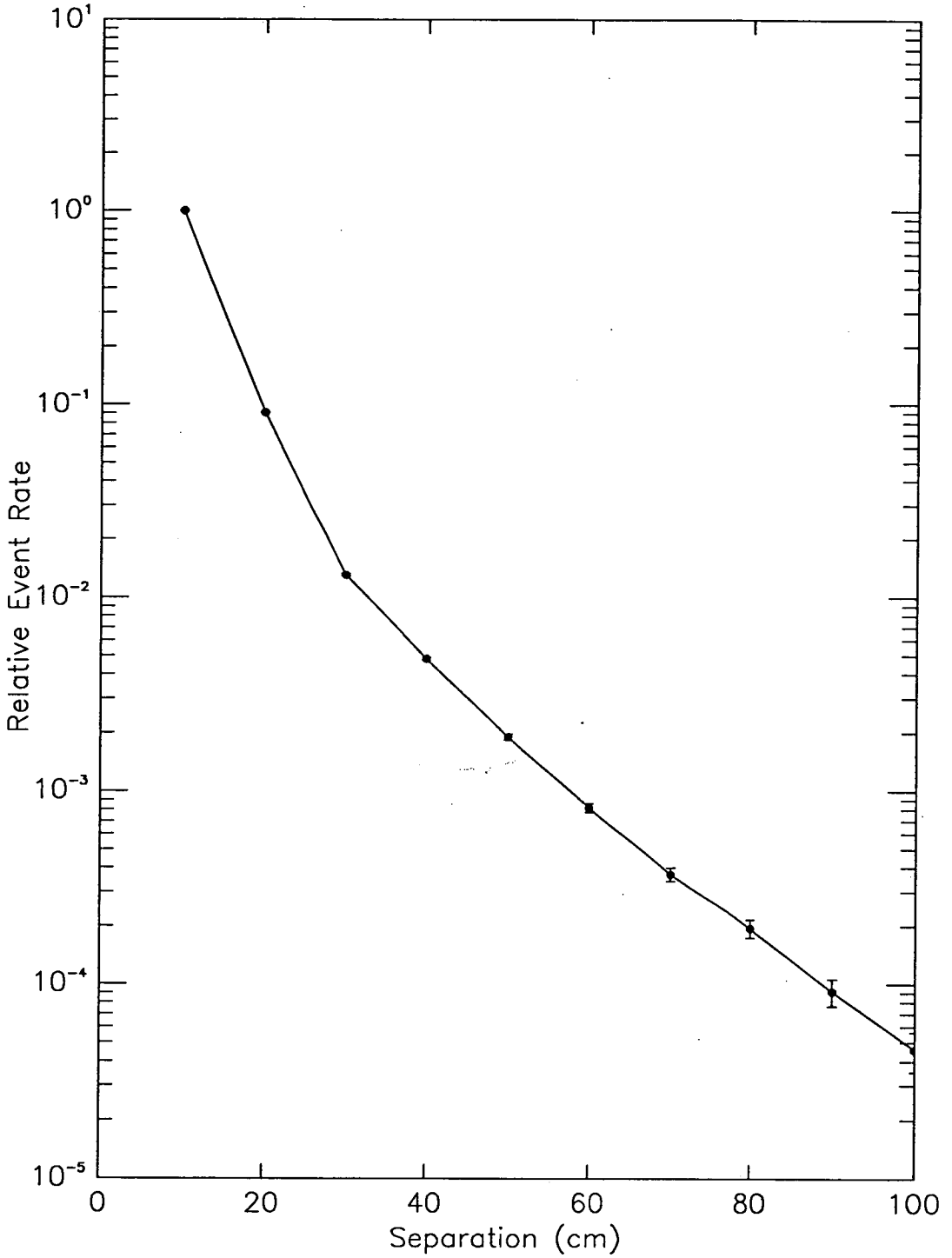

Figure 3.15 Relative detection rate of multiple particle events as a function of particle separation.

Chapter 4

Narrow-Angle Anisotropy Search

4.1 Introduction

This chapter presents the results of a search for narrow-angle anisotropies in the high-energy cosmic ray flux. The search method consisted of measuring the distribution of arrival directions in celestial coordinates, with a subsequent search for statistically significant deviations from the expected distribution based on the assumption of an isotropic primary cosmic ray flux.

The following section presents a brief review of previously reported detections of narrow-angle anisotropies. The remaining sections of the chapter detail the analysis of the 18×10^6 events recorded over the period August 1987 to January 1989 of the current investigation.

4.2 Observed Narrow-Angle Features in the Cosmic Ray Flux

There have been many searches for narrow-angle anisotropies in the cosmic ray flux, originating with the observations of Sekido *et al.* (1959). Three distinct types of narrow-angle effects have since been reported. These are:

i) Isolated Anisotropies: narrow-angle deviations in the primary flux at energies less than 1 TeV which appear to exhibit modulation by the solar magnetic field.

ii) Mottled Intensity Patterns: numerous small scale deviations at primary energies above 1 TeV as reported by Bazer-Bachi *et al.* (1975). These anisotropies disappeared over a period of a few years.

iii) Point Sources: high-energy cosmic ray flux from neutron star binary X-ray sources and pulsars in which the characteristic temporal signature of the source is observed.

A common feature of many of these anisotropies is that they appear to follow Griesen's Law - *the anisotropy tends to decrease in amplitude with the accumulation of additional years of data* (Barrowes 1972). This feature has to a large extent been responsible for the lack of confirming observations by other workers which may have established the existence or otherwise of the anisotropies. The evidence (as limited as it is) indicates that the variability of the lower energy anisotropies may be related to the solar cycle, whereas the transient nature of the point source observations is almost certainly related to some episodic behaviour of the source itself.

4.2.1 Isolated Anisotropies

The first reported detection of a narrow-angle anisotropy was by Sekido *et al.* (1959) using a Geiger-Muller counter telescope sensitive to muons originating from primaries with median energy 280 GeV. The excess observed over the period 1952 - 1956 comprised a 6σ deviation from isotropy, with the angular extent of the observed anisotropy being smaller than the resolution of the telescope (i.e. $2.5° \times 4°$). Similar isolated deviations from isotropy were observed by Jokisch *et al.* (1975) in 1974, and by Allkofer *et al.* (1979) in 1977. A common feature of these three observations is that the narrow-angle anisotropies had similar statistical significance, disappeared over periods of about 1 to 4 years, and were all similarly located, after geomagnetic

correction, along the celestial equator (near $\alpha = 80°$) as shown in Figure 4.1.

An intense isolated anisotropy was detected by Bukata *et al.* (1965) using a narrow-angle telescope (resolution $15° \times 15°$) sensitive to primary particles with energy above 40 GeV. In this case, a 15σ excess was observed which lasted for 10 months in 1963 - 1964. More significantly, the existence of the anisotropy was confirmed, at least for 3 out of the 10 months, by the concurrent observations of Wang *et al.* (1969) using a wide angle telescope (resolution $70° \times 70°$).

As was noted by Barrowes (1972), the above mentioned anisotropies coincide with periods of low solar activity. In particular, even though Sekido *et al.* (1959) continued observing until 1961, the narrow-angle excess was not detected after 1956 (Barrowes 1972). Furthermore, the anisotropy observed by Allkofer *et al.* (1979) appeared to be enhanced for positive interplanetary magnetic field (IMF) direction but disappeared for negative IMF direction. These facts are suggestive of modulation of the incident particles by the IMF, leading to the conclusion that charged particles are responsible for the anisotropies. The model of adiabatic propagation, as proposed by Barrowes (1972), predicts such anisotropies due to charged primary particles from unknown nearby sources propagating in a smooth galactic magnetic field on a small scale. Solar modulation of the cosmic ray beam could occur through a defocusing effect exerted by the solar cavity, which would be enhanced at solar maximum due to the increased size of the solar cavity.

4.2.2 Mottled Intensity Patterns

A comprehensive survey of the northern celestial sky was performed by Bazer-Bachi *et al.* (1975) using an underground muon telescope (resolution $1° \times 1°$) located in the Mont Blanc Tunnel. The celestial sky as seen by this experiment ($\delta > 25°$N) appeared to have many small regions of increased (a positive anisotropy) and

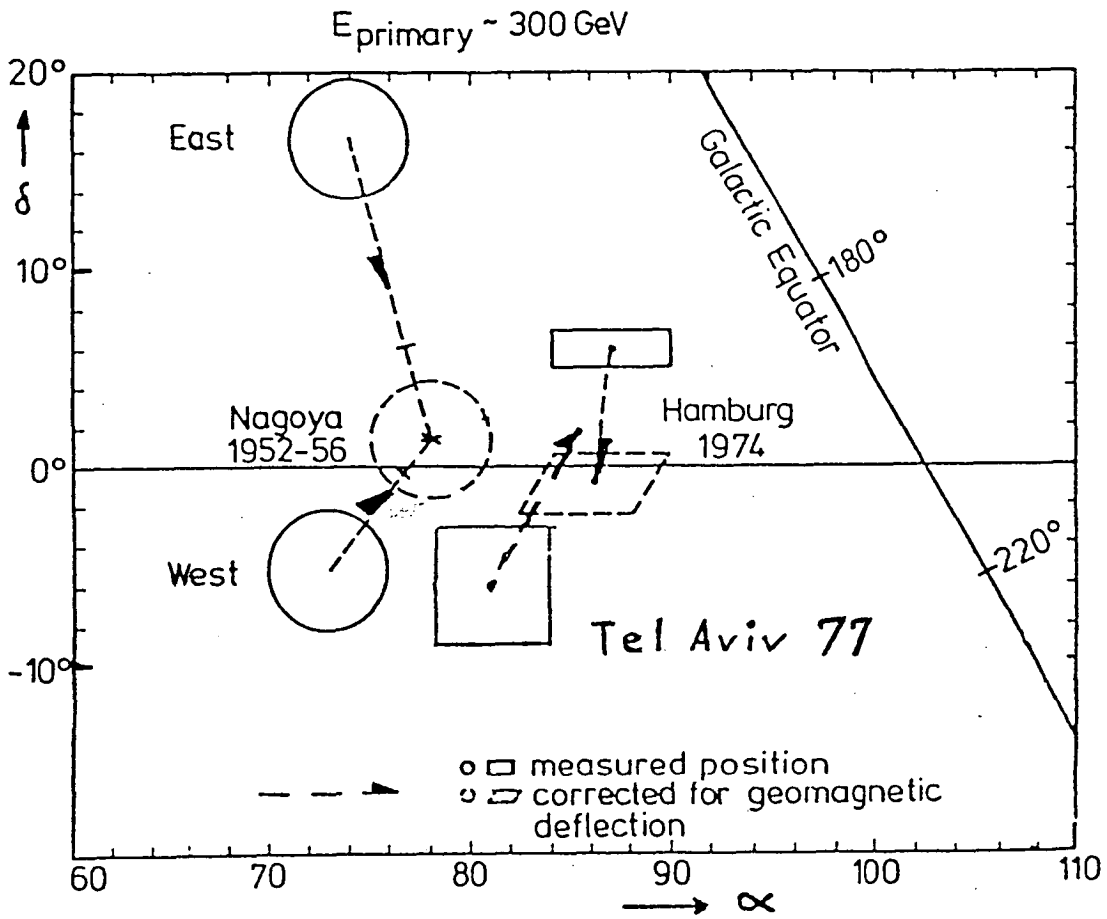

Nagoya ..... Sekido *et al.* (1959)

Hamburg ..... Jokisch *et al.* (1975)

Tel Aviv ..... Allkofer *et al.* (1979)

Figure 4.1 Location of anisotropy near $\alpha = 80°$ and $\delta = 0°$ (from Allkofer *et al.* 1979)

decreased (a negative anisotropy) muon intensity. The deviations were seen to have a typical amplitude of 30% of the isotropic background flux, and lasted for 1 to 3 years. Only one of the anisotropies was observed to persist throughout the six year period of the experiment (July 1968 - April 1975). Further observations made between September 1977 and January 1979 gave evidence for a similar intensity pattern which behaved qualitatively in much the same manner as previously reported (Bazer-Bachi *et al.* 1979).

Observations carried out by Wilson (1985a) employing an underground muon telescope (resolution $5° \times 5°$) located at the Poatina cosmic ray station, give support for this view of a mottled celestial sky. In this case, observations of the southern sky (13°S - 67°S) made between August 1983 and September 1984 support the existence of both positive and negative small scale ($> 4\sigma$) deviations from isotropy, although the excesses were not as numerous as those observed by Bazer-Bachi *et al.* (1975). Moreover, the largest observed excess (a 4.7σ deviation), which appeared to be constant throughout the entire observing period, coincided with a previously reported sidereal anisotropy detected at the same station using wide angle telescopes (Wilson 1985b).

Negative anisotropies are not predicted by a theory such as that proposed by Barrowes (1972), which recognizes point-like sources of cosmic rays as the cause of anisotropies. Bazer-Bachi *et al.* (1975) suggest that the mottled intensity effect may be due to "moving, nearby irregularities in the galactic magnetic field".

Several higher energy sky surveys have been made employing extensive air shower (EAS) techniques. To date, none have detected a significant narrow-angle deviation from isotropy or a mottled intensity (e.g. Morello *et al.* 1983, Gerhardy *et al.* 1983, Abdullah *et al.* 1983).

4.2.3 Point Sources

In the energy range 10^{11} eV - 10^{14} eV (very-high-energy or VHE) the atmospheric Cerenkov technique is used to detect the Cerenkov radiation of those secondary particles which are travelling faster than the speed of light in air. Cygnus X–3 was discovered as a TeV source by use of this technique when an excess of events coincident with the source position was observed by the Crimean Astrophysical Observatory group (Vladimirsky *et al.* 1973). The observed events are depicted in Figure 4.2 as a function of right ascension, showing clearly the excess at the source position. Centaurus A, our nearest active galaxy, was first observed at TeV energies by Grindlay *et al.* (1975a, 1975b) using the atmospheric Cerenkov technique; a 4.5σ time-averaged excess was detected. Partial rejection of cosmic ray events was achieved by the use of a muon veto, based on the assumption that gamma-ray initiated showers would be deficient in muons (see Section 1.3).

The main stumbling block to using atmospheric Cerenkov and EAS techniques (and more recently underground muon measurements) to search for emission from celestial sources is the extremely high rate of background events. Assuming the source events are gamma-rays, this situation will improve somewhat with increasing energy, due to the flatter energy spectrum of gamma-ray sources compared with the total cosmic ray particle energy spectrum (Wdowczyk and Wolfendale, 1983). Even so, at lower energies it is possible to achieve an improved signal to background ratio if the source has a known periodicity. Such a source can be detected by searching for an excess above the non-periodic background. This method has been successfully used to detect a number of TeV sources, e.g. the neutron star binary system Hercules X-1 (Dowthwaite *et al.* 1984), and the Crab and Vela pulsars (Gibson *et al.* 1982; Bhat *et al.* 1980).

At energies above 10^{14} eV (ultra-high-energy or UHE) EAS techniques are used to directly detect air shower particles. The most notable detection using this

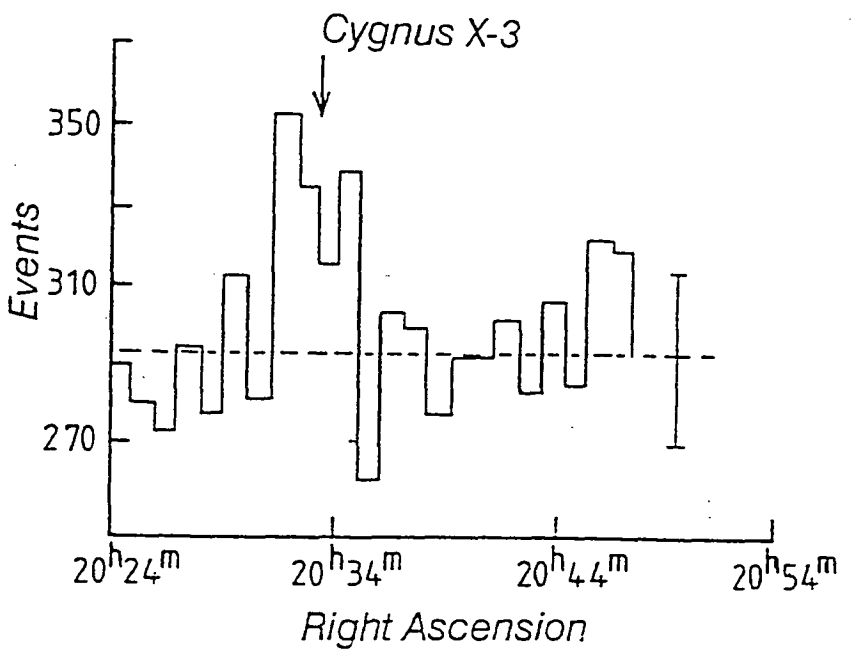

Figure 4.2 Intensity time profile of Cygnus X-3 (from Vladimirsky *et al.* 1973)

technique was that of UHE emission from Cyg X-3 by Samorski and Stamm (1983) using the University of Kiel air shower array. A statistically significant excess of air showers was observed in a $4° \times 3°$ bin centred on Cyg X-3, which subsequently were found to display the 4.8 hour periodicity of the source. This result was later confirmed by the observations of Lloyd-Evans *et al.* (1983) using data from the Haverah Park array.

As at lower energies, an improvement in signal to background ratio can be achieved by analysing data at the known or suspected source periodicity, and other UHE sources have been detected in this manner. Some examples are the binary X-ray sources Vela X-1 (Protheroe *et al.* 1984) and LMC X-4 (Protheroe and Clay, 1985).

4.3 Measured Distribution of Arrival Directions

To measure the distribution of arrival directions in celestial coordinates, a celestial grid with a spacing of 5° in right ascension and 5° in declination was used. The intensity associated with any particular $5° \times 5°$ celestial bin was derived from events recorded by the set of telescope direction bins that had central viewing directions located within the celestial bin.

The hour angle and declination of the central viewing directions of all the telescope direction bins are shown in Figure 4.3. Since all points on the celestial sphere having a particular declination pass through the field of view of the telescope in exactly the same way, celestial bins within the same declination band will have identical sensitivity. The total sensitivity of a celestial bin will be the sum of the sensitivities of those telescope direction bins that have central viewing directions which pass through the celestial bin during one sidereal rotation of the earth. The sensitivity of celestial bins within each of the 5° declination bands are shown in Figure 4.4.

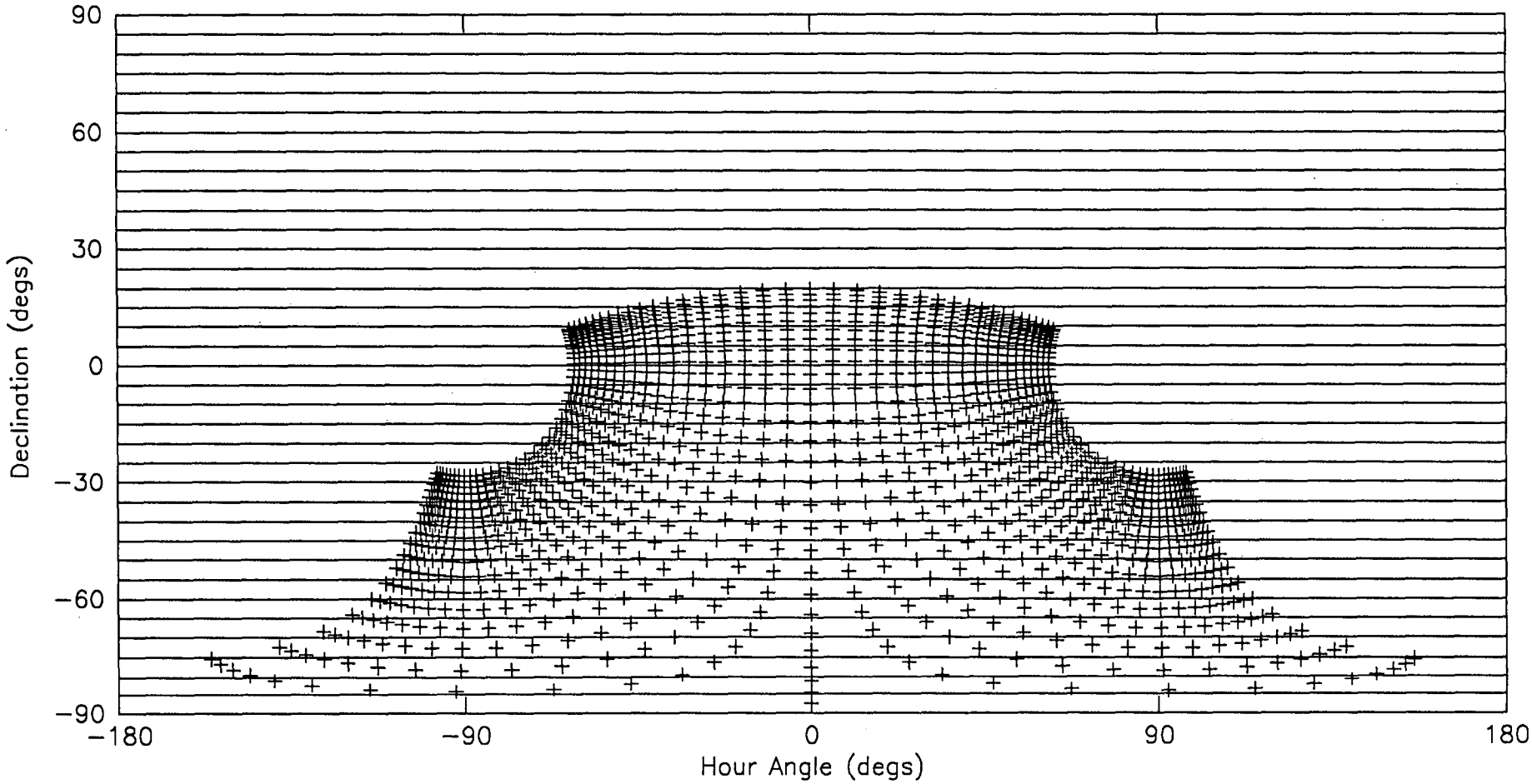

Figure 4.3 Celestial coordinates of the central viewing directions of the telescope directions bins.

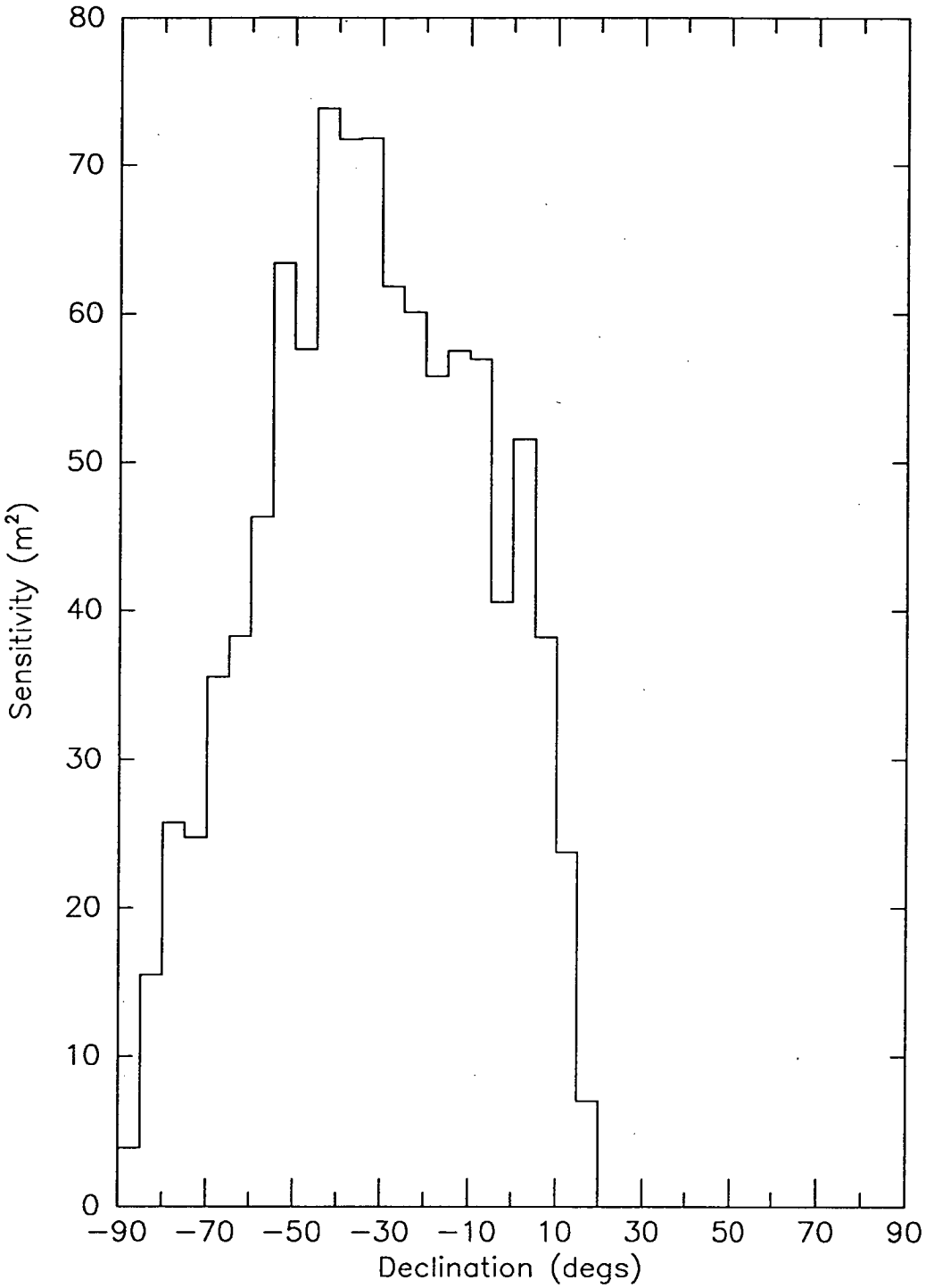

Figure 4.4 Sensitivity of the 5° declination bands.

Similarly, the *density function* of a celestial bin (i.e. the distribution in celestial coordinates of recorded events) is the sum of the density functions of those telescope directions bins located within the celestial bin. Since the direction bins represent the minimum directional unit of the telescope, it is not possible to measure the exact distribution of events recorded by a direction bin. But, given that the direction bins closely resemble those for an ideal telescope, the event distribution can be represented approximately by the gathering power formulae given in Appendix B, and determined by a procedure similar to that described in Section 3.4. The density function for a celestial bin is then calculated by projecting the direction bin density functions onto the celestial sphere and summing over all appropriate direction bins.

The resulting density functions for two different declination bands are shown in Figures 4.5 and 4.6. The angular extent of the function depends on the declination of the celestial bin, but in each case extends outside the $5° \times 5°$ celestial bin. Thus, if a highly localized anisotropy does exist, it might be expected to show up as a deviation within one or two neighbouring bins. Whether or not it will exceed the statistical fluctuations within each bin will depend on the magnitude of the anisotropy.

To produce a map of sky intensity from the set of recorded arrival directions, it was necessary to make several assumptions concerning the cosmic ray flux and the response of the telescope to the flux. These are:

(1) The primary cosmic ray flux is approximately isotropic with respect to celestial coordinates.

Cosmic rays are remarkably isotropic even up to the highest energies (Wolfendale 1973). At very-high-energies the majority of sidereal anisotropy measurements have been made using underground detectors. It has been well established from such measurements that the amplitude of the sidereal anisotropy is small (~ 0.05%) and is constant up to about 10^{14} eV (e.g. Humble *et al.* 1985).

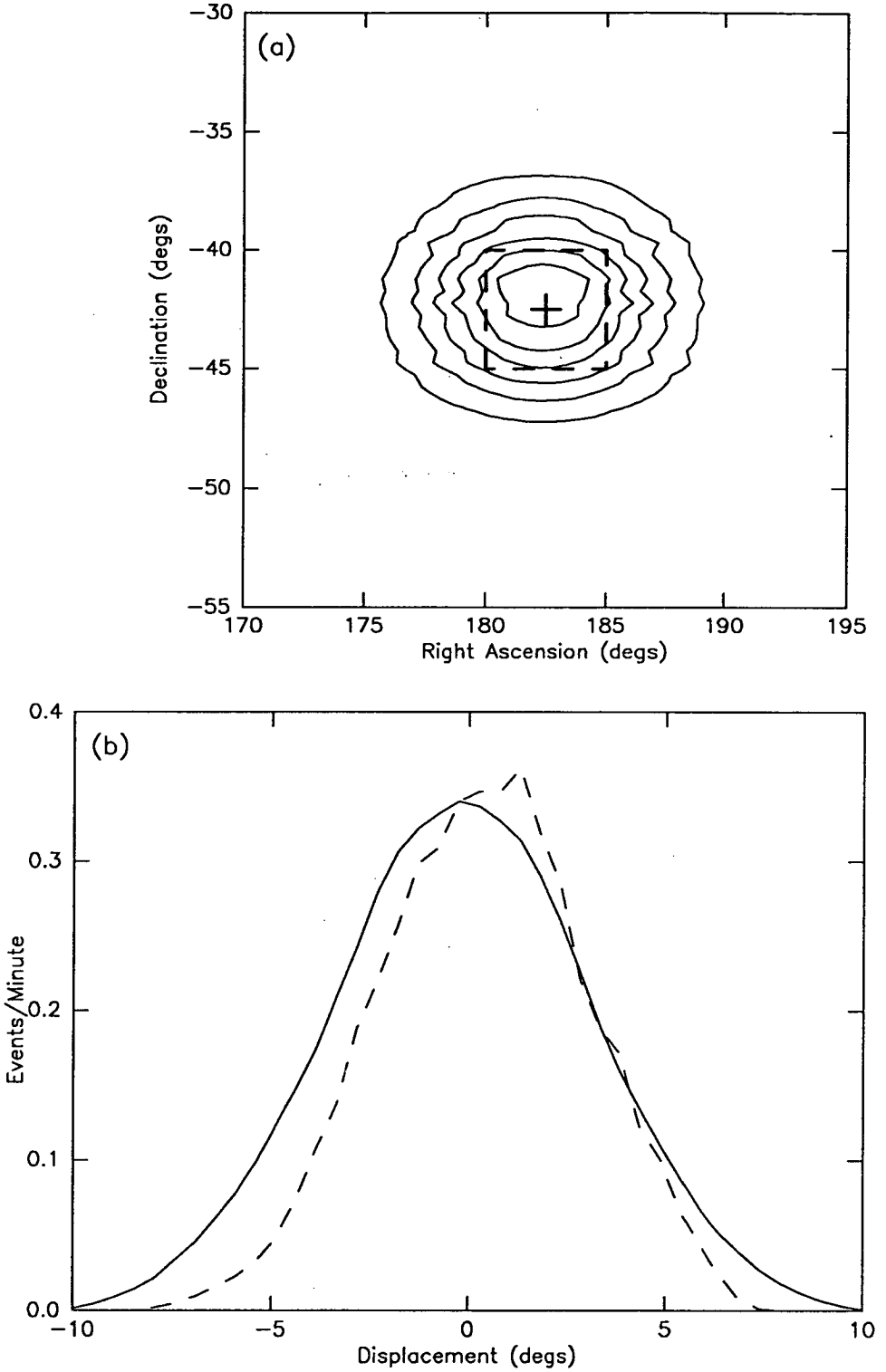

Figure 4.5 (a) Density function of a celestial bin in the declination band 40°S - 45°S. The dashed lines indicate the boundaries of the bin and the cross marks the centre of the bin. (b) Profiles of the density function in right-ascension (solid) and declination (dashed). The FWHM of the profiles are 7.0° and 6.2° respectively.

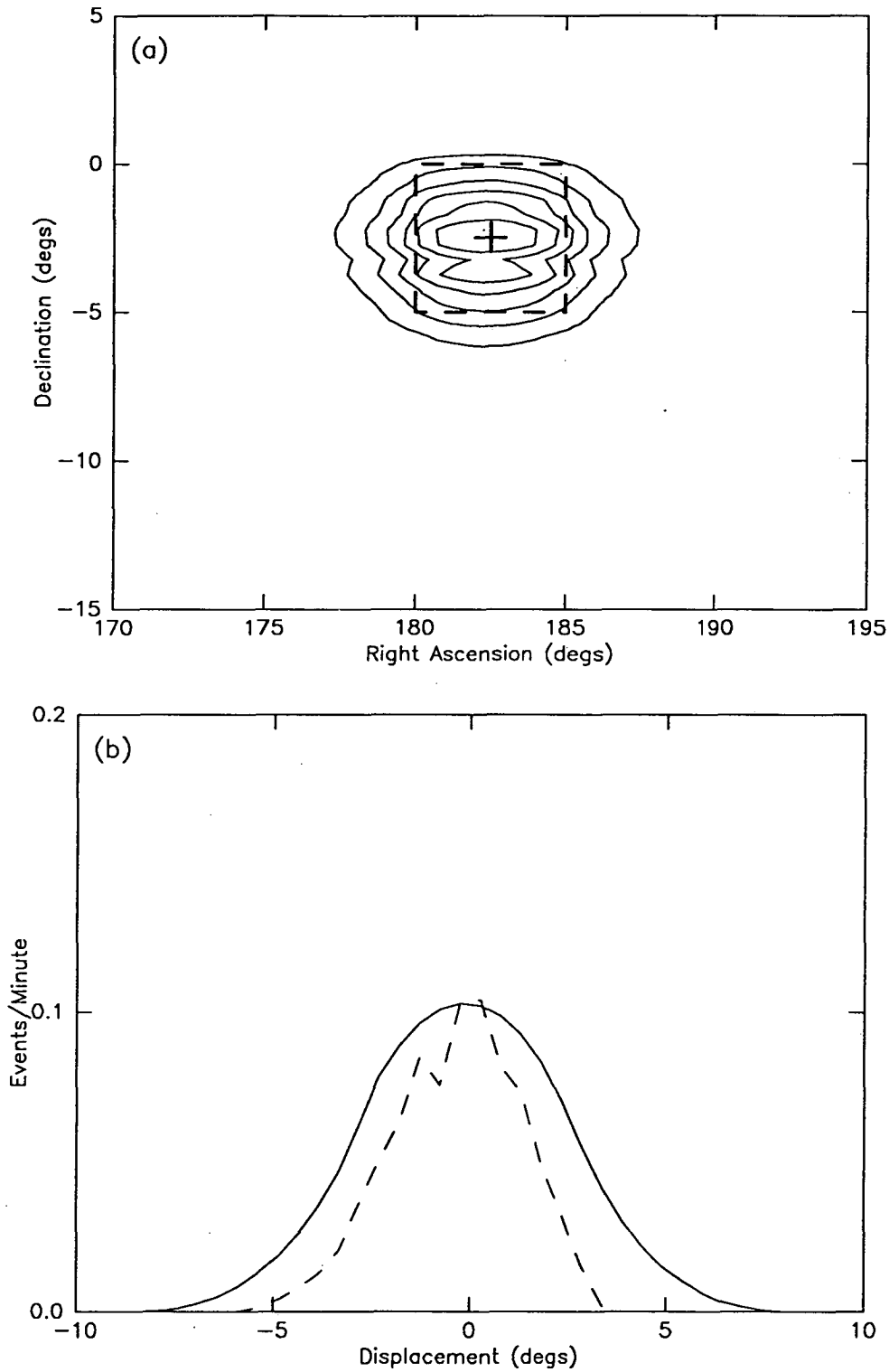

Figure 4.6 (a) Density function of a celestial bin in the declination band 0° - 5°S. The dashed lines indicate the boundaries of the bin and the cross marks the centre of the bin. (b) Profiles of the density function in right-ascension (solid) and declination (dashed). The FWHM of the profiles are 5.9° and 4.7° respectively.

(2) The direction of the detected muon is the same as that of the primary particle within the resolution of the telescope.

The main source of angular uncertainty of particle arrival directions at the depth of the Poatina station is multiple Coulomb scattering in the overburden. From the examples given in Section 1.2.5 it is expected that most of the particles detected by the telescope will be within a cone of 1° half-aperture centred on the original primary direction.

(3) Any atmospheric modulation of intensity will be the same in all directions over the field of view of the telescope.

Lyons *et al.* (1981) have made detailed calculations of the partial atmospheric coefficients at the Poatina station; the results are $b_P = -0.025$ % mb^{-1} and $b_T = +0.070$ % K^{-1} using data collected over the period 1972 - 1976. The height coefficient, b_H, was not included in the analysis, since small changes in the mean muon production height are expected to have a negligible effect on the muon intensity at this depth. The typical day-to-day pressure variation at the station is 15 mb, while the typical temperature range is about 5° (in the 100 - 200 mb level). These values indicate that atmospheric effects on the muon intensity at Poatina are small compared to the statistical fluctuations of the data themselves. Therefore, no atmospheric corrections were made to the current data-set.

On the basis of the above assumptions, the accumulation of recorded events onto the celestial intensity map is straightforward and proceeds as follows:

i) The event reconstruction analysis assigns each event to a telescope direction bin.

ii) The recorded event arrival time (to the nearest millisecond) is converted to a local sidereal time, τ.

iii) The celestial coordinate of the event is then calculated as

$$(\alpha,\delta) = (h,\delta) + (\tau,0)$$

where (h,δ) are the precalculated hour angle and declination of the central viewing direction of the telescope direction bin.

iv) The event is then assigned to the celestial bin that contains the coordinates (α,δ).

The measured distribution of arrival directions was produced on a monthly basis so that the intensity as a function of time was available for each celestial bin.

4.4 Expected Distribution of Arrival Directions

The main problem in the calculation of the expected distribution of arrival directions is to make proper allowance for the fact that the telescope did not view each part of the celestial sky for the same amount of time, primarily due to power failures. Therefore, the measured distribution of arrival directions would be expected to be anisotropic to some degree even if the primary flux were isotropic. There are two common methods for correcting the data to allow for this non-uniform exposure. The first is a relatively simple procedure which involves randomly rejecting data from *over-exposed* regions to smooth out the distribution of events in right-ascension to its lowest level. This method is usually appropriate when the distribution of events in right-ascension is nearly uniform to begin with, otherwise a large portion of the data (which has so painstakingly been collected) is not used in subsequent data analysis. The second, and the preferred, method is to maintain an exact record of the amount of time the telescope viewed each region of the celestial sky. The observing live-time information can then be coupled with the known response of the telescope to

determine the expected distribution of arrival directions.

Since the arrival time of each event had been recorded with excellent precision, the second method was used for the current investigation, i.e. by using the known observing time distribution combined with the measured average response of the telescope. The observation *on-time* function $Q(t)$, which represents the number of sidereal minutes the telescope was observing at time t, was defined such that

$$\int_0^{24} Q(t)\,dt = T_{obs} \tag{4.1}$$

where

T_{obs} is the total experimental live-time.

The relatively high event rate of 0.6 Hz enabled the function to be obtained directly from the arrival times recorded with each event, allowing all data gaps greater than a few minutes to be accounted for. The on-time function for the entire observing period is shown in Figure 4.7.

For each declination band a response function, $R_\delta(t)$, was calculated from the measured response of those direction bins that had central viewing directions located in the band, i.e.

$$R_\delta(t) = \sum_{u,v} A(u,v) \tag{4.2}$$

where

$A(u,v)$, the average response of the (u,v) direction bin, is given by

$$A(u,v) = {}^1/_{\Delta T} \sum_{\Delta T} C(u,v) \tag{4.3}$$

and, $C(u,v)$ is the event rate for the (u,v) direction bin.

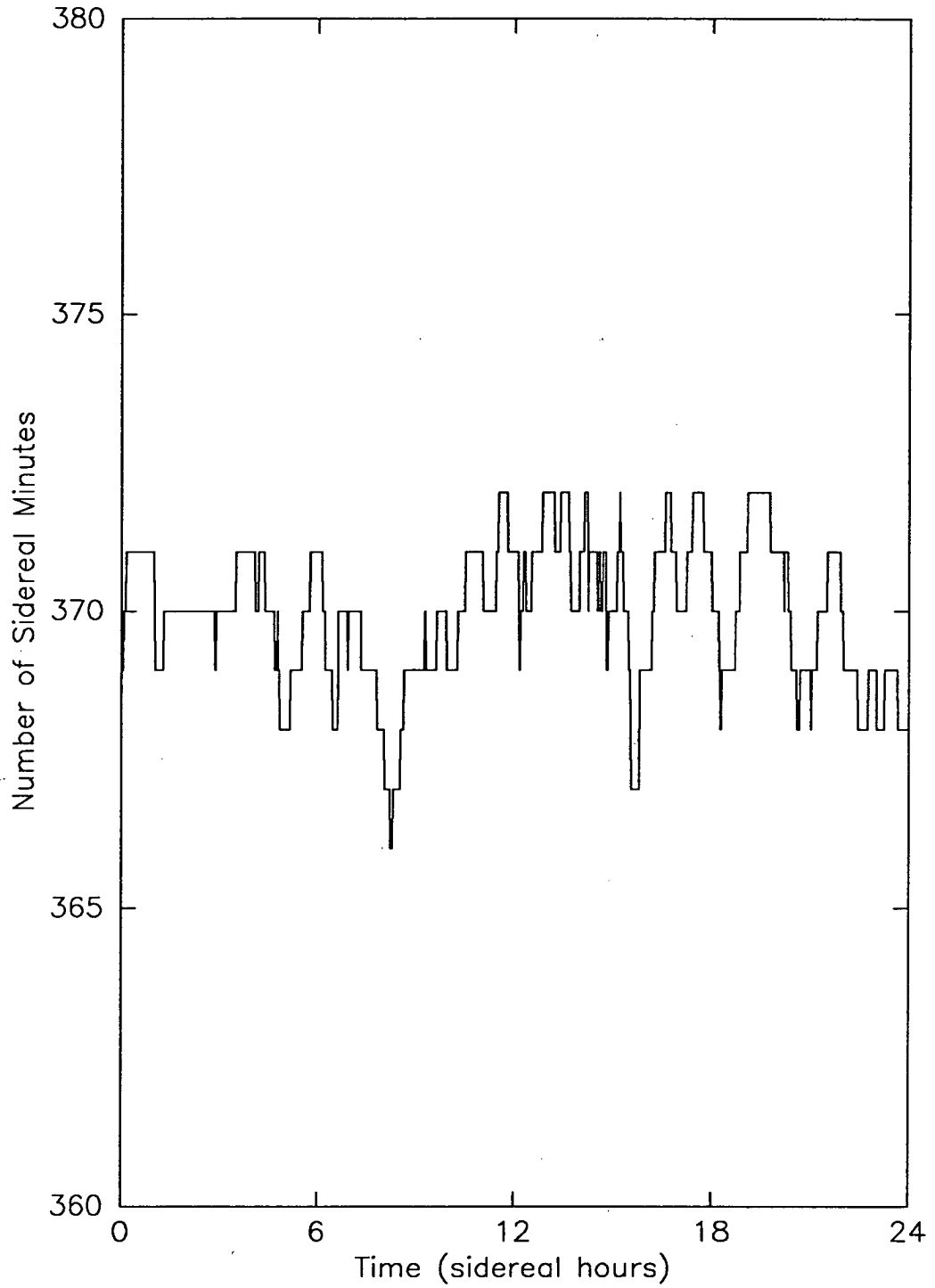

Figure 4.7 Observation on-time function, $Q(t)$, as determined from the event arrival times.

The summation in Equation (4.2) is over all direction bins which have central directions located in the declination band δ. The averaging period ΔT was chosen to be one month so as to remove the effects of any slowly varying changes in telescope sensitivity due to changes in counter efficiency. As stated in Chapter 2, each of the proportional counters was regularly monitored to ensure that there were no sudden variations in counter efficiency. An example of a response function for the declination band 40°S - 45°S is shown in Figure 4.8. The discontinuous nature of the function merely reflects the discreteness with which arrival directions are measured.

The expected distribution of arrival directions for a declination band was then determined by convolving the *on-time* function with the appropriate response function, i.e.

$$E_\delta(r) = \int_0^{24} R_\delta(t)\, Q(r-t)\, dt \qquad (4.4)$$

A final normalization was done by requiring that the total number of expected events from (4.4) be equal to the total number of observed events.

The error in the measured distribution of arrival directions is the Poisson statistical error from the number of events counted in a celestial bin. The error in the expected distribution is comparatively negligible since the relative error in $A(u,v)$ is much smaller than the relative error in $C(u,v)$. The measured and expected distributions for the entire observing period for each declination band are shown in Appendix C.

The above method of calculating the expected distribution of arrival directions has the advantage of reducing the effects of wide angle intensity modulations (atmospheric effects and large angle anisotropies) which cause a variation in count rate over the entire, or at least a large proportion of, the field of view of the telescope. On the other hand, a highly localized anisotropy would only affect the observed

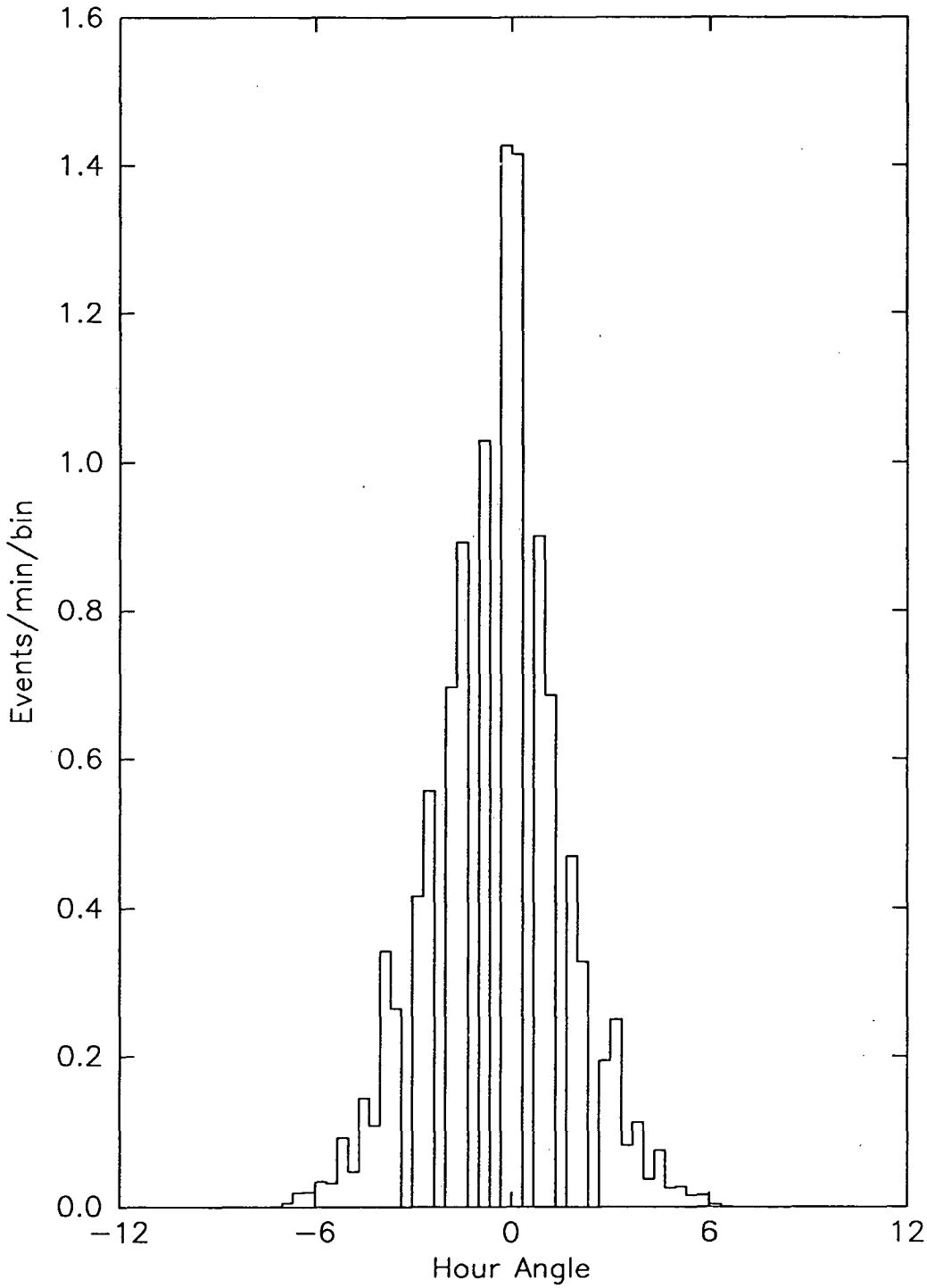

Figure 4.8 Response function, $R_\delta(t)$, for the declination band 40°S - 45°S. Derived from the average response of those direction bins with central viewing directions located in the band.

distribution of arrival directions in a small portion of the field of view for a few hours. The above procedure would therefore only slightly reduce the magnitude of the observed narrow-angle anisotropy. This again is advantageous in that if the observed distribution of arrival directions does show evidence for a narrow angle excess then the evidence will tend to be more believable.

4.5 Anisotropy Analysis

A sky map showing the fluctuations of the measured distribution from the expected, in terms of standard deviations, is shown in Figure 4.9. It is apparent that there are no regions in which there is a general clustering of either positive or negative excesses. To test for the presence of a *lumpy* anisotropy in a more quantitative way, the chi-squared test was applied to the data in each 5° declination band. The rationale behind this is that celestial bins within the same declination band have identical sensitivity, and therefore similar statistical significance for a reasonably long observation period. The test results for each of the 22 declination bands are shown in Figure 4.10. The largest value obtained was $\chi^2 = 1.3$ per degree of freedom for the band 40°S to 45°S. The observed and expected distributions for this band are shown in Figure 4.11. The probability of exceeding this value of χ^2 in one or more of 22 independent bands is 57%.

This result is not statistically significant, but nevertheless interesting in that the declination band exhibiting the largest value of χ^2 is the same band as seen by three other groups (Kamata *et al.* 1968, Clay *et al.* 1984, Sun 1987) to have the largest deviation in their maps of sky intensity (as noted by Clay *et al.* 1984). In each case there was a large, although again not significant, deviation corresponding to the general direction of Centaurus A, our nearest active galaxy. Cen A was first observed at TeV energies by Grindlay *et al.* (1975a, 1975b) using the stellar interferometer located at Narrabri, Australia as a VHE gamma-ray telescope employing the air

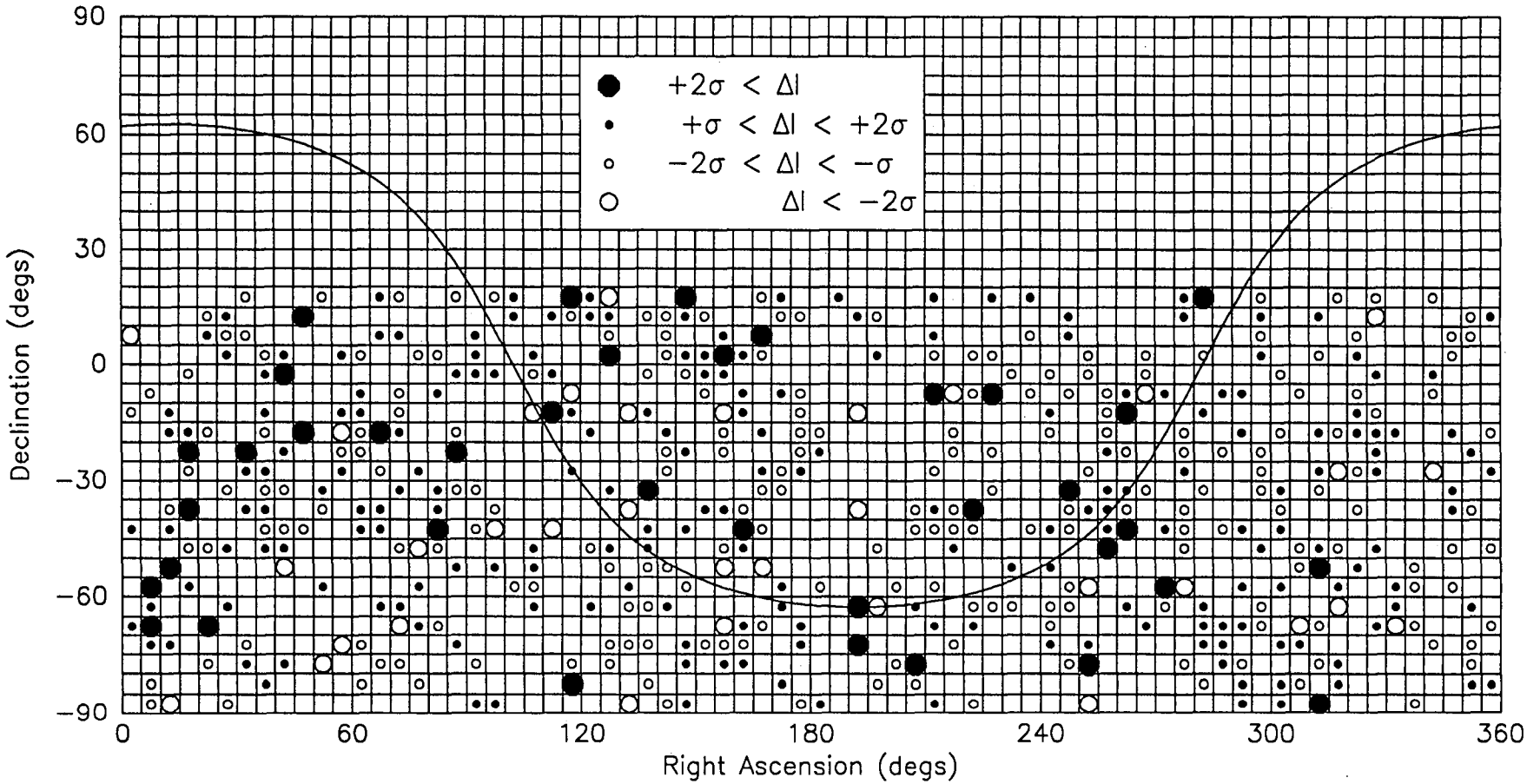

Figure 4.9 Sky map showing deviations of the measured distribution of arrival directions from the expected distribution.

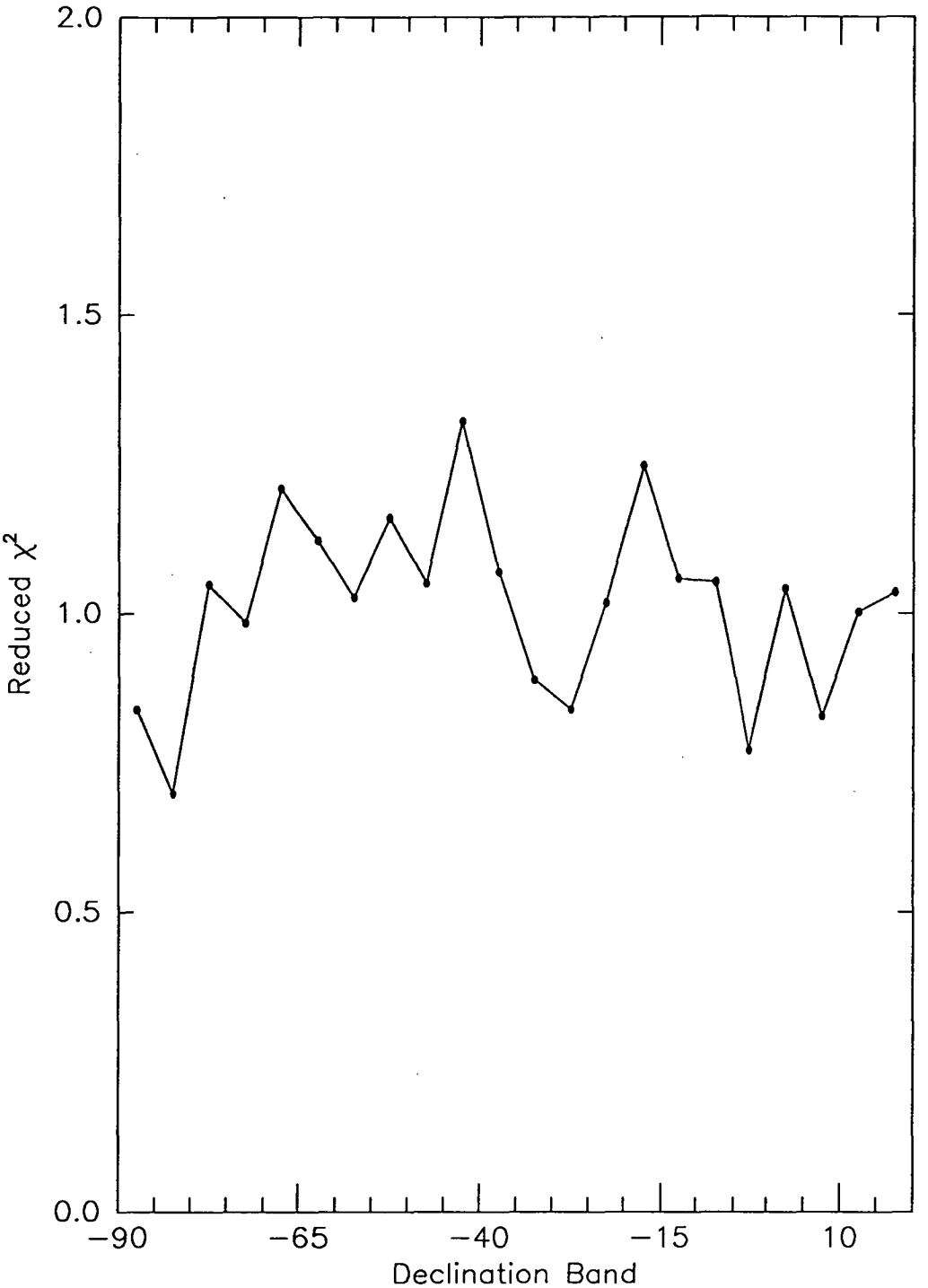

Figure 4.10 Chi-squared test results for each 5° declination band.

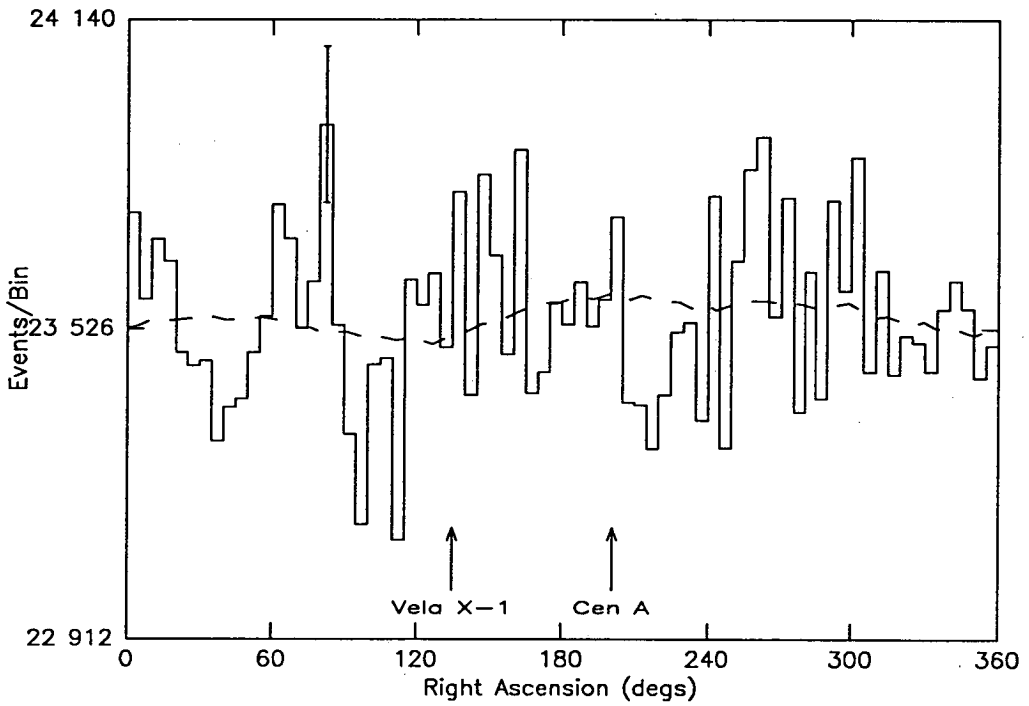

Figure 4.11 Distribution of events for the declination band 40°S - 45°S. The dashed line is the expected distribution. The right ascensions of the sources Vela X-1 and Cen A are indicated on the plot. Note that the right ascension of the Vela pulsar is close to that of Vela X-1.

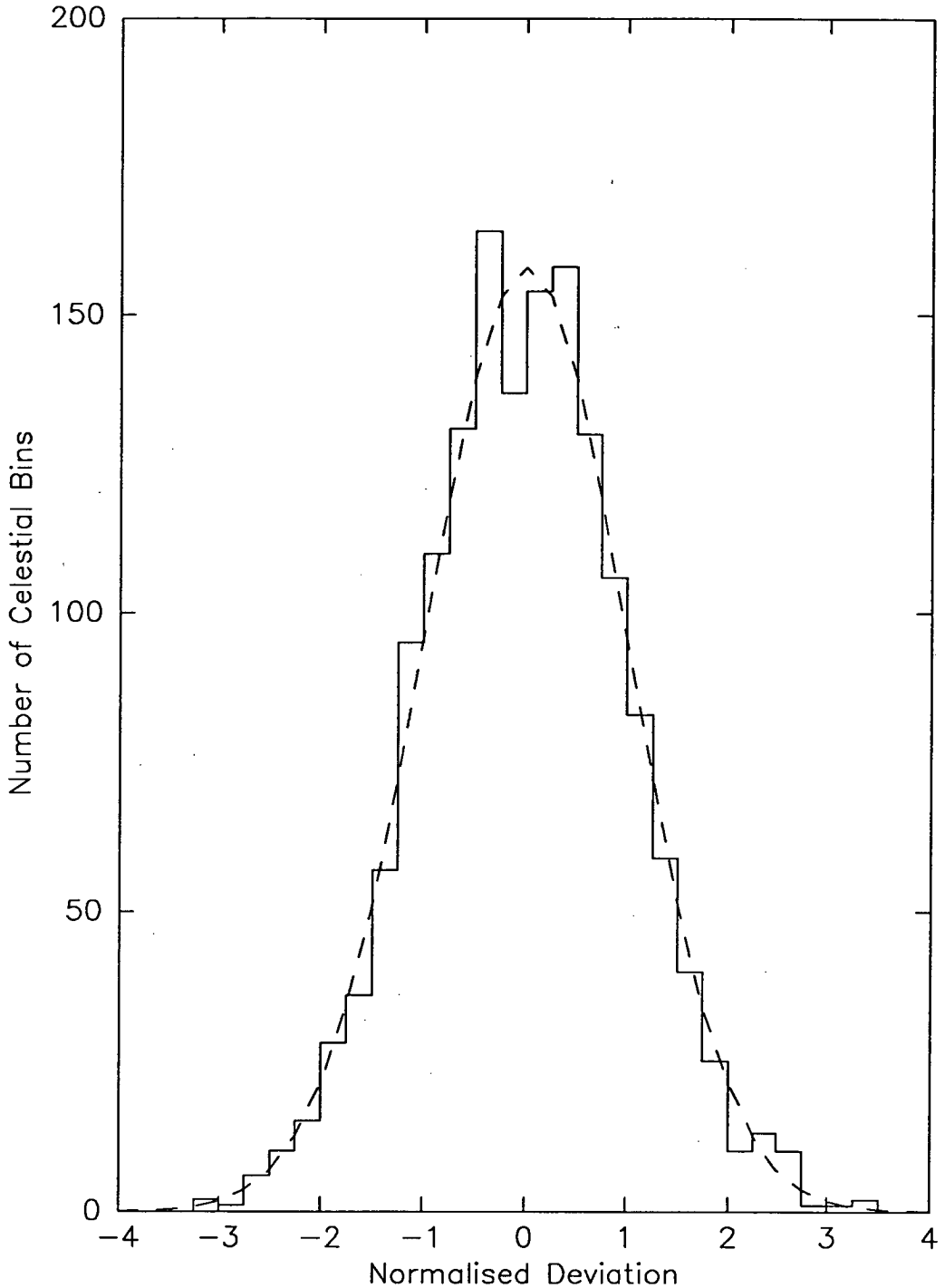

Figure 4.12 Distribution of normalized deviations of intensity. The dashed line is the expected Gaussian distribution with zero mean and unit standard deviation.

Cerenkov technique. A 4.5σ time-averaged excess was observed. This particular declination band also contains the high-energy gamma-ray sources Vela X-1 (Protheroe *et al.* 1984) and the Vela pulsar (Bhat *et al.* 1980). The right-ascensions of each of these sources are indicated in Figure 4.11 and show no correspondence to any peaked structure in the distribution.

The distribution of normalized deviations is shown in Figure 4.12. Comparison with the expected Gaussian distribution with zero mean and unit standard deviation gives $\chi^2 \simeq 1.0$ per degree of freedom. Thus, there is no evidence for non-statistical effects. The location of the bins with excess larger than 3 standard deviations (both positive and negative) are listed in Table 4.1. The largest excess found is a 3.4σ deviation corresponding to a probability of 3.4×10^{-4} of being due to a random fluctuation. When the number of bins searched (i.e. 22×72) is taken into consideration the overall chance probability for this occurrence becomes 41%.

Table 4.1

Celestial Bins with $> 3\sigma$ Excess

α (hours)	δ (degs)	Excess
21.83	+12.5	−3.0σ
2.83	−57.5	−3.0σ
20.83	−57.5	+3.3σ
0.50	−72.5	+3.1σ
13.83	−82.5	+3.4σ

4.6 Summary

Data collected over the period August 1987 to January 1989 have been used to search for possible galactic narrow angle anisotropies in the declination band 20°N to

90°S. No significant deviation from an isotropic distribution of arrival directions has been found. In particular, the observations fail to confirm the existence of a previously reported narrow-angle excess of particles observed at the same station (Wilson 1985b); providing further evidence of the apparent limited duration of such anisotropies.

An upper limit at a 95% confidence level to the flux ($E > 100$ GeV) from a point source has been calculated as follows. The excess of particles required to give a significant detection (at the 95% C.L.) is calculated to be 2.6% (i.e. a 4σ deviation) from the average event rate of those celestial bins within the most sensitive declination band (i.e. 40°S - 45°S). Assuming the anisotropy would be point-like within the angular resolution of the telescope, the excess would be detected over a solid angle of 0.013 sr (i.e. 7° × 6° from Figure 4.5). Thus, taking the vertical intensity to be $1.8 \times 10^{-5}\,cm^{-2}\,s^{-1}\,sr^{-1}$ (from Section 3.3) gives

$$\text{Excess Flux Upper Limit} = 0.026 \times 0.013 \times 1.8 \times 10^{-5}$$

$$= 6.1 \times 10^{-9}\ cm^{-2}\,s^{-1}$$

This value is comparable to the conservative flux calculations by Wilson, i.e. $(1.3 \pm 0.5) \times 10^{-8}\,cm^{-2}\,s^{-1}$, bearing in mind that the energy threshold and telescope acceptance for the two experiments are identical.

Chapter 5

Search for Very-High-Energy Emission from the Vela Pulsar

5.1 Introduction

This chapter will present the results of a search for very-high-energy emission from the Vela pulsar. The method used consisted of searching for periodic emission employing the timing information recorded with each event. First however, a summary of observations of the Vela pulsar over various energy ranges will be presented, together with a brief review of emission models which have been proposed to explain the high-energy observations.

5.2 History of Observations

The Vela pulsar (PSR 0833–45) was discovered in a search for southern pulsars performed by Large *et al.* (1968) at the Molonglo Radio Observatory (Australia). At the time it is one of the fastest known pulsars, with a period of about 89 milliseconds. Since then, the pulsed radio emission of the pulsar has been detected in the radio wavelength range from approximately 300 MHz to above 8 GHz. The radio pulse profile depends on the frequency and the intensity of the emission. Below 2000 MHz the average pulse profile shows a single peak (half-intensity width ~ 2 ms) with a sharp rise and a more gradual decay (Gardner and Whiteoak, 1969). At higher frequencies a broader (half-intensity width ~ 3.5 ms) and more complex pulse is observed, probably comprising two or more components (Krishnamohan and Downs, 1983).

The pulsar was first observed at optical wavelengths by Wallace *et al.* (1977) using the Anglo-Australian Telescope (Siding Spring, Australia). The pulsar was observed as a 24^{th} magnitude star with two broad optical pulses, separated by ~ 0.25 in phase, and delayed in phase with respect to the radio peak (see Figure 5.1). Further observations revealed the existence of an unpulsed component (steady emission) which accounts for about half the optical luminosity of the pulsar (Peterson *et al.* 1978).

There appears to be no significant pulsed emission from the Vela pulsar at X-ray energies. There was a marginally significant detection (chance probability 2×10^{-3} over 0.5 - 1.5 keV) by Harnden and Gorenstein (1973), although this result has never been confirmed. Indeed, subsequent observations have resulted in upper limits on the pulsed flux at or considerably below that reported by Harnden and Gorenstein, e.g. Moore *et al.* 1974 (0.5 - 1.0 keV), Rappaport *et al.* 1974 (1.5 - 10 keV) and Ricker *et al.* 1973 (23 - 80 keV). The most accurate and sensitive X-ray observations of the pulsar have been performed using satellite observatories. The Einstein satellite observations (0.1 - 4.5 keV) revealed a point-like source coincident with the pulsar position and embedded in a compact (2' diameter) nebula, but no pulsed emission was detected (Harnden *et al.* 1985). This result was subsequently confirmed by the EXOSAT (0.03 - 2.4 keV) satellite observations (Ogelman and Zimmermann, 1989).

High-energy (HE) gamma-ray emission from the pulsar was first observed by Albats *et al.* (1974) using a balloon-borne spark chamber detection system sensitive to gamma-rays in the energy range 10 - 30 MeV. The data comprised 357 events from within 15° of the pulsar position, which when folded at the pulsar period showed a sharp peak coincident with the radio pulse. This result has never been confirmed and is, in fact, contradicted by the later observations of Tumer *et al.* (1984) using the Riverside double-scatter gamma-ray telescope (1 - 30 MeV). In this case, a double-peaked light curve (a 4.8σ and 3.8σ peak) was observed in agreement with the SAS-2 and COS-B satellite observations as outlined below.

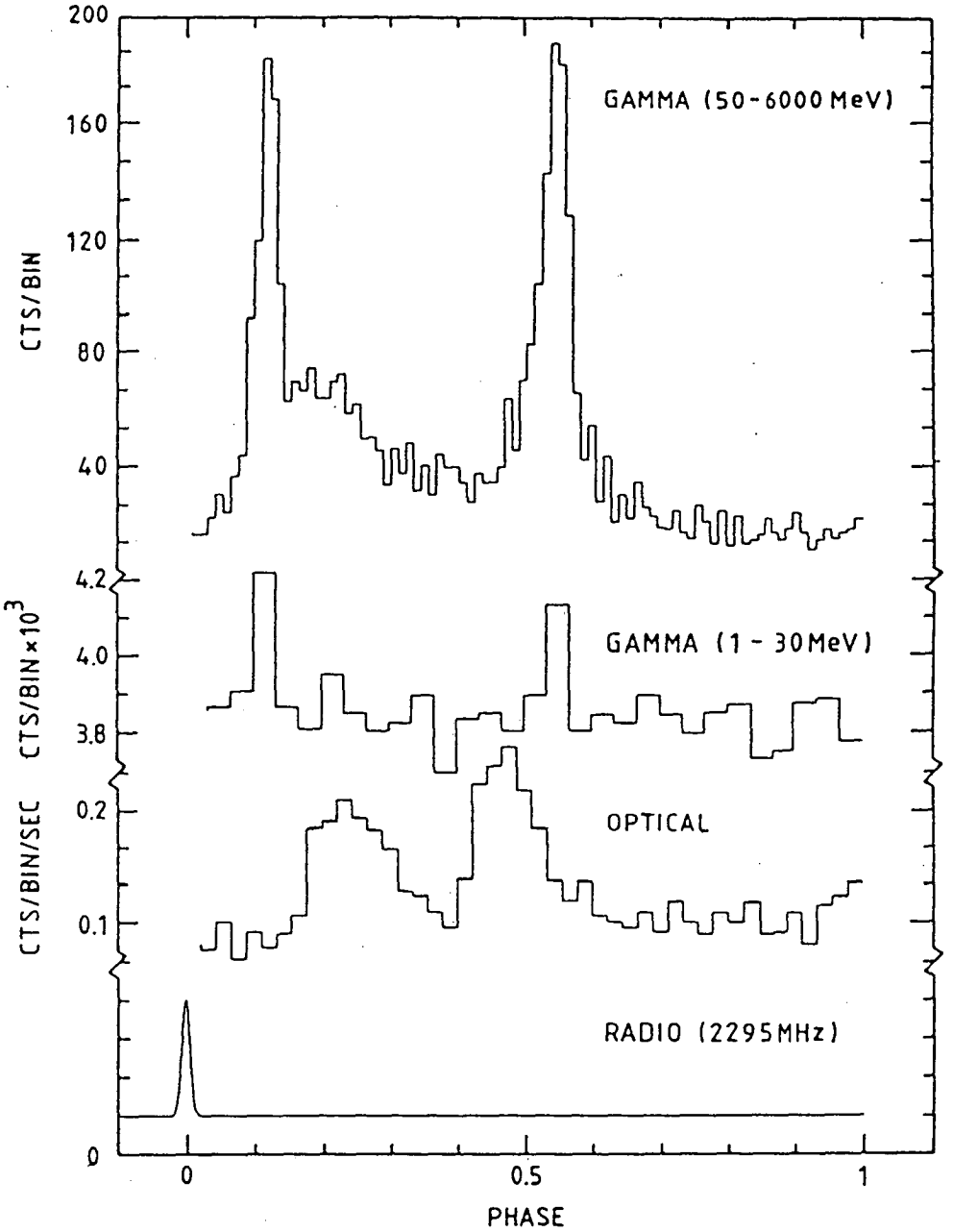

Figure 5.1 Vela pulsar light curves in different wavelength regimes (from Greiner *et al.* 1988).

Both the SAS-2 and COS-B satellites detected HE emission from the pulsar at a much higher level of significance than was possible with ground based and balloon-borne detectors. SAS-2 operated over the energy range 35 - 200 MeV. Analysis of the 223 gamma-ray events from within 8° of the pulsar showed two peaks, separated by ~0.39 in phase, following the radio pulse (Thompson *et al.* 1975). This result was subsequently confirmed by the COS-B satellite observations over the energy range 50 - 6000 MeV (Bennett *et al.* 1977). The HE emission from the pulsar was found to be entirely pulsed, with the light curve showing several distinct phase components, all of which were observed to be highly variable with time. As shown in Figure 5.1, the HE light curve is dominated by two narrow peaks, separated by ~0.43 in phase, following the radio pulse. However, about one third of the total HE emission occurs between the pulses. An interesting feature of this interpulse emission, in the context of more recent very-high-energy (VHE) observations (see below), is the presence of an emission structure following the first HE gamma-ray pulse, approximately in phase with the first optical pulse. This feature persists up to the highest COS-B energy, and is by far the most variable of all the light curve components (Kanbach *et al.* 1980). The statistical significance of the interpulse feature (~ 3.5σ) is not compelling, but it has been suggested that it might be related to the VHE gamma-ray activity of the pulsar (Grenier *et al.* 1988). Over the HE gamma-ray energy range the differential energy spectrum can be described by a single power law,

$$(1.46 \pm 0.07) \times 10^{6}\, E^{-(1.89 \pm 0.06)} \text{ photons cm}^{-2}\text{ s}^{-1}\text{ GeV}^{-1}$$

with the hint of a possible break in the spectrum at a few hundred MeV. The measured HE gamma-ray luminosity surpasses by several orders of magnitude the luminosities measured in other energy ranges, i.e. radio, optical and VHE gamma-rays.

The first reported detection of VHE emission from the pulsar resulted from observations performed by Grindlay *et al.* (1975b) using an optical intensity interferometer (located at Narrabri, Australia) to detect atmospheric Cerenkov light

from extensive air showers at energies > 300 GeV. Although a 4σ peak nearly coincident in phase with the radio pulse was observed, this was regarded by the authors as an upper limit within the limits of their systematic errors. The only other positive VHE detection of pulsed emission was by the Tata Institute group using a VHE gamma-ray telescope (detection threshold energy 500 GeV) located at Ooty in Southern India. VHE emission was first observed by this group in 1979; the light curve comprising an intense narrow peak (4.4σ significance) and a possible second peak (2.5σ significance) separated by ~ 0.42 in phase (Bhat *et al.* 1980). It was natural to associate these two peaks with the same double peaked structure seen at lower energies, however no absolute phase determination was possible due to lack of knowledge of the dispersion-corrected phase of the radio pulse. The pulsar was further observed by the same group for ~ 131 hours over the 5 year period 1979 - 1980; the light curve showing a 4.0σ peak coincident in phase with the first optical pulse (Bhat *et al.* 1987). The reported VHE flux levels are substantially lower than the value expected from a direct extrapolation of the spectrum observed at lower energies, as shown in Figure 5.2. This has led to the suggestion that the production mechanisms and sites of production of HE and VHE emission are different.

The light curve structure of the Vela pulsar varies considerably with energy (as shown in Figure 5.1). This particular feature of the Vela pulsar emission is in striking contrast to the pulsed emission from the Crab pulsar (PSR 0531+21), where the light curve has a double-peaked structure occurring at the same phase independent of energy (e.g. Bennett *et al.* 1977; Warner *et al.* 1969). Other differences in emission characteristics of the two most well-known pulsars are the HE luminosity of Vela is about 3.6 times that of the Crab (Thompson *et al.* 1975), whereas the pulsed optical emission from Vela is less than 0.02% of that from the Crab (Manchester *et al.* 1978). Moreover, pulsed X-ray emission has been observed from the Crab pulsar (Bennett *et al.* 1977). These marked differences in emission characteristics place severe constraints on models of the emission mechanisms.

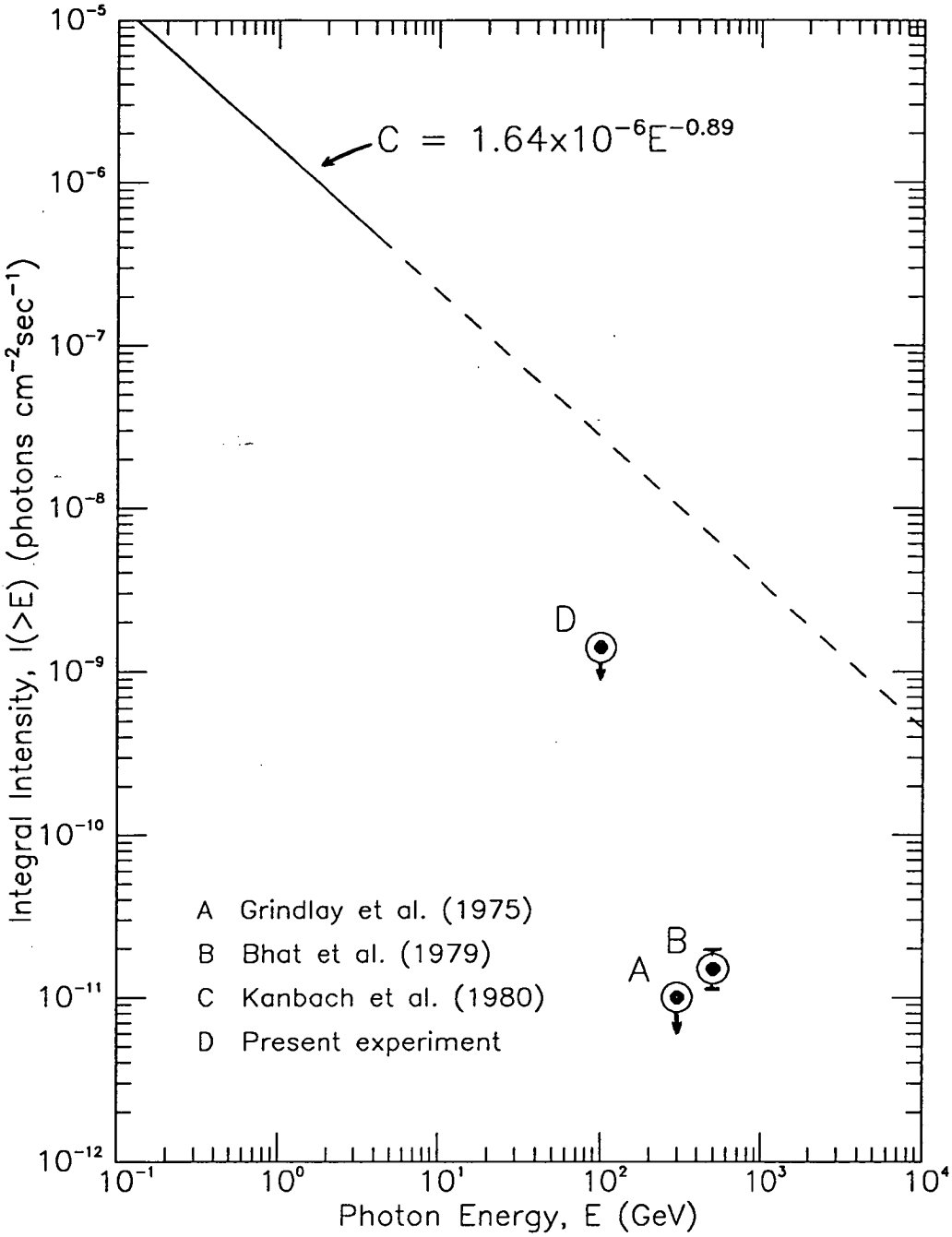

Figure 5.2 Integral intensity spectrum for pulsed gamma-ray flux from the Vela pulsar. Note that the result of the present experiment (refer to Section 5.4.2) is heretofore the only underground observation of this source.

5.3 Pulsar Gamma-Ray Emission Models

Many models have been proposed to explain the pulsed radiation at different wavelengths from pulsars. It is beyond the scope of this thesis to review all the various physical processes developed by these models. However, with regard to HE and VHE emission, there are sufficient similarities between the models to allow them to be broadly categorized into two groups based on the emission production site.

In the *polar cap* models (e.g. Hayvaerts and Signore, 1981; Harding 1981) the emission occurs near the polar surface of the neutron star. Electrons are accelerated at the polar cap producing gamma-rays by means of curvature radiation from the primary electrons and synchrotron radiation from secondary pairs. The radiation is highly beamed in a direction tangent to the magnetic field lines, and pulsed radiation occurs if the magnetic moment of the pulsar is not aligned with the rotation axis. The main attenuation mechanism is magnetic field induced pair production by the primary gamma-rays, which results in a high-energy cutoff in the gamma-ray spectrum. The cutoff point is strongly dependent on pulsar parameters in such a way that VHE gamma-ray emission is only possible in pulsars with low surface magnetic fields and short periods (e.g. the millisecond pulsar PSR 1937+21).

Models which overcome these problems at the polar cap have the highest energy emission being produced further out in the magnetosphere near the light cylinder, i.e. the radius at which co-rotation with the pulsar implies a tangential speed equal to the speed of light. For example, in the *outer gap* model of Cheng *et al.* (1986a, 1986b), high-energy gamma-rays are produced by the acceleration of electrons in a slab-like outer gap (where $\underline{E}\cdot\underline{B} \neq 0$) which is bounded by the closed magnetic field region on one side, and open magnetic field lines on the other side. The exact mechanisms for gamma-ray emission and the resulting spectrum are strongly dependent on pulsar parameters. For this model, VHE emission is only possible in young pulsars in which the kinetic energy loss rate is sufficient to form an *outer gap*

(i.e. $\dot{E} > 10^{34}$ ergs s^{-1}). As noted by De Jager *et al.* (1987), this and certain other conditions select a group of 9 pulsars to which all 5 reported TeV gamma-ray pulsars belong.

Most high-energy emission models are capable of explaining certain general features of the pulsed radiation observed from particular pulsars, i.e. light curve and/or spectral shape. However, no single model can explain the entire pool of observational evidence. As mentioned previously, even though there are basic similarities between the Vela and Crab light curves at high energies, there are marked differences at other wavelengths. This indicates that the emission processes are much more complex than suggested by existing models. Obviously, a much larger data-base of experimental evidence is required before the physical processes responsible for the pulsed radiation are completely understood.

5.4 Search for Gamma-Ray Emission

5.4.1 Event Selection

The number of events observed from a region of the sky bounding a particular source (i.e. the *source region*) will vary as the source passes through the field of view of a fixed telescope, due to the variation with zenith angle of the sensitivity of the telescope. The angular size of the source region, which primarily determines the signal-to-background ratio, is limited by the angular resolution of the telescope, and will vary with the elevation and declination of the source. The Vela pulsar (declination 45°S) at transit is almost directly overhead at Poatina (latitude 41.8°S), and therefore passes through the most sensitive portion of the field of view of the Poatina telescope.

Events recorded by the telescope are tagged as *source events* if they are

assigned to a telescope direction bin whose celestial field of view includes the source position. The density function (distribution of events in celestial coordinates) corresponding to this event selection criteria is shown in Figure 5.3, and indicates that 80% of selected events will be within a cone of half-angle aperture 8° about the source position. The density function was determined by a procedure identical to that described in Section 4.3. The number of events observed from this particular source region during one sidereal rotation of the earth (i.e. one *scan* of the source) is shown in Figure 5.4. Although the sensitivity of the telescope is symmetrical about a north-south line, the slight asymmetry of the response curve in Figure 5.4 arises due to variations in ground depth which are most pronounced for east-west viewing directions (as detailed in Chapter 3).

Over the 18 month duration of this investigation (August 1987 - January 1989) more than 150 000 source events were selected for further analysis. The daily rate of these events for the entire observing period is shown in Figure 5.5. Most of the data gaps were due to power and equipment failure (as detailed in Chapter 3), except for one period (observing day numbers 200 to 320 in Figure 5.5) where a discrepancy in the clock referencing procedure resulted in unacceptable uncertainties (~ 1 sec) in the event arrival times. Consequently, events recorded during this period were not included in the data set to be analysed for periodic emission.

The results of Chapter 4 have already demonstrated that there is no tendency for a significant number of events to arrive from any preferential region of the celestial sky, including the region about the Vela pulsar. Indeed, the extremely low flux levels observed from VHE sources suggest that it is unlikely that a DC excess of events would be detected over the relatively short observation time of this experiment. The lack of any significant feature in Figure 5.5 is therefore not surprising, and indicates that the source event data are consistent with an isotropic distribution of arrival directions.

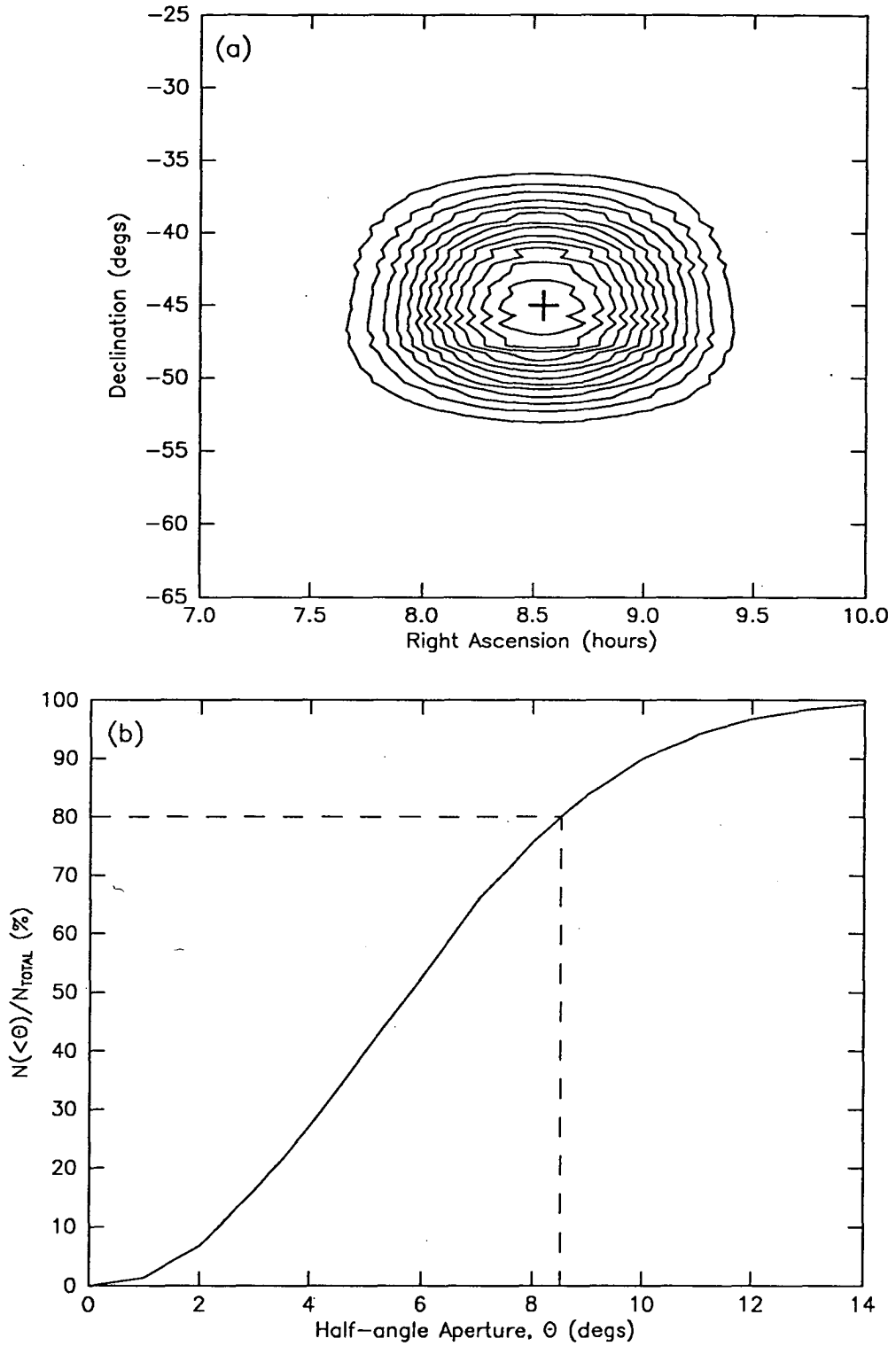

Figure 5.3 (a) Density function corresponding to the *source event* selection criteria for the Vela pulsar (PSR 0833–45). (b) Cumulative distribution of the number of observed events as a function of half-angle aperture.

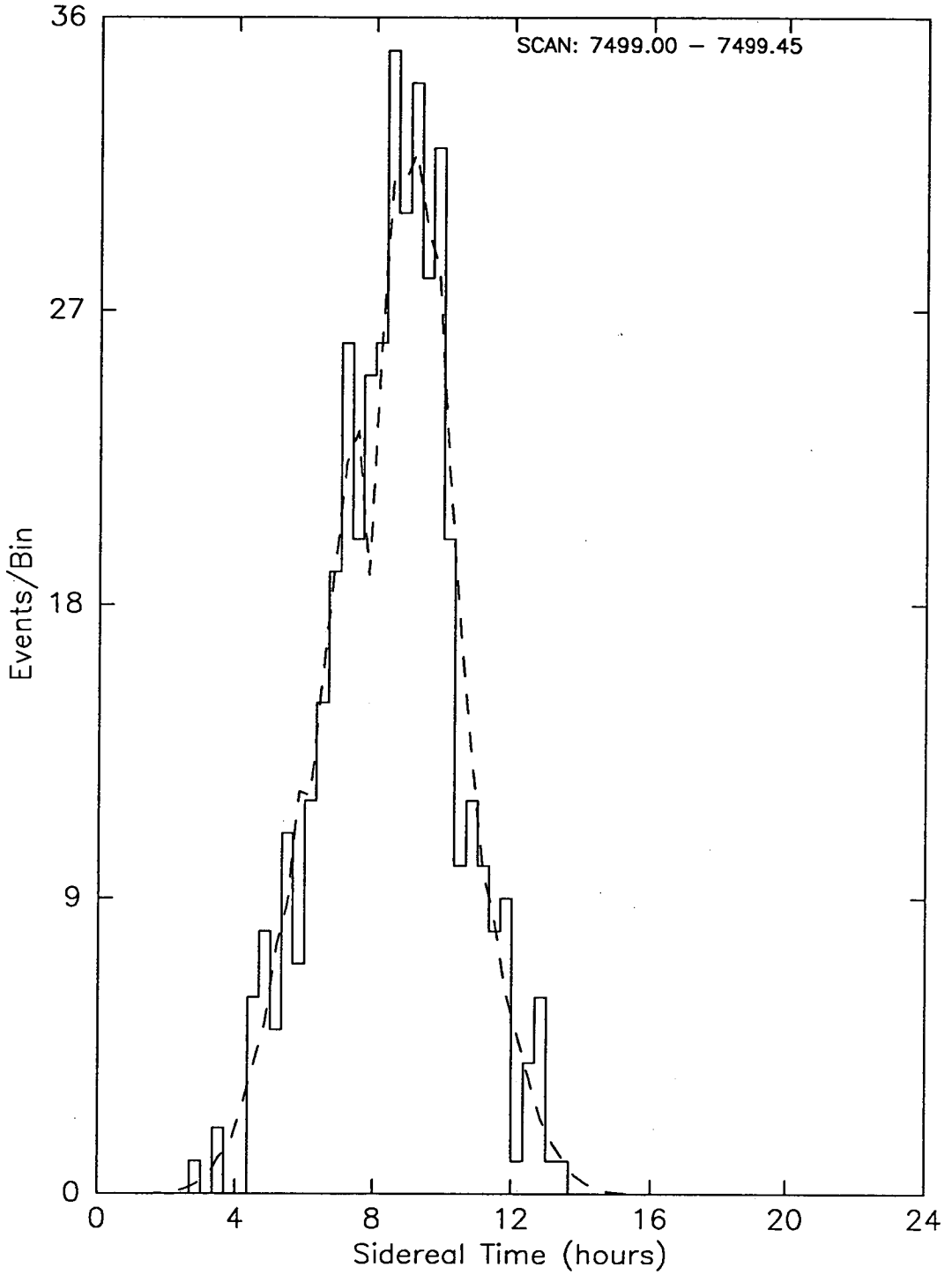

Figure 5.4 A typical response curve for one scan of the Vela pulsar. The dashed line is the expected curve, based on the long-term average response of the telescope direction bins.

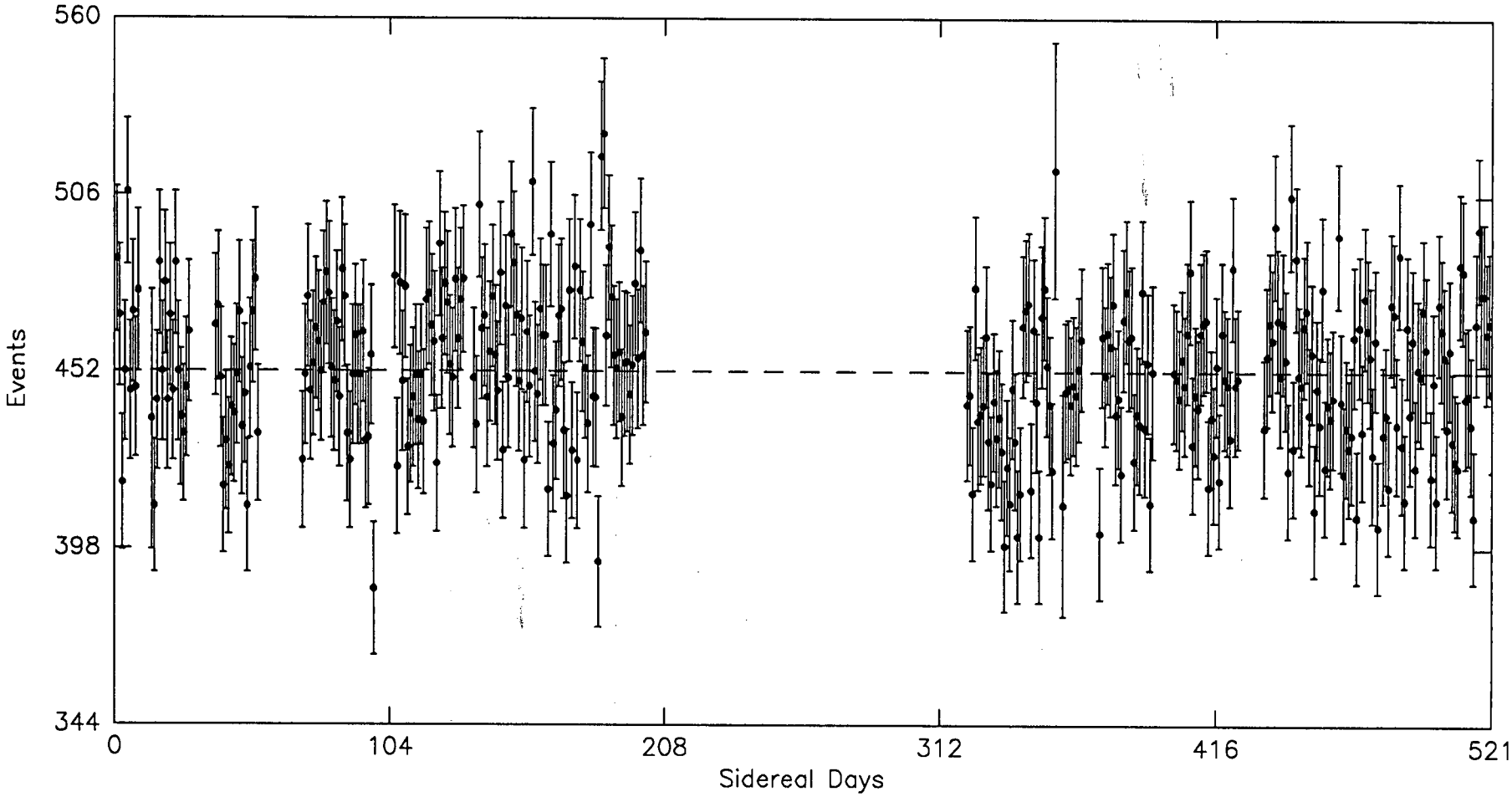

Figure 5.5 Daily (sidereal) event rate from the direction of the Vela pulsar.

5.4.2 Search for Steady Emission

The most sensitive method employed to detect emission from VHE and UHE sources is to fold the arrival times of selected events with the known or suspected period of the source. The periodic source signal, if present, should then rise above the isotropic unmodulated background. If the source signal is weak relative to the high cosmic ray background flux, it is obviously advantageous to be able to perform such an analysis over long periods of observation, since the signal should appear from the background with the additional accumulation of data. The observing time required for a weak signal to rise to a level at which a detection could be claimed, will depend on the properties of the signal (pulse shape, strength and variability) and the characteristics of the observing equipment (collection area and angular resolution). However, long periods of observation necessitate the use of extremely accurate pulsar timing parameters, since a folding of a large number (typically $> 10^9$) of pulsar periods has to be performed during the data analysis.

The radio astronomy group at the University of Tasmania have a long-standing observational programme which includes continuously monitoring the Vela pulsar, so appropriate timing parameters were readily available. However, the accuracy of such parameters is limited by the fact that the rotation rate of the pulsar does undergo abrupt increases, the so-called *glitches*. Giant glitches correspond to an increase in spin frequency ν of magnitude $\Delta\nu/\nu \sim 10^{-6}$, and in the frequency derivative, $\Delta\dot{\nu}/\dot{\nu} \sim 10^{-2}$, and occur, on average, once every few years (e.g. McCulloch *et al.* 1983, 1987, 1990). Micro-glitches are less detectable, with $\Delta\nu/\nu < 10^{-9}$ and $\Delta\dot{\nu}/\dot{\nu} < 10^{-4}$, but occur ten times more often (e.g. Cordes *et al.* 1988). Uncertainties in the timing parameters due to such period variations have an accumulative effect when analysing cosmic-ray data, making it difficult to maintain a constant pulse phase over long periods of observation. In an attempt to avoid these phase coherence problems the data were split into 4 smaller data sets of approximately 100 days duration, each data set being analysed independently for evidence of periodic emission.

The arrival times in each data set were corrected to the barycenter of the Solar System (using the JPL Solar System ephemeris) and converted to a phase using the standard pulsar timing function (Manchester and Taylor, 1977):

$$\phi(t) = \phi_0 + \nu\,(t-T_0) + \tfrac{1}{2}\,\dot{\nu}(t-T_0)^2 + \tfrac{1}{6}\,\ddot{\nu}(t-T_0)^3 \qquad (5.1)$$

where

ν, $\dot{\nu}$ and $\ddot{\nu}$ are the pulsar frequency, frequency derivative and frequency double derivative respectively (i.e from the Taylor series expansion of ν), at the reference epoch T_0,

ϕ_0 is a phase shift, chosen (where possible) so the maximum of the radio pulse occurs at $\phi = 0$.

The second derivative term was included in Equation (5.1), since a typical value for the Vela pulsar of $\ddot{\nu} = 8 \times 10^{-22}$ Hz s^{-2} produces a significant phase shift of ~ 0.1 for $\Delta T = 100$ days.

The Vela pulsar exhibited a giant glitch on the 24 December 1988 (Hamilton *et al.* 1989), so arrival times recorded after this date were converted to a phase using the so-called *glitch function.* The function describes the post-glitch behaviour of the pulsar in terms of a simple sum of exponential decays (McCulloch *et al.* 1983):

$$\nu(t) = \nu_p(t) + \Delta\nu_c + \Delta\nu_1 \exp(-(t-T_g)/\tau_1) + \Delta\nu_2 \exp(-(t-T_g)/\tau_2) \qquad (5.2)$$

where

T_g is the glitch epoch,

$\nu_p(t)$ is the extrapolated pre-glitch frequency,

$\Delta\nu_c$ is the permanent part of the frequency jump, and

$\Delta\nu_1$ and $\Delta\nu_2$ are the frequency jump terms which subsequently decay with time constants τ_1 and τ_2 respectively. These two sets of parameters describe the short-term (time constant a few days) and long-term (time constant a few hundred days) recovery of

the pulsar frequency.

Pulsar timing parameters applicable to the epoch of each data set were derived from contemporaneous radio observations made at the Mt. Pleasant Radio Observatory near Hobart (McCulloch 1989).

There exists no single most powerful statistic for testing phase distributions for uniformity in the presence of weak periodic signals (e.g. De Jager *et al.* 1986; Protheroe 1987). The generally accepted practice is to choose a statistic based on *a priori* information of the form of the suspected light curve. Since the Vela pulsar light curve at VHE energies has been observed to consist of one, or possibly two, narrow peaks, the Z_5^2-test was used for this investigation. The family of statistics, Z_n^2, are based on an extension of the Rayleigh statistic to n harmonics (Buccheri 1985):

$$Z_n^2 = {}^2/_N \sum_{k=1}^{n} \{ (\sum_{i=1}^{N} \cos 2\pi k\phi_i)^2 + (\sum_{i=1}^{N} \sin 2\pi k\phi_i)^2 \} \qquad (5.3)$$

where

ϕ_i is the residual phase of the i'th event (i.e. $0 < \phi_i < 1$), and

N is the total number of events.

For a uniform phase distribution, Z_n^2 is distributed asymptotically as χ^2 with $2n$ degrees of freedom. Use of Z_n^2 with low n gives a test which is sensitive to broad phase distributions, whereas using Z_n^2 with higher n makes the test more sensitive to higher harmonics and therefore more powerful against narrow peaked light curves. The H-test (De Jager *et al.* 1989) and Protheroe test (Protheroe 1985) are also powerful tests for narrow peaks (i.e. small duty cycles) in the light curve. The disadvantages of these two tests in the present case are that the H-test performs relatively poorly against double peaked light curves (e.g. Vela and Crab pulsar light curves at 100 MeV energies), and the Protheroe test is only documented for small data sets (i.e. $N < 200$). Furthermore, with such a large data set computational time

becomes an important factor in the analysis process, and the Z_5^2-test requires fewer computational steps than the other two.

The phase distributions for the 4 independent data sets are shown in Figure 5.6. No significant excess is seen at any of the phases reported previously, or at any other phase. Application of the Z_5^2-test to each data set results in a largest value of 14.9, which corresponds to a probability of the distribution arising from random fluctuations of 15%. When the fact that 4 independent data sets were analysed is taken into account, this becomes even less significant (i.e. 48%). Therefore no evidence for a steady pulsed emission is found.

An upper limit at the 95% confidence level to the pulsed underground muon flux from the direction of the Vela pulsar has been calculated using a method developed by Protheroe (1987). The method assumes a delta-function plus uniform background phase distribution, and uses the highest value of the test statistic, Z_5^2, obtained from the 4 independent data sets analysed. Using this method, the upper limit (95% c.l.) on the pulsed fraction of recorded events is calculated to be 0.8%. This has been converted to an upper limit to the pulsed flux of muons by solving,

$$\alpha \bar{n} = \varepsilon F(>E_{th}) \sum_i \frac{G_i T_i}{\Omega_i} \qquad (5.4)$$

where

α is the fraction of recorded events that are pulsed,

$\bar{n}$ is the average number of events recorded during one scan of the source,

ε is the detection efficiency - in this case, the proportion of single particle events to the total number of events,

$F(>E_{th})$ is the pulsed flux of underground muons above the threshold energy, E_{th}, from the source direction, and

G_i, Ω_i, T_i are the geometrical factor, viewing aperture (FWHM), and live-time of the i'th telescope direction bin. The live-time

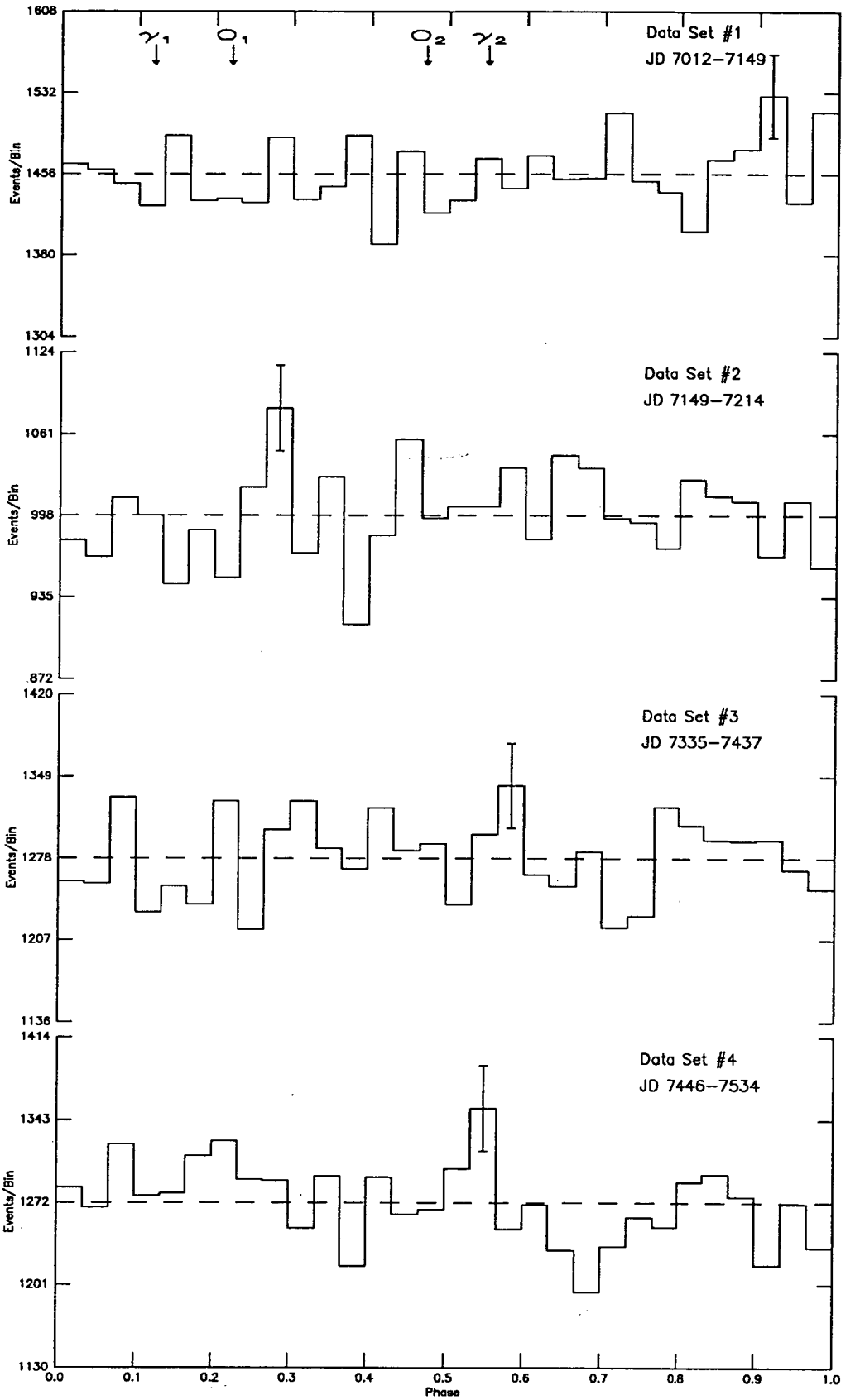

Figure 5.6 Phase distributions for the 4 independently analysed data sets. The phase positions of the two optical (O_1, O_2) and high-energy gamma-ray (γ_1, γ_2) peaks are indicated. The radio pulse occurs at ϕ=0.

refers to the time the source position is located within the direction bin aperture.

This takes account of the zenith dependence of the angular resolution and collection area of the telescope. The summation in Equation (5.4) is over those telescope direction bins involved in the selection of source events. The resulting upper limit (95% c.l.) on $F(>100\ GeV)$ is 1.4×10^{-9} cm^{-2} s^{-1}.

5.4.3 Search for Transient Emission

There are many indications that pulsars are transient sources of VHE radiation. The Durham group observed two episodes of pulsed TeV emission, each lasting approximately 15 minutes, during 150 hours of observation of the Crab pulsar (Gibson *et al.* 1982). The Tata Institute group also reported one such episode during 170 hours observation of the same source (Bhat *et al.* 1986). The first observations of the pulsar suspect 1802–23, by the Potchefstroom group, showed evidence of transient TeV emission (Raubenheimer *et al.* 1986). In this case, pulsed radiation was observed to occur in bursts of duration 10 - 50 minutes on six occasions over an observing period of 1 month.

Accordingly, the data collected during this investigation have been examined for evidence of a burst of pulsed emission from the Vela pulsar. The data were subdivided into many smaller runs, and since the observed count rate varies as the pulsar passes through the field of view of the telescope (see Figure 5.4), the subdivision was based on having an approximately equal number of events within each run. The corresponding time duration of each run depends on the pulsar elevation and was, on average, several hours. Each run was made to overlap by half with adjacent runs so as not to split any excess of events which may be present, thereby reducing the significance of the pulsed signal. For each run the Z_5^2-test was used to

search for evidence of a non-uniform phase distribution. The resulting distribution of Z_5^2 values is shown in Figure 5.7, together with the expected χ^2 distribution for 10 degrees of freedom. It is apparent that the two distributions agree to within statistical fluctuations except for the occurrence of two high Z_5^2 values of about 34.4, each of which corresponds to a probability of the phase distribution arising from random fluctuations of 1.7×10^{-4}. The Poisson chance probability for two such occurrences given that 1666 overlapping runs, and therefore $\frac{2}{3} \times 1666$ independent runs, were searched is approximately 1.6%.

The phase distributions for these two runs (hereafter run *A* and *B*) are shown in Figure 5.8. The shape of the two distributions appears to be significantly different, with the distribution for run *B* displaying a more broader shape than that for run *A*. However, the largest excess in both distributions occurs at a phase (~ 0.26) nearly coincident with the main optical pulse (phase ~ 0.22). This is consistent with the VHE pulse position reported by Bhat *et al.* (1987) and indeed, as mentioned previously, with the inter-pulse feature coincident with the main optical pulse as seen in the lower energy COS-B data.

To see whether the observed excesses are associated exclusively with the radio frequency, a frequency search about the radio frequency was performed for each run separately and for both runs combined coherently; the results are shown in Figure 5.9. The coherently combined data shows a peak probability of $\sim 10^{-6}$ at a frequency offset by ~ 5 μHz from the radio frequency. The two runs, when analysed separately, show highest probability peaks offset by ~ 5 μHz and ~ 30 μHz respectively. In each case, however, the width of the probability peak is such that the effect is associable with the radio frequency. This association and the near phase coherence of the two phase distributions tend to increase one's confidence that the observed effects are not spurious signals caused by random fluctuations of the background, although on purely statistical grounds the evidence is not compelling. Furthermore, there was no significant D.C. excess for either run.

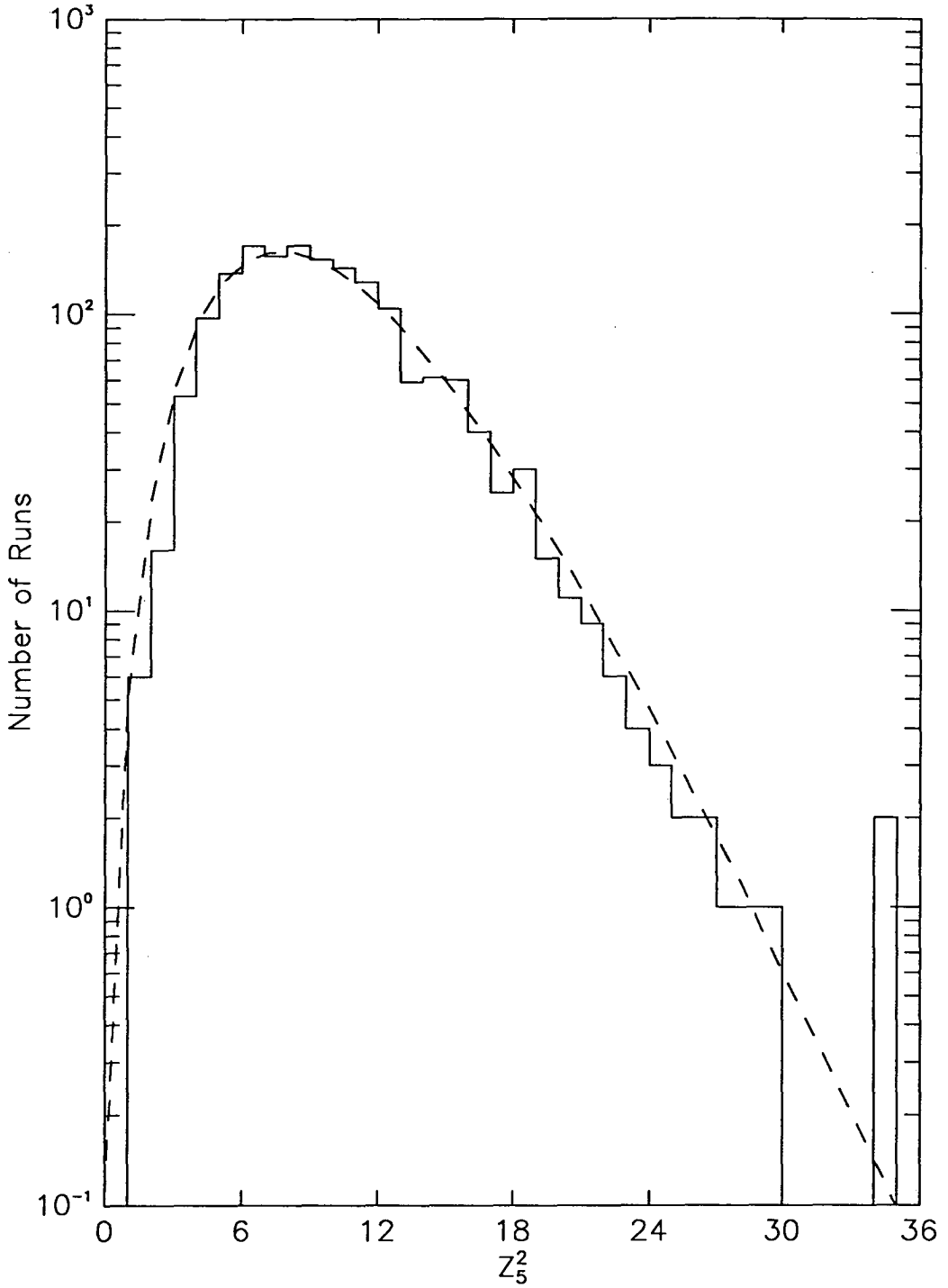

Figure 5.7 Distribution of Z_5^2 values. The dashed line is the expected χ^2 distribution for 10 degrees of freedom.

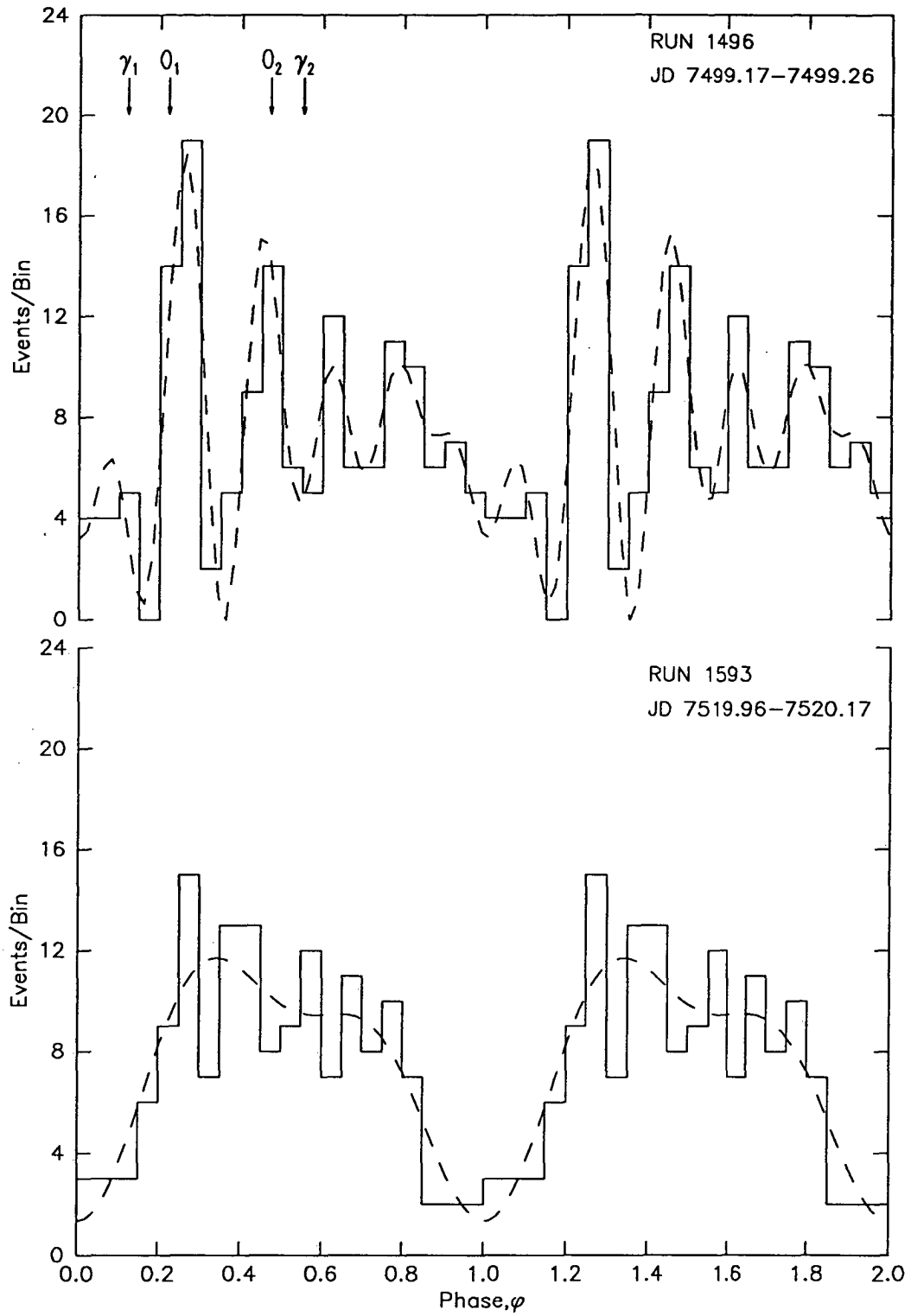

Figure 5.8 Phase distributions for run *A* (top) and run *B* (bottom). The phase positions of the two optical (O_1, O_2) and high-energy gamma-ray (γ_1, γ_2) peaks are indicated. The radio pulse occurs at ϕ=0. The dashed lines are the Fourier series estimators of the light curves (see text for details).

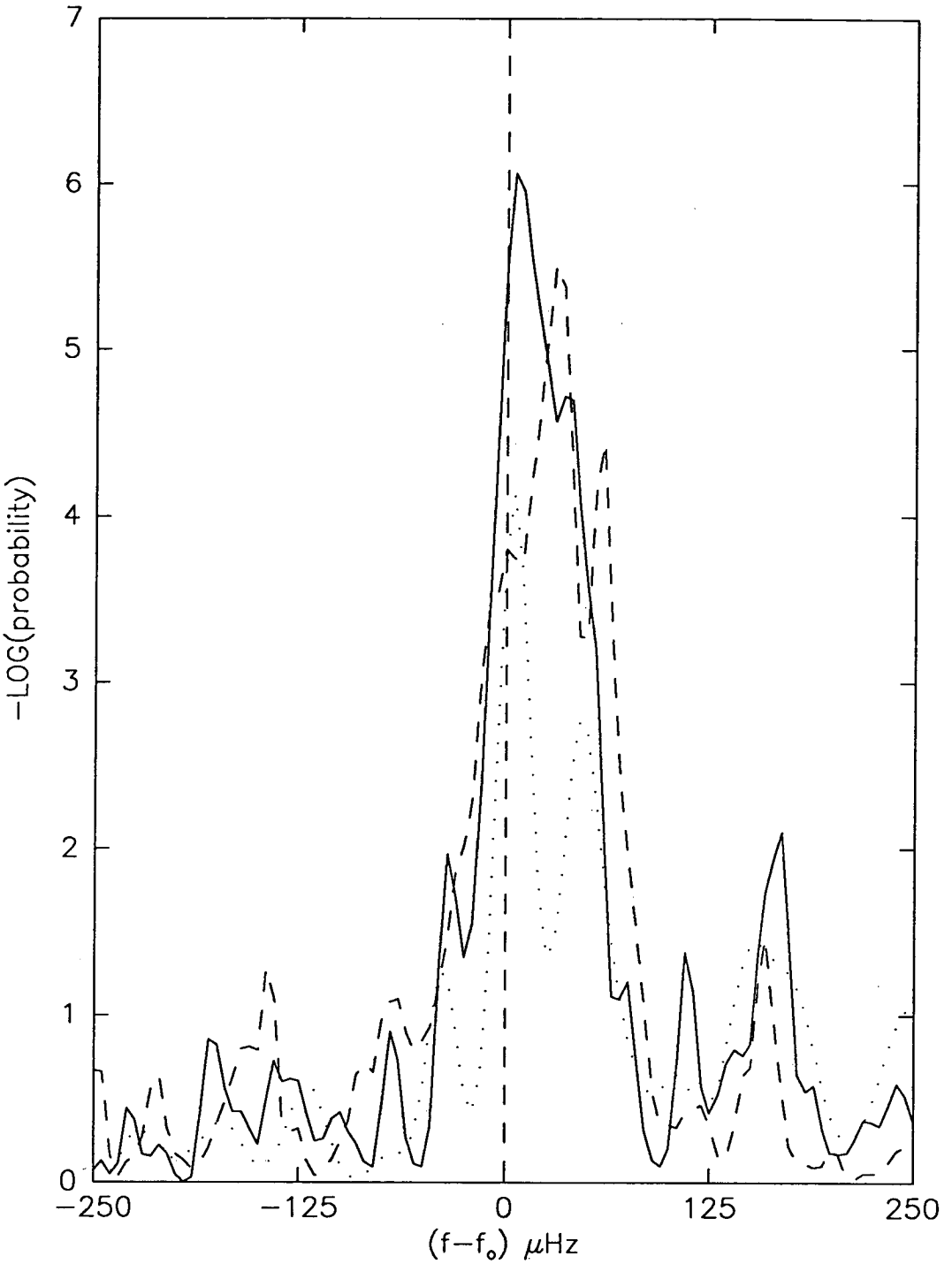

Figure 5.9 Chance probability for uniformity as a function of test frequency, f, about the pre-glitch radio frequency, f_o. Curves are drawn for run A (dotted), run B (dashed), and the coherent sum of run A and B (solid).

The underground muon flux levels corresponding to the apparent excesses observed in runs *A* and *B* were obtained using a Fourier series estimator of the respective light curves (De Jager *et al.* 1986). The estimated light curve parameters for run *A* are illustrated in Figure 5.10. The broad shape displayed by the phase distribution for run *B* precludes an accurate estimate of the pulsed fraction of events. Therefore, the pulsed fraction for run *B* was assumed equal to that estimated for run *A*. The pulsed fractions of recorded events were converted to an underground muon flux by solving Equation (5.4), with the summation over all telescope direction bins involved in the selection of source events for the particular run under consideration. The resulting flux estimates are $1.7 \times 10^{-8}\,\mathrm{cm^{-2}\,s^{-1}}$ and $3.9 \times 10^{-8}\,\mathrm{cm^{-2}\,s^{-1}}$ for runs *A* and *B* respectively.

It is of further interest to note that runs *A* and *B* are close to the time of occurrence of the 24 December 1988 (= JD 2447520.30) Vela glitch. Run *A* occurs about 20 days before the glitch (i.e. JD 2447499.17 - 2447499.26) and run *B* ends just a few hours before the initial frequency jump (i.e JD 2447519.96 - 2447520.17). The chance probability of all data runs near the time of the glitch are shown in Figure 5.11. During run *A* the pulsar was almost directly overhead, whereas during run *B* the pulsar was just moving into the field of view of the telescope.

The 1988 Vela glitch is the first glitch to be observed at radio wavelengths as it happened; it was seen to occur without warning and in less than 2 minutes (McCulloch *et al.* 1990). The frequency recovery described by Equation (5.3) began immediately after an initial frequency jump of

$$\Delta\nu_c + \Delta\nu_1 + \Delta\nu_2 = 20.17\ \mu\mathrm{Hz}.$$

The magnitude of the initial jump is typical for the Vela pulsar. It has been suggested that the pulsar frequency may vary erratically immediately preceding and following a glitch, although no such effect has been seen near previous glitches (McCulloch *et al.*

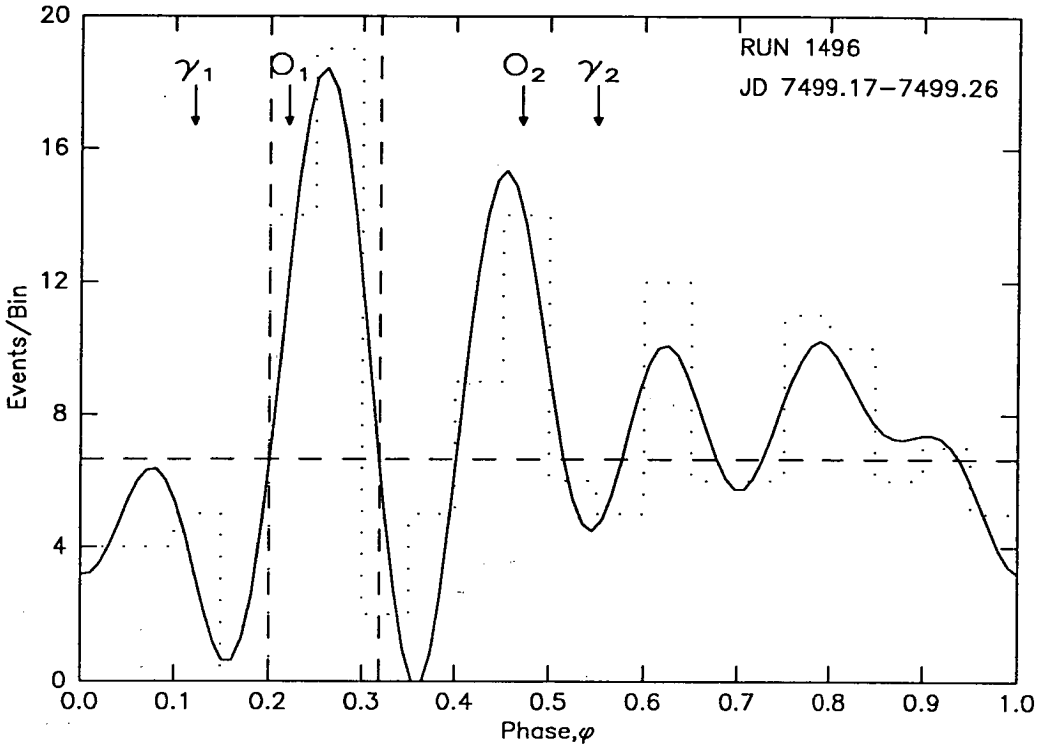

Pulse phase.....0.26

Pulsed Fraction (signal strength).....11.5 %

Duty cycle (FWHM).....0.05

Figure 5.10 Estimation of light curve parameters for run *A*. The solid line is the Fourier series estimator of the light curve, and the dotted line is the phase histogram. The horizontal dashed line is the estimated background level, and the two vertical dashed lines indicate the full width of the pulsed signal.

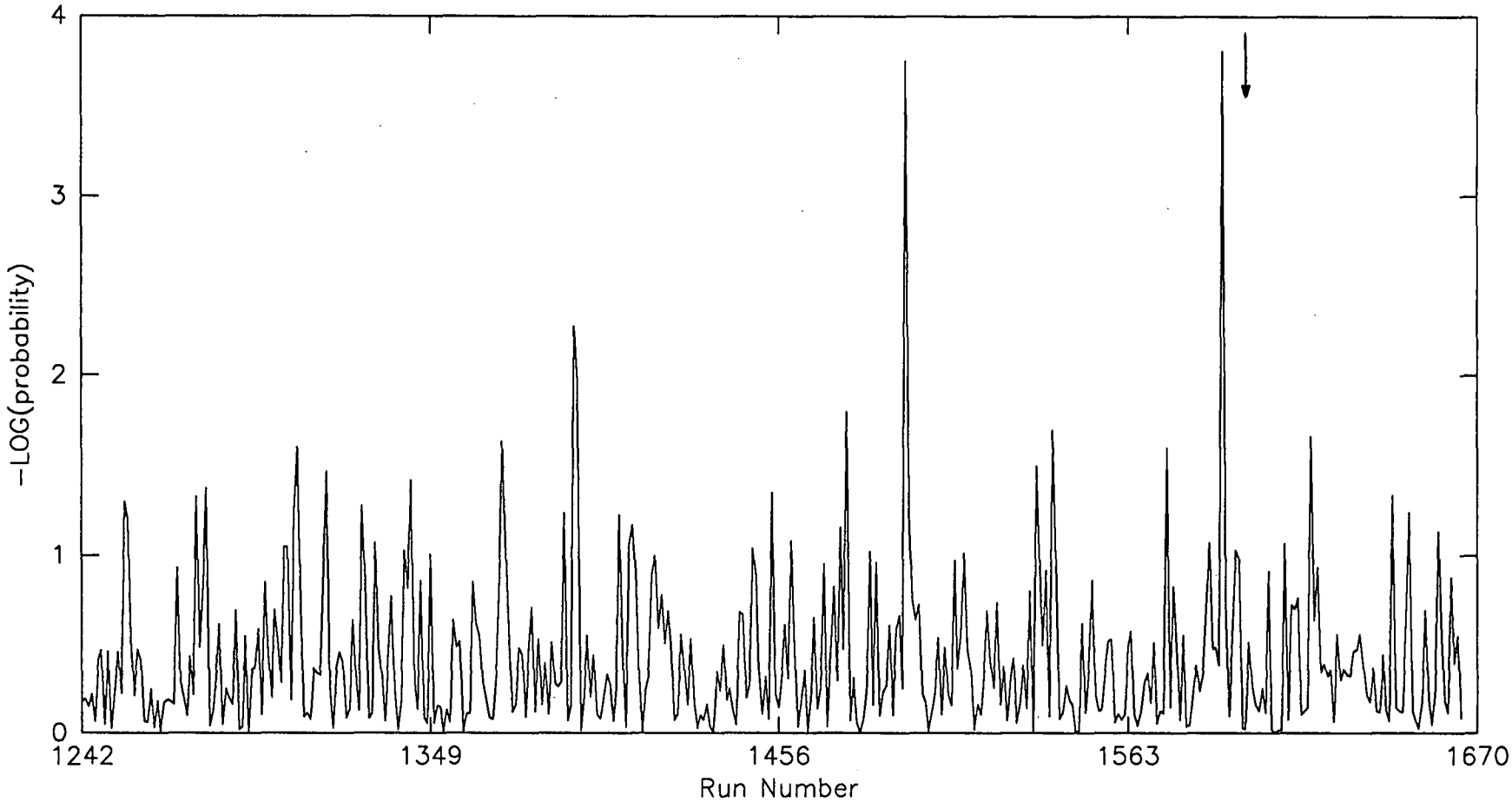

Figure 5.11 Chance probability for uniformity from runs near the 1988 Vela glitch (as indicated by the arrow).

1983). However, a significant feature of the 1988 Vela pulsar glitch was the fact that arrival times of radio pulses after the glitch were seen to differ from the smoothly predicted times according to a damped sinusoidal oscillation with a period of about 25 days. McCulloch *et al.* (1990) suggest that this might be the result of oscillations of the neutron star superfluid. A similar oscillation, with a period of a few tens of days, was also evident in the pre-glitch timing data. Moreover, it has been suggested that if the production site of VHE emission is located in the outer parts of the pulsar magnetosphere, near which co-rotation of the magnetosphere may break down, then differences between the observed high-energy pulsation and the pulsar spin period may arise (e.g. Holloway and Pryce, 1981). It may be possible that such a breakdown in co-rotation could be initiated by the occurrence of a glitch.

Accordingly, the underground muon data immediately preceding and following the 1988 Vela glitch have been examined for evidence of a pulsed signal at an anomalous frequency near the Vela radio frequency. The data were split into two groups; one group comprising all data runs from run *A* up to the glitch, and the second group comprising all data runs following the glitch. The independent Fourier frequency (IFF) spacing for a run of average duration is $\sim 100\,\mu$Hz, so all runs within each data group were analysed at 1000 frequencies spaced by $5\,\mu$Hz (i.e. with an oversampling factor of 20). The search window therefore covered a frequency range of ± 25 IFF or $\pm 0.022\%$ about the pre-glitch radio frequency. The test statistic used was that suggested by Buccheri *et al.* (1987), where the chance probability for emission at a particular frequency is derived from the statistic

$$\beta_j = -2 \sum_{i=1}^{n} \ln \alpha_{ij} \qquad (5.4)$$

where

α_{ij} is the chance probability of exceeding the value of Z_5^2 obtained from analysing run i at frequency f_j,

n is the number of data runs included in the search.

In the absence of a periodic signal, β is distributed as a χ^2 distribution with $2n$ degrees of freedom. Comparative tests carried out by Protheroe (1987) indicate that this particular search strategy gives the best hope of detecting a weak periodic signal. The search results for the pre-glitch and post-glitch data are shown in Figures 5.12 and 5.13 respectively. Taking into consideration the number of degrees of freedom involved in the search, there is no evidence for a burst of emission within any of the runs at any of the frequencies tested.

Bhat *et al.* (1980) have suggested that there is higher probability of observing high-energy emission from pulsars during a post-glitch period. Indeed, in the past, there have been several attempts to associate unusual cosmic-ray phenomena with pulsar glitches. Fegan *et al.* (1983) observed a simultaneous increase in cosmic-ray shower rate which lasted for 20 seconds at two widely separated (250 km) recording stations. It was the first such increase seen in 3 years of observation, and it was suggested that the effect might have been a gamma-ray burst related to a glitch of the Crab pulsar which had occurred ~21 days earlier. Similarly, COS-B observed a two-fold increase in the pulsed high-energy gamma-ray flux from the Vela pulsar about one month after the 1975 glitch (Grenier *et al.* 1988). The Vela pulsar was not in the COS-B field of view at the time of the 1975 glitch, nor at the time of several other Vela pulsar glitches which occurred during the COS-B lifetime. A common feature in both instances is that the purported glitch-related cosmic-ray phenomena occurred a few tens of days after a glitch, unlike the present case where the apparent periodic enhancements occurred before a glitch. It is unfortunate that, due to unforeseen circumstances, the observations pertaining to this investigation were discontinued soon (~ 14 days) after the 1988 Vela glitch.

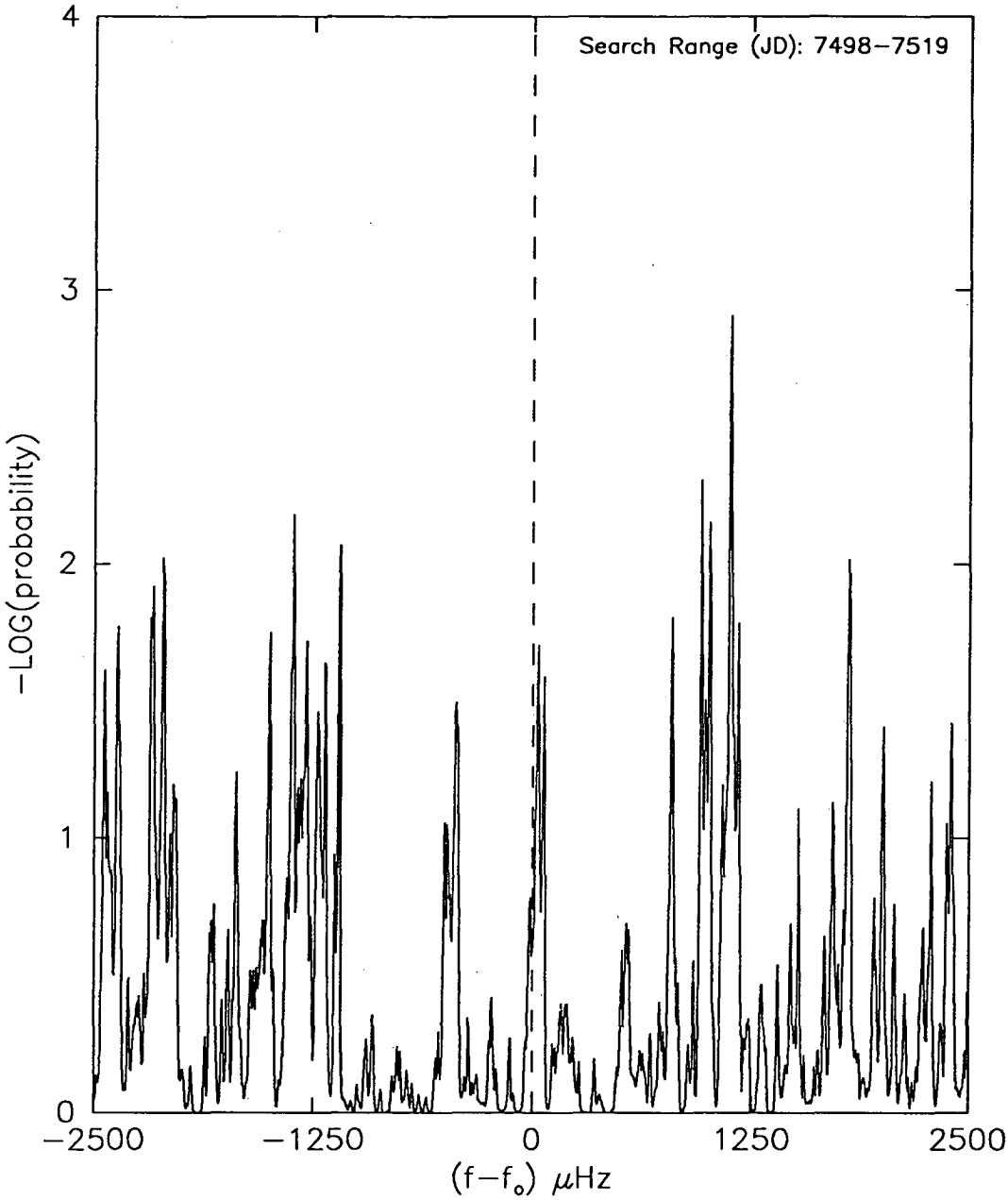

Figure 5.12 Chance probability for uniformity as a function of test frequency, f, about the pre-glitch radio frequency, f_o. The search covered all runs from run *A* up to the glitch.

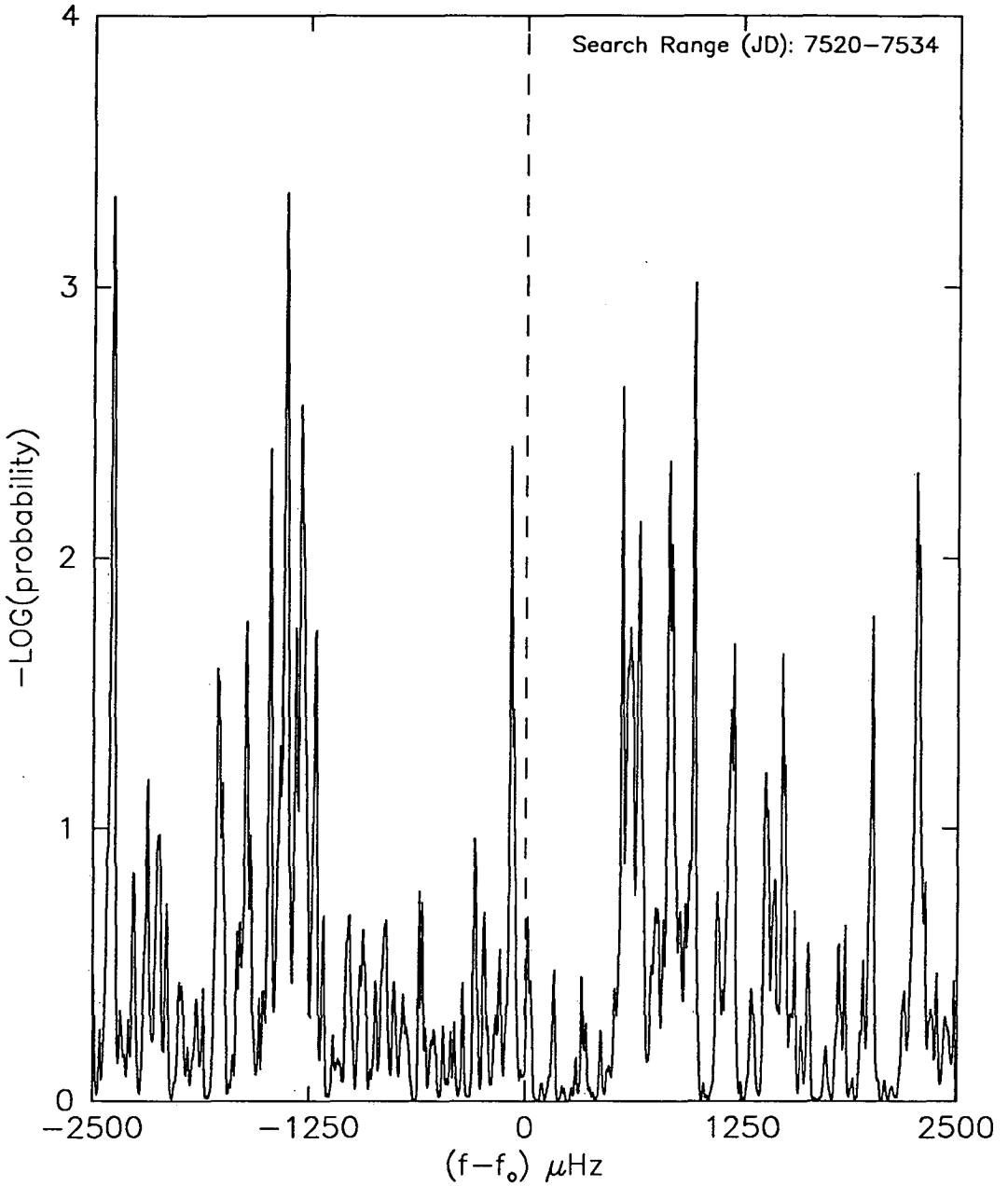

Figure 5.13 Chance probability for uniformity as a function of test frequency, f, about the pre-glitch radio frequency, f_o. The search covered all runs after the glitch.

5.5 Summary

Underground muon data collected over the 18 month period August 1987 to January 1989 have been used to search for evidence of pulsed VHE emission from the Vela pulsar. The analysis reveals no evidence for steady pulsed emission over this observing period. However, two episodes of pulsed emission of duration several hours were observed with marginal statistical significance (at a 98.4% confidence level). Perhaps more significantly, these enhancements were observed near the time of occurrence of a glitch of the pulsar, and although there is no compelling evidence to directly associate the enhancements with the glitch phenomenon, the results are at least sufficiently encouraging to warrant an extended program of observation of this source.

Chapter 6

Conclusion

It has been well established from wide-angle underground and surface measurements that at very-high-energies there exists a small sidereal anisotropy (~ 0.05%) having constant phase. Whether or not narrow-angle anisotropies also exist is still an open question. Even though there have been several reported observations of deviations from isotropy within a narrow band of directions, confirmation of their existence has been restricted by the apparent limited duration of the deviations. The present observations, utilizing an underground muon telescope, extend an earlier search program at the same station to cover the entire southern celestial hemisphere. Data collected over the period August 1987 to January 1989 show no evidence for significant narrow-angle deviations from an isotropic distribution of arrival directions. In particular, this result fails to confirm the existence of an excess of particles detected by the earlier observing program, which further indicates that such deviations appear not to be stable features.

In addition, the data were used to search for evidence of a time modulated underground muon flux from the direction of the Vela pulsar. No evidence for a steady pulsed emission was found. However, two episodes of pulsed emission of duration several hours were observed with marginal statistical significance. Perhaps more significantly, these apparent enhancements were observed near the time of occurrence of a glitch of the pulsar, although no compelling evidence was found to directly associate the enhancements with the glitch phenomenon.

The viability and usefulness of narrow-angle intensity measurements at Poatina have been clearly demonstrated by the present work. However, the apparent

transient nature of narrow-angle anisotropies suggests that a far longer period of investigation than the duration of this experiment would be required to establish their origin. Any future investigation would need to span one or more solar cycles to determine whether or not they are linked in some way to the solar cycle, as suggested by previous observations at slightly lower energies. Moreover, a long-term experiment would enable the temporal structure of any observed deviations to be measured, thus allowing any possible association with particular celestial objects to be determined.

With regard to observations of the Vela pulsar, a long-term experiment is not necessarily required, since the judicious use of periodic analysis techniques allows lower levels of detectability to be attained over much shorter time scales. Even so, detection and verification become difficult if the pulsar exhibits episodic behaviour, particularly so if the bursts of emission are exclusively related to glitches which only occur once every few years. One only has to look at the success (or lack thereof) of radio-astronomers in observing glitch phenomena, to realise the difficulties associated with such a task. However, the Vela pulsar transits almost directly overhead at Poatina, and this fact alone should be reason enough for carrying out continuous long-term observations of this source. Indeed, the relatively unexplored southern sky contains many known and potential high-energy gamma-ray sources. Certainly, detections of underground muon signals from gamma-ray sources remain controversial, and will remain so unless concerted attempts to observe such signals are made.

It could be said that such observations might best be done by an atmospheric Cerenkov experiment which would have the advantages of a larger collecting area and somewhat improved angular resolution. However, such an experiment requires ideal weather and atmospheric conditions (i.e. clear, moonless nights), and these are obviously major impediments to conducting continuous long-term observations of any source. Certainly, there has been no such observations of the Vela pulsar since its discovery as a possible VHE source in 1975, even though there are a number of

atmospheric Cerenkov installations located in the southern hemisphere. The main challenge of any high-energy astronomical program should be not only to determine what celestial objects are sources of VHE emission, but also, and perhaps more importantly in the light of recent underground results, what is the nature of the emission. Such challenges can only be met by the collaborative efforts of research groups operating both surface and underground detectors, ideally with simultaneous observational programs.

In view of these requirements, serious consideration should be given to making directional measurements a permanent part of the experimental setup at the Poatina station. Such measurements would allow many more avenues of research to be undertaken in addition to the wide-angle anisotropy studies currently performed. This is of particular importance when consideration is given to the fact that the Poatina telescope is the only relatively deep underground muon telescope so located as to allow complete coverage of the entire southern celestial sky.

It would be desirable in future investigations to increase the sensitivity of the observations, by increasing the angular resolution and/or collection area of the telescope. The angular resolution of the telescope, however, is fixed by its construction, that is, by the diameter of the proportional counters and the vertical separation of the counter trays. A second telescope, identical to the one used in the present investigation, is currently in operation at the Poatina observing site and a third telescope is also under construction. Severe financial limitations restricted the present experiment to the use of one telescope. This might not be so for future investigations, in which case it would be possible to increase the total collection area of the observations by up to three-fold. This would result in a corresponding three-fold increase in intensity resolution for narrow-angle anisotropy studies.

During the present investigation, data handling procedures initially presented an information bottle-neck in the system, because data analysis software had to be

developed from scratch. This situation was progressively relieved, however, as software was developed. Any increase in collection area will produce a corresponding increase in the volume of data generated at the station, placing an increased burden on the existing data-storage facilities. On-line event reconstruction, as done in the present work, would reduce the quantity of data leaving the station to a significant degree, as would discarding those events that cannot be usefully analysed (i.e. complex and lost events). It is doubtful whether any further compression of the data could be achieved without reducing the flexibility and scope of subsequent data analysis.

It would be worthwhile considering locating one of the telescopes at a second observing site. Such an arrangement would offer the possibility of measuring the energy-dependence of detected narrow-angle anisotropies, if the two observing sites had different threshold energies. In fact, previous observations have suggested that such anisotropies are confined to a narrow band of energies. Furthermore, with regard to VHE emission from the Vela pulsar, the coordinated observations would aid in distinguishing a weak genuine periodic signal from a spurious signal caused by random fluctuations of the background, since the genuine signal, unlike the spurious signal, would be observed simultaneously by both telescopes at the same phase. This of course, would depend heavily on the energy-spectrum of the pulsed signal and the comparative threshold energies at the two observing sites. An ideal site for this purpose would be the Cambridge observing station (located $\sim$ 10 km north-east of Hobart in an abandoned railway tunnel) at which the threshold energy is $\sim$ 10 GeV.

Alternatively, the two telescopes currently in operation at the Poatina site could be combined to form a *double-telescope* which would provide an increase in angular resolution with minimal effort and cost. The proposed arrangement would be to locate one of the telescopes on the station floor directly above or below the other telescope and similarly orientated, as illustrated in Figure 6.1. The telescopes would be combined via a common recording system, which would enable the registering of events passing through both telescopes. With this arrangement, the increased

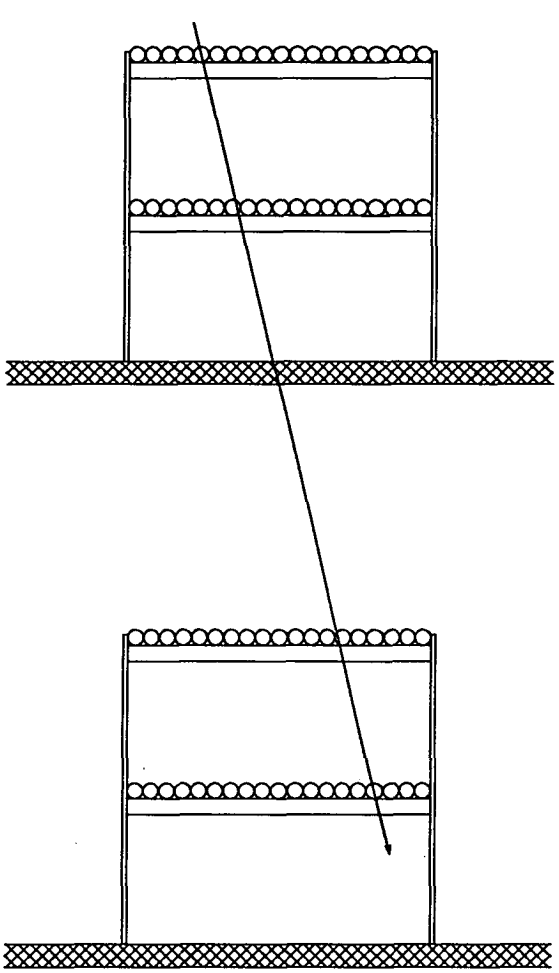

Single Telescope

Angular Resolution = 5.7°
Max. Viewing Angle = 63°
Geometrical Factor = 45000 cm^2sr

Double Telescope

Angular Resolution = 1.2°
Max. Viewing Angle = 22°
Geometrical Factor = 6700 cm^2sr

Figure 6.1 Proposed arrangement of the two telescopes currently in operation at the Poatina site to form a *double-telescope* . Concrete floors are indicated by the shaded areas.

separation of the counter trays would result in an approximate five-fold improvement in angular resolution, i.e. from $5.7°$ to $\sim 1.2°$ for vertical viewing directions. The only constructional modifications required to bring such a system on-line, would be an expansion of the existing data logger to accommodate the signals from the second telescope, or preferably, a new data logger specifically designed to the needs of the new system. This of course would be more cost effective than duplicating the existing recording system at a second observing site. Moreover, such an arrangement, being modular in nature, would allow for future increases in collection area, and hence sensitivity, with the addition of further telescopes as they became available.

With regard to underground muon astronomy, there are several benefits to be gained from the use of the proposed double-telescope. Firstly, the telescope would generate a much cleaner sample of underground high-energy muon data, since knock-on electrons and low-energy muons would be absorbed or deflected by the intervening concrete floor. Also, the doubling of the number of counter trays would enable almost complete detection of secondary particles produced within the telescope or surrounding rock, unlike the present system where the non-detection of these secondary particles results in a relatively large portion ($\sim 17\%$) of data that cannot be usefully analysed. Secondly, the double-telescope would provide the opportunity of using a variety of data collection channels simultaneously. As an example, for the purpose of narrow-angle anisotropy studies, both telescopes could be used independently to achieve a comparable angular resolution, but slightly larger collection area, to that of the present work. In fact, using the double-telescope for this purpose would be somewhat disadvantageous due to the reduced sky coverage afforded by the double-telescope. On the other hand, the double-telescope would be ideally suited to observations of particular celestial objects, where the benefits of the 25-fold increase in sensitivity would be fully realised. The total data output from the double-telescope arrangement, taking into account all likely data collection channels, would not be significantly different from that generated by a single telescope. Moreover, the extensive software database developed during the present work would relieve, to a large degree, the burden of data handling in any future investigation.

Appendix A

Multiple Particle Event Analysis

The multiple particle event analysis is basically a comparison of the pattern of traversed counters in an upper and lower tray pair, based on the assumption that the particles associated with such an event will have parallel trajectories. The following algorithm for analysing multiple particle events was developed by Wilson (1985a).

As stated in Chapter 2, each event is viewed in two orthogonal planes (*U* and *V*). The event reconstruction analysis determines a classification and a direction coordinate from each view. The final description of the event is formed by combining the results from each of these views. That is, the event direction is given by the relative coordinate *(u,v)* and the classification by the maximum of the two class numbers (see Table 2.2). For multiple particle events, the multiple particle algorithm is applied separately to each view of the event. The final multiplicity of the event is taken as the maximum of the estimates from each view, since it is possible for particles to be hidden in one or both planes. The final lateral spread of the event is taken as the square root of the sum of squares of the lateral spreads from each view.

The various steps involved in the multiple particle event analysis are outlined below. By way of example, a single view of a typical 2 particle event is depicted in Figure A.1, together with illustrations of the various steps involved in the analysis of the event.

(1) For ease of computation, the tray patterns are rearranged so that the particle directions appear vertical. This is done by right justifying both patterns so the rightmost counter in each tray

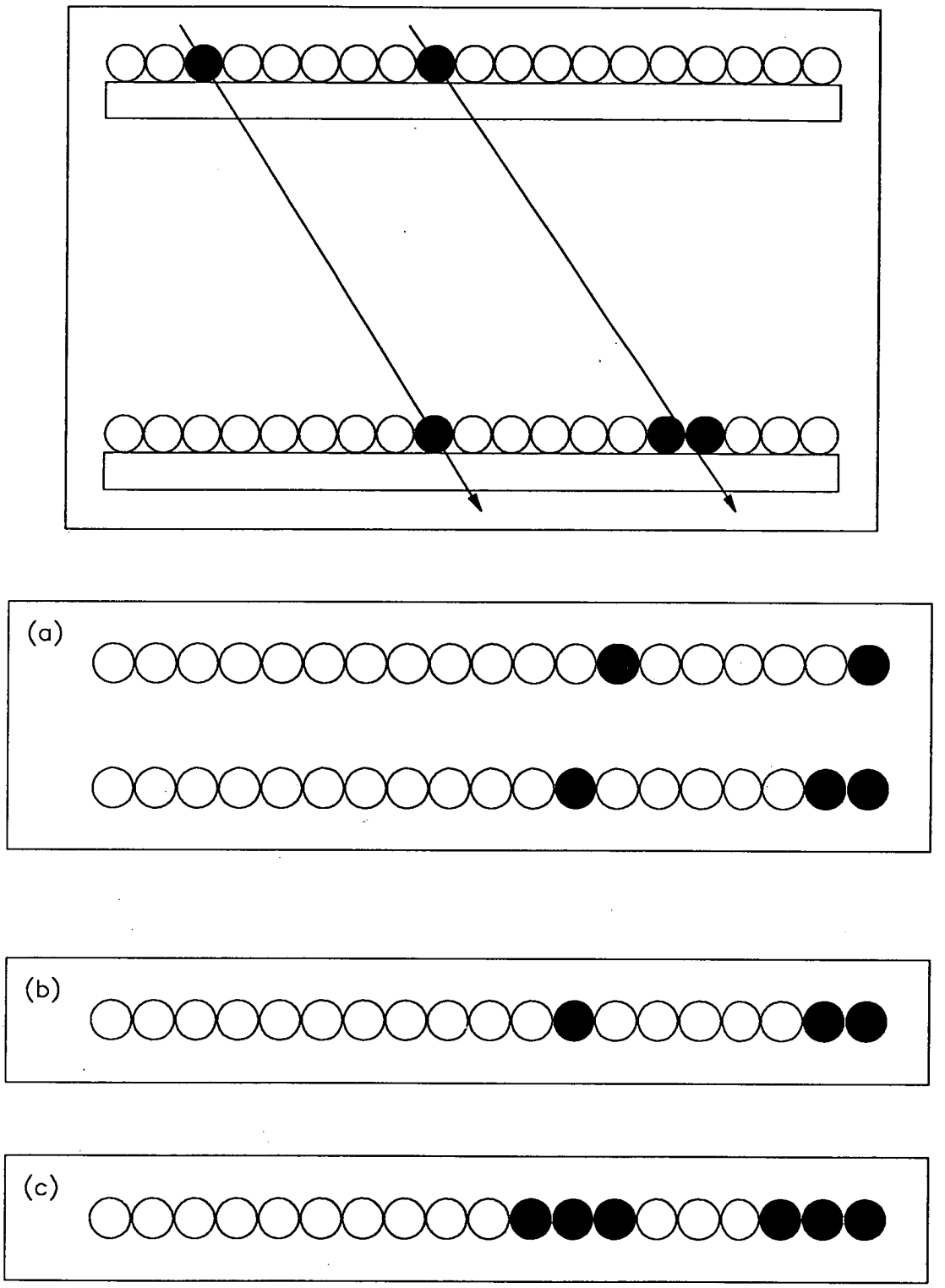

Figure A.1 The analysis of a two particle event.
(a) Right shifted tray patterns. The direction coordinate is 3–10 = –7.
(b) The *inside-mask*. The multiplicity is 2 (with adjacent active counters taken as one). The lateral spread is 7 (i.e. 7 counter diameters).
(c) The *outside-mask*. The event is classified as *multiple* (rather than *complex*) since all active counters in (a) are active in the outside-mask.

appears active. The difference in shifts is the direction coordinate (u or v) of the event relative to the telescope.

(2) The patterns are compared by generating an *inside-mask* by logically ANDing respective counters in both trays, ANDing the upper tray with the lower tray shifted one counter to the left, ANDing the lower tray with the upper tray shifted one counter to the left, then ORing these three patterns together.

The inside-mask is designed to contain features that are common to both the upper and lower patterns with allowances made for possible dislocation of traversed counters by one counter between the two trays. The multiplicity is taken as the number of active counters in the inside-mask, but if the direction coordinate is outside the range -2 to +2, adjacent active counters are scored as one. The rationale behind this being that a single particle with a direction coordinate outside the range -2 to +2, is capable of discharging more than one counter per tray. The lateral spread is taken as the maximum distance between active counters in the inside-mask.

(3) An *outside-mask* is generated by ORing the inside-mask with itself shifted both left and right.

The outside-mask represents the extreme or largest set of counters that could be traversed in either tray. For the event to be classed as *multiple*, all active counters in the right justified trays should correspond to active counters in the outside-mask. If a counter in the shifted representation is not indicated in the outside-mask, then the event is classified as *complex* and the direction coordinate, multiplicity and lateral spread are disregarded.

Appendix B

Analytic Calculation of Telescope Acceptance

Assume the telescope is constructed of two planar rectangular detectors of size k by l, which are are positioned one directly above the other, and separated by a height h. Futhermore, assume both detectors have 100% detection effeciency (i.e. ideal detectors). A particle is detected if it passes through both detectors.

The sensitivity of the telescope to particles from a particular direction is the active area of the telescope perpendicular to that direction. It can be easily shown that the area of intersection of the two detectors when viewed from (θ,ϕ) is given by

$$A(\theta,\phi) = (k - h\tan\theta\cos\phi)(l - h\tan\theta\sin\phi)\cos\theta. \qquad \text{(B.1)}$$

This is the *directional response function* of the telescope. The *gathering power* (or *acceptance*) of the telescope is given by

$$\Gamma = \int\int F(\theta,\phi)\,A(\theta,\phi)\sin\theta\,d\theta\,d\phi, \qquad \text{(B.2)}$$

where $F(\theta,\phi)$ is the angular dependence of the incident radiation and where the bounds of integration cover all trajectories through both detectors. Wilson (1985a) has derived the following solution to Equation (B.2) for $F(\theta,\phi) = \cos^2\theta$:

$$\begin{aligned}\Gamma(h,k,l) = \tfrac{1}{2}\{ &\frac{l\,(h^2+2k^2)}{(h^2+k^2)^{1/2}}\tan^{-1}\frac{l}{(h^2+k^2)^{1/2}} - lh\tan^{-1}\frac{l}{h} \\ &+ \frac{k\,(h^2+2l^2)}{(h^2+l^2)^{1/2}}\tan^{-1}\frac{k}{(h^2+l^2)^{1/2}} - kh\tan^{-1}\frac{k}{h}\ \}\end{aligned} \qquad \text{(B.3)}$$

The *geometrical factor* (or acceptance for isotropic flux) of the telescope will be

$$G = \int\int A(\theta,\phi) \sin\theta \, d\theta \, d\phi \tag{B.4}$$

The solution to Equation (B.4) is given by Sullivan (1971):

$$\begin{aligned} G(h,k,l) \;=\; & h^2 \ln \frac{(h^2+k^2)\,(h^2+l^2)}{h^2\,(h^2+k^2+l^2)} \\ & + \; 2k\,(h^2+l^2)^{1/2} \tan^{-1}\frac{k}{(h^2+k^2)^{1/2}} \;-\; 2kh \tan^{-1}\frac{k}{h} \\ & + \; 2l\,(h^2+k^2)^{1/2} \tan^{-1}\frac{l}{(h^2+l^2)^{1/2}} \;-\; 2lh \tan^{-1}\frac{l}{h} \end{aligned} \tag{B.5}$$

Expressions (B.3) and (B.5) can be used to calculate the geometrical factor and gathering power of telescopes consisting of laterally displaced ideal detectors (from Wilson 1985a).

Conside a telescope consisting of two planes of ideal detectors as shown in Figure B.1a, with detector elements A and C having the same dimensions (i.e. a x b). Let $\Gamma_{X\to Y}$ denote the gathering power of the elementary telescope formed by the detector element X in the upper plane and detector element Y in the lower plane. Then the gathering power of the telescope can be divided up as

$$\begin{aligned} \Gamma_{ABC\to ABC} = \; & \Gamma_{A\to A} + \Gamma_{B\to A} + \Gamma_{C\to A} + \Gamma_{A\to B} + \Gamma_{B\to B} \\ & + \Gamma_{C\to B} + \Gamma_{A\to C} + \Gamma_{B\to C} + \Gamma_{C\to C}. \end{aligned} \tag{B.6}$$

Assuming the incident particle flux is not dependent on azimuthal angle, ϕ, then by symmetry of the detectors, Equation (B.6) can be simplified to

$$\Gamma_{ABC\to ABC} = 2\,\Gamma_{A\to A} + \Gamma_{B\to B} + 2\,\Gamma_{A\to C} + 4\,\Gamma_{A\to B}. \tag{B.7}$$

Similarly, the gathering power of the elementary telescope formed by detector

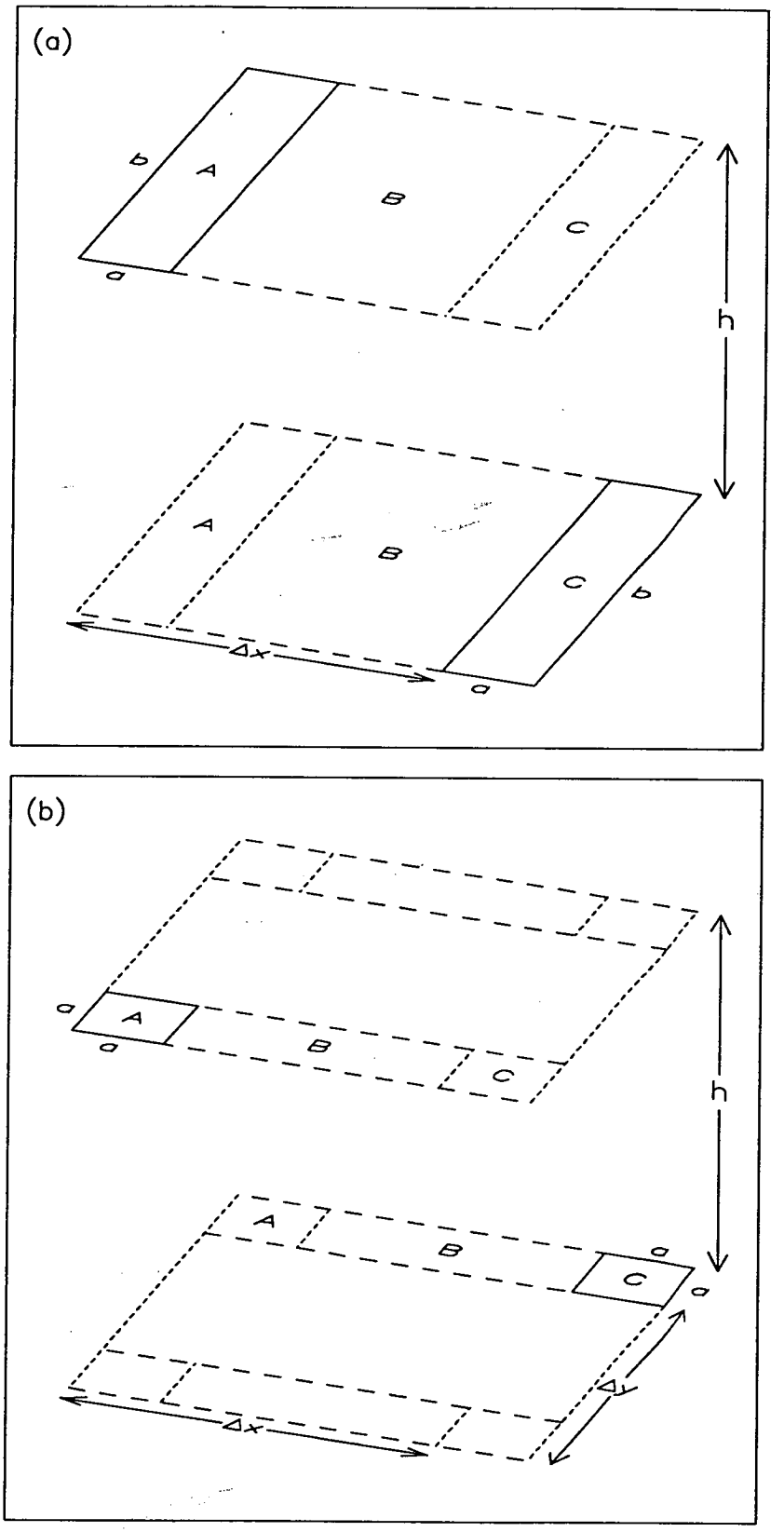

Figure B.1 Segmentation of detector trays for the calculation of the gathering power and geometrical factor of telescopes consisting of laterally displaced ideal detectors

elements A and B in both upper and lower planes can be written as

$$\Gamma_{AB\rightarrow AB} = \Gamma_{A\rightarrow A} + \Gamma_{B\rightarrow B} + 2\,\Gamma_{A\rightarrow B}. \tag{B.8}$$

Combining Equations (B.7) and (B.8) gives

$$\Gamma_{ABC\rightarrow ABC} = 2\,\Gamma_{AB\rightarrow AB} - \Gamma_{B\rightarrow B} + 2\,\Gamma_{A\rightarrow C}. \tag{B.9}$$

Therefore, the gathering power of the elementary telescope formed by detector element A in the upper plane and detector element C in the lower plane is given by

$$\Gamma_{A\rightarrow C} = \tfrac{1}{2}\Gamma_{ABC\rightarrow ABC} + \tfrac{1}{2}\Gamma_{B\rightarrow B} - \Gamma_{AB\rightarrow AB}, \tag{B.10}$$

for which all terms can be explicitly calculated using Equation (B.3) for two identical rectangular detectors situated one above the other. Therefore, the gathering power of two detectors with dimensions as shown in Figure B.1a, and laterally displaced along one axis by Δx, is given by

$$\Gamma_x(h,a,b,\Delta x) = \tfrac{1}{2}\Gamma(h,b,\Delta x+a) + \tfrac{1}{2}\Gamma(h,b,\Delta x-a) - \Gamma(h,b,\Delta x) \tag{B.11}$$

Similarly, the detector planes can be subdivided as shown in Figure B.1b to calculate the gathering power of an elementary telescope formed by two square detector elements laterally displaced along each of two orthogonal axes. If the lateral displacements are Δx and Δy, and the size of the elements is a x a, then in terms of the previously defined function Γ_x, the gathering power for these elements is given by

$$\Gamma_{xy}(h,a,\Delta x,\Delta y) = \tfrac{1}{2}\Gamma_x(h,a,\Delta x+a,\Delta y) + \tfrac{1}{2}\Gamma_x(h,a,\Delta x-a,\Delta y) - \Gamma_x(h,a,\Delta x,\Delta y) \tag{B.12}$$

In the same manner, expressions for the geometrical factor for telescopes consisting of

laterally displaced ideal detectors, can be derived in terms of Equation (B.5):

$$G_x(h,a,b,\Delta x) = \tfrac{1}{2}\, G(h,b,\Delta x+a) + \tfrac{1}{2}\, G(h,b,\Delta x-a) - G(h,b,\Delta x) \qquad \text{(B.13)}$$

$$G_{xy}(h,a,\Delta x,\Delta y) = \tfrac{1}{2}\, G_x(h,a,\Delta x+a,\Delta y) + \tfrac{1}{2}\, G_x(h,a,\Delta x-a,\Delta y) - G_x(h,a,\Delta x,\Delta y) \qquad \text{(B.14)}$$

The directional response, geometrical factor and gathering power of direction bins for an ideal telescope of the same dimensions as the Poatina telescope, have been calculated using expressions (B.1) and (B.11) to (B.14); the results are shown in Figures B.2, B.3 and B.4 respectively.

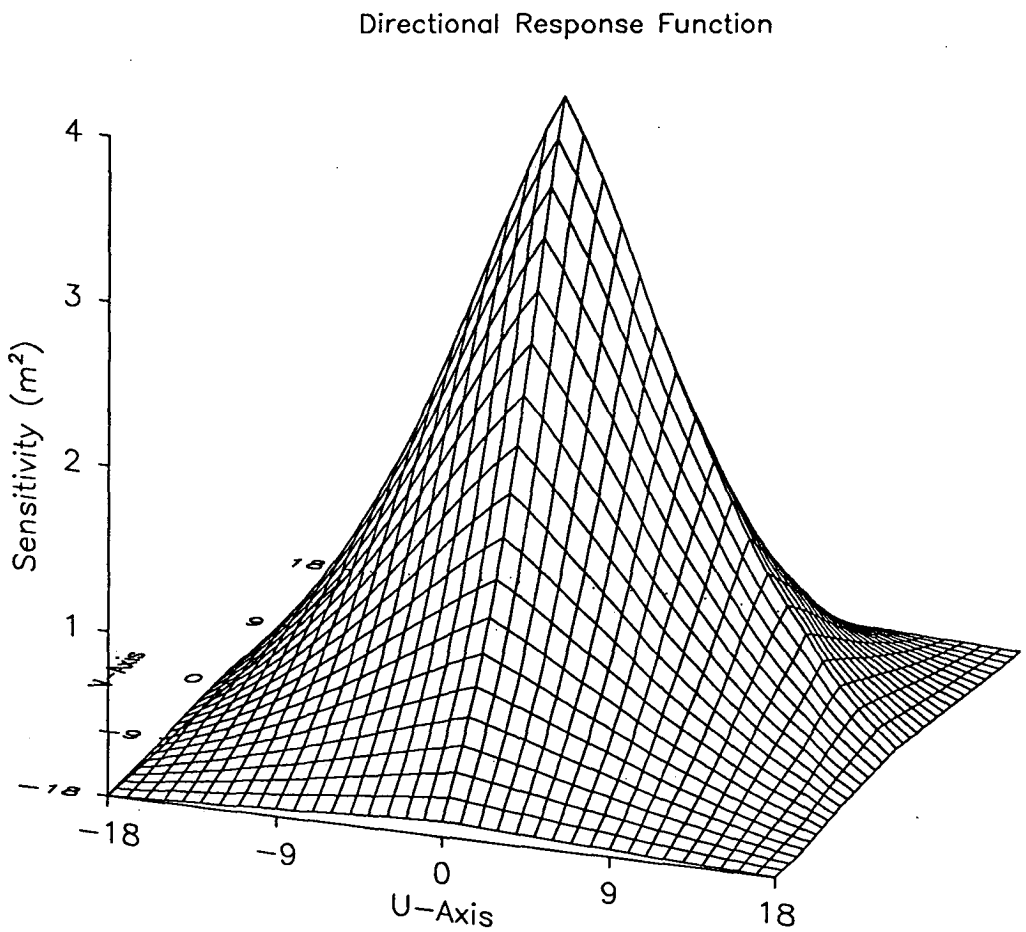

Figure B.2 Directional response for each direction bin of an ideal telescope having the same dimensions as the Poatina telescope.

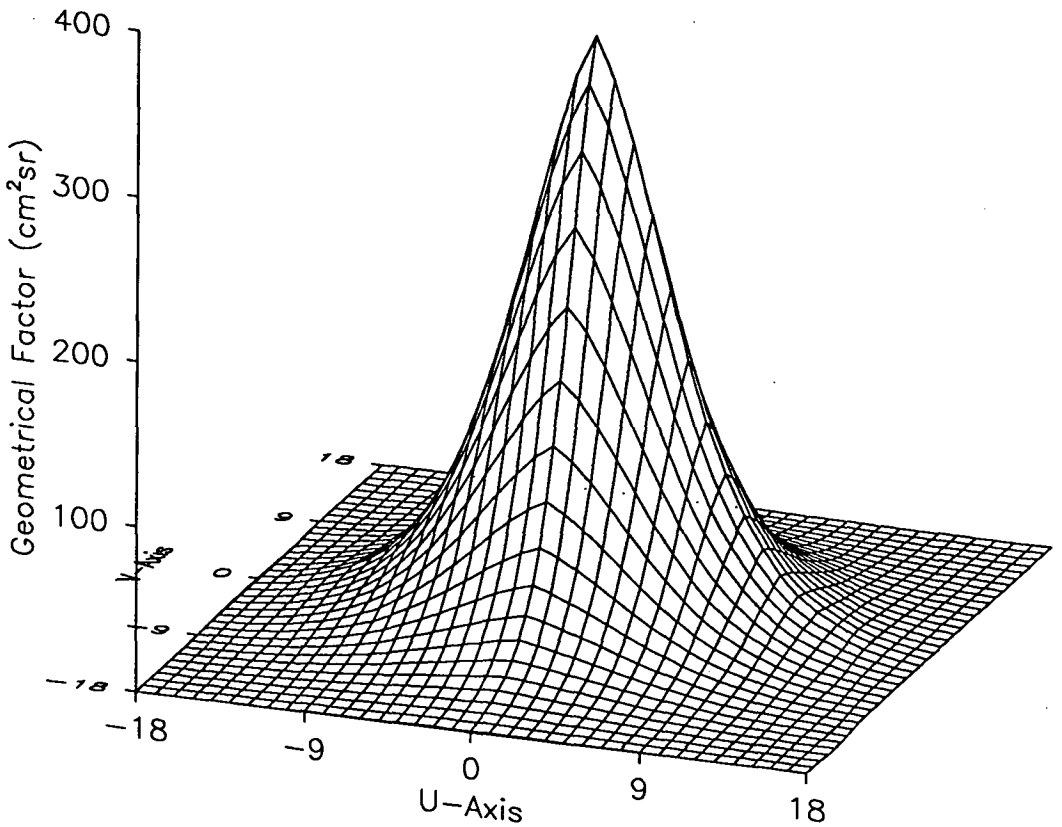

Figure B.3 Geometrical factor for each direction bin of an ideal telescope having the same dimensions as the Poatina telescope.

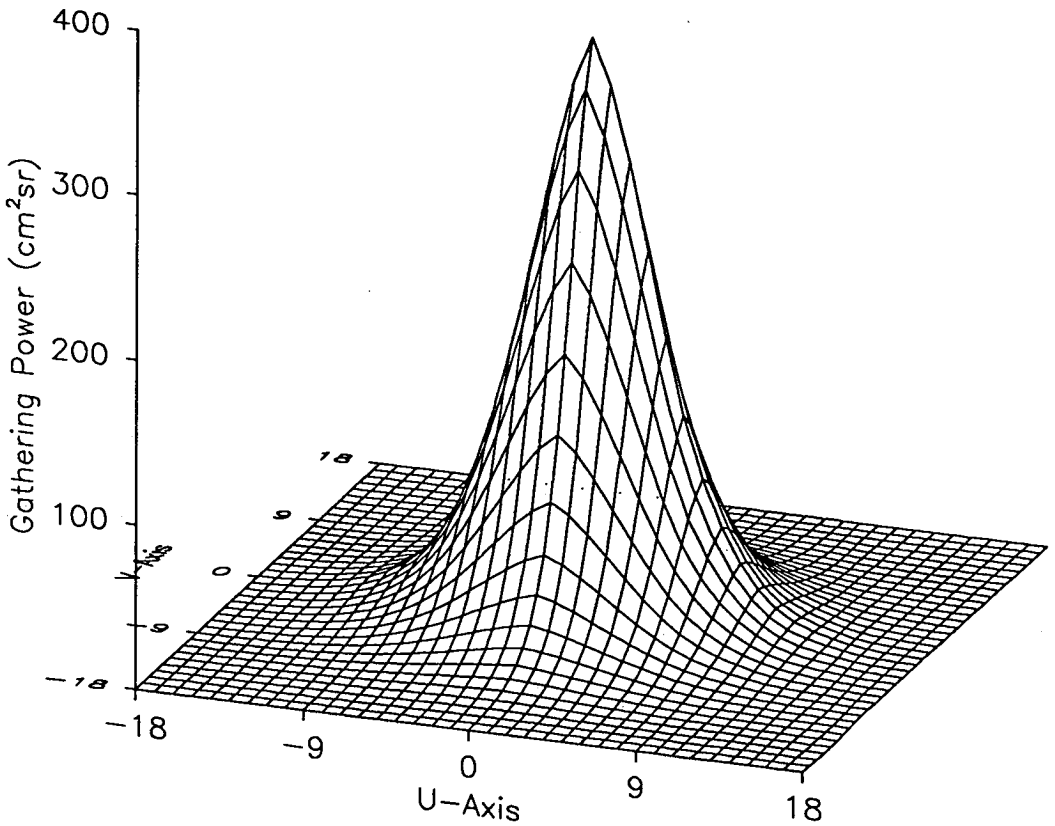

Figure B.4 Gathering power for each direction bin of an ideal telescope having the same dimensions as the Poatina telescope.

Appendix C

Celestial Intensity Maps

The measured and expected distributions of arrival directions for each 5° declination band from 20°N to 90°S, are shown in Figures C.1 to C.22. Also shown are the on-time and declination band response functions used to determine the expected distribution (see below). Note that the on-time functions are identical because the telescope live-time is not dependent on declination.

The expected distribution of arrival directions for each declination band was determined by convolving the telescope *on-time* function with the declination band response function and normalizing to the total number of observed events, i.e.

$$E_\delta(r) = \int_0^{24} R_\delta(t)\, Q(r-t)\, dt \qquad \text{(C.1)}$$

where

$Q(t)$ is the telescope *on-time* function, representing the number of sidereal minutes the telescope was observing at time t, and defined such that

$$\int_0^{24} Q(t)\, dt = T_{obs} \qquad \text{(C.2)}$$

where T_{obs} is the total experimental live-time.

$R_\delta(t)$ is the declination band response function, calculated from the measured response of those direction bins that have central viewing directions located in the band, i.e.

$$R_{\delta}(t) = \sum_{u,v} A(u,v) \qquad \text{(C.3)}$$

where $A(u,v)$, the average response of the (u,v) direction bin, is given by

$$A(u,v) = {}^{1}/_{\Delta T} \sum_{\Delta T} C(u,v) \qquad \text{(C.4)}$$

where $C(u,v)$ is the event rate for the (u,v) direction bin and ΔT is the averaging period.

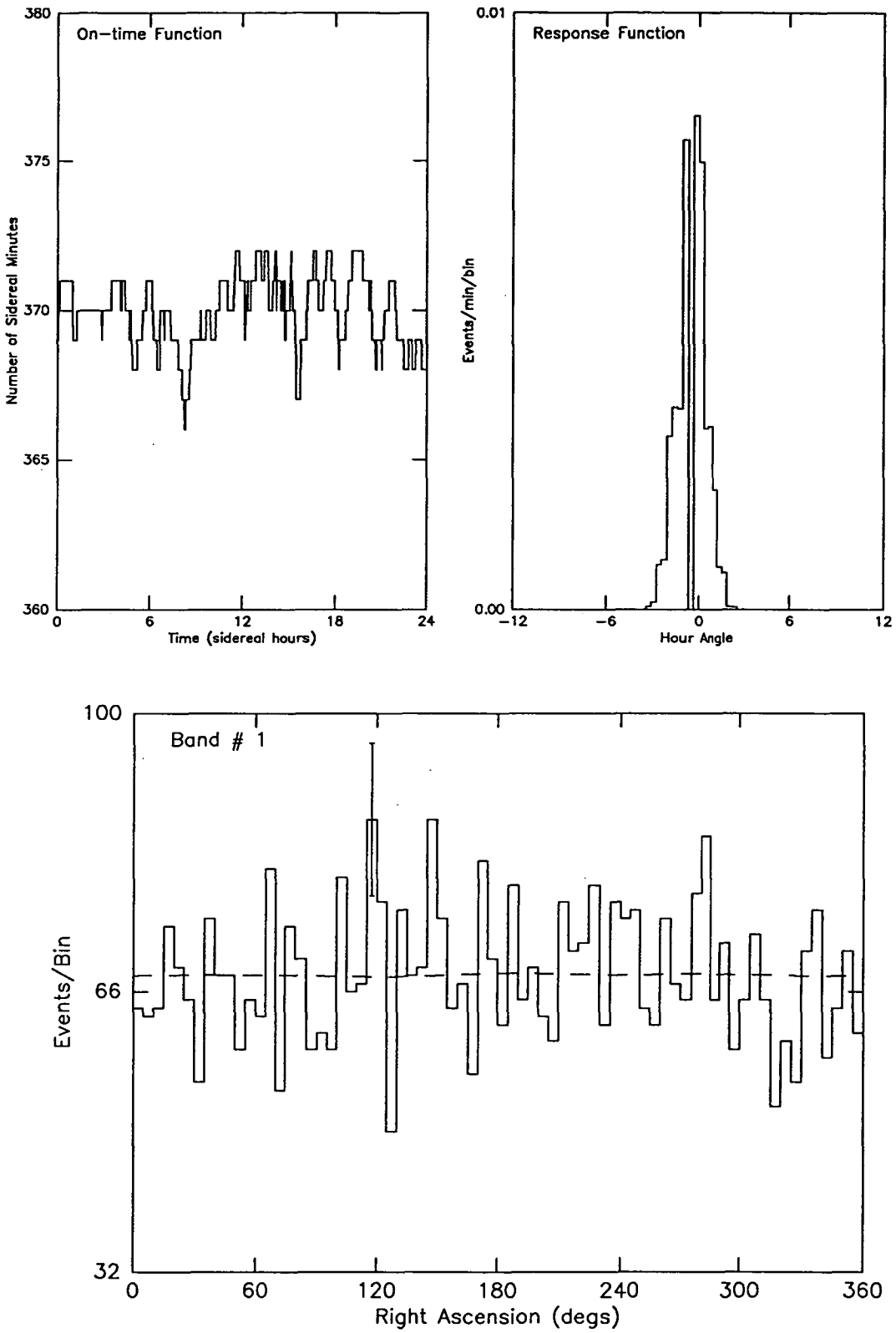

Figure C.1 Declination Band 20°N - 15°N.

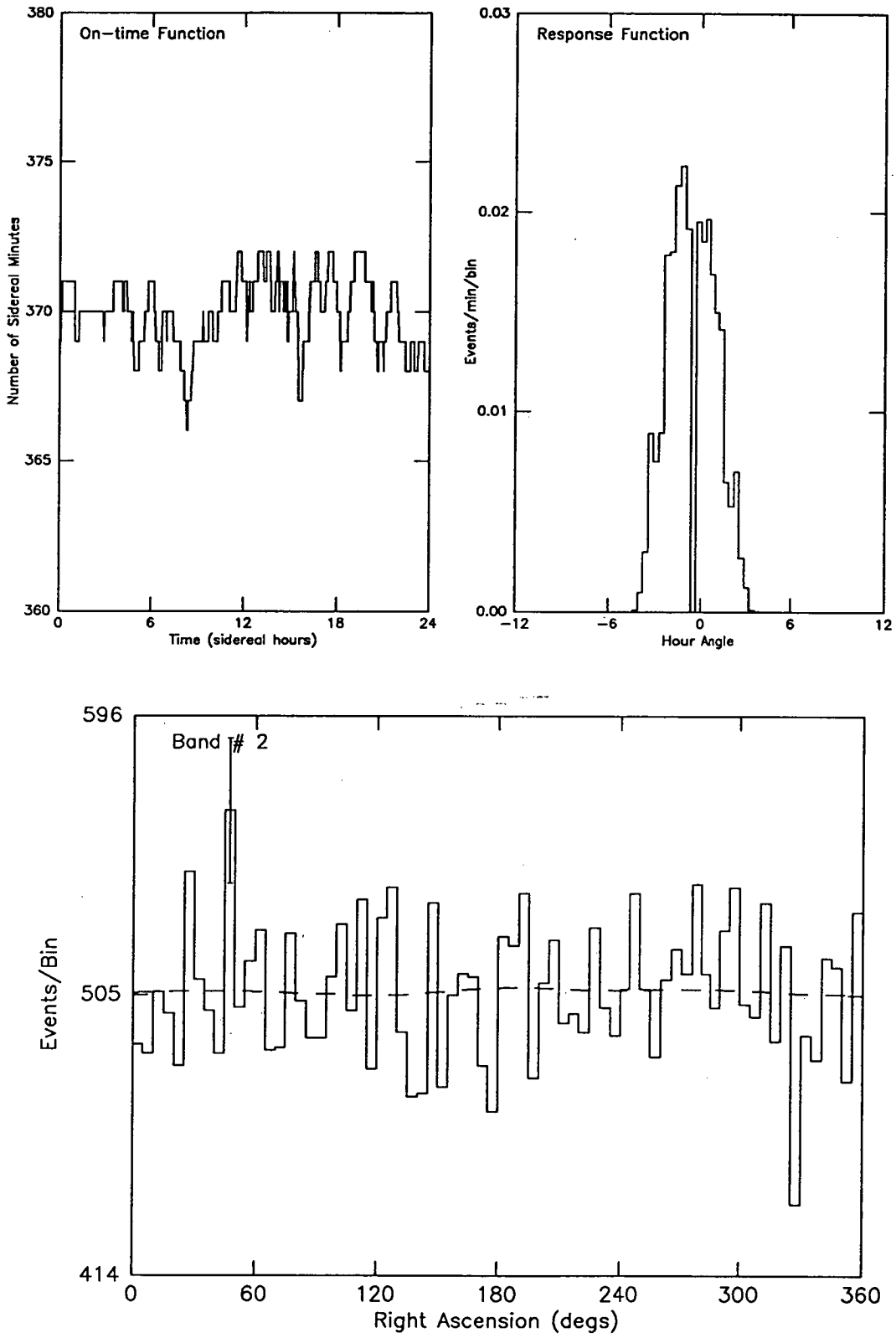

Figure C.2 Declination Band 15°N - 10°N.

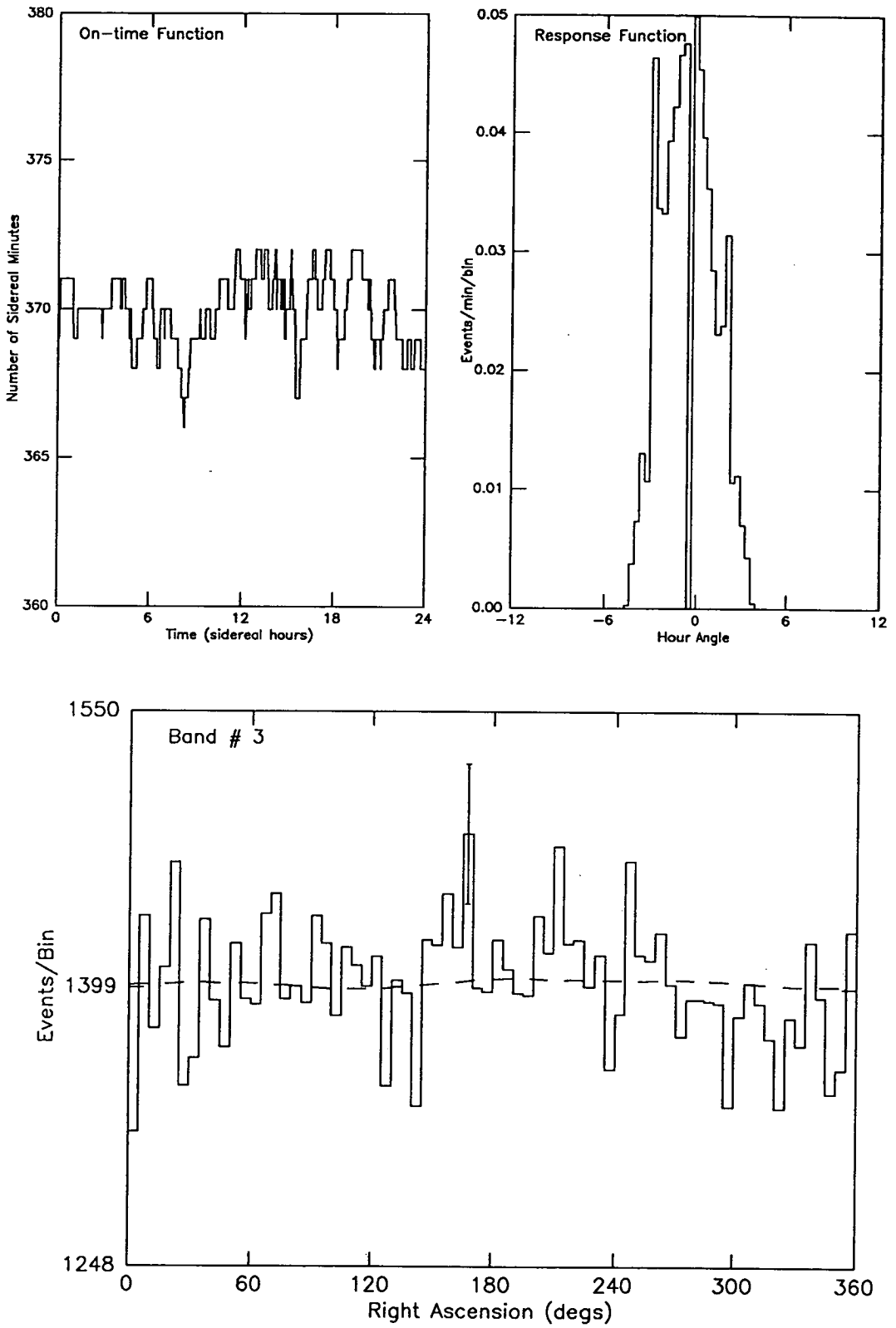

Figure C.3 Declination Band 10°N - 5°N.

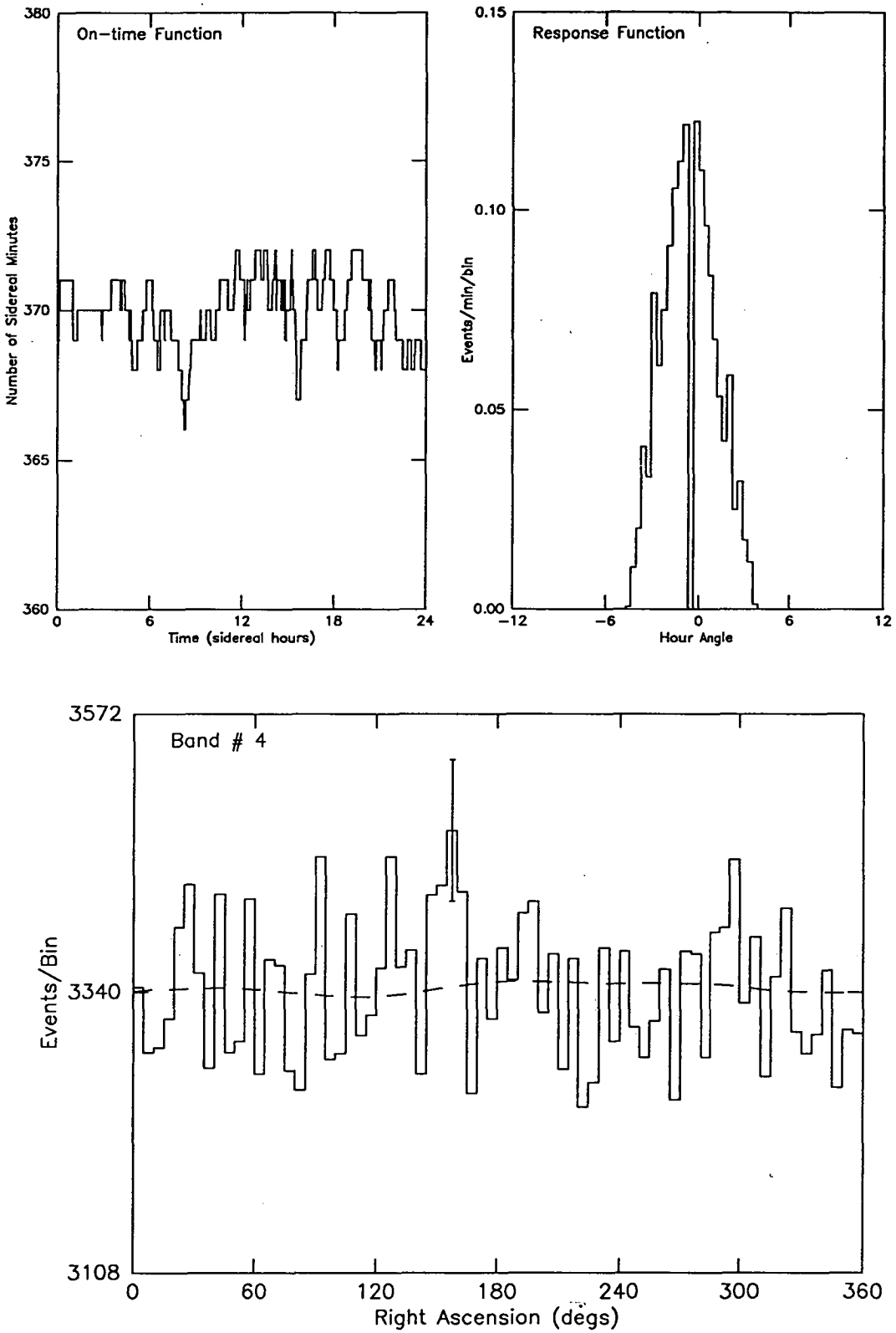

Figure C.4 Declination Band 5°N - 0°.

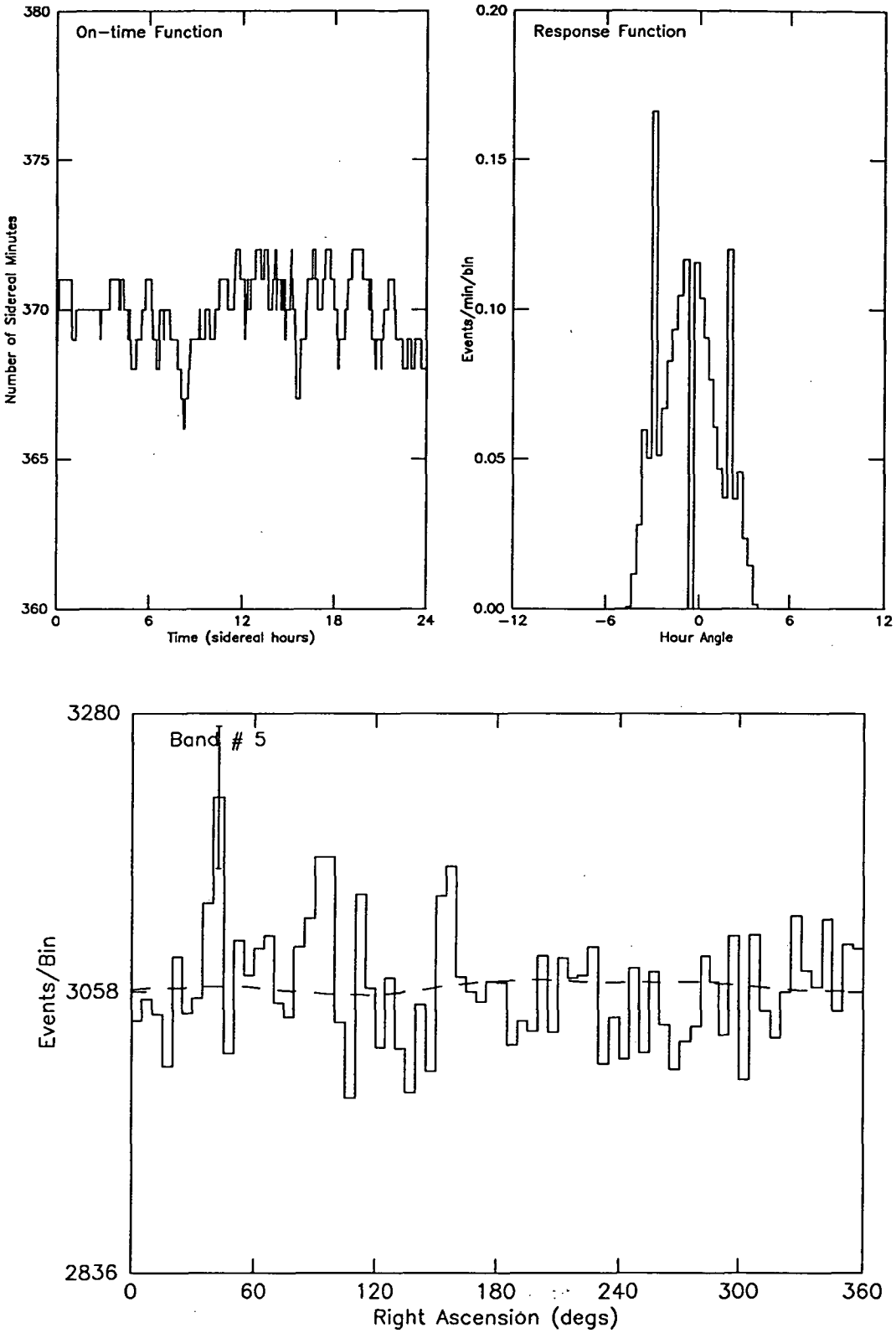

Figure C.5 Declination Band 0° - 5°S.

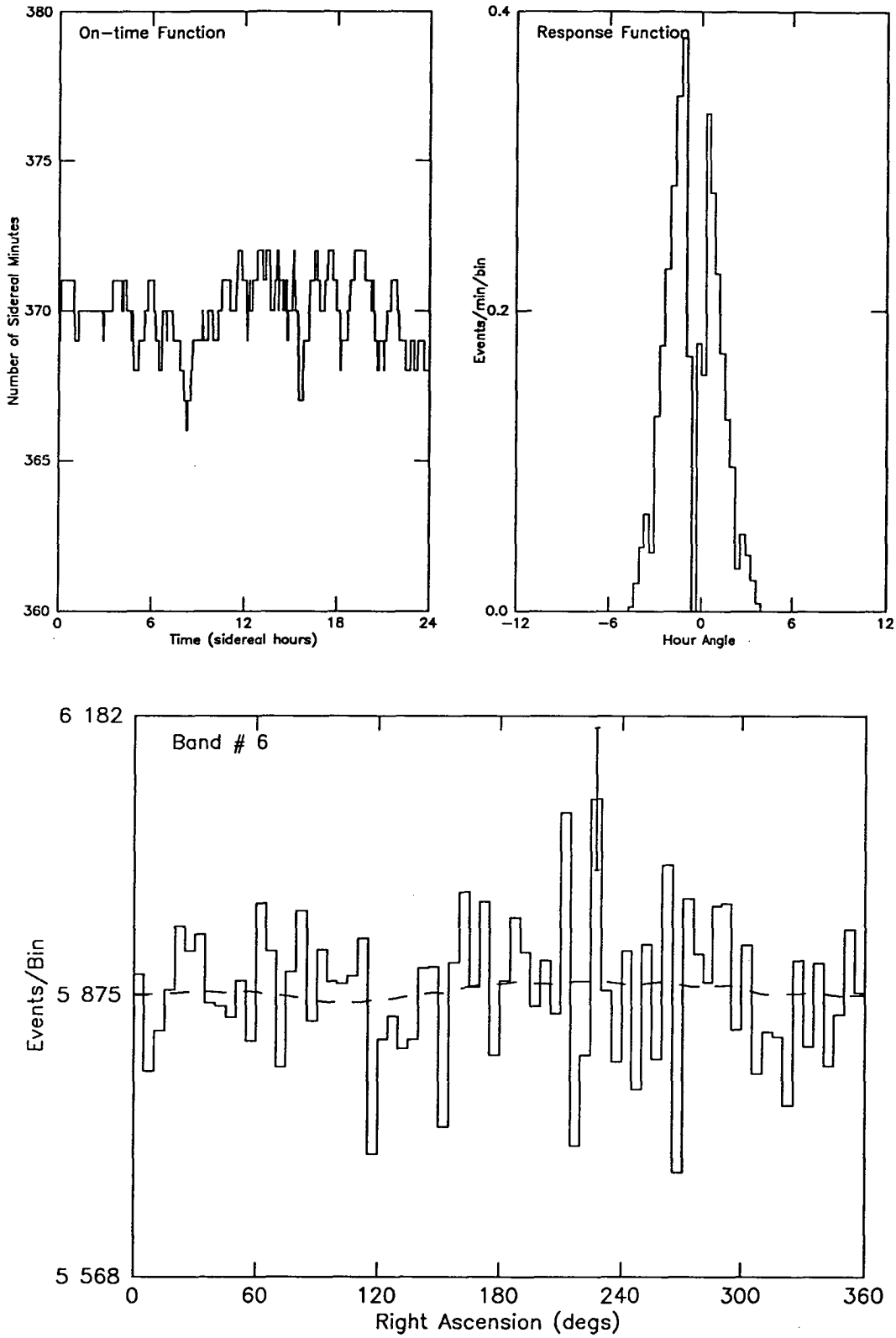

Figure C.6 Declination Band 5°S - 10°S.

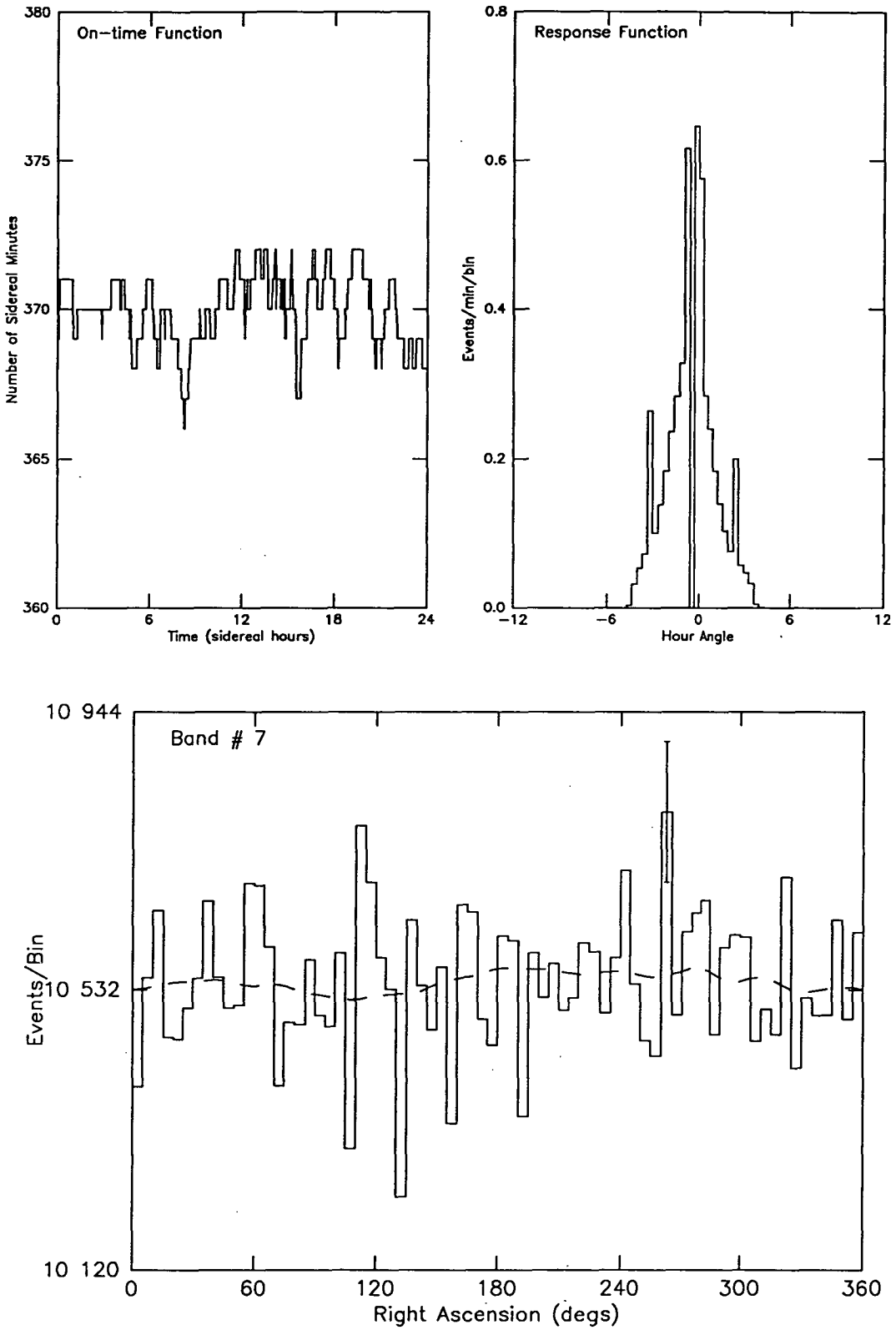

Figure C.7 Declination Band 10°S - 15°S.

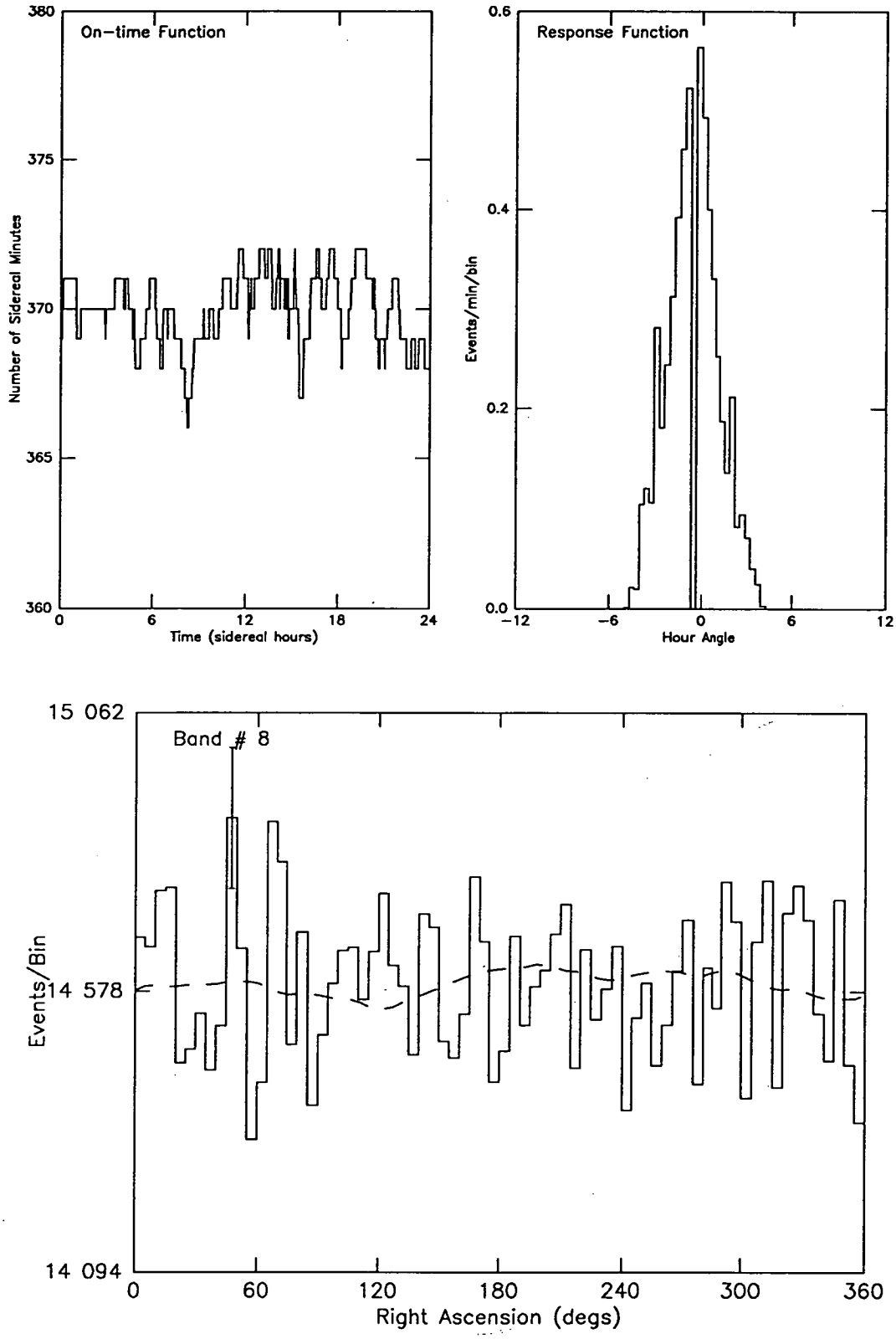

Figure C.8 Declination Band 15°S - 20°S.

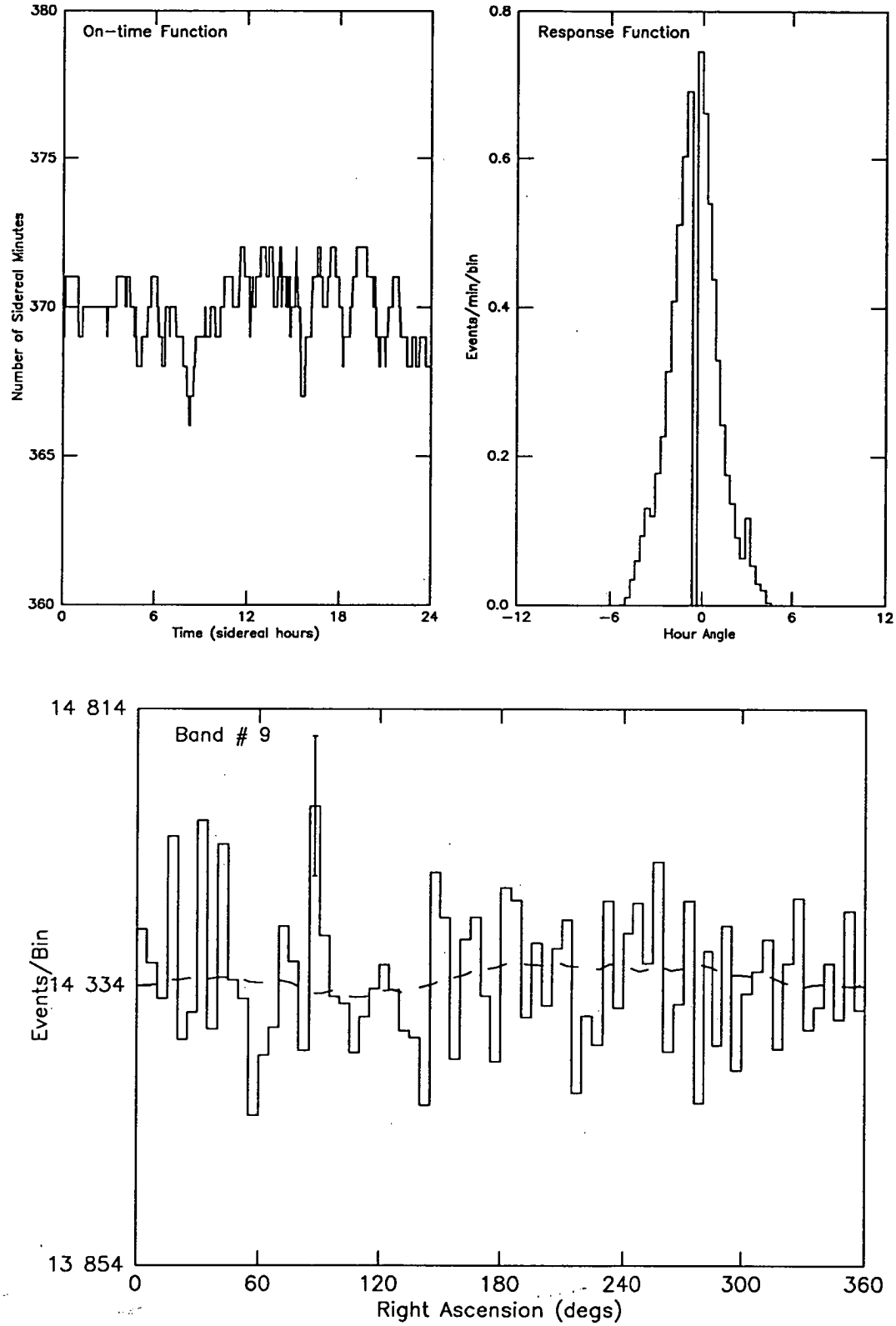

Figure C.9 Declination Band 20°S - 25°S.

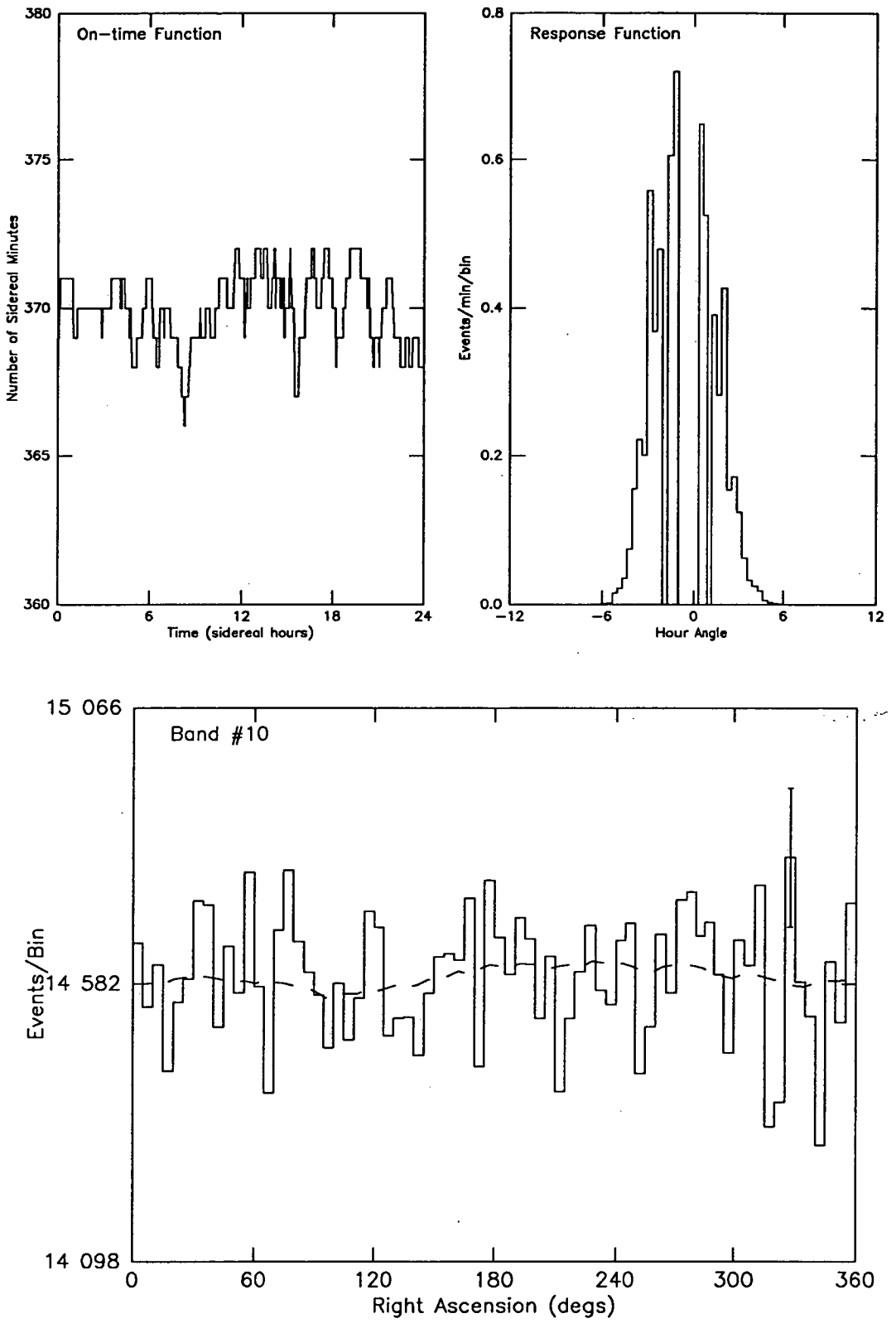

Figure C.10 Declination Band 25°S - 30°S.

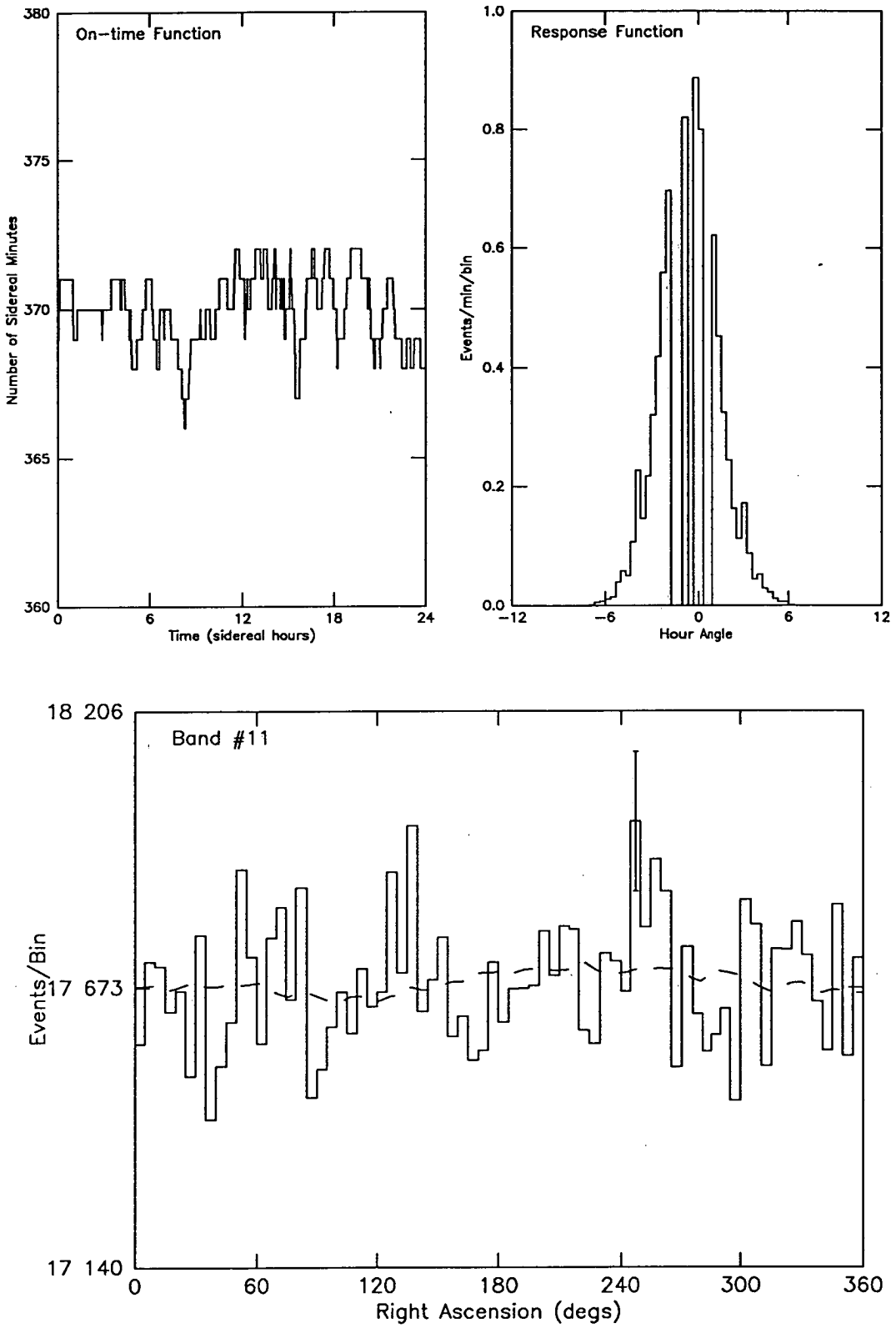

Figure C.11 Declination Band 30°S - 35°S.

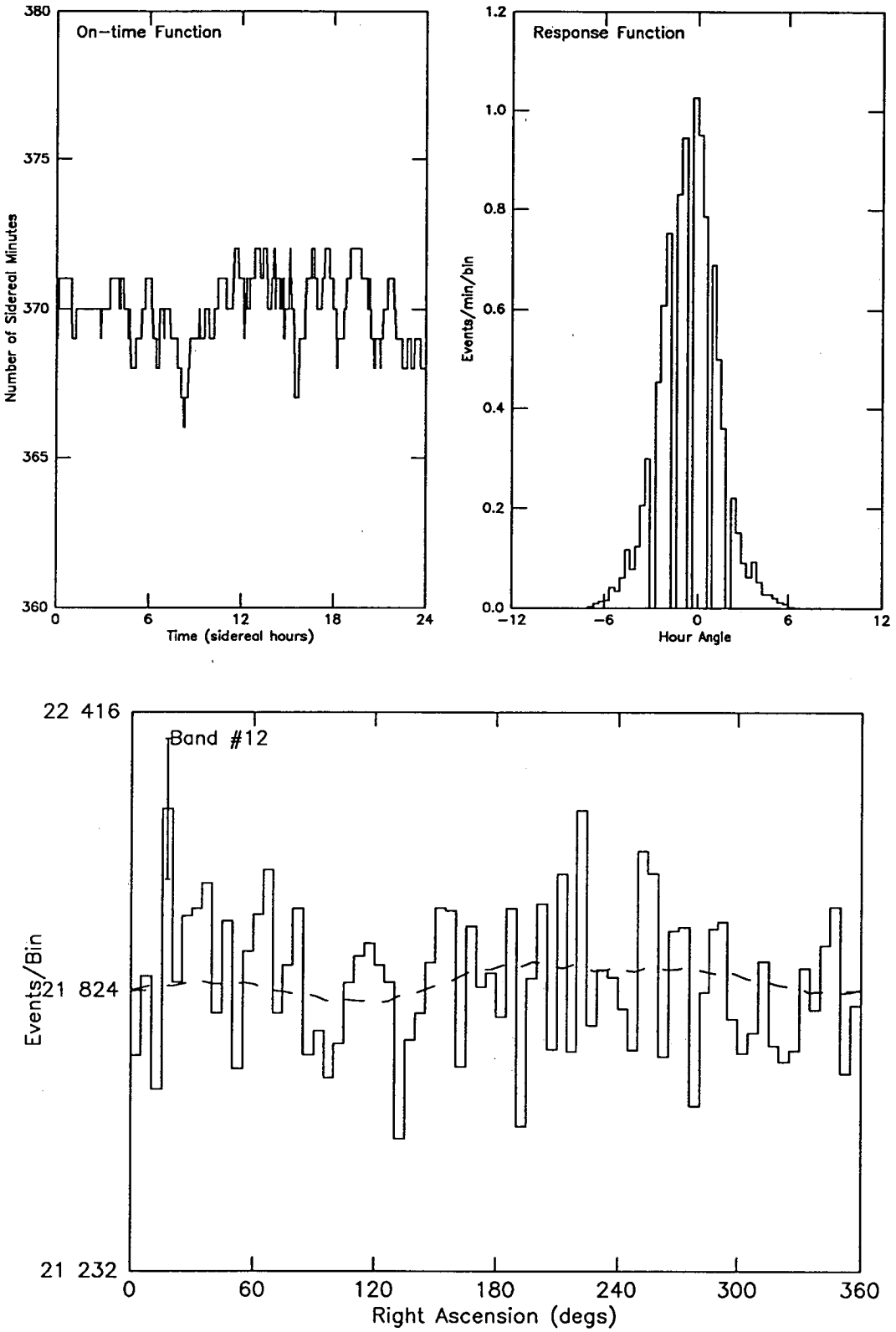

Figure C.12 Declination Band 35°S - 40°S.

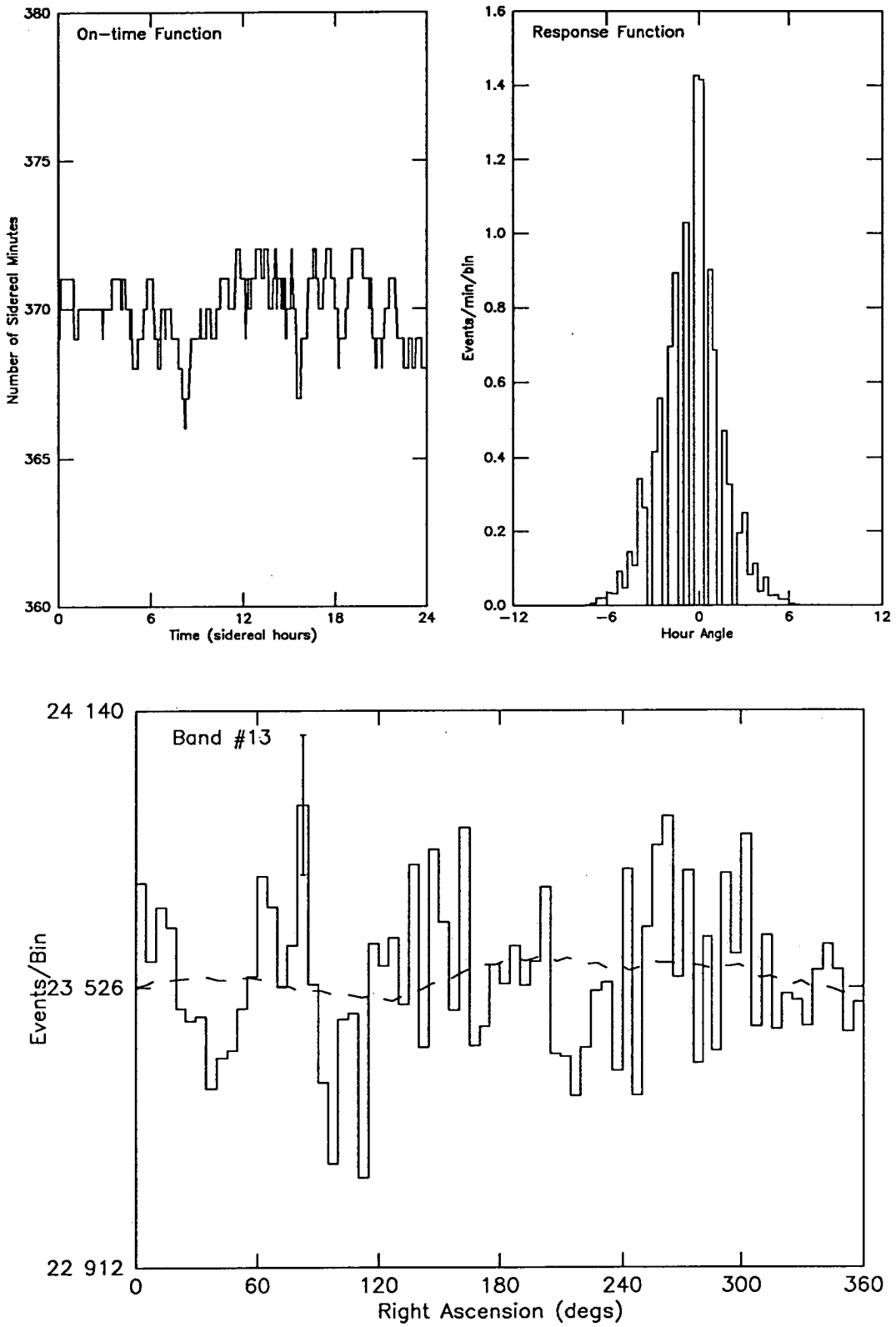

Figure C.13 Declination Band 40°S - 45°S.

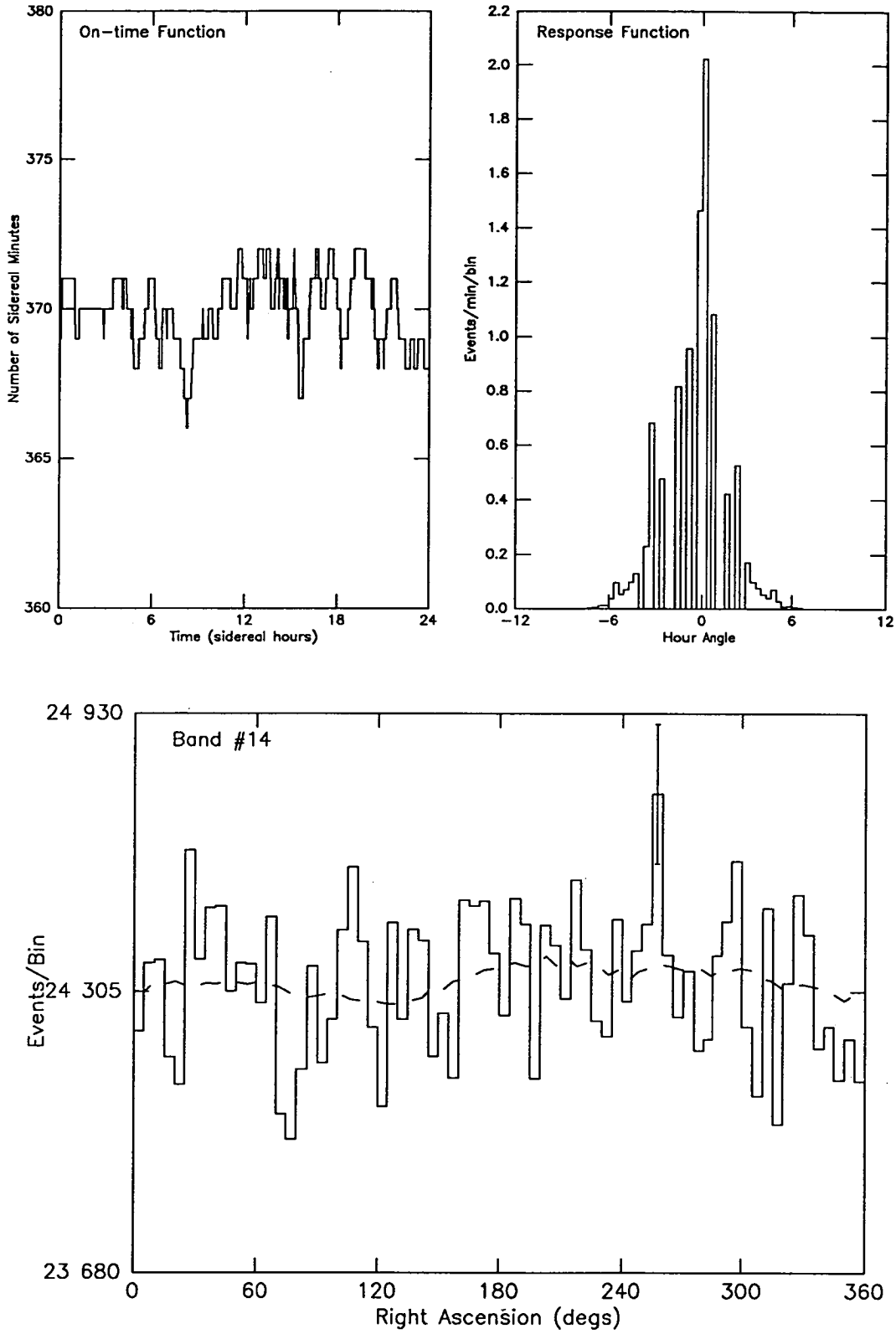

Figure C.14 Declination Band 45°S - 50°S.

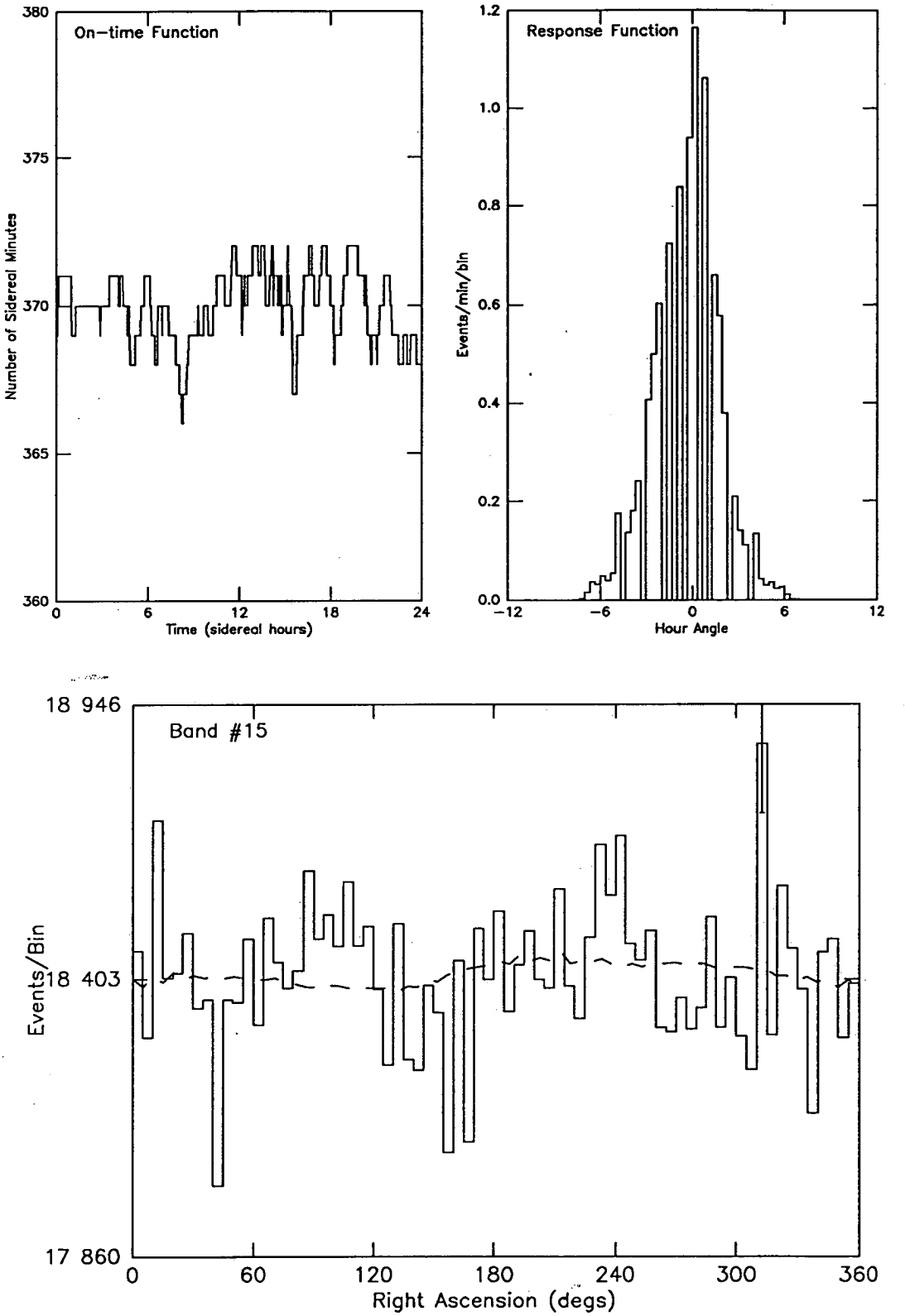

Figure C.15 Declination Band 50°S - 55°S.

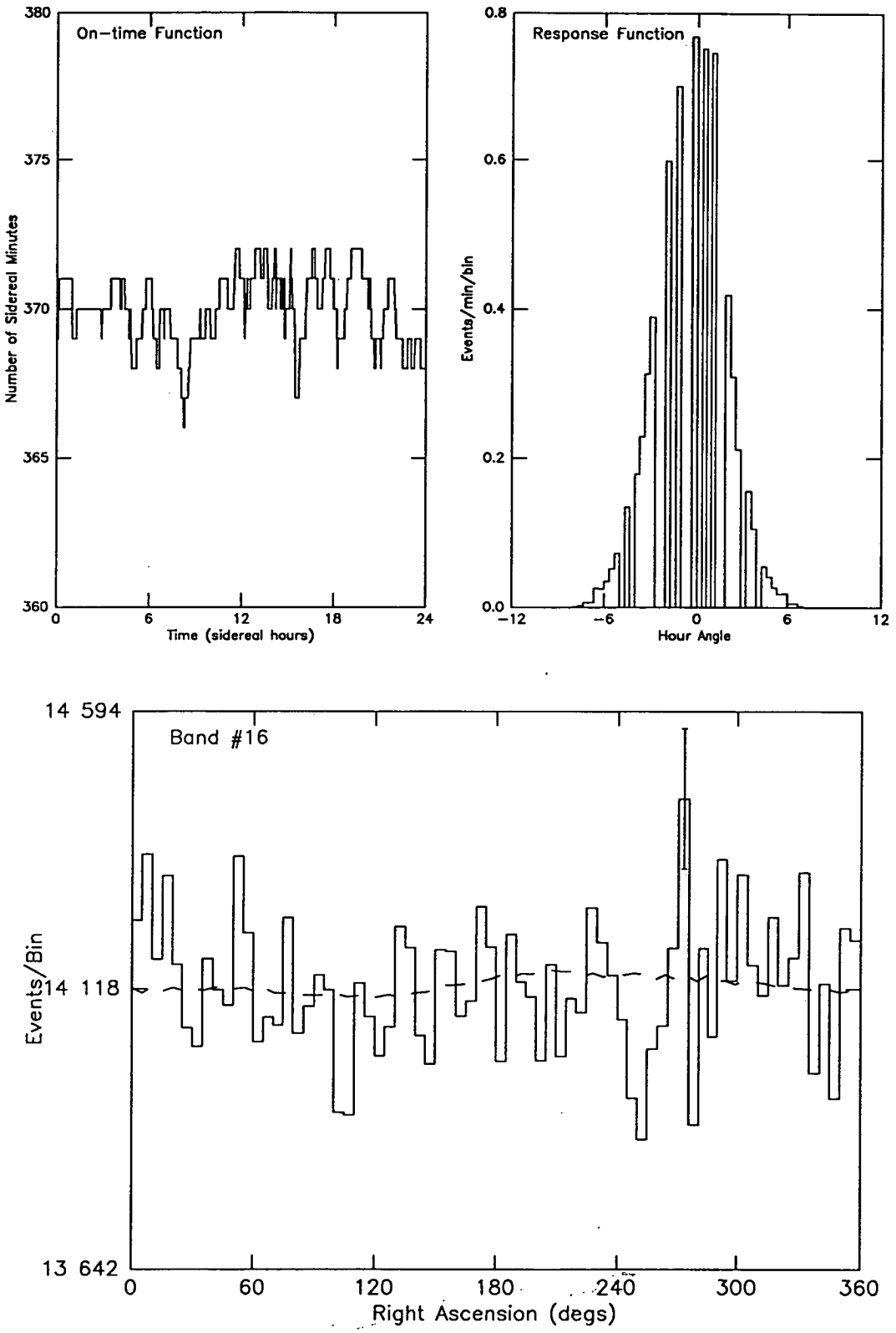

Figure C.16 Declination Band 55°S - 60°S.

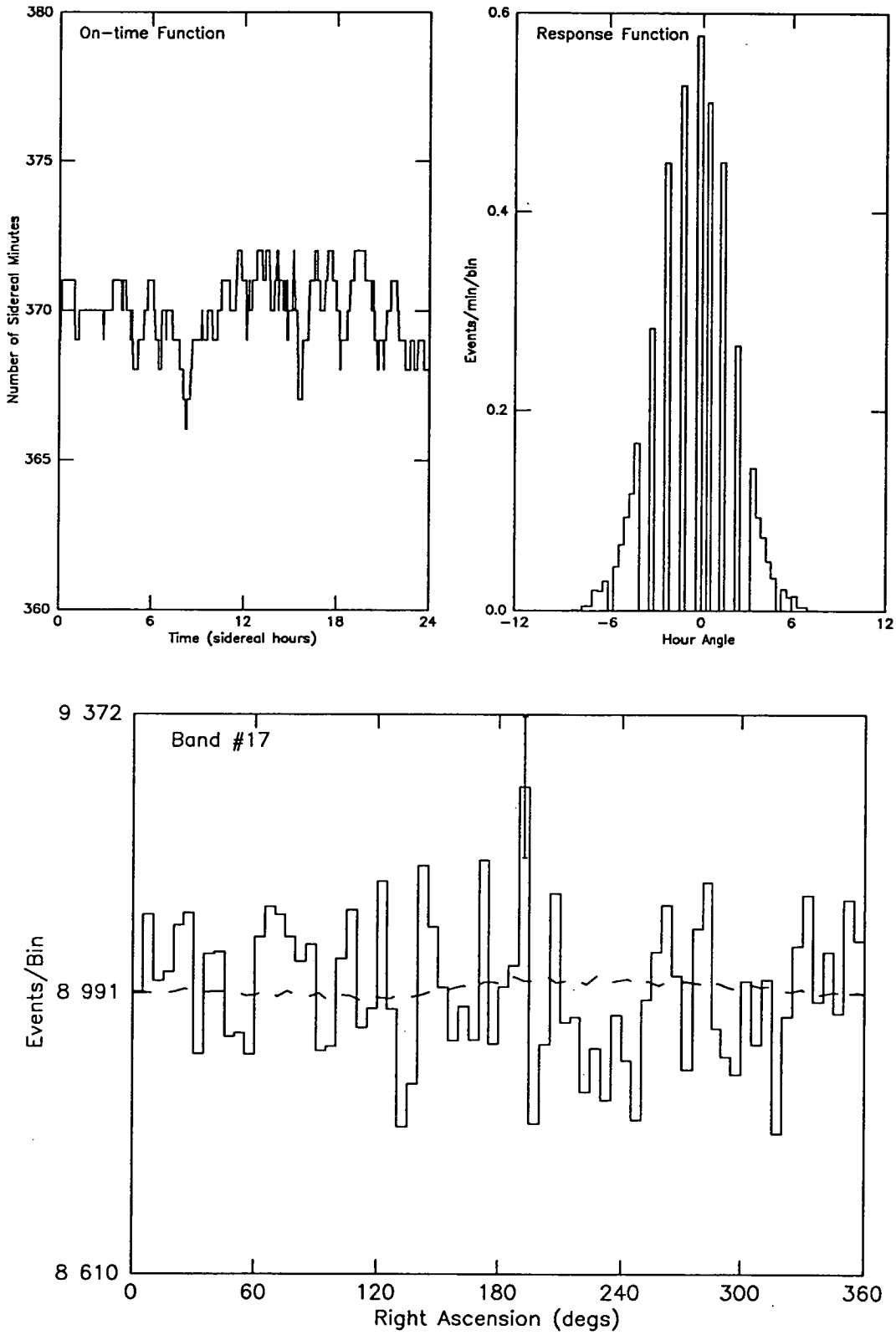

Figure C.17 Declination Band 60°S - 65°S.

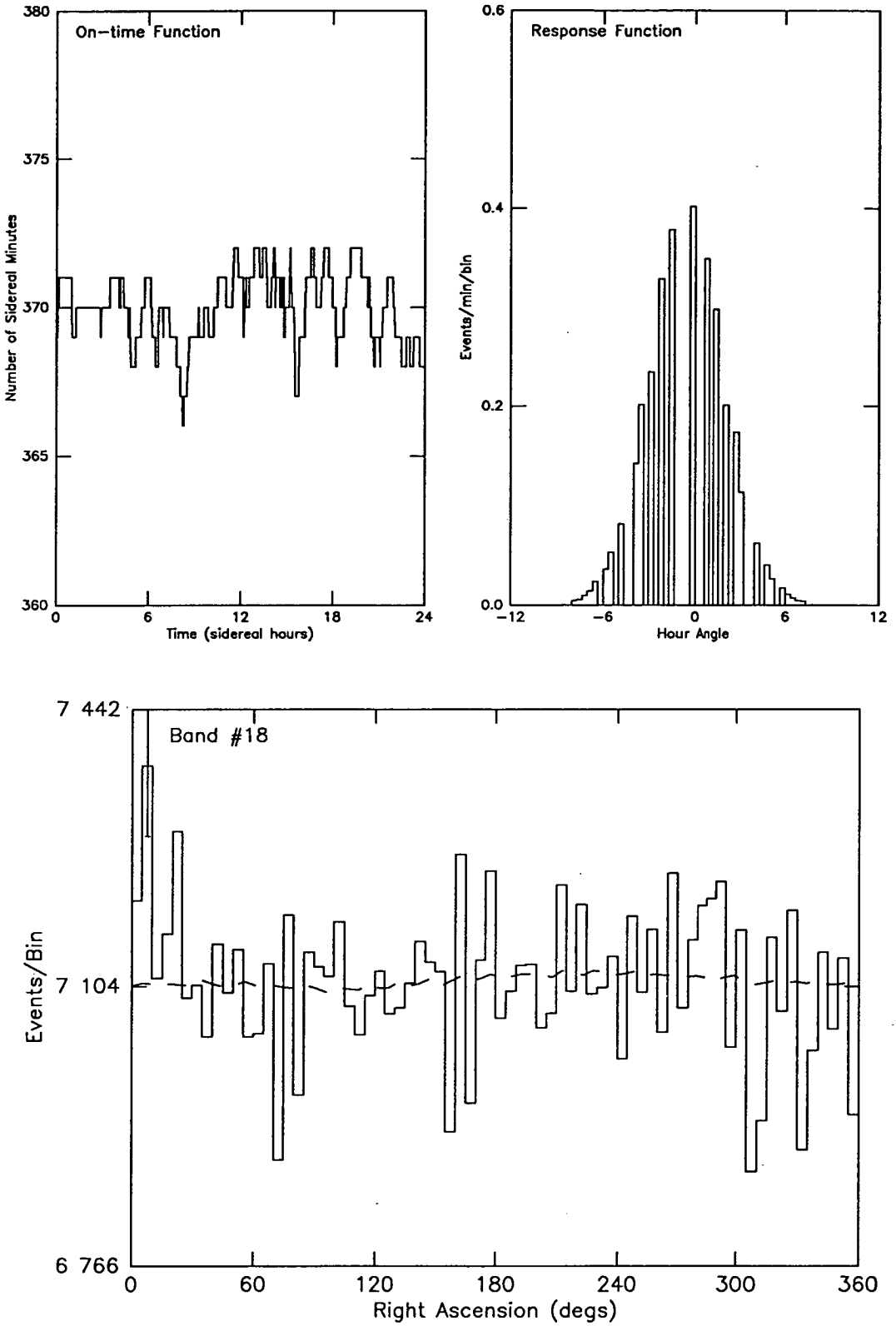

Figure C.18 Declination Band 65°S - 70°S.

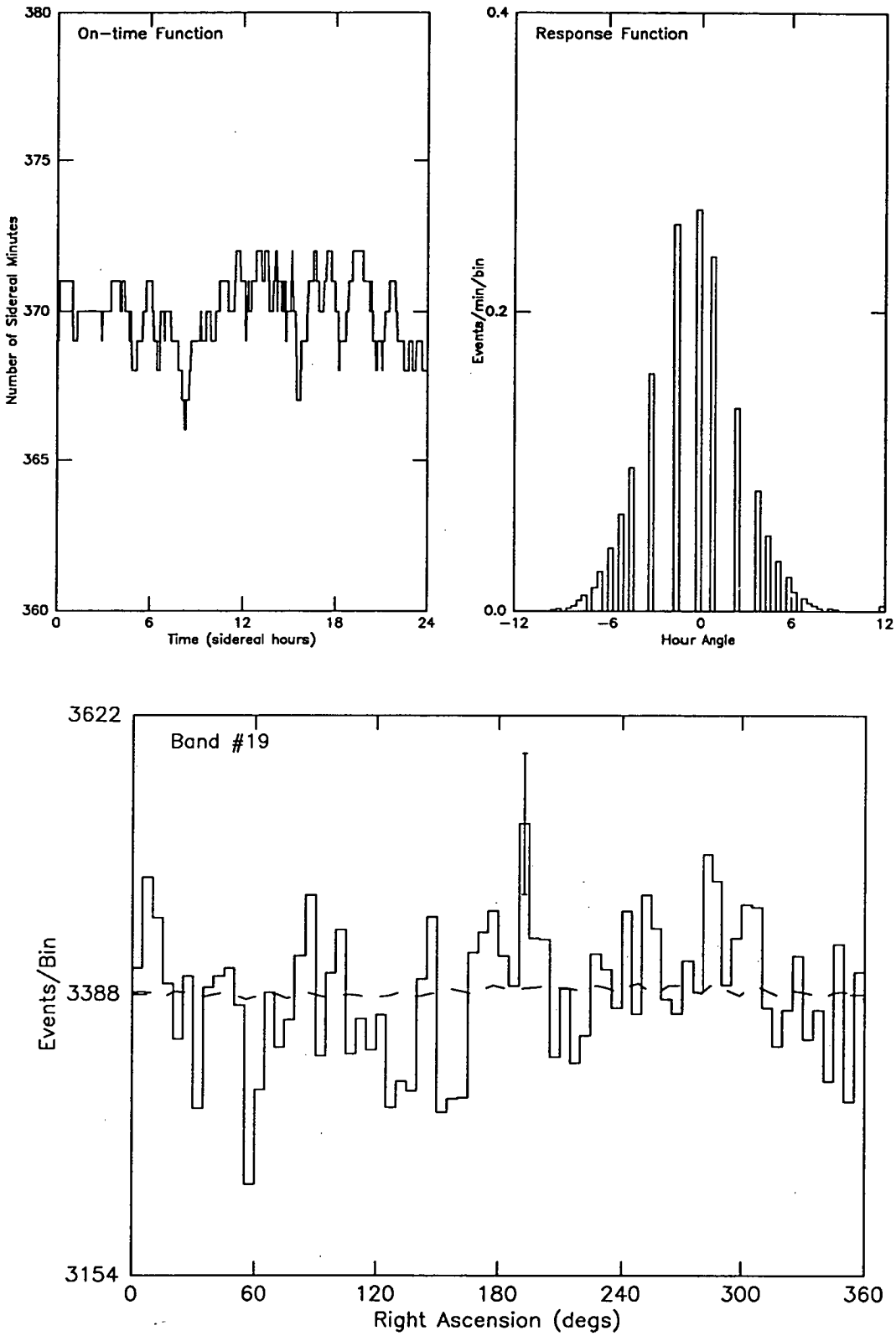

Figure C.19 Declination Band 70°S - 75°S.

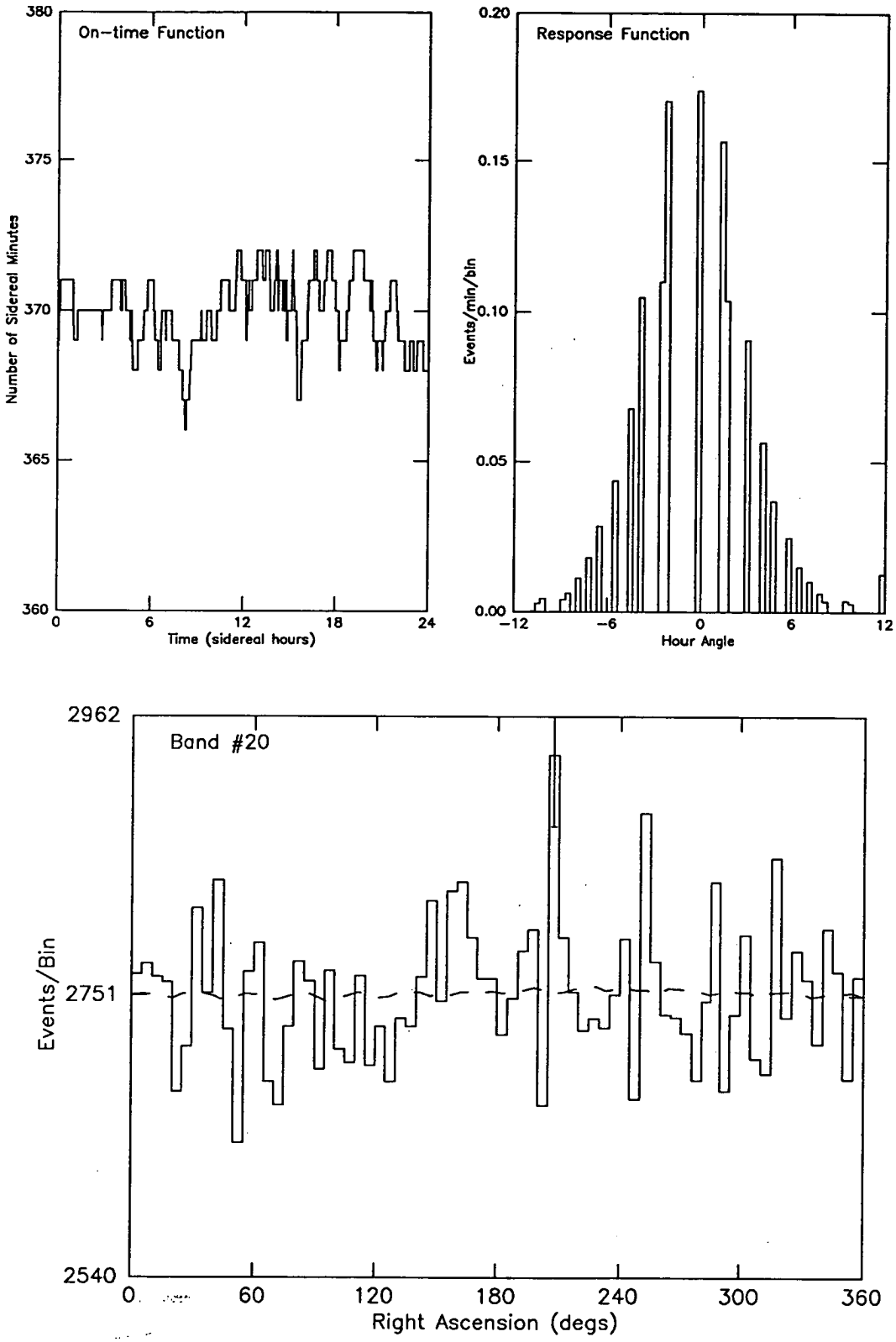

Figure C.20 Declination Band 75°S - 80°S.

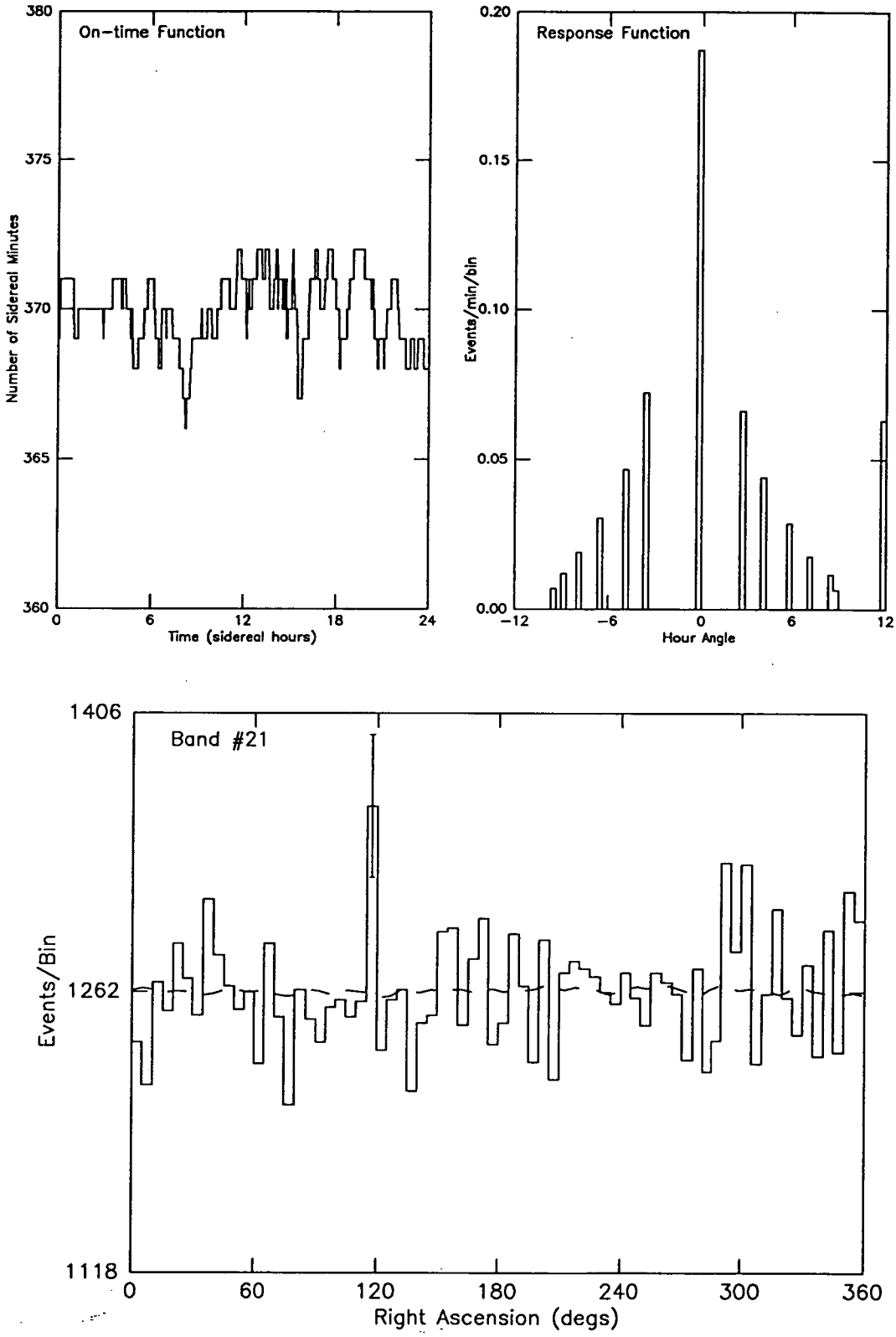

Figure C.21 Declination Band 80°S - 85°S.

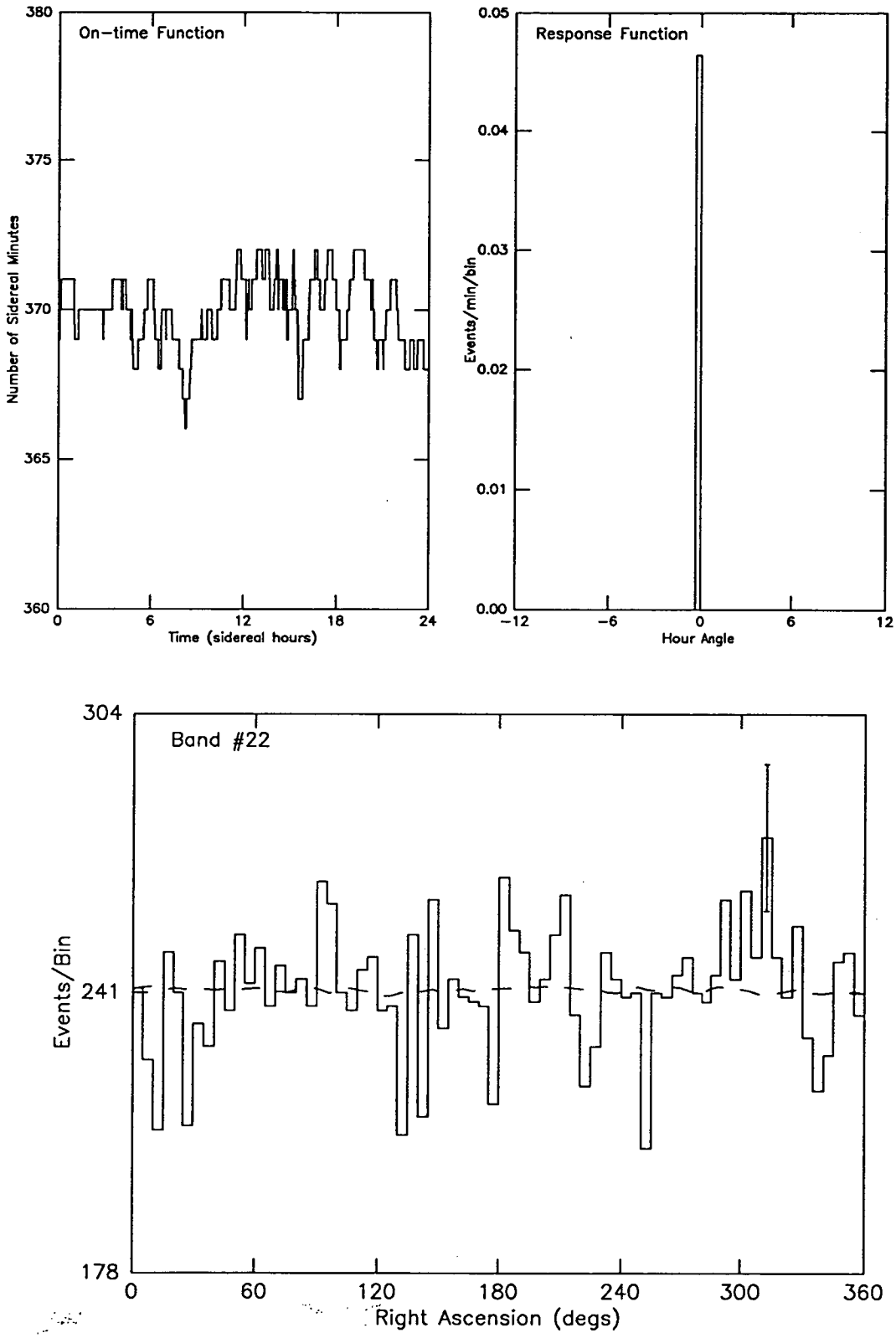

Figure C.22 Declination Band 85°S - 90°S.

References

Abdullah. M.M., Ashton, F., Fatemi, J., 1983, *Proc. 18th ICRC* (Bangalore) **9**, 141.

Acharya, B.S. and Capdevielle, J.N., 1985, *J. Phys. G: Nucl. Phys.* **11**, 1387.

Albats, P., Frye, G.M. Jr., Thomson, G.B., Hopper, V.D., Mace, O.B., Thomas, J.A., 1974, *Nature* **251**, 400.

Allkofer, O.C., Carstensen, K., Dau, W.D., 1971, *Proc. 12th ICRC* (Hobart) **4**, 1314.

Allkofer, O.C., *et al.*, 1979, *Proc. 16th ICRC* (Kyoto) **4**, 170.

Barret, P.H., Bollinger, L.M., Cocconi, G., Eisenberg, Y., Greisen, K., 1952, *Rev. Mod. Phys.* **24** (3), 133.

Barrowes, S.C., 1972, *Astrophys. J.* **177**, 45.

Battistoni, G., *et al.*, 1985, *Phys. Lett. B.* **155**, 465.

Baym, G., Kolb, E.W., McLerran, L., Walker, T.P., Jaffe, R.L., 1985, *Phys. Lett. B.* **160**, 181.

Bazer-Bachi, A.R., Vedrenne, G., Sheldon, W.R., Benbrook, J.R., 1975, *Proc. 14th ICRC* (Munchen) **12**, 4151.

Bazer-Bachi, A.R., *et al.*, 1979, *Proc. 16th ICRC* (Kyoto), paper MG 7-11 (summary only).

Bennett, K., *et al.*, 1977, *Astron. Astrophys.* **61**, 279.

Bergamasco, L., *et al.*, 1983, *Nuovo Cimento C.* **6**, 569.

Berger, C.H., *et al.*, 1986, *Phys. Lett. B.* **174**, 118.

Bevington, P.R., 1969, *Data Reduction and Error Analysis for the Physical Sciences* (McGraw Hill).

Bhat, P.N., Gupta, S.K., Ramana Murthy, P.V., Sreekantan, B.V., Tonwar, S.C., Viswanath, P.R., 1980, *Astron. Astrophys.* **81**, L3.

Bhat, P.N., Ramana Murthy, P.V., Sreekantan, B.V., Viswanath, P.R., 1986, *Nature* **319**, 127.

Bhat, P.N., Gupta, S.K., Ramana Murthy, P.V., Sreekantan, B.V., Tonwar, S.C., Viswanath, P.R., 1987, *Astron. Astrophys.* **178**, 242.

Bilokon, H., Castellina, A., D'Ettorre Piazzoli, B., Mannocchi, G., Picchi, P., Vernetto, S., 1985, *Nuovo Cimento C.* **8**, 93.

Bionta, R.M., *et al.*, 1987, *Phys. Rev. D.* **36**, 30.

Bologna, G., *et al.*, 1985, *Nuovo Cimento C.* **8**, 76.

Buccheri, R., 1985, *Proc. Workshop on Techniques in Ultra High Energy Gamma Ray Astronomy* (La Jolla) eds. R.J. Protheroe and S.A. Stephens (University of Adelaide), p98.

Buccheri, R., Ozel, M.E., Sacco, B., 1987, *Astron. Astrophys.* **175**, 353.

Bugaev, E.V., Zaslavskaya, E.S., Naumov, V.A., Sinegovsky, S.I., 1987, *Proc. 20th ICRC* (Moscow) **6**, 305.

Bukata, R.P. and Standil, S., 1965, *Can. J. Phys.* **43**, 883.

Cassidy, G.L., Keuffel, J.W., Thompson, J.A., 1973, *Phys. Rev. D.* **7**, 2022.

Cheng, K.S., Ho, C., Ruderman, M., 1986a, *Astrophys. J.* **300**, 500.
1986b, *Astrophys. J.* **300**, 522.

Clay, R.W., Gerhardy, P.R., Liebing, D.F., 1984, *Aust. J. Phys.* **37**, 91.

Cordes, J.M., Downs, G.S., Krause-Polstorff, J., 1988, *Astrophys. J.* **330**, 847.

Crookes, I.N. and Rastin, B.C., 1971, *Proc. 12th ICRC* (Hobart) **4**, 1325.

Crouch, M.F., *et al.*, 1978, *Phys. Rev. D.* **18**, 2238.

Crouch, M.F., 1987, *Proc. 20th ICRC* (Moscow) **6**, 165.

De Jager, O.C., Swanepoel, J.W.H., Raubenheimer, B.C., 1986, *Astron. Astrophys.* **170**, 187.

De Jager, O.C., De Jager, H.I., Raubenheimer, B.C., 1987, *Proc. 20th ICRC* (Moscow) **1**, 298.

De Jager, O.C., Swanepoel, J.W.H., Raubenheimer, B.C., 1989, *Astron. Astrophys.* **221**, 180.

Dingus, B.L., *et al.*, 1988, *Phys. Rev. Lett.* **61**, 1906.

Dorman, L.I., 1987, *Proc. 20th ICRC* (Moscow) **8**, 186.

Dowthwaite, J.C., Harrison, A.B., Kirkman, I.W., Macrae, H.J., Orford, K.J., Turver, K.E., Walmsley, M., 1984, *Nature* **309**, 691.

Dzikowski, T., Gawin, J., Grochalska, B., Wdowczyk, J., 1983, *J. Phys. G: Nucl. Phys.* **9**, 459.

Edwards, P.G., Protheroe, R.J., Rawinski, E., 1985, *J. Phys. G: Nucl. Phys.* **11**, L101.

Fegan, D.J., McBreen, B., O'Sullivan, C., 1983, *Phys. Rev. Lett.* **51**, 2341.

Fujii, Z. and Jacklyn, R.M., 1979, *Proc. 16th ICRC* (Kyoto) **4**, 336.

Fujimoto, K., Murakami, K., Kondo, I., Nagashima, K., 1977, *Proc. 15th ICRC* (Plovdiv) **4**, 321.

Gaisser, T.K. and Stanev, T., 1985, *Nucl. Instr. and Meth.* **A235**, 183.

Gardner, F.F. and Whiteoak, J.B., 1969, *Nature* **224**, 891.

Gerhardy, P.R. and Clay, R.W., 1983, *Proc. 18th ICRC* (Bangalore) **2**, 142.

Gibson, A.I., *et al.*, 1982, *Nature* **296**, 833.

Greiner, L.A., Hermsen, W., Clear, J., 1988, *Astron. Astrophys.* **204**, 117.

Grindlay, J.E., Helmken, H.F., Hanbury Brown, R., Davies, J., Allen, L.R., 1975a, *Astrophys. J.* **197**, L9.
1975b, *Astrophys. J.* **201**, 82.

Halzen, F., Hoyer, P., Yamdagni, N., 1987, *Phys. Lett. B.* **190**, 211.

Hamilton, P.A., King, E.A., McConnell, D., McCulloch, P.M., 1989, *IAU Circ.* **4708**.

Harding, A.K., 1981, *Astrophys. J.* **245**, 267.

Harnden, F.R. Jr., Grant, P.D., Seward, F.D., Kahn, S.M., 1985, *Astrophys. J.* **299**, 828.

Harnden, F.R. Jr. and Gorenstein, P., 1973, *Nature* **241**, 107.

Hayvaerts, J. and Signore, M., 1981, *Astron. Astrophys.* **96**, 36.

Hirata, K.S., *et al.*, 1988, *Phys. Lett. B.* **205**, 416.

Hoel, P.G., 1971, *Introduction to Mathematical Statistics* (John Wiley & Sons).

Holloway, N.J. and Pryce, M.H.L., 1981, *Mon. Not. Roy. Astron. Soc.* **194**, 95.

Humble, J.E., Fenton, A.G., Fenton, K.B., 1985, *Proc. 19th ICRC* (La Jolla) **5**, 39.

Jokisch, H. and Carstensen, K., 1975, *Proc. 14th ICRC* (Munchen) **2**, 578.

Kamata, K., *et al.*, 1968, *Can. J. Phys.* **46**, S72.

Kanbach, G., *et al.*, 1980, *Astron. Astrophys.* **90**, 163.

Krishnamohan, S. and Downs, G.S., 1983, *Astrophys. J.* **265**, 372.

Krishnaswamy, M.R., *et al.*, 1986, *Nuovo Cimento C.* **9**, 167.

Large, M.I., Vaughan, A.E., Mills, B.Y., 1968, *Nature* **220**, 340.

Lloyd-Evans, J., Coy, R.N., Lambert, A., Lapikens, J., Patel, M., Reid, R.J.O., Watson A.A., 1983, *Nature* **305**, 784.

Lyons, P.R.A., 1981, Ph.D. Thesis, University of Tasmania.

Lyons, P.R.A., Fenton, A.G., Fenton, K.B., 1981, *Proc. 17th ICRC* (Paris) 4, 300.

Manchester, R.N. and Taylor, J.H., 1977, *Pulsars* (Freeman).

Manchester, R.N., *et al.*, 1978, *Mon. Not. Roy. Astron. Soc.* **184**, 159.

Marshak, M.L., *et al.*, 1985, *Phys. Rev. Lett.* **54**, 2079.

McCulloch, P.M., Hamilton, P.A., Royle, G.W.R., Manchester R.N., 1983, *Nature* **302**, 319.

McCulloch, P.M., Klekociuk, A.R., Hamilton, P.A., Royle, G.W.R., 1987, *Aust. J. Phys.* **40**, 725.

McCulloch, P.M., 1989, Private Communication.

McCulloch, P.M., Hamilton, P.A., McConnell, D., King, E.A., 1990, *Nature* **346**, 822.

Miyake, S., 1963, *J. Phys. Soc. Japan* **18**, 1093.
1973, *Proc. 13th ICRC* (Denver) **5**, 3638.

Moore, W.E., Agrawal, P.C., Garmire, G., 1974, *Astrophys. J.* **189**, L117.

Morello, C., Navarra, G., Vallania, P., 1983, *Proc. 18th ICRC* (Bangalore) **2**, 137.

Nakatsuka, T., Kobayakawa, K., Kitamura, T., 1987, *Proc. 20th ICRC* (Moscow) **6**, 261.

Ogelman, H. and Zimmermann, H.U., 1989, *Astron. Astrophys.* **214**, 179.

Oyama, Y., *et al.*, 1986, *Phys. Rev. Lett.* **56**, 991.

Particle Data Group, 1986, *Phys. Lett. B.* **170**, 1.

Peterson, B.A., *et al.*, 1978, *Nature* **276**, 475.

Protheroe, R.J., Clay, R.W., Gerhardy, P.R., 1984, *Astrophys. J.* **280**, L47.

Protheroe, R.J., 1985, *Proc. 19th ICRC* (La Jolla) **3**, 485.
1987, *Proc. Astron. Soc. Aust.* **7** (2), 167.

Protheroe, R.J. and Clay, R.W., 1985, *Nature* **315**, 205.

Rappaport, S., Bradt, H., Doxsey, R., Levine, A., Spada, G., 1974, *Nature* **251**, 471.

Raubenheimer, B.C., North, A.R., De Jager, O.C., van Urk, G., van Tonder, A.J., 1986, *Astrophys. J.* **307**, L43.

Ricker, G.R., Gerassimenko, M., McClintock, J.E., Ryckman, S.G., Lewin, W.H.G., 1973, *Astrophys. J.* **186**, L111.

Rossi, B.B., 1952, *High-Energy Particles* (Constable, London).

Sagisaka, S., Murakami, K., Inoue, K., Inoue, A., Nagashima, K., 1979, *Proc. 16th ICRC* (Kyoto) **4**, 235.

Samorski, M. and Stamm, W., 1983a, *Astrophys. J.* **268**, L17.
1983b, *Proc. 18th ICRC* (Bangalore) **11**, 244.

Scott, W.I., 1963, *Rev. Mod. Phys.* **35**, 231.

Sekido, Y., Yoshida, S., Kamiya, Y., 1959, *Phys. Rev.* **113**, 1108.

Sheldon, W.R., *et al.*, 1973, *Nucl. Instr. and Meth.* **111**, 133.

Stanev, T., Gaisser, T.K., Halzen, F., 1985, *Phys. Rev. D.* **32**, 1244.

Stenger, V.J., 1985, *Nature* **317**, 411.

Stephens, S.A. and Golden, R.L., 1987, *Proc. 20th ICRC* (Moscow) **6**, 173.

Sullivan, J.D., 1971, *Nucl. Instr. and Meth.* **95**, 5.

Sun, L., 1987, *Proc. 20th ICRC* (Moscow) **2**, 27.

Svoboda, R., *et al.*, 1987, *Astrophys. J.* **315**, 420.

Thompson, D.J., Fichtel, C.E., Kniffen, D.A., Ogelman, H.B., 1975, *Astrophys. J.* **200**, L79.

Thompson, M.G., 1973, in *"Cosmic Rays at Ground Level"* ed. A.W. Wolfendale (The Institute of Physics), p17

Tumer, O.T., Dayton, B., Long, J., O'Neill, T., Zych, A., White, R.S., 1984, *Nature* **310**, 214.

Vladimirsky, B.M., Stepanian, A.A., Fomin, V.P., *et al.*, 1973, *Proc. 13th ICRC* (Denver) **1**, 456.

Wallace, P.T., *et al.*, 1977, *Nature* **266**, 692.

Wang, C.P., Lee, A.H., 1969, *J. Geophys. Res.* **74**, 2439.

Warner, B., Nather, R.E., Macfarlane, M., 1969, *Nature* **222**, 233.

Wdowczyk, J., 1965, *Proc. 9th ICRC* (London) **2**, 691.

Wdowczyk, J. and Wolfendale, A.W., 1983, *Nature* **305**, 609.

Wilson, C.W., 1985a, Ph.D. Thesis, University of Tasmania.

Wilson, C.W., Fenton, A.G., Fenton, K.B., 1985b, *Proc. 19th ICRC* (La Jolla) **8**, 175.

Wolfendale, A.W., 1973, in *"Cosmic Rays at Ground Level"* ed. A.W. Wolfendale (The Institute of Physics), p1.